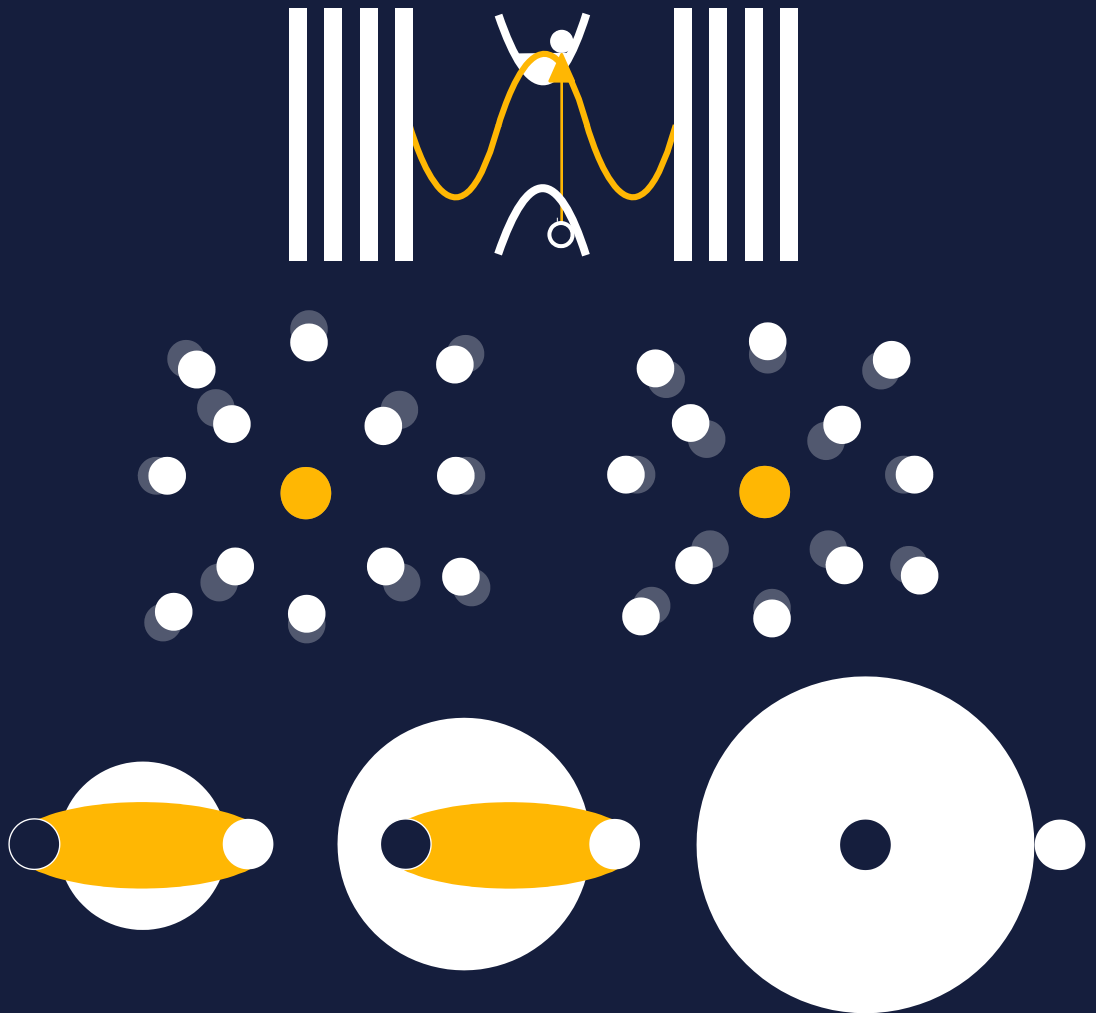


Antonio Tiene

---

# Charged Polaritons in Two-Dimensional Semiconductors

---





---

# Charged Polaritons in Two-Dimensional Semiconductors

---

Tesis Doctoral presentada para la obtención del  
**TÍTULO DE DOCTOR EN CIENCIAS FÍSICAS**

de la

**UNIVERSIDAD AUTÓNOMA DE MADRID,  
DEPARTAMENTO DE FÍSICA DE  
LA MATERIA CONDENSADA**

por

**ANTONIO TIENE**

Directora:  
Dra. Francesca M. Marchetti

Tribunal:  
Dr. Carlos Tejedor  
Dr. Johannes Feist  
Dr. Atac Imamoglu  
Dr. Jonathan Keeling  
Dra. Maria J. Calderon  
Dr. Luis Brey  
Dr. Charles Creffield

**Madrid, junio de 2023**



*Ai miei genitori, per esserci sempre stati.*

*A mia sorella ed il mio futuro nipote.*

*A me stesso, per averci creduto.*

*Ad Inés, la mia città.*



# Acknowledgments

I want to start by thanking my thesis advisor, Francesca, for her unwavering support, encouragement, and guidance throughout this research journey. Francesca's scientific expertise and rigorous approach have been instrumental in shaping my analytical skills and research interests. But what I appreciate most about Francesca is her patience and willingness to always make time for me, whether through in-person meetings or lengthy Skype calls. Her mentorship has been an incredible gift, and I am grateful to have had the opportunity to learn from her.

I am also deeply grateful to the distinguished scholars who served on my committee, Drs. Carlos Tejedor, Johannes Feist, Atac Imamoglu, Jonathan Keeling, Maria Jose Calderon, Luis Brey, and Charles Creffield. Their high standards have challenged me to push the boundaries of my research and strive for excellence. It was an honor to defend my work in front of such inspiring and supportive individuals.

I want to thank Drs. Jonathan Keeling, Meera Parish, and Jesper Levinsen. They have been fundamental in guiding my research and fostering my academic growth. I am grateful for their guidance, feedback, and support, and for the enriching and inspiring research environment they provided. I also want to thank Meera and Jesper for their hospitality and generosity during my stay in Melbourne. They welcomed me into their academic community and provided me with invaluable expertise and insights.

No puedo dejar de dedicar unas palabras de agradecimiento a todos aquellos nuevos y viejos amigos que me han acompañado en este viaje, un viaje repleto de momentos preciosos pasados con personas increíbles. Con la certeza de que esto no es un adiós, les expreso mi más sincero agradecimiento.

Un agradecimineto alle mie due famiglie. Mi familia española, que desde mi llegada ha estado siempre a mi lado haciendome sentir en casa. E alla mia famiglia, senza la quale non sarei la persona che sono oggi.

Y por ultimo al mio fiore prezioso, fonte di amore e gioia.



# Abstract

The injection of charged carriers in two-dimensional semiconductors, either through gating or doping, has recently opened numerous novel exciting research directions and potential applications in the development of high-performing optoelectronic devices. A significant benefit is the ability to combine optical and electrical control of carriers, which forms one of the main focuses of this thesis. Among two-dimensional semiconductors, transition metal dichalcogenide monolayers have been demonstrated to possess exceptional optical properties, such as a significant exciton resonance even at room temperature, making them ideal for generating nanophotonic devices. Crucially for this dissertation, transition metal dichalcogenide monolayers allow for both optical and electrical control of carriers, offering easy electrical tunability of excitonic properties through Coulomb interactions and Pauli blocking effects. Further, the injection of charges can lead to the realization of charged exciton complexes, such as trions.

The possibility of achieving strong coupling between matter and light is another essential ingredient in this thesis background. Strong light-matter coupling can be routinely achieved in optical microcavities with embedded quantum wells or transition metal dichalcogenide monolayers. The interaction between an exciton and the confined optical cavity mode in these structures can result in the creation of exciton-polaritons, which are hybrid quasiparticles that combine the properties of both matter and light. The field of cavity polaritons has seen a remarkable surge in interest over the past few decades, some of the most notable achievements include the observation of condensation and lasing, the realization of superfluid phases, and the study of topology.

The focus of this dissertation revolves around exploring the interplay between the physics of charged semiconductors and strong light-matter coupling. Thanks to recent technological advancements, semiconductor devices can now be precisely and effectively manipulated, providing a means to explore the complex interplay between electronic doping and strong light-matter coupling. This presents an opportunity to generate, control, and detect novel phases involving photons, electron-hole pairs, and an electron gas.

The thesis is structured into 5 chapters. Chapters 1 and 2 serve as an

introduction, providing a self-contained overview of the relevant background material, covering the key theoretical and experimental aspects that are necessary to understand the research objectives and findings presented in later chapters. Chapters 3, 4, and 5 present the original results of this thesis, which have led to the publications listed in the “List of publications”. Conclusions and perspectives of this work are gathered in the final chapter “General conclusions and future perspectives”. The subsequent text provides a brief summary of the primary objectives and implications of the research presented in chapters 3, 4, and 5.

Chapter 3 of this thesis explores the interplay between temperature and the optical response of doped two-dimensional semiconductors. By investigating the problem of a few excitons generated in a Fermi sea of charge carriers, we employ the Fermi polaron formalism to study how quantum excitations of the fermionic bath dress the excitonic impurity, resulting in two polaron quasiparticles, the attractive polaron and the repulsive polaron. We reveal a crossover between two regimes, the first at low temperatures and high doping where the attractive branch is a well defined quasiparticle and the second at high temperatures and low doping where this branch subsumes into the continuum of trion-hole scattering states, ceasing to be a well-defined quasiparticle resonance. A recent debate has arisen over how this many-body picture compares with the standard description of the system in terms of few-body particles, such as excitons and trions, and which of the two approaches is more appropriate for describing the optical response of the system in the limit of strong imbalance of charges. Our research provides a crucial insight into this debate by demonstrating that the two descriptions are connected only when the critical role of temperature is considered. The crossover leads to important changes in the system spectral lineshape that would be overlooked if the crucial role of temperature would not be properly taken into account. In the low-doping and/or high-temperature regimes, we use a perturbatively exact quantum virial expansion and analyze the optical response and discover that the coherent dressing cloud of the attractive polaron quasiparticle is disrupted by thermal fluctuations. This approach predicts new photoluminescence features, such as a non-trivial behavior of the attractive peak near the trion energy that is connected to resonant exciton-electron scattering in two dimensions, and a Lorentzian repulsive peak. The findings of our study are compared to a recent experiment conducted on a monolayer of doped MoSe<sub>2</sub>, and we find an excellent agreement. Our analysis demonstrates analytically that the virial expansion recovers the predictions of the trion model when the Fermi energy approaches zero.

In chapter 4, we investigate the optical properties of a doped two-dimensional semiconductor in the *indistinguishable carrier polaron* (ICP) regime, where one of the charges forming the exciton is indistinguishable from

---

the Fermi sea formed by doping the system. Most notably, the indistinguishability requires the three-body trion state to have  $p$ -wave symmetry. We use a polaron description to study the effects of the Fermi sea, where the exciton is dressed by a single particle-hole excitation. We compare our findings to those obtained in the *distinguishable carrier polaron* (DCP) case and observe that the spectral function of the DCP case is characterized by attractive and repulsive branches due to the ground state  $s$ -wave trion being bound, while in the ICP case, two branches are present only when the  $p$ -wave trion is bound. We demonstrate that there is a transfer of oscillator strength from the repulsive to the attractive branch as doping increases in both cases. Although the  $p$ -wave trion state does not couple directly to light, this transfer of spectral weight is possible because the trion-hole complex indirectly couples to light via its coupling to the exciton. We find that the spectral weight of the attractive branch has a different dependence on doping in the ICP and DCP cases. Specifically, in the DCP case, it grows linearly with the Fermi sea density at low doping, while in the ICP case, it grows quadratically due to the  $p$ -wave nature of the trion state. In the regime of strong light-matter coupling, the transfer of oscillator strength to the attractive branch results in the appearance of three polariton modes. We discuss how the Rabi splittings in the strong-coupling polariton spectrum enable effective measurement of the weak-coupling quasiparticle weights. We also observe that the difference in the nature of the repulsive branch in the ICP and DCP cases arises from the orbital character of the states involved. At high doping, the repulsive branch and continuum states have different orbital characters and do not mix for the ICP case. Additionally, we find that the orbital characters of attractive and repulsive branches swap as doping increases, with the Fermi sea hole in the attractive branch having  $s$ -wave symmetry at high doping.

In chapter 5, we explore the interplay between carrier density imbalances, photon fields, and electron-hole pairing in two-dimensional structures. Our investigation builds on previous research and dives deeper into the intriguing phenomenon of the Fulde-Ferrell-Larkin-Ovchinnikov (FFLO) phase, which arises due to a high density of excess charge leading to a roton minimum in the exciton dispersion. With the help of a variational state, we unveil the phase diagram of this complex system, shedding light on the impact of photon coupling on the excitonic FFLO roton minimum. Our findings demonstrate that while coupling to low mass cavity photons suppresses the roton minimum, the formation of an FFLO phase limits the coupling to light, thus introducing new insights into the nature of pairing phenomena in these structures. Moreover, we discover that the excess charge also affects the energy of the cavity photon mode, providing us with a tool to observe and compare structures with different light-matter coupling, by changing the Rabi splitting by embedding different numbers of quantum wells into the planar cavity.

Overall, our study provides insights into the complex behavior of doped two-dimensional semiconductors and contributes to the understanding of optical properties in strongly correlated electron-hole systems.

# Resumen

La inyección de portadores cargados en semiconductores bidimensionales, ya sea mediante gating o dopaje, ha abierto numerosas e interesantes vías de investigación y aplicaciones potenciales en el desarrollo de dispositivos optoelectrónicos de alto rendimiento. Una ventaja significativa es la capacidad de combinar el control óptico y eléctrico de los portadores, que constituye uno de los principales focos de esta tesis. Entre los semiconductores bidimensionales, se ha demostrado que las monocapas de dicalcogenuros de metales de transición poseen propiedades ópticas excepcionales, como una resonancia excitónica significativa incluso a temperatura ambiente, lo que las hace ideales para generar dispositivos nanofotónicos. Para esta tesis, las monocapas de dicalcogenuro de metales de transición permiten el control óptico y eléctrico de los portadores, ofreciendo una fácil sintonización eléctrica de las propiedades excitónicas a través de las interacciones de Coulomb y los efectos de bloqueo de Pauli. Además, la inyección de cargas puede conducir a la realización de complejos excitónicos cargados, como los triones.

La posibilidad de lograr un fuerte acoplamiento entre la materia y la luz es otro ingrediente esencial en el trasfondo de esta tesis. En microcavidades ópticas con pozos cuánticos embebidos o monocapas de dicalcogenuros de metales de transición se puede conseguir de forma rutinaria un fuerte acoplamiento luz-materia. La interacción entre un excitón y el modo confinado de la cavidad óptica en estas estructuras puede dar lugar a la creación de excitones-polaritones, que son cuasipartículas híbridas que combinan las propiedades tanto de la materia como de la luz. El campo de los polaritones de cavidad ha experimentado un notable aumento de interés en las últimas décadas; algunos de los logros más notables incluyen la observación de la condensación y el lasing, la realización de fases superfluidas y el estudio de la topología.

Esta tesis se centra en explorar la interacción entre la física de los semiconductores cargados y el fuerte acoplamiento luz-materia. Gracias a los recientes avances tecnológicos, los dispositivos semiconductores pueden manipularse con precisión y eficacia, lo que la compleja interacción entre el dopaje electrónico y el fuerte acoplamiento luz-materia. entre

el dopaje electrónico y el fuerte acoplamiento luz-materia. Esto brinda la oportunidad de generar, controlar y detectar nuevas fases con fotones, pares electrón-hueco y un gas de electrones.

La tesis se estructura en 5 capítulos. Los capítulos 1 y 2 sirven de una visión general de los antecedentes relevantes, cubriendo los aspectos teóricos y experimentales clave necesarios para teóricos y experimentales necesarios para comprender los objetivos y los resultados de la investigación que se presentan en los capítulos posteriores. Los capítulos 3, 4, y 5 presentan los resultados originales de esta tesis, que han dado lugar a las publicaciones enumeradas en la “Lista de publicaciones”. Las conclusiones y perspectivas de este trabajo se recogen en el capítulo final “Conclusiones generales y perspectivas futuras”. El texto siguiente ofrece un breve resumen de los principales objetivos e implicaciones de la investigación presentada en los capítulos 3, 4, y 5.

El capítulo 3 de esta tesis explora la interacción entre la temperatura y la respuesta óptica de semiconductores bidimensionales dopados. Investigando el problema de unos pocos excitones generados en un mar de Fermi de portadores de carga, empleamos el formalismo del polaron de Fermi para estudiar cómo las excitaciones cuánticas del baño fermiónico visten la impureza excitónica, dando lugar a dos cuasipartículas polares, el polaron atractivo y el polaron repulsivo. También revelamos un cambio gradual de un estado en el que la rama atractiva se comporta como una cuasipartícula distinta a un estado en el que se combina con un amplio continuo de estados de dispersión trión-hueco. Recientemente ha surgido un debate sobre cómo se compara esta imagen de muchos cuerpos con la descripción estándar del sistema en términos de partículas de pocos cuerpos, como excitones y triones, y cuál de los dos enfoques es más apropiado para describir la respuesta óptica del sistema en el límite de un fuerte desequilibrio de cargas. Nuestra investigación proporciona una visión crucial de este debate al demostrar que las dos descripciones están conectadas sólo cuando se considera el papel crítico de la temperatura. Utilizando una expansión cuántica virial perturbativamente exacta, analizamos la respuesta óptica y descubrimos que la nube de aderezos coherente de la cuasipartícula polaron atractiva se ve perturbada por fluctuaciones térmicas en los regímenes de bajo dopaje y/o alta temperatura. Este enfoque predice nuevas características de fotoluminiscencia, como un comportamiento no trivial del pico atractivo cerca de la energía del trión que está conectado a la dispersión resonante excitón-electrón en dos dimensiones, y un pico repulsivo Lorentziano. Los resultados de nuestro estudio se comparan con un experimento reciente llevado a cabo en una monocapa de  $\text{MoSe}_2$  dopado, y encontramos una concordancia excelente. Nuestro análisis demuestra analíticamente que la expansión virial recupera las predicciones del modelo de triones cuando la energía de Fermi se aproxima a cero.

En el capítulo 4, investigamos las propiedades ópticas de un semiconductor bidimensional dopado en el régimen *indistinguishable carrier polaron* (ICP), donde

una de las cargas que forman el excitón es indistinguible del mar de Fermi formado al dopar el sistema. Más notablemente, la indistinguibilidad requiere que el estado triónico de tres cuerpos tenga simetría de onda  $p$ . Utilizamos una descripción polaron para estudiar los efectos del mar de Fermi, donde el excitón está vestido por una única excitación partícula-hueco. Comparamos nuestros resultados con los obtenidos en el caso *distinguishable carrier polaron* (DCP) y observamos que la función espectral del caso DCP se caracteriza por ramas atractivas y repulsivas debidas a que el trión de onda  $s$  en estado básico está ligado, mientras que en el caso ICP, dos ramas están presentes sólo cuando el trión de onda  $p$  está ligado. Demostramos que existe una transferencia de la fuerza del oscilador de la rama repulsiva a la atractiva a medida que aumenta el dopaje en ambos casos. Aunque el estado del trión de onda  $p$  no se acopla directamente a la luz, esta transferencia de peso espectral es posible porque el complejo trión-hueco se acopla indirectamente a la luz a través de su acoplamiento al excitón. Encontramos que el peso espectral de la rama atractiva tiene una dependencia diferente del dopaje en los casos ICP y DCP. Concretamente, en el caso DCP, crece linealmente con la densidad del mar de Fermi a bajo dopaje, mientras que en el caso ICP, crece cuadráticamente debido a la naturaleza de onda  $p$  del estado trión. En el régimen de fuerte acoplamiento luz-materia, la transferencia de la fuerza del oscilador a la rama atractiva da lugar a la aparición de tres modos polaritónicos. Discutimos cómo los desdoblamientos Rabi en el espectro de polaritones de acoplamiento fuerte permiten una medida efectiva de los pesos de las cuasipartículas de acoplamiento débil. También observamos que la diferencia en la naturaleza de la rama repulsiva en los casos ICP y DCP surge del carácter orbital de los estados implicados. A alto dopaje, la rama repulsiva y los estados continuos tienen caracteres orbitales diferentes y no se mezclan para el caso ICP. Además, descubrimos que los caracteres orbitales de las ramas atractiva y repulsiva cambian a medida que aumenta el dopaje, y que el hueco del mar de Fermi de la rama atractiva tiene simetría de onda  $s$  a alto dopaje.

En el capítulo 5, exploramos la interacción entre los desequilibrios de la densidad de portadores, los campos de fotones y el emparejamiento electrón-hueco en estructuras bidimensionales. Nuestra investigación se basa en investigaciones anteriores y profundiza en el intrigante fenómeno de la fase Fulde-Ferrell-Larkin-Ovchinnikov (FFLO), que surge debido a una alta densidad de exceso de carga que conduce a un mínimo de roton en la dispersión de excitones. Con la ayuda de un estado variacional, desvelamos el diagrama de fases de este complejo sistema, arrojando luz sobre el impacto del acoplamiento de fotones en el mínimo de roton excitónico FFLO. Nuestros hallazgos demuestran que, mientras que el acoplamiento a fotones de cavidad de baja masa suprime el mínimo de roton, la formación de una fase FFLO limita el acoplamiento a la luz, introduciendo así nuevos conocimientos sobre la naturaleza de los fenómenos

de emparejamiento en estas estructuras. Además, descubrimos que el exceso de carga también afecta a la energía del modo fotónico de la cavidad, lo que nos proporciona una herramienta para observar y comparar estructuras con diferentes acoplamientos luz-materia, cambiando la división Rabi mediante la incrustación de diferentes números de pozos cuánticos en la cavidad planar.

En conjunto, nuestro estudio proporciona información sobre el complejo comportamiento de los semiconductores bidimensionales dopados y contribuye a la comprensión de las propiedades ópticas en sistemas electrón-hueco fuertemente correlacionados.

# List of publications

- A. TIENE, B. C. MULKERIN, J. LEVINSEN, M. M. PARISH, and F. M. MARCHETTI:  
Crossover from exciton polarons to trions in doped two-dimensional semiconductors at finite temperature,  
[10.48550/ARXIV.2212.05635 \(2022\)](#).
- B. C. MULKERIN, A. TIENE, F. M. MARCHETTI, M. M. PARISH and J. LEVINSEN:  
Virial expansion for the optical response of doped two-dimensional semiconductors,  
[10.48550/ARXIV.2212.05627 \(2022\)](#).
- A. TIENE, J. LEVINSEN, J. KEELING, M. M. PARISH and F. M. MARCHETTI:  
Effect of fermion indistinguishability on optical absorption of doped two-dimensional semiconductors,  
[Phys. Rev. B 105, 125404 \(2022\)](#).
- A. TIENE, J. LEVINSEN, M. M. PARISH, A. H. MACDONALD, J. KEELING, and F. M. MARCHETTI:  
Extremely imbalanced two-dimensional electron-hole-photon systems,  
[Phys. Rev. Research 2, 023089 \(2020\)](#).



# Acronyms

**1D, 2D, 3D** One-, Two-, Three-dimensional

**TMD** Transitional metal dichalcogenide

**LP, MP, UP** Lower, Middle, Upper polariton

**FFLO** Fulde–Ferrell–Larkin–Ovchinnikov

**SF** Superfluid

**N** Normal

**FWHM** Full Width at Half Maximum

**HWHM** Half Width at Half Maximum

**DCP** Distinguishable carrier polaron

**ICP** Indistinguishable carrier polaron

**CoM** Center-of-mass

**RPA** Random phase approximation



# Contents

<b>Acknowledgments</b>	<b>i</b>
<b>Abstract</b>	<b>iii</b>
<b>List of publications</b>	<b>xi</b>
<b>Acronyms</b>	<b>xiii</b>
<b>1 Excitons and polaritons</b>	<b>1</b>
1.1 Excitons in bulk semiconductors	1
1.2 Quantum well excitons	7
1.2.1 Second quantization formalism	9
1.3 Transition metal dichalcogenide monolayers	11
1.4 Electron-hole bilayer and indirect excitons	16
1.5 Polaritons	18
1.5.1 Coupled oscillator model	20
1.5.2 Microscopic model	28
1.5.3 Optical absorption and photoluminescence in weak and strong coupling	33
1.5.4 Polariton condensation	36
<b>2 Charged excitons and polaritons</b>	<b>39</b>
2.1 Doped and gated 2D semiconductors	39
2.2 Distinguishable trions	42
2.3 Fermi polarons	50
2.3.1 Experiments	51
2.3.2 Zero temperature model	56
2.3.3 Simplified model for the distinguishable trion	58
2.3.4 Chevy ansatz and self-energy	60
2.3.5 Connection to the trion theory	69
2.3.6 Strong light-matter coupling	71
2.3.7 Ultracold atoms	75

2.4	Pairing phenomena with charge imbalance	78
<b>3</b>	<b>Crossover from polarons to trions at finite temperature</b>	<b>81</b>
3.1	Introduction	82
3.2	Model	83
3.2.1	Variational approach	84
3.2.2	Exciton self-energy and $T$ matrix	86
3.2.3	Optical absorption and photoluminescence	87
3.2.4	Numerical implementation	88
3.3	Weak coupling regime	90
3.3.1	Loss of the attractive polaron quasiparticle: polaron to trion-hole continuum crossover	94
3.3.2	Virial expansion and connection to the trion wave function at high temperature or low doping	96
3.3.3	Comparison with experiments	100
3.3.4	Connection to the trion theory of electron recoil	102
3.4	Strong light-matter coupling	103
3.5	Conclusions and perspectives	105
<b>4</b>	<b>Indistinguishable carrier polarons</b>	<b>107</b>
4.1	Spin-valley polarized limit	107
4.2	Model	110
4.2.1	Renormalization of contact interactions	111
4.3	Distinguishable and indistinguishable trions	113
4.3.1	Limit of large mass imbalance	113
4.3.2	Trion binding energy	115
4.3.3	Coupling to light	118
4.4	Polaron state	119
4.4.1	Numerical implementation	122
4.4.2	Spectral functions	124
4.4.3	Weak coupling	126
4.4.4	Hole angular momentum in the trion-hole complex	130
4.4.5	Strong coupling	133
4.5	Experiments	134
4.6	Conclusions and perspectives	138
<b>5</b>	<b>Pairing at extreme imbalance</b>	<b>141</b>
5.1	Introduction	142
5.2	Model	143
5.2.1	Renormalization of the cavity photon energy	144
5.2.2	Variational ansatz: FF, SF, and normal states	146
5.2.3	Effective photon energy in presence of a Fermi gas	148
5.3	Weak coupling regime	151

---

5.4	Strong coupling regime	155
5.4.1	Quantum wells in planar microcavities	155
5.4.2	TMD monolayer in planar microcavities	163
5.5	Conclusions and perspectives	164
<b>General conclusions and future perspectives</b>		<b>167</b>
<b>Appendices</b>		<b>175</b>
A	Momentum discretization and matrix diagonalization	175
B	Iterative method	176
C	Finite momentum polaron state	179
D	Polaron masses at zero temperature	181
E	Renormalization procedure beyond the weak coupling limit	182
F	Origin of $E_F^*$ and $\delta^*$	183
<b>References</b>		<b>189</b>



# Chapter 1

## Excitons and polaritons

*This chapter summarizes some of the fundamental properties of neutral semiconductors focusing on their optical response. We introduce concepts such as those of excitons and cavity polaritons and discuss their properties in various semiconductor structures. We introduce the theoretical framework that will be needed in the rest of this thesis. Further, we will describe some of the main experiments in this research field that represent the background of this work.*

### 1.1 Excitons in bulk semiconductors

When a direct bandgap semiconductor<sup>1</sup> absorbs a photon, the promotion of a valence electron to the conduction band leaves a vacancy behind — see the sketch in Fig. 1.1 (a). The generated conduction electron and valence hole attract each other because of Coulomb interaction and may form a bound state which takes the name of exciton [2]. The exciton is charge neutral and analogous to a hydrogen atom or a positronium atom, i.e., the bound state between an electron and a positron.

The concept of exciton was first introduced by Yakov Frenkel in 1931 [3]<sup>2</sup>. In his proposal, Frenkel treated the crystal potential as a perturbation to the Coulomb interaction between an electron and a hole within the same crystal cell. Nowadays, the name “Frenkel excitons” refers to small and tightly bound excitons, typically localized at a single atom or molecule, that can move through the crystal via hopping. Frenkel excitons were first observed in alkali alides [4].

---

<sup>1</sup> As the name suggests, in direct bandgap semiconductors the conduction band minimum coincides with the valence band maximum [1]. In this case, interband transitions can be photon-mediated. In contrast, in indirect bandgap semiconductors, the conduction and valence band edges are separated in momentum and thus excitation and recombination must involve both photons and phonons.

<sup>2</sup> The term “exciton” was coined by the same Yakov Frenkel later in 1936.

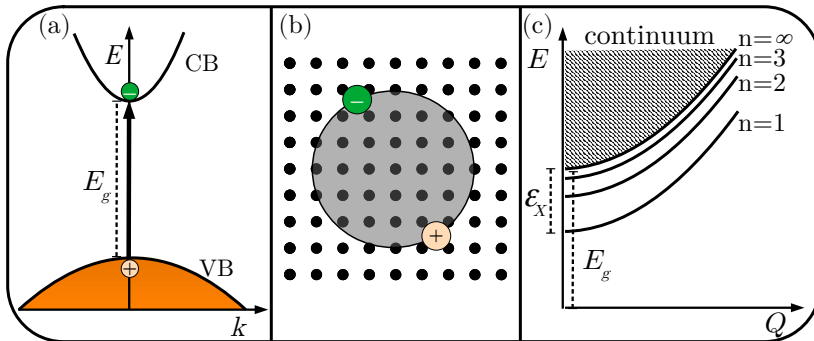


**Fig. 1.1:** (a) Optical transition in a direct bandgap semiconductor where the absorption of a photon generates an electron-hole pair. (b) Sketch of a Wannier-Mott exciton extending over several crystal lattice sites. (c) Exciton  $ns$  Rydberg series as a function of the exciton center of mass momentum  $Q$ .

More recently, they have been widely studied in organic molecular crystals like tetracene and pentacene [5], as well as organic materials [6], where they dominate the optical response. The binding energy of Frenkel excitons is in the range of  $0.1 - 1$  eV. In the late 30s, Wannier [7] and Mott [8] made significant contributions to understanding exciton behavior in semiconductor crystals. Unlike Frenkel excitons, Wannier-Mott excitons have a much larger size, typically on the order of tens of lattice constants, and a relatively small binding energy, as depicted in Fig. 1.1 (b). These excitons can be found in semiconductors crystal with a high dielectric constant and their binding energies are typical of the order of  $1 - 25$  meV. However, we will see later exceptions to these relatively small values. Examples of Wannier-Mott excitons can be found in semiconducting compounds of the II-VI group such as cadmium telluride (CdTe) and zinc selenide (ZnSe), for which the exciton binding energy is around 11 meV [9] and 20 meV [10] respectively. Other examples are the III-V group compounds like gallium arsenide (GaAs), gallium nitride (GaN), and Indium phosphide (InP), with an exciton binding energy of around 4.1 meV [11], 23 meV [12], and 5 meV [13] respectively. However, as explained in Sec. 1.3, the exciton binding energy can reach  $0.1 - 1$  eV in purely two-dimensional structures such as the case of transition metal dichalcogenide monolayers. Wannier-Mott excitons can also be found in liquid xenon [14]. Further, hybrid Frenkel-Wannier-Mott excitons can be engineered in mixed organic and inorganic heterostructures [15]. Besides Frenkel and Wannier-Mott excitons, there are a few other types of excitons, such as charge transfer excitons [16]<sup>3</sup> and anyon excitons [17]<sup>4</sup>. In this

<sup>3</sup> Charge-transfer excitons are spatially separated Coulomb-bound electron-hole pairs with a dipole momentum. They are usually extended over two near molecules in a molecular crystal, generating a donor-acceptor complex.

<sup>4</sup> Anyon excitons are anyon-hole complex formed by Coulomb attraction and applies to

thesis, we consider exclusively the case of Wannier-Mott excitons.

The theoretical description of Wannier excitons is relatively simple because the electron and hole are delocalized across several lattice sites and the effect of the crystal lattice can be approximated as a background field. In this case, we can approximate the electron and hole as moving like free particles, with a parabolic dispersion and effective masses  $m_{e,h}$  (throughout this work we use units such that  $\hbar = 1$ ):

$$\epsilon_{e,h\mathbf{k}} = \frac{E_g}{2} + \frac{\mathbf{k}^2}{2m_{e,h}}. \quad (1.1)$$

Let us consider here the case of bulk semiconductors, while the two-dimensional (2D) case will be analyzed in Sec. 1.2. The value of the electron and hole effective masses in bulk semiconductors depends strongly on the material considered. Further, the valence band in most cases is split so that to give light and heavy holes. This is because, for III-V or II-VI group compounds such as GaAs, CdS, CdTe, or ZnO, the valence band is formed by  $p$ -like orbitals with two possible configurations resulting from total angular momentum  $J = \frac{3}{2}$  and  $J = \frac{1}{2}$  — see Fig. 1.3 (a) for a comparison between the bulk and quantum well cases. The spin-orbit coupling splits the valence band into different subbands. The two higher energy subbands have total angular momentum  $J = \frac{3}{2}$  and are split into two doubly degenerate subbands with different values of momentum projection  $J^z$ , which are fourfold degenerate at zero momentum: the heavy-hole (hh) ( $J^z = \pm\frac{3}{2}$ ) and the light-hole (lh) ( $J^z = \pm\frac{1}{2}$ ) subband. As the name suggests  $m_{hh} > m_{lh}$ . The  $J = \frac{3}{2}$  subbands have large energy split with the lower energy subband with  $J = \frac{1}{2}$ , which is known as the split-off band<sup>5</sup>. For example, for GaAs, the heavy and light hole effective masses are approximately  $m_{hh} = 0.4 - 0.6m_0$  and  $m_{lh} = 0.06 - 0.08m_0$ , respectively [19], where  $m_0$  is the free electron mass. The conduction band, on the other hand, is formed by  $s$ -like orbitals with a total angular momentum  $J = \frac{1}{2}$  and is not affected by the spin-orbit coupling<sup>6</sup>. In GaAs, typically the electron mass is  $m_e \simeq 0.05m_0$  [21].

In the parabolic band approximation, the exciton energy  $E$  can be found by solving the Schrödinger equation for the exciton wave function  $\Psi(\mathbf{r}_e, \mathbf{r}_h)$

$$\left[ -\frac{\nabla_e^2}{2m_e} - \frac{\nabla_h^2}{2m_h} - V(\mathbf{r}_e, \mathbf{r}_h) \right] \Psi(\mathbf{r}_e, \mathbf{r}_h) = (E - E_g)\Psi(\mathbf{r}_e, \mathbf{r}_h). \quad (1.2)$$

In the simplest description, one can include the effect of the material surrounding the spectroscopy of an incompressible quantum liquid.

<sup>5</sup> For GaAs, the split at zero momentum between the  $J = \frac{3}{2}$  and  $J = \frac{1}{2}$  bands is around 0.34 eV [18].

<sup>6</sup> Note that all bands and subbands are double degenerate in  $J^z$ . Such degeneracy can be lifted by a magnetic field because of Zeeman splitting. Typically, GaAs has a small electron  $g$ -factor  $g \simeq -0.44$  [20].

ing the electron-hole pair in the dielectric constant  $\varepsilon$  and consider the Coulomb interaction of two equal and opposite charges as if they were otherwise in a vacuum:

$$V(\mathbf{r}_e, \mathbf{r}_h) = \frac{e^2}{\varepsilon |\mathbf{r}_e - \mathbf{r}_h|}, \quad (1.3)$$

where we are using Gaussian units such that  $4\pi\epsilon_0 = 1$ . In doped semiconductors, where the exciton size can be comparable to the average distance between the excess carriers, the effects of screening can become important — see Ch. 5.

The Schrödinger equation (1.2) describing an exciton in three-dimensions (3D) is almost identical to the hydrogen atom problem and thus admits an analytical solution in terms of the relative and center of mass coordinates:

$$\mathbf{R} = \frac{m_e \mathbf{r}_e + m_h \mathbf{r}_h}{m_e + m_h} \quad \mathbf{r} = \mathbf{r}_e - \mathbf{r}_h \quad (1.4a)$$

$$\nabla_{\mathbf{R}} = \nabla_e + \nabla_h \quad \nabla_{\mathbf{r}} = \frac{m_h}{m_e + m_h} \nabla_e - \frac{m_e}{m_e + m_h} \nabla_h. \quad (1.4b)$$

Eq. (1.2) can thus be written as

$$\left[ -\frac{\nabla_{\mathbf{r}}^2}{2\mu} - \frac{\nabla_{\mathbf{R}}^2}{2m_X} - V(r) \right] \Psi(\mathbf{r}, \mathbf{R}) = (E - E_g) \Psi(\mathbf{r}, \mathbf{R}), \quad (1.5)$$

where  $\mu$  and  $m_X$  are the reduced and exciton masses, respectively:

$$\mu = \frac{m_e m_h}{m_e + m_h} \quad m_X = m_e + m_h. \quad (1.6)$$

The center of mass and relative degrees of freedom thus factorize, giving

$$\Psi(\mathbf{r}, \mathbf{R}) = e^{i\mathbf{R}\cdot\mathbf{Q}} \varphi(\mathbf{r}) \quad (1.7a)$$

$$\left[ -\frac{\nabla_{\mathbf{r}}^2}{2\mu} + \frac{Q^2}{2m_X} - V(r) \right] \varphi(\mathbf{r}) = (E - E_g) \varphi(\mathbf{r}). \quad (1.7b)$$

Let us consider the  $\mathbf{Q} = \mathbf{0}$  case. The relative motion can be solved exactly using spherical coordinates<sup>7</sup>, as it is possible to factorize the radial component from the angular ones and solve them separately, giving [22]:

$$E_n - E_g = -\frac{\text{Ry}_X}{n^2}, \quad (1.8)$$

<sup>7</sup> The Laplace operator in spherical coordinates is:

$$\nabla_{\mathbf{r}}^2 = \frac{1}{r^2} \frac{\partial}{\partial r} \left( r^2 \frac{\partial}{\partial r} \right) + \frac{1}{r^2 \sin \theta} \frac{\partial}{\partial \theta} \left( \sin \theta \frac{\partial}{\partial \theta} \right) + \frac{1}{r^2 \sin^2 \theta} \frac{\partial^2}{\partial \phi^2}.$$

and

$$\varphi_{nlm}(r, \theta, \phi) = -\sqrt{\left(\frac{2}{na_X}\right)^3 \frac{(n-l-1)!}{2n[(n+l)!]^3}} e^{-\frac{r}{na_X}} \quad (1.9a)$$

$$\times \left(\frac{2r}{na_X}\right)^l L_{n+l}^{2l+1}(2r/na_X) Y_{lm}(\theta, \phi) \quad (1.9b)$$

$$Y_{lm}(\theta, \phi) = (-1)^m \sqrt{\frac{(2l+1)(l-m)!}{4\pi(l+m)!}} P_l^m(\cos \theta) e^{im\phi}. \quad (1.9c)$$

Here,  $P_l^m(x)$  are Legendre polynomials<sup>8</sup> and  $L_{n+l}^{2l+1}(x)$  are Laguerre polynomials<sup>9</sup>. The quantum numbers  $n$ ,  $l$ , and  $m$  are the principal, azimuthal, and magnetic quantum numbers, respectively. The exciton Bohr radius  $a_X$  and the Rydberg energy  $Ry_X$  are given by:

$$a_X = \frac{\varepsilon}{\mu e^2} \quad Ry_X = \frac{\mu e^4}{2\varepsilon^2} = \frac{1}{2\mu a_X^2}, \quad (1.10)$$

Higher values of the reduced mass  $\mu$  correspond to higher values of  $Ry_X$ . Thus the ground state exciton in inorganic semiconductors is the one involving the hh. For the majority of III-V and II-VI group compounds, values of  $\mu$  are of the order of  $0.05 - 0.15m_0$  [23] and the medium dielectric constant  $\varepsilon$  is of the order of  $8 - 10\varepsilon_0$ , where  $\varepsilon_0$  is the vacuum dielectric constant [24, 25]. This leads to a Bohr radius in the range of  $2 - 25$  nm [1, 26]<sup>10</sup>.

We now discuss the exciton's ability to couple to light and how to characterize the exciton-light coupling strength, which is represented by the exciton oscillator strength. Typically, the photon generating the electron-hole pair does not carry orbital angular momentum, and thus only those exciton states with  $l = 0 = m$  and characterized by the principal quantum number  $n$  can be generated or probed in absorption. One refers to this also as the  $ns$  Rydberg

<sup>8</sup> We use the definition

$$P_l^m(x) = (-1)^m 2^l (1-x^2)^{m/2} \sum_{\nu=m}^l \frac{\nu!}{(\nu-m)!} x^{\nu-m} \binom{l}{\nu} \left(\frac{l+\nu-1}{l}\right).$$

<sup>9</sup> We use the definition

$$L_q^p(x) = \sum_{\nu=0}^{q-p} (-1)^{\nu+p} \frac{(q!)^2 x^\nu}{(q-p-\nu)!(p+\nu)!\nu!}.$$

<sup>10</sup> In semiconductors such as GaAs, the lattice constant is typical of the order of 0.5 nm and thus much smaller than typical values of the exciton Bohr radius (1.10). This justifies the Wannier-Mott approximation.

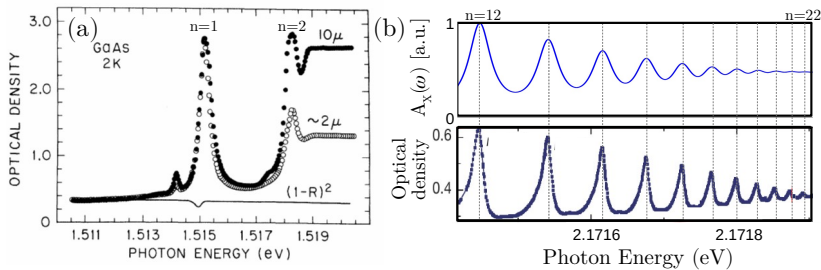


**Fig. 1.2:** (a) Optical density of a sample of GaAs with two different thicknesses –  $10\mu\text{m}$  (solid circles) and  $2\mu\text{m}$  (open circles) [27]. (b) Comparison between the optical absorption of a  $\text{Cu}_2\text{O}$  crystal displaying the  $ns$  Rydberg energy levels  $n \in [12, 22]$  (bottom panel, adapted from [28]) and the theoretical absorption spectrum — for details on how to define the exciton spectral function see Sec. 1.5.

series, whose wave functions are spherically symmetric, and simplifies to

$$\varphi_{ns}(r) = -\sqrt{\frac{1}{\pi(na_X)^3} \frac{1}{(n!)^2}} e^{-\frac{r}{na_X}} L_n^1(2r/na_X). \quad (1.11)$$

The exciton wave function gives information about the exciton coupling strength to light. Absorbing or emitting a photon occurs when the electron and hole are at the same spatial location  $r = 0$ . Thus the probability for one of these processes to occur is proportional to the dimensionless parameter [29]

$$f_{ns} = a_X^3 |\varphi_{ns}(0)|^2, \quad (1.12)$$

which takes the name of exciton optical oscillator strength. For the ground state, the  $1s$ –exciton state, the oscillator is

$$f_{1s} = \frac{1}{\pi}. \quad (1.13)$$

As at large  $n$ ,  $f_{ns} \sim n^{-3}$ , the exciton oscillator strength is strongly suppressed for higher Rydberg states. In both II-VI and III-V compounds, the small Rydberg energy only allows resolving the first few Rydberg states [11, 27]. In Fig. 1.2 (a) the optical response of GaAs is shown, obtained by Sell et al. [27] measuring the optical density of the material as a function of the photon energy. However, in other semiconducting crystals, such as  $\text{Cu}_2\text{O}$ , the exciton binding energy reaches about 90 meV and Rydberg states up to  $n = 25$  have been resolved [28] — see Fig. 1.2 (b).

## 1.2 Quantum well excitons

The exciton binding energy as well as its coupling to light can be greatly increased by confining excitons in one or more directions. In two-dimensional (2D) quantum wells confinement occurs in one direction, where a nanometer-thin layer of a low bandgap energy material is sandwiched between two layers of a material with higher bandgap energy. Because of their advantageous electronic and optical properties, II-VI and III-V compound semiconductors are commonly employed to generate quantum wells [30, 31]. The bandgap of these materials can be engineered by adjusting the composition, enabling the achievement of the desired optical and electronic properties. In the particular case of GaAs, the bandgap energy can be increased through alloying it with aluminum, resulting in the compound  $\text{Al}_x\text{Ga}_{1-x}\text{As}$  [32].

In order to solve the exciton problem in a 2D quantum well, we will consider an approximate solution of the problem where the in-plane  $\mathbf{r} = (x, y)$  degrees of freedom factorize from those that control the confinement in the  $z$ -direction:

$$\left[ -\frac{\nabla_{\mathbf{r}}^2}{2\mu} - \frac{\nabla_{\mathbf{R}}^2}{2m_X} + \sum_{\sigma=e,h} U_{\sigma}(z_{\sigma}) - V(r) \right] \Psi(\mathbf{r}, \mathbf{R}) = (E - E_g)\Psi(\mathbf{r}, \mathbf{R}) \quad (1.14a)$$

$$\Psi(\mathbf{r}, \mathbf{R}) = e^{i\mathbf{Q}\cdot\mathbf{R}}\varphi(\mathbf{r})u_e(z_e)u_h(z_h). \quad (1.14b)$$

where  $U_{e,h}(z)$  are confining potentials in the  $z$ -direction and  $\mathbf{r}$  and  $\mathbf{R}$  are the 2D relative and center of mass coordinates Eq. (1.4a), respectively. Note that if the width is of the same order or larger than the exciton Bohr radius, one has to include the exciton 3D internal structure [1]. In the pure 2D limit  $U_{e,h}(z) \propto \delta(z)$  and considering the  $\mathbf{Q} = \mathbf{0}$  case, the relative degrees of freedom for the  $ns$  series admit the following exact solution [33]<sup>11</sup>

$$E_{ns} - E_g = -\frac{Ry_X}{(n - \frac{1}{2})^2} + E_z \quad (1.15a)$$

$$\varphi_{ns}(r) = \sqrt{\frac{1}{4\pi a_X^2 (n - 1/2)^3}} \frac{e^{-\frac{r}{(2n-1)a_X}}}{(n-1)!} L_{n-1}^0 \left( \frac{2r}{(2n-1)a_X} \right), \quad (1.15b)$$

<sup>11</sup> For the general case of finite orbital angular momentum the exciton wave function reads as:

$$\varphi_{nm}(r, \phi) = \sqrt{\frac{1}{4\pi a_X^2 (n - 1/2)^3} \frac{(n-1-|m|)!}{[(n-1+|m|)!]^3}} e^{-\frac{r}{(2n-1)a_X}} \left( \frac{2r}{(2n-1)a_X} \right)^{|m|} L_{n-1+|m|}^{2|m|} \left( \frac{2r}{(2n-1)a_X} \right) e^{im\phi}.$$

where the energy  $E_z$  takes into account the energy shift because of the confining potential in the  $z$ -direction and  $Ry_X$  has been defined in Eq. (1.10). The 2D Bohr radius

$$a_X = \frac{\varepsilon}{2\mu e^2}, \quad (1.16)$$

is half the value of the 3D Bohr radius (1.10), while the exciton binding energy, i.e., the energy of the  $n = 1$  state,

$$\varepsilon_X = 4Ry_X = \frac{2\mu e^4}{\varepsilon^2} = \frac{1}{2\mu a_X^2}, \quad (1.17)$$

is four times larger than the 3D binding energy (1.10). The oscillator strength of the 2D exciton Rydberg series scales as  $f_{ns} \sim (n-1/2)^{-3}$ , with a  $1s$ -exciton oscillator strength

$$f_{1s} = a_X^2 |\varphi_{1s}(0)|^2 = \frac{2}{\pi}, \quad (1.18)$$

that is twice the one of the 3D  $1s$ -exciton (1.13).

In III-V and II-VI compound quantum wells, the exciton binding energy depends on whether one considers the binding of the conduction electron with either the heavy-hole or the light-hole. As explained in Sec. 1.1 and shown in Fig. 1.3, for bulk samples, the  $J = \frac{3}{2}$  valence bands are split into a hh (which is doubly degenerate  $J_z = \pm\frac{3}{2}$ ) and lh ( $J_z = \pm\frac{1}{2}$ ) subbands that are fourfold degenerate at zero momentum. This fourfold degeneracy is lifted in a quantum well, giving a hh-lh splitting between the doubly degenerate  $J_z = \pm\frac{3}{2}$  hh and  $J_z = \pm\frac{1}{2}$  lh. Note that the adjectives heavy and light now refers to the larger and smaller effective masses, respectively, for the motion in the growth direction [34] — i.e., confinement in the growth direction makes the hh states to be more confined than the lh states. However, for the in-plane motion, the mass of the hh  $J_z = \pm\frac{3}{2}$  is smaller than that of the lh  $J_z = \pm\frac{1}{2}$ , i.e., the band dispersion is steeper for the strongly bound hh states and flatter for the weakly bound lh states. The off-diagonal hh-lh mixing characterizes the hh-lh anticrossing depicted in Fig. 1.3, which implies that at large momenta the parabolic approximation of the two subband dispersions breaks down.

The width of the quantum well strongly affects the values of the measured exciton binding energies. For example, in GaAs, the heavy-hole exciton binding energy has been measured to be in the range 5–15 meV for different quantum well widths, while for the light-hole exciton has been found to be in the range 7–17 meV [35]. In particular, the binding energy decreases for increasing well widths. Quantum well widths are usually of the order of 5–100 nm [36], i.e., the same order of magnitude as the 3D exciton Bohr radius and thus accurate modelling should include the effects of finite well width. A simple approach to include them is provided by the fractional-dimensional model [37, 38], a model that interpolates the 3D case and the purely 2D results by introducing an

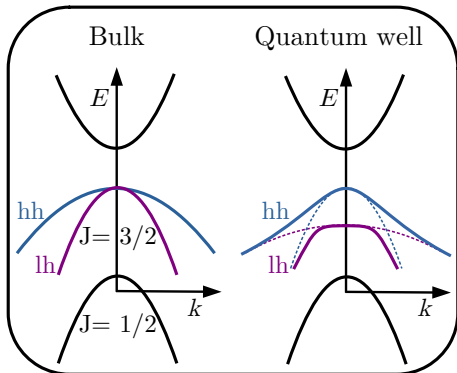


**Fig. 1.3:** Sketch of the band structure of III-V and II-VI group compounds [34]. For the bulk case, the higher energy valence band with  $J = \frac{3}{2}$  total angular momentum is split into a hh ( $J_z = \pm \frac{3}{2}$ ) and lh ( $J_z = \pm \frac{1}{2}$ ) subbands, with  $m_{hh} > m_{lh}$ . In a quantum well, the  $k = 0$  degeneracy of the two subbands is lifted and the more strongly confined hh bands have a lighter mass than the more weakly confined lh.

effective dimensionality  $d_{eff}$ . In this model, the exciton binding energy reads as

$$\varepsilon_X = \frac{Ry_X}{\left(1 + \frac{d_{eff}-3}{2}\right)^2} \quad d_{eff} = 3 - e^{-\frac{L_W}{4a_X}}, \quad (1.19)$$

where  $L_W$  is the width of the quantum well. As shown in Ref. [38], this model reproduces results in reasonable agreement with experiments.

## 1.2.1 Second quantization formalism

The exciton two-body problem can be reformulated in momentum space by making use of a second quantization formalism. We will see later in Sec. 1.5.3 that this formalism is useful for deriving the exciton Green's function and evaluating the optical absorption and emission spectra that are measured in experiments. Further, it allows us to extend calculations to the many-body case where the optically excited exciton is surrounded by a Fermi sea of excess charges in doped/gated semiconductors which is the main subject of this thesis — this setup is introduced and studied in Ch. 2.

The Hamiltonian describing a system of interacting spin-polarized conduction electrons and valence holes is given by

$$\hat{H} = \hat{H}_0 + \hat{H}_{eh}, \quad (1.20a)$$

$$\hat{H}_0 = \sum_{\mathbf{k}, \sigma=e,h} \epsilon_{\sigma\mathbf{k}} \hat{c}_{\sigma\mathbf{k}}^\dagger \hat{c}_{\sigma\mathbf{k}} \quad (1.20b)$$

$$\hat{H}_{eh} = \sum_{\sigma\sigma'} \sum_{\mathbf{k}\mathbf{k}'\mathbf{q}} \frac{W_{\mathbf{q}}^{\sigma\sigma'}}{2\mathcal{A}} \hat{c}_{\sigma\mathbf{k}}^\dagger \hat{c}_{\sigma'\mathbf{k}'}^\dagger \hat{c}_{\sigma'\mathbf{k}'+\mathbf{q}} \hat{c}_{\sigma\mathbf{k}-\mathbf{q}}, \quad (1.20c)$$

where  $\sigma, \sigma' = e, h$  is the electron-hole index,  $\mathcal{A}$  is the system area and  $\hat{c}_{\sigma\mathbf{k}}^\dagger$  ( $\hat{c}_{\sigma\mathbf{k}}$ )

are the creation (destruction) electron-hole operators:

$$\{\hat{c}_{\sigma\mathbf{k}}^\dagger, \hat{c}_{\sigma'\mathbf{k}'}^\dagger\} = \{\hat{c}_{\sigma\mathbf{k}}, \hat{c}_{\sigma'\mathbf{k}'}\} = 0 \quad \{\hat{c}_{\sigma\mathbf{k}}, \hat{c}_{\sigma'\mathbf{k}'}^\dagger\} = \delta_{\sigma,\sigma'}\delta_{\mathbf{k},\mathbf{k}'} . \quad (1.21)$$

The electron and hole kinetic energies have been defined in Eq. (1.1). The bare intra- and inter-species Coulomb interactions are given respectively by

$$W_{\mathbf{q}}^{ee} = W_{\mathbf{q}}^{hh} = V_{\mathbf{q}} = \frac{2\pi e^2}{\epsilon q} \quad (1.22a)$$

$$W_{\mathbf{q}}^{eh} = W_{\mathbf{q}}^{he} = -V_{\mathbf{q}} = -\frac{2\pi e^2}{\epsilon q} , \quad (1.22b)$$

where  $V_{\mathbf{q}}$  is the Fourier transform of Eq. (1.3).

In the second quantization formalism, the two-body exciton state with a finite center of mass momentum  $\mathbf{Q}$  can be written as

$$|\Psi_{\mathbf{Q}}\rangle = \sum_{\mathbf{k}} \frac{\varphi_{\mathbf{k}}^{(\mathbf{Q})}}{\sqrt{\mathcal{A}}} \hat{c}_{e\mathbf{k}}^\dagger \hat{c}_{h\mathbf{Q}-\mathbf{k}}^\dagger |0\rangle , \quad (1.23)$$

where  $\varphi_{\mathbf{k}}^{(\mathbf{Q})}$  is the electron-hole wave function,  $\mathbf{k}$  is the electron momentum, and  $|0\rangle$  is the vacuum state — i.e., a state where the valence band is filled and the conduction band is empty. The Fourier transform in momentum space of the Schrödinger equation (1.14a) can be found by solving exactly  $\hat{H}|\Psi_{\mathbf{Q}}\rangle = E|\Psi_{\mathbf{Q}}\rangle$ :

$$(\epsilon_{e\mathbf{k}} + \epsilon_{h\mathbf{Q}-\mathbf{k}}) \varphi_{\mathbf{k}}^{(\mathbf{Q})} - \sum_{\mathbf{k}'} \frac{V_{\mathbf{k}-\mathbf{k}'}}{\mathcal{A}} \varphi_{\mathbf{k}'}^{(\mathbf{Q})} = E \varphi_{\mathbf{k}}^{(\mathbf{Q})} . \quad (1.24)$$

While the center of mass momentum  $\mathbf{Q}$  is the conjugate variable of the center of mass coordinate  $\mathbf{R}$  (1.4a), in order to make a connection between the relative coordinate  $\mathbf{r}$  and its conjugate variable, is it profitable to introduce the relative momentum in the center of mass frame  $\mathbf{q}_r$ , in terms of the electron  $\mathbf{k}$  and hole  $\mathbf{Q} - \mathbf{k}$  momenta:

$$\mathbf{k} = \mathbf{q}_r + \mathbf{Q}_e \quad \mathbf{Q}_e = \frac{m_e}{m_X} \mathbf{Q} \quad (1.25a)$$

$$\mathbf{Q} - \mathbf{k} = -\mathbf{q}_r + \mathbf{Q}_h \quad \mathbf{Q}_h = \frac{m_h}{m_X} \mathbf{Q} . \quad (1.25b)$$

This results in the factorization of the relative and center of mass degrees of freedom, as we already know from the real space analysis:

$$\epsilon_{e\mathbf{k}} + \epsilon_{h\mathbf{Q}-\mathbf{k}} = \frac{\mathbf{q}_r^2}{2\mu} + \frac{\mathbf{Q}^2}{2m_X} + E_g . \quad (1.26)$$

As in real space, also in momentum space, one can solve analytically the 2D

exciton problem. Here, the  $1s$  wave function and binding energy are given by

$$E_{1s} - E_g = -\varepsilon_X \quad \varphi_{1s\mathbf{k}} = \frac{\sqrt{8\pi}a_X}{[1 + (ka_X)^2]^{3/2}}, \quad (1.27)$$

where the exciton binding energy  $\varepsilon_X$  has been defined in Eq. (1.17) and the exciton Bohr radius  $a_X$  in Eq. (1.16).

### 1.3 Transition metal dichalcogenide monolayers

The possibility of achieving exciton confinement down to atomically thin structures in 2D layered materials has opened novel perspectives for basic and applied research in this area. 2D materials have shown exceptional mechanical, electronic, and optical properties [39–42], not shown in their bulk counterparts. Further, the 2D layers can be easily integrated into other structures or can be stacked layer-by-layer to engineer heterostructures with specific functionalities [43, 44] — see Sec. 1.4.

The first 2D material discovered has been graphene, consisting of a single layer of carbon atoms arranged in a honeycomb structure [45]. Its unique electronic and optical properties arise from its distinctive linear dispersion relation [39, 40, 46]. Graphene has been widely used in various photonic and optoelectronic devices, operating at a broad spectral range [44, 47], but the lack of an energy gap restricts its applicability in semiconductor-based applications. Monolayers of group-VI transition metal dichalcogenides (TMDs) have instead a direct energy gap in the near-infrared to visible spectral range [42, 48], complementing graphene’s properties and opening new prospects in photonics and optoelectronics. TMD monolayers have a unique electronic band structure leading to valley- and spin-dependent electrical and optical properties that may have significant implications for information technology [49, 50]. Moreover, TMD monolayers exhibit strong excitonic effects because of reduced dielectric screening of Coulomb interactions, reduced dimensionality, and large electron effective mass [51–55]. In this section, we discuss the electronic and optical properties of TMD monolayers and their impact on the light-matter interaction properties, the radiative recombination of electron-hole pairs, and the material’s optoelectronic response.

TMD monolayers are composed of hexagonally arranged metal atoms (Mo, W) sandwiched between two planes of hexagonally arranged chalcogen atoms (S, Se) — see Fig. 1.4 (a). Although bulk and multilayer TMDs are indirect bandgap semiconductors, at the monolayer limit, i.e., achieved by exfoliation, TMDs become direct bandgap semiconductors [42, 48]. The conduction and valence bands of TMD monolayers have a minimum and maximum, respectively,

at the two high-symmetry points K and K', where the direct gap occurs [56, 57]. These two points are located at the corners of the hexagonal Brillouin zone and are related by time-reversal symmetry. So most of the optical properties of TMD monolayers can be described by considering the structure of valence and conduction bands at the K and K' points. The strong spin-orbit coupling in these materials splits the spin degeneracy of the bands at each valley. In particular, it results that the spin-splitting in the valence band is several hundred meV [41, 57], while in the conduction band, it is only a few meV [58–60]. Furthermore, the sign of the spin-splitting in Mo-based and W-based TMDs is opposite, as illustrated in Fig. 1.4 (b). The magnitude and sign of the spin-splitting are determined by the detailed composition of the atomic orbitals in TMDs [59], which involves a mix of *d*-orbitals from the transition metal and *p*-orbitals from the chalcogen. The broken inversion symmetry of TMD monolayers results in an opposite sign for their corresponding orbital magnetic moments. This, in combination with the strong spin-orbit coupling effect, leads to a phenomenon known as spin-valley locking, i.e., the correlation between the spin and valley degrees of freedom. Spin-valley locking also implies optical selection rules where a  $\sigma+$  ( $\sigma-$ ) circularly polarized light can excite only electrons from a valence to a conduction band with the same spin component [61].

Spin-valley locking makes TMD monolayers ideal candidates for valleytronics [49] and spintronics [50] applications. In particular, there has been an intense investigation in the direction of valleytronic applications [49, 62], including valley filtering [63], valley polarization [64], and valley-based logic [65]. Another promising application is the use of TMD monolayers for valley-based spintronics, in which the spin and valley degrees of freedom are used to encode information. This could potentially lead to engineering new types of spin-valley transistors [66], which could have advantages over traditional electronic transistors in terms of speed and energy efficiency.

TMD monolayers have been studied extensively for their unique electronic and optical properties. In particular, their strong excitonic effects have attracted significant interest [67–69]. Here, excitons can have large binding energies due to the reduced screening of Coulomb interactions in two-dimensional systems. In addition, the effective masses of charge carriers in TMDs are typically much larger than those in conventional semiconductors, leading to stronger Coulomb interactions between the electrons and holes in the excitonic complexes. In the near-infrared and visible spectral regions, the optical absorption of TMD monolayers is dominated by direct transitions between the valence and conduction band states. Due to the significant spin splitting of the valence band, two types of optical excitations are observed: A- and B-excitons, corresponding to holes in the top and bottom spin valence subbands, respectively. In this thesis, the focus is on the A-exciton states, which have the lowest energy.

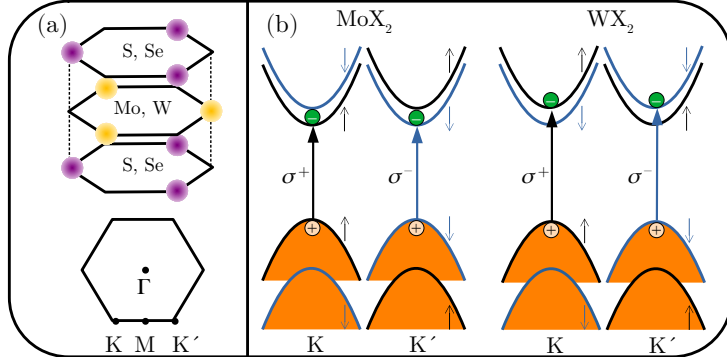


**Fig. 1.4:** (a) Hexagonal atomic distribution of a TMD monolayer and Brillouin zone with the high-symmetry points  $\Gamma$ , M, K, and  $K'$ . (b) Electronic bands around the K and  $K'$  points, which are spin-split by spin-orbit interactions: Mo-based (left) and W-based (right) TMD monolayers. Valley-dependent optical selection rules for the A-exciton are illustrated as vertical arrows.

TMD monolayers based on tungsten (W), such as WSe<sub>2</sub> and WS<sub>2</sub>, are commonly referred to as “darkish” while those based on molybdenum (Mo) as “bright”. This is due to the differences in their band arrangement. In Mo-based TMD monolayers, the highest valence band and lowest conduction band have the same spin and the bright A-exciton corresponds to the lowest energy exciton. In W-based TMD monolayers, instead, the conduction bands are inverted compared to Mo-based TMD monolayers — see Fig. 1.4 (b). Here, the A-exciton corresponds to one electron excited to the highest conduction band, while the lower energy exciton is dark — optical selection rules require spin matching of electron and hole pairs and thus for opposite spin pairs the corresponding exciton is dark.

Dark excitons are difficult to access optically as they require a spin-flip mechanism of either the electron or the hole. One option to measure these dark exciton states is via magneto-photoluminescence experiments, where an in-plane magnetic field is required to mix dark and bright states [70, 71]. Experiments have measured A-excitons binding energies of around 0.4–0.5 eV for MoS<sub>2</sub> [72], 0.5–0.6 eV for MoSe<sub>2</sub> [73], 0.4–0.7 eV for WS<sub>2</sub> [55], and 0.4–0.5 eV for WSe<sub>2</sub> [74]. Crucially, particularly from a device application point of view, the large binding energies of excitons in TMD monolayers, roughly an order of magnitude larger than those in conventional quasi-2D semiconductors, allow their observation up to room temperature.

As mentioned, the much higher values of the exciton binding energy in TMD monolayer compared to III-V or II-VI semiconductor quantum wells can be explained in terms of the enhanced electron-hole Coulomb interaction and the reduced dielectric screening. As schematically drawn in Fig. 1.5 (a), the dielec-

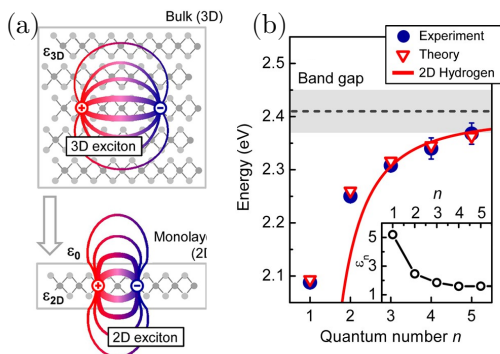


**Fig. 1.5:** (a) Schematic representation of the field lines in both a bulk semiconductor and a TMD monolayer. (b) Exciton energies as a function of the quantum number  $n$  obtained both experimentally and theoretically, including the Rydberg series of 2D hydrogen (1.15a). The inset shows the corresponding effective dielectric constants (see text). Figures adapted from Ref. [55].

tric screening is reduced because the electric field lines between the electron and the hole extend outside the TMD monolayer, enhancing thus the effects of the Coulomb attraction between the electron and the hole.

In the presence of a surrounding material with a weaker dielectric screening than the one of the TMD material, the Coulomb interaction is enhanced. While making use of a conventional Coulomb potential to describe a monolayer surrounded by a material with a similar dielectric constant is a good approximation, this becomes inaccurate when a TMD monolayer is either suspended in air or else is encapsulated in between low-dielectric materials. Note that TMD monolayers are very sensitive to the external environment since almost all atoms forming the layer are located on the surface. The environmental degradation of TMD monolayers can be prevented by encapsulating them in hexagonal boron nitride (hBN), a graphene analog insulator, chemically inert, thermally stable, doping-free, and transparent material [75], which provides an ideal environment to address properties of TMDs [76, 77]. Moreover, it has been proved that the encapsulation leads to a significant reduction of the inhomogeneous linewidth observed in photoluminescence experiments, approaching the homogeneous linewidth limit [78, 79].

One can show that the electron-hole interaction is accurately described by the Rytova-Keldysh potential [80, 81]:

$$V_{\text{RK}}(r) = \frac{\pi e^2}{2r_0} \left[ H_0 \left( \frac{\bar{\epsilon}r}{r_0} \right) - Y_0 \left( \frac{\bar{\epsilon}r}{r_0} \right) \right], \quad (1.28)$$

where  $H_0$  is the Struve function and  $Y_0$  is the Bessel function of the second kind. While at large distances the Rytova-Keldysh potential recovers the  $\sim 1/r$  Coulomb potential, at short distances, diverges logarithmically. The distance that determines the crossover between short and large distances is given by the screening length  $r_0$ . The screening length  $r_0$  can be approximately written in terms of the monolayer effective thickness  $d$  and its dielectric constant  $\epsilon$ , as well as the sum of the dielectric constants of the two surrounding materials

$\bar{\epsilon} = \epsilon_1 + \epsilon_2$ ,  $r_0 = d\epsilon/\bar{\epsilon}$  [80, 81]. In the strictly 2D limit ( $d \rightarrow 0$ ) with the TMD monolayer assumed to be in a vacuum, the screening length is given by the 2D polarizability  $\chi_{2D}$  of the dielectric sheet as  $r_0 = 2\pi\chi_{2D}$  [51]. Values of the vacuum polarizability have been obtained via DFT and GW calculations giving 0.5 – 0.9 nm, which correspond to a vacuum screening length of  $r_0 \sim 3 - 6$  nm [53].

The Fourier transform of the Rytova-Keldysh potential (1.28) in momentum space reads as

$$V_{\text{RK}\mathbf{q}} = \frac{2\pi e^2}{q} \frac{1}{(1 + r_0 q)}. \quad (1.29)$$

By using these results and typical effective masses for electrons and holes in TMD monolayers,  $m_e \simeq m_h = 0.5 - 0.8m_0$  [59, 82], theoretical calculations obtain large exciton binding energy in the range 0.4–0.6 eV [51–53], in agreement with experimental results [55, 72–74].

The modifications introduced by the Rytova-Keldysh potential (1.29) compared to the unscreened Coulomb potential (1.22b) imply that the  $ns$  series of exciton energies are modified with respect to the hydrogenic Rydberg series of Eq. (1.15a), particular for small values of  $n$ , as shown in Fig. 1.5 (b).

It has been demonstrated in Ref. [55] that while for small values of the principal quantum numbers, such as  $n = 1, 2$ , the exciton binding energies deviate substantially from the values expected from the hydrogenic model (1.14a), for larger principal quantum numbers such as  $n = 3, 4, 5$ , the agreement is very good. By determining the effective dielectric constant  $\epsilon_n$  needed to obtain the TMD exciton binding energy by using the hydrogenic 2D Rydberg series (1.15a). (see inset of Fig. 1.5 (b)), the authors of Ref. [55], have been able to show that  $\epsilon_n$  decreases as  $n$  increases, reaching values very close to 1 for  $n \geq 3$ . For  $n = 1, 2$  significant deviations of  $\epsilon_n$  from 1 are due to a nonuniform dielectric environment, as sketched in Fig. 1.5 (a). This suggests that the electron-hole interaction is far more screened at short distances, while at larger distances screening is reduced. The electric field between the electron and hole forming the exciton permeates both the thin layer of material with strong screening and the surrounding medium with weak screening. As the electron-hole distance increases, a larger portion of the electric field is located in the low-dielectric surrounding medium, leading to reduced effective screening, a phenomenon known as “antiscreeing” [83].

As far as the oscillator strength of the Rydberg states in TMD monolayers is concerned, at small values of principal number  $n$ , the higher screening effects at short distances result in a smaller oscillator strength compared to the unscreened Coulomb case. On the other hand, at larger values of  $n$ , thanks to the antiscreeing phenomenon, the oscillator strength is expected to behave as for the ideal 2D unscreened Coulomb case. Hence, the decrease of the oscillator strength with  $n$  is weaker for TMD monolayers than that for the ideal

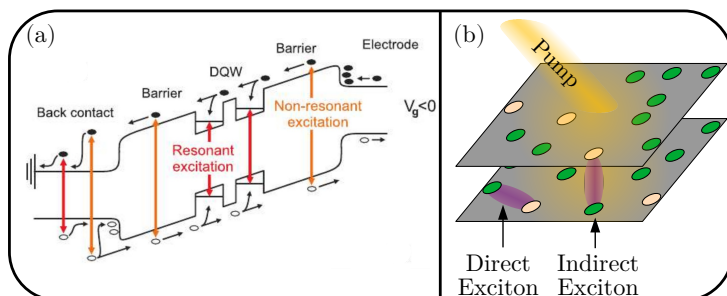


**Fig. 1.6:** (a) Optical pumping by resonant (red) and non-resonant (orange) excitation of indirect excitons in coupled quantum wells with an electric field perpendicular to the growth direction. Non-resonant excitation leads to the formation of both direct and indirect excitons. However, direct excitons recombine faster than indirect ones, thus leaving electrons and holes in separate layers. Resonant excitations initially generate only direct excitons, however, tunneling and scattering mechanisms leads eventually to the formation of also indirect excitons. Adapted from Ref. [94] (b) Schematic representation of an electron-hole bilayer where both direct and indirect excitons are generated optically.

2D hydrogen atom [84, 85].

## 1.4 Electron-hole bilayer and indirect excitons

In order to conclude the discussion about exciton properties in semiconductors, we review in this section some of the recent advances on excitons in different geometries, such as the case of electron-hole bilayers, i.e., quantum well structures where electrons and holes are confined in separate layers. The interest in this geometry comes from the fact that, as explained below, the electron and hole forming the indirect exciton [86–88] and spatially separated, implying longer lifetimes compared to direct excitons. At the same time, the spatial separation leads to stronger exciton-exciton interactions. The enhanced inter-particle interaction of indirect excitons, together with the possible realization of macroscopic quantum effects, make electron-hole quantum well systems relevant for applications in optoelectronic devices, such as excitonic transistor [89, 90], switching devices [91, 92] and LED [93].

Longer lifetimes and stronger interactions are beneficial for the realization of macroscopically coherent collective phases [94, 95]. Several collective phases have been predicted for electron-hole bilayers [96–98], such as charge density wave states [99], as well as the competition between exciton condensation and Wigner crystallization [100]. We will investigate pairing phenomena in electron-hole bilayers in the limit of extreme charge imbalance in Ch 5.

Electron-hole bilayers can be realized in two coupled quantum wells separ-

ated by a thin barrier layer by applying a perpendicular electric field which lifts the degeneracy of conduction and valence bands in the two wells, creating an asymmetric potential [101–105] — see Fig. 1.6. The energy level in the well that is closer to the positive electrode is shifted to higher energies, while the energy levels in the well that are closer to the negative electrode are shifted to lower energies. As a result, electrons and holes redistribute so that electrons move to the lower energy states in one well, while holes move to the higher energy states in the other well. Alternative approaches to create indirect excitons include doping and/or electrostatic gating [106]. In this case, quantum wells have separate contacts, allowing for an independent load of carriers. More details about this configuration will be given in Ch. 2.

When light is shined on a coupled quantum well structure, both direct excitons (electron and hole belong to the same well) and indirect excitons (electron and hole belong to different wells) are generated. Indirect excitons have longer lifetimes because electrons and holes are spatially separated, thus reducing the probability of tunneling, while direct excitons recombine faster, thus eventually leaving only electrons and holes in separate layers [94]. Note that the layer separation must be large enough to reduce recombination by tunneling, while small enough to maximize Coulomb attraction. Further, some tunneling is necessary to allow final detection.

Initial studies of optically generated indirect excitons in GaAs/AlGaAs structures have led to the generation of macroscopically coherent ring-shaped patterns around the laser spot [101, 102, 104], hundreds of micrometers away from the excitation area. This phenomenon has been interpreted by assuming that excitons remain in a dark state until they collectively recombine when reaching a critical distance because they enter a collective coherent phase.

Interestingly, indirect excitons have a permanent dipole moment and thus they are characterized by a dipole-dipole repulsive interaction [101, 107–109]. The enhanced dipole-dipole interaction of indirect excitons compared to direct ones<sup>12</sup> can have important consequences for the realization of a condensed phase of excitons [101, 102, 104], as explained next. There has been a long and strenuous search for exciton condensation since when it was first proposed [114, 115]. In a thermal equilibrium description, i.e., neglecting recombination, and at low densities, exciton condensation can be described as Bose-Einstein condensation of tightly bound bosons. However, at higher densities, the electrons and holes start to overlap and the description of exciton condensation resembles that one of the theory of superconductivity [116]. Even at low densities, the generation of a cold thermalized gas of excitons starting from a hot population of optically

<sup>12</sup> Even at low densities, i.e., much smaller than the exciton inverse squared Bohr radius, where excitons can be approximated as tightly bound bosons [110], excitons acquire their interaction properties from their fermionic constituents. A microscopic analysis of exciton-exciton interaction can be found in several works, such as Refs. [111–113].

generated particle-hole pairs is far from trivial. In a single quantum well, cooling is prevented by the short lifetime of (direct) excitons [117]. Here, recombine faster than thermalize to low-enough temperatures [118]. Further, two excitons in opposite spin states attract each other and form a lower-energy molecular state named biexciton [119]. In order to overcome these limitations, already in 1975 it was suggested to consider indirect excitons [120]. The lifetime of indirect excitons can be as long as microseconds [121]. At the same time, the repulsive dipole-dipole interaction helps to stabilize them against the formation of biexcitons. Strong dipole-dipole interaction has however the drawback of leading to a rapid expansion of a dense dipolar exciton fluid [122, 123]. Still, spatially indirect excitons have been observed to exhibit long-range spontaneous coherence in coupled structures made of GaAs quantum wells separated by a thin AlGaAs barrier, with coherence being observed at temperatures around 1 K [104, 124].

With the advent of 2D materials such as TMD monolayers, it is possible to build several electron-hole bilayer structures by combining TMDs of different chemical compositions. The weak interlayer bonding in these layered crystals allows engineering layered heterostructures through the vertical or lateral stacking of the different monolayers, which are held together by van der Waals forces [43]. For TMD van der Waals heterostructures, theoretical calculations of their band structures show, in most cases, a staggered/type-II alignment, where the conduction band minimum and valence band maximum are located in different layers [125, 126]. Electrons and holes can thus be confined in separate layers, leading to strongly bound indirect excitons [127, 128], with binding energies of hundreds of meV, making them stable at room temperature [129]. Thus, these materials are potentially more promising for optoelectronic devices and should enable them to be operational at elevated temperatures.

Superfluidity of spatially indirect excitons has been predicted also for TMDs van der Waals heterostructures [130–132]. Considering TMD layers separated by insulating hexagonal boron nitride and making use of an effective mass theory, it has been estimated that the indirect exciton degeneracy temperature can reach 100 K. Very recently, evidence of exciton condensation at temperatures as high as 100 K has been obtained in a MoSe<sub>2</sub>–WSe<sub>2</sub> electron–hole double-layer structure [133].

## 1.5 Polaritons

In this section, we are going to introduce the concept of cavity polaritons, the quasiparticles resulting from the entanglement of one exciton and a cavity photon. These strongly coupled light-matter quasiparticles display properties of both components, allowing to tune of the properties of matter by light and vice

versa, opening a wealth of novel possibilities and research directions. Excitons have a finite lifetime, after which the generated electron-hole pair recombines emitting a photon. If however the photon is confined, recurrent processes of exciton annihilation and emission of a photon and photon reabsorption to create another exciton with the same energy and momentum can repeat themselves until the photon is able to escape confinement. When the exciton–photon coupling exceeds the exciton and photon decay rates, new polariton quasiparticles give rise to spectrally separated normal modes.

Photon confinement is thus an essential ingredient to the formation of polaritons. Planar microcavities are one possibility of achieving optical confinement. Here, two flat reflecting mirrors are disposed at a distance of the same order of the light wavelength. Other alternatives are photonic crystals that confine light in small volumes around crystal defects, or convex cavities with a high refractive index, such as spherical or pillar microcavities [1].

Here, we briefly discuss the structure and properties of planar microcavities. Fabry-Pérot resonators [134] are typical examples of planar microcavities. They are made of two parallel reflecting mirrors at a distance  $L_C$ . If light is perfectly confined within this length, the resulting confined photon mode has a quantized orthogonal momentum  $k_z = N \frac{\pi}{L_C}$  so that its energy is related to the in-plane momentum  $\mathbf{k}$  by

$$\epsilon_{C\mathbf{k}} = \frac{c}{n} \sqrt{\mathbf{k}^2 + k_z^2}, \quad (1.30)$$

where  $n$  is the medium refractive index [1],  $c$  is the speed of light, and  $N$  is the index of the transverse mode in the cavity. For small values of the in-plane momentum, the photon thus acquires a parabolic dispersion [1]:

$$\epsilon_{C\mathbf{k}} \simeq \epsilon_{C\mathbf{0}} + \frac{k^2}{2m_C}, \quad (1.31)$$

where

$$\epsilon_{C\mathbf{0}} = \frac{\pi c}{nL_C} \quad m_C = \frac{n}{c} \frac{\pi}{L_C}. \quad (1.32)$$

The effective photon mass  $m_C$  is orders of magnitude smaller than the exciton mass, typically,  $m_C \sim 10^{-5} m_X$  [135]. Note that the cavity photon energy  $\epsilon_{C\mathbf{0}}$  can be tuned by changing the cavity effective length  $L_C$ . This possibility is exploited in planar cavities by growing one of the two mirrors with a wedge. As a result, different regions of the microcavity have different values of the effective length and thus the photon energy can be detuned to different values.

We have provided an approximated ideal description of a Fabry-Pérot resonator, while real systems can deviate from this ideal scenario of perfect reflectivity. In particular, if mirrors are not exactly parallel, the light slowly “walks” towards regions of larger cavity length, eventually escaping from the cavity.

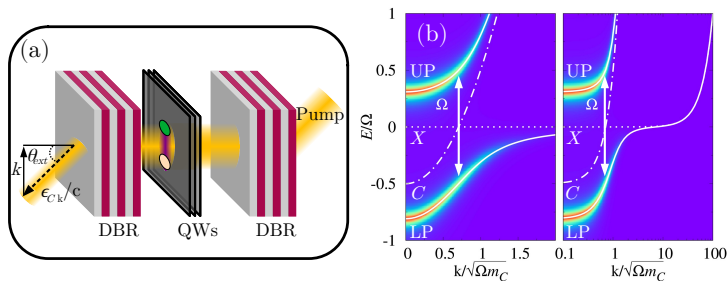


**Fig. 1.7:** (a) Schematic representation of a polariton heterostructure, consisting of a planar microcavity made of distributed Bragg reflectors with embedded quantum wells. This configuration allows measuring the polariton in-plane dispersion by angle-resolved measurements. (b) Photon absorption  $A_C(\omega)$  as a function of momentum (in linear [left panel] and logarithmic scale [right panel]) and energy  $E$  obtained from a coupled oscillator model (see text). Lower (LP) and upper (UP) polariton dispersions are plotted as solid (white) lines. The uncoupled cavity (dot-dashed) and exciton (dotted) modes are also shown. We have fixed  $m_C = 10^{-4}m_X$  and  $\eta_C = \bar{\eta}_X = 0.05\Omega$ .

To avoid lateral walk-off is possible to stack together multiple layers of mirrors with alternating refractive index, as done in distributed Bragg reflectors (DBR) — see Fig. 1.7 (a). A quarter-wave mirror is one of the most common designs, with each optical layer thickness corresponding to one-quarter of the desired wavelength for which the mirror is designed.

Crucially, the photon in-plane momentum  $\mathbf{k}$  is proportional to the angle  $\theta_{ext}$  with respect to the normal direction in which the photon is shown or is emitted outside the cavity:

$$\mathbf{k} = \frac{\epsilon_C \mathbf{k}}{c} \sin \theta_{ext} . \quad (1.33)$$

This gives a powerful tool for probing polariton properties by performing angle-resolved measurements.

We are now able to describe the effects of the strong coupling between one exciton and one cavity photon. In the following section, we first use a simplified description where the exciton is assumed as structureless, while, in Sec. 1.5.2, we will introduce a microscopic model which includes the exciton internal structure.

### 1.5.1 Coupled oscillator model

The simplest model describing a coupled exciton and photon system neglects the composite nature of the exciton, considers 1s exciton level only, and neglects its spin degree of freedom. Further, as a starting point, we are going to assume that both excitons and cavity photons are infinitely long-lived, and we introduce

the effects of a finite lifetime later in the section. The Hamiltonian describing the coupled oscillator model is:

$$\hat{H} = \sum_{\mathbf{k}} \begin{pmatrix} \hat{a}_{\mathbf{k}}^\dagger & \hat{x}_{\mathbf{k}}^\dagger \end{pmatrix} \mathbb{H} \begin{pmatrix} \hat{a}_{\mathbf{k}} \\ \hat{x}_{\mathbf{k}} \end{pmatrix} \quad \mathbb{H} = \begin{pmatrix} \epsilon_{C\mathbf{k}} & \frac{\Omega}{2} \\ \frac{\Omega}{2} & \epsilon_{X\mathbf{k}} \end{pmatrix}, \quad (1.34)$$

where  $\hat{a}_{\mathbf{k}}$  and  $\hat{x}_{\mathbf{k}}$  are the photonic and excitonic bosonic operators, respectively. While the first two terms are the photon and exciton kinetic energy terms, where  $\epsilon_{C\mathbf{k}}$  is given by (1.31) and  $\epsilon_{X\mathbf{k}} = \epsilon_{X0} + \frac{k^2}{2m_X} = E_g - \epsilon_X + \frac{k^2}{2m_X}$ , the terms proportional to  $\Omega$  describe the conversion of an exciton into a photon and vice versa with a coupling strength  $\Omega$ , the Rabi frequency. This simple model, also known as Jaynes-Cummings model [136], employs the rotating wave approximation [137], which is valid for light-matter coupling strengths smaller than the exciton energy. In this approximation, processes involving the simultaneous creation or annihilation of both an exciton and a photon are neglected. These processes do not conserve energy and are oscillating fast in time if  $\Omega \ll \epsilon_{C0} + \epsilon_{X0}$ . Thus, in this limit, they average to zero on time scales of the order of  $1/\Omega$  and can be neglected.

We are going to see that experimental values of the Rabi frequency can be obtained directly from polariton absorption spectra. At the same time, it can be shown that  $\Omega$  can be determined starting from the microscopic system properties, such as the cavity photon energy  $\epsilon_{C0}$ , the cavity width  $L_C$ , and the 1s exciton oscillator strength  $f_{1s}$  [138]:

$$\Omega \propto \sqrt{\frac{4\pi\epsilon_{C0}f_{1s}}{L_C}}. \quad (1.35)$$

The dependence of  $\Omega$  on the exciton oscillator strength  $f_{1s}$  will be derived from a microscopic polariton model in the following Sec. 1.5.2.

The Hamiltonian (1.34) can be diagonalized by rotating into the polariton basis:

$$\hat{H} = \sum_{\mathbf{k}} \begin{pmatrix} \hat{u}_{\mathbf{k}}^\dagger & \hat{l}_{\mathbf{k}}^\dagger \end{pmatrix} \begin{pmatrix} \epsilon_{UP\mathbf{k}} & 0 \\ 0 & \epsilon_{LP\mathbf{k}} \end{pmatrix} \begin{pmatrix} \hat{u}_{\mathbf{k}} \\ \hat{l}_{\mathbf{k}} \end{pmatrix}, \quad (1.36)$$

where

$$\begin{pmatrix} \hat{u}_{\mathbf{k}}^\dagger \\ \hat{l}_{\mathbf{k}}^\dagger \end{pmatrix} = \begin{pmatrix} \cos \theta_{\mathbf{k}} & -\sin \theta_{\mathbf{k}} \\ \sin \theta_{\mathbf{k}} & \cos \theta_{\mathbf{k}} \end{pmatrix} \begin{pmatrix} \hat{a}_{\mathbf{k}}^\dagger \\ \hat{x}_{\mathbf{k}}^\dagger \end{pmatrix} \quad (1.37a)$$

$$\cos \theta_{\mathbf{k}} = \pm \frac{1}{\sqrt{2}} \left[ 1 \pm \frac{\epsilon_{C\mathbf{k}} - \epsilon_{X\mathbf{k}}}{\sqrt{(\epsilon_{C\mathbf{k}} - \epsilon_{X\mathbf{k}})^2 + \Omega^2}} \right]^{1/2} \quad (1.37b)$$

$$\epsilon_{\text{LP,UP}\mathbf{k}} = \frac{1}{2} \left[ \epsilon_{C\mathbf{k}} + \epsilon_{X\mathbf{k}} \mp \sqrt{(\epsilon_{C\mathbf{k}} - \epsilon_{X\mathbf{k}})^2 + \Omega^2} \right]. \quad (1.37c)$$

The Hopfield coefficients [139]  $\cos^2 \theta_{\mathbf{k}}$  and  $\sin^2 \theta_{\mathbf{k}}$  are the exciton (photon) and photon (exciton) fraction in the lower (upper) polariton quasiparticle at momentum  $\mathbf{k}$ . When the lifetime of exciton and photon are negligible, the Rabi frequency  $\Omega$  coincides with the upper (UP) and lower polariton (LP) energy difference at resonance, i.e., when the exciton and photon energies coincide  $\epsilon_{C\mathbf{k}} = \epsilon_{X\mathbf{k}}$  — see Fig. 1.7 (b). The LP and UP dispersions are plotted in Fig. 1.7 (b) as solid lines. Note that in Fig. 1.7 (b), the cavity photon dispersion is shown as a dot-dashed line and, because of the very small photon mass, the cavity photon dispersion is much steeper than that of the exciton (dotted line). Thus, in the range of angles probed by the photons, the dependence of the exciton on its center of mass momentum is negligible. As previously discussed, the cavity photon energy can be tuned in cavities grown with a wedge. Here, it is possible to thus change the photon-exciton detuning, defined as:

$$\delta = \epsilon_{C\mathbf{0}} - \epsilon_{X\mathbf{0}}. \quad (1.38)$$

In the limit  $k \ll \sqrt{2m_C\Omega}$ , the lower and upper polariton dispersions can be approximated as parabolic

$$\epsilon_{\text{LP,UP}\mathbf{k}} \simeq \epsilon_{\text{LP,UP}\mathbf{0}} + \frac{k^2}{2m_{\text{LP,UP}}}, \quad (1.39)$$

where the LP and UP effective masses are a sum of photon and exciton masses weighted by the corresponding Hopfield factors [135]:

$$\frac{1}{m_{\text{LP}}} \simeq \frac{\sin^2 \theta_{\mathbf{0}}}{m_C} + \frac{\cos^2 \theta_{\mathbf{0}}}{m_X} \quad \frac{1}{m_{\text{UP}}} \simeq \frac{\sin^2 \theta_{\mathbf{0}}}{m_X} + \frac{\cos^2 \theta_{\mathbf{0}}}{m_C}. \quad (1.40)$$

In the simplified description provided by the coupled oscillator model, the photon and exciton Green's functions in the strong coupled regime between matter and light can be evaluated by inverting the matrix

$$\mathbb{G}(\omega, \mathbf{k}) \equiv (\omega - \mathbb{H})^{-1} = \begin{pmatrix} \omega - \epsilon_{C\mathbf{k}} & -\frac{\Omega}{2} \\ -\frac{\Omega}{2} & \omega - \epsilon_{X\mathbf{k}} \end{pmatrix}^{-1}, \quad (1.41)$$

and evaluating the diagonal elements [140]:

$$G_C(\omega, \mathbf{k}) = \mathbb{G}_{11}(\omega, \mathbf{k}) = \frac{1}{\omega - \epsilon_{C\mathbf{k}} - \frac{\Omega^2/4}{\omega - \epsilon_{X\mathbf{k}}}} = \frac{\sin^2 \theta_{\mathbf{k}}}{\omega - \epsilon_{\text{LP}}} + \frac{\cos^2 \theta_{\mathbf{k}}}{\omega - \epsilon_{\text{UP}}} \quad (1.42a)$$

$$G_X(\omega, \mathbf{k}) = \mathbb{G}_{22}(\omega, \mathbf{k}) = \frac{1}{\omega - \epsilon_{X\mathbf{k}} - \frac{\Omega^2/4}{\omega - \epsilon_{C\mathbf{k}}}} = \frac{\cos^2 \theta_{\mathbf{k}}}{\omega - \epsilon_{\text{LP}}} + \frac{\sin^2 \theta_{\mathbf{k}}}{\omega - \epsilon_{\text{UP}}} . \quad (1.42b)$$

Photon and exciton Green's function in the frequency domain are related by the Dyson equation [141]:

$$G_C(\omega, \mathbf{k}) = G_C^{(0)}(\omega, \mathbf{k}) + \left(\frac{\Omega}{2}\right)^2 G_C^{(0)}(\omega, \mathbf{k}) G_X(\omega, \mathbf{k}) G_C(\omega, \mathbf{k}) , \quad (1.43)$$

where  $G_C^{(0)}(\omega, \mathbf{k}) = (\omega - \epsilon_{C\mathbf{k}})^{-1}$  is the bare photon Green's function when the light-matter coupling is zero  $\Omega = 0$ . It can be shown that this relation holds in general, beyond the validity of the coupled oscillator model.

We now discuss how to introduce the effects of broadening due to the exciton and photon decay, as well as a quantum well disorder or other non-radiative processes. In order to do this, we have to separate different experimental configurations: in one case the quantum well or the TMD monolayer is not embedded into a microcavity and it is probed by light — we will refer to this as the *weak coupling* regime; in the other case, the active medium where excitons can be generated is embedded into a microcavity — the *strong coupling* regime.

In the weak coupling regime, one is interested in the exciton response and the effects of the exciton lifetime and the broadening caused by, e.g., disorder in the quantum well or other non-radiative processes, which can be included in a frequency shift into the complex plane  $\omega \mapsto \omega + i\eta_X$ , giving:

$$G_X(\omega, \mathbf{k}) = \frac{1}{\omega + i\eta_X - \epsilon_{X\mathbf{k}}} . \quad (1.44)$$

One physical observable in this regime can be optical absorption, i.e., the transfer rate from an initial state containing no exciton to a final state with one photo-generated exciton. Using Fermi's golden rule it is easy to demonstrate that the optical absorption in the weak coupling regime coincides with the exciton spectral function (we will carry on a formal derivation of this result in the case where the exciton cannot be treated as tightly bound boson in Sec. 1.5.3):

$$A_X(\omega, \mathbf{k}) = -\frac{1}{\pi} \text{Im} G_X(\omega, \mathbf{k}) . \quad (1.45)$$

Thus, shifting the frequency into the complex plane implies that the exciton optical absorption is a Lorentzian centered at the exciton energy and with a Full

Width at Half Maximum (FWHM) equal to  $2\eta_X$ . Different nonradiative decay processes can lead to the broadening of the exciton line, such as exciton–exciton and exciton–phonon scattering, as well as disorder induced by, e.g., impurities or defects. These contribute to what is generally referred to as inhomogeneous broadening [29, 142]. We should note here that inhomogeneous broadening leads to a lineshape which is Gaussian-like rather than Lorentzian [143, 144]. One way to model this could be to consider a Gaussian convolution of the exciton spectral function<sup>13</sup>.

In the strong coupling regime, when the active medium is embedded into the optical cavity, the couple oscillator model (1.34) already takes into account that the exciton can decay into a cavity photon (with a probability given by the Rabi coupling  $\Omega$ ). However, we have neglected both the fact that the cavity photon can leak out from the cavity, with a decay rate inversely proportional to the cavity photon linewidth  $2\eta_C$ , and that the exciton line can be broadened because of inhomogeneous broadening effects, as discussed previously. We will indicate the inhomogeneous broadening as  $2\bar{\eta}_X$ . Both these effects can be included in the photon and exciton Green’s function as follows:

$$G_C(\omega, \mathbf{k}) = \frac{1}{\omega - \epsilon_{C\mathbf{k}} + i\eta_C - \frac{\Omega^2/4}{\omega - \epsilon_{X\mathbf{k}} + i\bar{\eta}_X}} \quad (1.46a)$$

$$G_X(\omega, \mathbf{k}) = \frac{1}{\omega - \epsilon_{X\mathbf{k}} + i\bar{\eta}_X - \frac{\Omega^2/4}{\omega - \epsilon_{C\mathbf{k}} + i\eta_C}}. \quad (1.46b)$$

The calculation of optical absorption in the strong coupling regime differs depending on the quality of the cavity confining the photon. For good cavities, i.e., when  $\eta_C \ll \Omega$ , one can use Fermi’s golden rule which establishes that the optical absorption coincides with the photon spectral function

$$A_C(\omega, \mathbf{k}) = -\frac{1}{\pi} \text{Im}G_C(\omega, \mathbf{k}). \quad (1.47)$$

The plot shown in Fig. 1.7 (b) depicts the spectral function  $A_C(\omega, \mathbf{k})$  with a fixed value of  $\eta_C = \bar{\eta}_X = 0.05\Omega$ . The plot clearly shows a good agreement between the peaks of the spectral function and the two eigenvalues of the coupled oscillators model (1.37c). However, for those cavities where the decay into external photons is not negligible, one needs to resort to an input-output method [145–147]. Indeed, Fermi’s golden rule only describes the absorption of

<sup>13</sup> The Gaussian convolution of the spectral function (1.45) is defined as

$$\bar{A}_X(\omega) = \frac{1}{\sqrt{2\pi}\sigma} \int_{-\infty}^{\infty} d\omega' A_X(\omega') e^{-\frac{(\omega-\omega')^2}{2\sigma^2}}.$$

While the FWHM of a Gaussian is  $2\sqrt{2\ln 2}\sigma$ , if  $A_X(\omega')$  has a Lorentzian profile, the convolution implies  $\bar{A}_X(\omega)$  has a Voigt profile with FWHM  $\simeq \eta + \sqrt{\eta^2 + 8\sigma^2 \ln 2}$ .

a photon already inside the cavity and does not take into account reflection and transmission processes. Within the input-output method, one instead considers the scattering matrix  $\mathcal{S}$  that relates input (incident) waves ( $\Psi_{L,R}^i$ ) with the output (scattered) waves ( $\Psi_{L,R}^o$ ) at the left and right ( $L, R$ ) sides of the cavity:

$$\begin{pmatrix} \Psi_L^o \\ \Psi_R^o \end{pmatrix} = \mathcal{S} \begin{pmatrix} \Psi_L^i \\ \Psi_R^i \end{pmatrix} = \begin{pmatrix} s_{LL} & s_{RL} \\ s_{LR} & s_{RR} \end{pmatrix} \begin{pmatrix} \Psi_L^i \\ \Psi_R^i \end{pmatrix}. \quad (1.48)$$

Considering an incident wave only on one side of the cavity  $\alpha = L, R$ , reflection, transmission, and absorption are thus related to the matrix elements of  $\mathcal{S}$  by

$$R_{\alpha\alpha} = \frac{|\Psi_\alpha^o|^2}{|\Psi_\alpha^i|^2} = |s_{\alpha\alpha}|^2 \quad (1.49a)$$

$$T_{\alpha\beta} = \frac{|\Psi_\beta^o|^2}{|\Psi_\alpha^i|^2} = |s_{\alpha\beta}|^2 \quad (1.49b)$$

$$A_{\alpha\beta} = 1 - R_{\alpha\alpha} - T_{\alpha\beta}, \quad (1.49c)$$

where  $\beta \neq \alpha$ . In the simplified case of identical  $L$  and  $R$  mirrors, it is possible to relate the scattering matrix elements with the retarded Green's function as follows [147, 148]:

$$s_{LL} = s_{RR} = 1 - i\eta_C G_C(\omega, \mathbf{k}) \quad (1.50a)$$

$$s_{LR} = s_{RL} = -i\eta_C G_C(\omega, \mathbf{k}). \quad (1.50b)$$

The scattering process on the same side of the cavity  $s_{\alpha\alpha}$  has two contributions because bare reflection is also allowed together with propagation into the cavity. Thus, in the case of a single incident wave and identical mirrors, the photon reflection, transmission, and absorption can be written in terms of the retarded photon Green's function as:

$$R_{\alpha\alpha}(\omega, \mathbf{k}) = 1 + 2\eta_C \text{Im}G_C(\omega, \mathbf{k}) + \eta_C^2 |G_C(\omega, \mathbf{k})|^2 \quad (1.51a)$$

$$T_{\alpha\beta}(\omega, \mathbf{k}) = \eta_C^2 |G_C(\omega, \mathbf{k})|^2 \quad (1.51b)$$

$$A_{\alpha\beta}(\omega, \mathbf{k}) = -2\eta_C (\text{Im}G_C(\omega, \mathbf{k}) + \eta_C |G_C(\omega, \mathbf{k})|^2). \quad (1.51c)$$

It is easy to show that we can rewrite Eq. (1.51c) in the following equivalent form

$$A_{\alpha\beta}(\omega, \mathbf{k}) = \frac{2\eta_C [\eta_C - \text{Im}\Sigma_C(\omega, \mathbf{k})]}{[\omega - \epsilon_{C\mathbf{k}} - \text{Re}\Sigma_C(\omega, \mathbf{k})]^2 + [\eta_C - \text{Im}\Sigma_C(\omega, \mathbf{k})]^2}, \quad (1.52)$$

in terms of the photon self-energy:

$$\Sigma_C(\omega, \mathbf{k}) = \frac{\Omega^2/4}{\omega - \epsilon_{X\mathbf{k}} + i\bar{\eta}_X}. \quad (1.53)$$

In the limit of a “good quality” microcavity, i.e., more precisely when

$$\eta_C \ll |\text{Im}\Sigma_C(\omega, \mathbf{k})| = \frac{\Omega^2}{4} \frac{\bar{\eta}_X}{(\omega - \epsilon_{X\mathbf{k}})^2 + \bar{\eta}_X^2}, \quad (1.54)$$

the absorption  $A_{\alpha\beta}(\omega, \mathbf{k})$  recovers the spectral function  $A_C(\omega, \mathbf{k})$ .

To conclude this section, we analyze how the polariton energies (1.37c) are modified when we introduce the effects of the photon decay  $\eta_C$  and exciton inhomogeneous broadening  $\bar{\eta}_X$ . Let us consider the following non-Hermitian coupled oscillator Hamiltonian:

$$\mathbb{H} = \begin{pmatrix} \epsilon_{C\mathbf{k}} - i\eta_C & \frac{\Omega}{2} \\ \frac{\Omega}{2} & \epsilon_{X\mathbf{k}} - i\bar{\eta}_X \end{pmatrix}, \quad (1.55)$$

with complex eigenvalues:

$$\epsilon_{\mp, \mathbf{k}} = \frac{1}{2} \left\{ \epsilon_{C\mathbf{k}} + \epsilon_{X\mathbf{k}} - i(\eta_C + \bar{\eta}_X) \mp \sqrt{[\epsilon_{C\mathbf{k}} - \epsilon_{X\mathbf{k}} - i(\eta_C - \bar{\eta}_X)]^2 + \Omega^2} \right\}. \quad (1.56)$$

If  $\Omega \gg \eta_C, \bar{\eta}_X$  the effects of photon and exciton broadening are small and, at resonance  $\epsilon_{X\mathbf{k}} = \epsilon_{C\mathbf{k}}$ , the polariton splitting is

$$\Omega_{\pm} = \epsilon_{+\mathbf{k}} - \epsilon_{-\mathbf{k}} = \sqrt{\Omega^2 - (\eta_C - \bar{\eta}_X)^2} \simeq \Omega. \quad (1.57)$$

However, in the limit where either the exciton or the photon broadening is not negligible with respect to the Rabi splitting, the polariton energies measured in experiments differ from the eigenvalues (1.56) and depend on whether one considers reflection, transmission, or absorption experiments (1.51) [149]. This is particularly evident when the broadenings drive the coupled system into the weak coupling regime, i.e., when one cannot distinguish two separate polariton resonances. Considering absorption as the experimental way of probing polaritons, one can easily show that the maxima of the absorption spectrum at resonance  $\epsilon_{X\mathbf{k}} = \epsilon_{C\mathbf{k}}$  provide the following polariton splitting  $\Omega_{\pm}$  [149]:

$$\Omega_{\pm, A} = \sqrt{\Omega^2 - 2(\eta_C^2 + \bar{\eta}_X^2)} \quad (1.58)$$

This expression differs from the one evaluated from the eigenvalues (1.57). We plot in Fig. 1.8 the polaritons split at resonance  $\epsilon_{X\mathbf{k}} = \epsilon_{C\mathbf{k}}$  using the complex polariton eigenvalues expression (1.57) (dashed gray lines), the photon absorption  $A_{\alpha\beta}(\omega, \mathbf{k})$  (1.58) (solid black lines), and the spectral function  $A_C(\omega, \mathbf{k})$  (1.47) (dotted black lines). In Fig. 1.8 (a), it is shown that the three methods yield

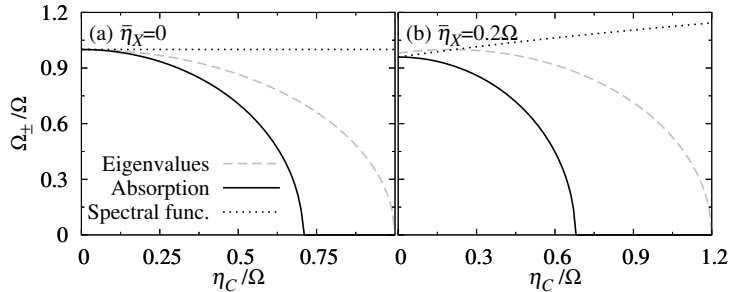


**Fig. 1.8:** Energy splitting between UP and LP at resonance ( $\epsilon_{X\mathbf{k}} = \epsilon_{C\mathbf{k}}$ ) as a function of the photon broadening  $\eta_C$  for (a)  $\bar{\eta}_X = 0$  and (b)  $\bar{\eta}_X = 0.2\Omega$ . Solid black lines are obtained from locations of the maxima of the photon absorption  $A_{\alpha\beta}(\omega, \mathbf{k})$ , dashed gray lines from the complex polariton eigenvalues, and dotted black lines are obtained from the photon spectral function  $A_C(\omega, \mathbf{k})$ .

identical results in the limit of a good cavity, i.e.,  $\eta_C \rightarrow 0$ , when  $\bar{\eta}_X = 0$ . However, in Fig. 1.8 (b), when  $\bar{\eta}_X$  has a finite value, the photon absorption and the spectral function approaches can still produce the same outcome as the limit  $\eta_C \rightarrow 0$ , while the split calculated using complex eigenvalues produces a different result. Note that the range of values in  $\eta_C$  in which absorption and spectral function give similar results is reduced by increasing  $\bar{\eta}_X$ .

The regime of polariton strong coupling has been achieved in a variety of semiconductor heterostructures [152–155]. Just to mention a few examples, strong coupling has been realized in GaAs quantum wells, with Rabi splitting values ranging from 5 to 20 meV [150, 156–158]. Note that the Rabi coupling can be increased by increasing the number of embedded quantum wells located at the maxima of the cavity photon field. One can show that  $\Omega$  rescales roughly as  $\Omega \sim \sqrt{N}$ , where  $N$  is the number of quantum wells embedded into the cavity [156, 158]. Larger values of  $\Omega$  can be achieved in inorganic quantum wells such as CdTe and GaN, where they can reach values of about 20 – 40 meV [150, 159–162], due to their higher exciton binding energy and higher oscillator strength.

Finally, for TMD monolayers embedded in optical microcavities Rabi splittings of the order of 20 to 60 meV [151, 163, 164] have been achieved. This has allowed observing strongly coupled valley-polarized polaritons up to room temperature [164–166].

Fig. 1.9 shows two experiments measuring polariton energies as a function of either the cavity to exciton detuning or the inplane momentum for two different heterostructures. In panel (a) GaAs quantum wells are embedded into a planar microcavity made of GaAlAs-based DBR [150]. Here, as explained before, the cavity wedge allows to modify the cavity to exciton detuning (1.38). Panel (b) shows a MoS<sub>2</sub> monolayer embedded in a Si-based DBR at room

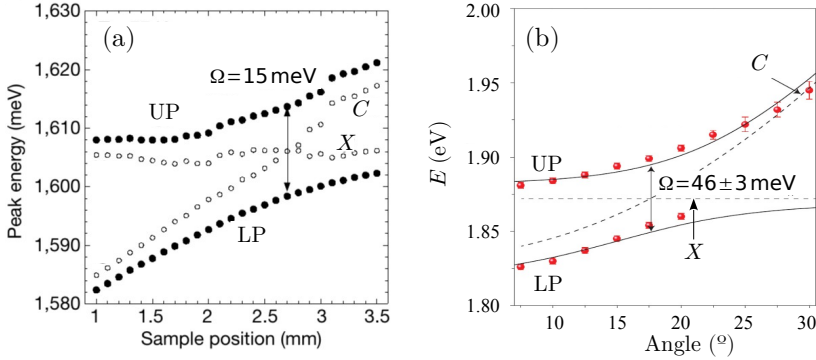


**Fig. 1.9:** (a) Polariton dispersion (filled circles) as a function of the photon-exciton detuning measured in a GaAs-based microcavity heterostructure [150]. (b) Polariton dispersion obtained from the angle-resolved reflectivity spectra in a MoS<sub>2</sub> monolayer embedded in a Si-based DBR [151]. Solid lines are theoretical fits using a coupled oscillator model.

temperature [151].

## 1.5.2 Microscopic model

While the coupled oscillator model provides a basic understanding of polariton formation mechanism and properties, this simplified description is bound to fail when the Rabi coupling  $\Omega$  is comparable to the exciton binding energy  $\varepsilon_X$ , i.e.,  $\Omega \sim \varepsilon_X \ll \varepsilon_{X0}$ . Here, while one can still make use of the rotating wave approximation (see Sec. 1.5.1) one can expect that the strong coupling to light can affect the exciton properties, which thus cannot be assumed to be a structureless “rigid” particle. Indeed, the interaction between light and matter begins to mix different excitonic levels, causing a modification in the wave function of the electron-hole pair. In this regime, which is referred to as the “very strong coupling” regime [167, 168], while the rotating wave approximation can still be applied, the composite nature of the exciton has to be taken into account. On the other hand, if  $\Omega$  is on the order of the exciton energy  $\varepsilon_{X0}$ , i.e.,  $\varepsilon_X \ll \Omega \sim \varepsilon_{X0}$ , the coupling is intense enough to hybridize states with different numbers of excitations, resulting in what is called the “ultrastrong coupling regime” [169–173]. In this case, the rotating wave approximation is bound to fail.

In this thesis, we focus on the consequences induced by the very strong coupling regime, yet, none of the experiments we compare our theory with enter the ultrastrong coupling regime. In inorganic quantum wells, values of  $\Omega \sim \varepsilon_X$  can be achieved by stacking multiple quantum wells in the central antinodes of the cavity field [150, 156–162], since, as explained before,  $\Omega$  scales

as  $\sqrt{N}$ , where  $N$  is the number of quantum wells embedded into the cavity [156, 158]. TMD monolayers embedded into cavities the very strong coupling regime has yet to be achieved because of the very large values of the exciton binding energies of about  $\sim 0.5$  eV, .

A microscopic model including the internal structure of the exciton, able to describe the modifications that a very strong coupling to light can lead to both exciton and photon mode, has been recently introduced in Ref. [140]. This model has been used to derive the results of Chs. 4 and 5 and thus we re-derive it here for clarity and completeness. We solve the problem of a single polariton by including all possible exciton states, such as the bound states and the continuum of unbound electron-hole scattering states. In order to make a connection between the microscopic parameters and those measured in experiments, we impose that, in the limit of weak coupling to light, when  $\Omega \ll \varepsilon_X$ , we recover the polariton energies predicted by the coupled oscillator model, which we expect to be valid in this limit. By allowing all possible exciton states, we give the possibility to the exciton wave function to be modified when values of  $\Omega$  increase into the very strong coupling regime to light. At the same time, we will also see that the cavity photon frequency is renormalized from its “bare” value, i.e., when it is uncoupled from the matter mode. Further, the upper polariton can strongly hybridize with the electron-hole scattering continuum, in which case, there are large deviations from the coupled oscillator model predictions.

Let us, therefore, start with the microscopic Hamiltonian

$$\hat{H} = \hat{H}_0 + \hat{H}_{eh} + \hat{H}_C + \hat{H}_{ehC} \quad (1.59a)$$

$$\hat{H}_0 = \sum_{\mathbf{k}\sigma} \epsilon_{\sigma\mathbf{k}} \hat{c}_{\sigma\mathbf{k}}^\dagger \hat{c}_{\sigma\mathbf{k}} \quad (1.59b)$$

$$\hat{H}_C = \sum_{\mathbf{k}} \epsilon_{C\mathbf{k}} \hat{a}_{\mathbf{k}}^\dagger \hat{a}_{\mathbf{k}}, \quad (1.59c)$$

$$\hat{H}_{ehC} = \frac{g}{\sqrt{\mathcal{A}}} \sum_{\mathbf{k}\mathbf{q}} \left( \hat{c}_{e\frac{\mathbf{q}}{2}+\mathbf{k}}^\dagger \hat{c}_{h\frac{\mathbf{q}}{2}-\mathbf{k}}^\dagger \hat{a}_{\mathbf{q}} + \text{h.c.} \right). \quad (1.59d)$$

All terms but the one referring to the coupling to light have been already introduced in Eq. (1.20). The last term  $H_{ehC}$  describes the electron-hole creation because of the absorption of a photon and vice versa. Because the electron and hole have to coincide in space when they recombine or are created, we have described this term as a contact interaction, i.e., the coupling  $g$  is momentum independent. However, if one would describe microscopically this process, it is clear that there is a momentum cutoff  $\Lambda$  in  $\mathbf{k}$  of the order of the inverse lattice constant of the material considered that thus makes the coupling  $g$  momentum- $\mathbf{k}$  dependent. It can be shown that, if  $\Lambda \rightarrow \infty$ , a contact electron-hole-photon interaction term leads to an ultraviolet logarithmic divergence of the polariton

energy [140]. As such, unless one wants to include microscopic details in the model, one needs to renormalize the divergence, as explained next.

Let us consider the following variational ansatz for a polariton state at zero center of mass momentum<sup>14</sup>:

$$|\Psi\rangle = \left( \alpha_0 \hat{a}_0^\dagger + \sum_{\mathbf{k}} \frac{\varphi_{\mathbf{k}}}{\sqrt{\mathcal{A}}} \hat{c}_{e\mathbf{k}}^\dagger \hat{c}_{h-\mathbf{k}}^\dagger \right) |0\rangle. \quad (1.60)$$

The polariton energies can be found by minimizing  $\langle \Psi | \hat{H} - E | \Psi \rangle$  with respect to the complex photon  $\alpha_0$  and exciton  $\varphi_{\mathbf{k}}$  amplitudes. One obtains the following coupled eigenvalue equations to solve:

$$E\alpha_0 = \epsilon_{C0}\alpha_0 + \frac{g}{\mathcal{A}} \sum_{\mathbf{k}} \varphi_{\mathbf{k}} \quad (1.61a)$$

$$E\varphi_{\mathbf{k}} = \bar{\epsilon}_{\mathbf{k}}\varphi_{\mathbf{k}} - \sum_{\mathbf{k}'} \frac{V_{\mathbf{k}-\mathbf{k}'}}{\mathcal{A}} \varphi_{\mathbf{k}'} + g\alpha_0, \quad (1.61b)$$

where  $\bar{\epsilon}_{\mathbf{k}} = \epsilon_{e\mathbf{k}} + \epsilon_{h\mathbf{k}}$ . Inserting Eq. (1.61b) into Eq. (1.61a) and rearranging, we obtain a relation between the polariton energy  $E$ , its photon amplitude  $\alpha_0$ , and the exciton wave function  $\varphi_{\mathbf{k}}$ :

$$\left( E - \epsilon_{C0} + \frac{g^2}{\mathcal{A}} \sum_{\mathbf{k}} \frac{1}{-E + \bar{\epsilon}_{\mathbf{k}}} \right) \alpha_0 = \frac{g}{\mathcal{A}^2} \sum_{\mathbf{k}\mathbf{k}'} \frac{V_{\mathbf{k}-\mathbf{k}'}}{-E + \bar{\epsilon}_{\mathbf{k}}} \varphi_{\mathbf{k}'}. \quad (1.62)$$

The sum on the left-hand side of this equation diverges logarithmically, while the sum on the right-hand side is finite. For this reason, we introduce an ultraviolet momentum cutoff  $\Lambda$ . As mentioned before, the cutoff  $\Lambda$  governs the high-energy behavior of the problem and could be proportional to the inverse crystal lattice spacing. Thus, one way out of the problem introduced by the divergence of the polariton equation is to model more accurately the system physics at this scale. However, we would like to extract universal properties of the system that are independent of microscopic modelling and details. We thus choose the option of sending  $\Lambda \rightarrow \infty$ , by renormalizing the system parameters so that the dependence on  $\Lambda$  is lost. Note that one option would be that, for energies  $E \sim \epsilon_{C0}$ , the photon amplitude  $\alpha_0$  approaches zero as  $1/\ln \Lambda$  when  $\Lambda \rightarrow \infty$ . However, in order to have a finite photon component in the polariton, the other option is to renormalize the cavity photon energy so that the divergence is canceled, which is the route we are going to follow next.

In order to relate the bare parameters in our microscopic model, such as the bare photon energy  $\epsilon_{C0}$  and the light-matter coupling strength  $g$ , to experiment observables, we impose that our model recovers the coupled oscillator results

<sup>14</sup> The generalization at finite center of mass momentum  $\mathbf{Q}$  can be found in Refs. [140, 174].

— see Sec. 1.5.1 — in the limit where the light-matter coupling strength is such that  $\Omega \ll \varepsilon_X$ , where we know that assuming the exciton state is not modified by the coupling to light is a good approximation. To do this, we rewrite the polariton eigenvalue Eqs. (1.61) in the following equivalent form

$$\left( E - \epsilon_{C0} + \frac{g^2}{\mathcal{A}} \sum_{\mathbf{k}} \frac{1}{-E + \bar{\epsilon}_{\mathbf{k}}} \right) \alpha_{\mathbf{0}} = \frac{g}{\mathcal{A}} \sum_{\mathbf{k}} \beta_{\mathbf{k}} \quad (1.63a)$$

$$(E - \bar{\epsilon}_{\mathbf{k}}) \beta_{\mathbf{k}} = - \sum_{\mathbf{k}'} \frac{V_{\mathbf{k}-\mathbf{k}'}}{\mathcal{A}} \beta_{\mathbf{k}'} + g \alpha_{\mathbf{0}} \sum_{\mathbf{k}'} \frac{V_{\mathbf{k}-\mathbf{k}'}}{\mathcal{A}} \frac{1}{(-E + \bar{\epsilon}_{\mathbf{k}})}, \quad (1.63b)$$

where

$$\beta_{\mathbf{k}} = \sum_{\mathbf{k}'} \frac{V_{\mathbf{k}-\mathbf{k}'}}{\mathcal{A}} \frac{\varphi_{\mathbf{k}'}}{-E + \bar{\epsilon}_{\mathbf{k}}}. \quad (1.64)$$

In the regime of weak coupling to light,  $g \ll a_X \varepsilon_X$ , we expect to recover the predictions of the coupled oscillator model where the exciton is not modified by the coupling to light. Here, we can thus approximate the exciton wave function as  $\varphi_{\mathbf{k}} \simeq \beta_{\mathbf{0}} \varphi_{1s\mathbf{k}}$ , where  $\beta_{\mathbf{0}}$  is a complex number. Further, the relevant energy scale  $E$  of the polariton problem can be set to the exciton energy  $E \simeq \epsilon_{X0} = E_g - \varepsilon_X$ , and thus Eq. (1.64) now reads as

$$\beta_{\mathbf{k}} \simeq \sum_{\mathbf{k}'} \frac{V_{\mathbf{k}-\mathbf{k}'}}{\mathcal{A}} \frac{\beta_{\mathbf{0}} \varphi_{1s\mathbf{k}'}}{-E_g + \varepsilon_X + \bar{\epsilon}_{\mathbf{k}}} = \beta_{\mathbf{0}} \varphi_{1s\mathbf{k}} = \beta_{\mathbf{0}} \frac{\sqrt{8\pi} a_X}{[1 + (ka_X)^2]^{3/2}}, \quad (1.65)$$

where we have used the Schrödinger equation (1.24) for  $\varphi_{1s\mathbf{k}}$ . Multiplying Eq. (1.63a) by  $\frac{1}{\mathcal{A}} \sum_{\mathbf{k}} \varphi_{1s\mathbf{k}}$  and applying the Schrödinger equation (1.24) for  $\varphi_{1s\mathbf{k}}$  to both Eq. (1.63a) and Eq. (1.63b), Eqs. (1.63) can thus be rewritten as [140]:

$$(E - \epsilon_{X0}) \beta_{\mathbf{0}} \simeq g \alpha_{\mathbf{0}} \frac{1}{\mathcal{A}} \sum_{\mathbf{k}} \varphi_{1s\mathbf{k}}, \quad (1.66a)$$

$$\left( E - \epsilon_{C0} + \frac{g^2}{\mathcal{A}} \sum_{\mathbf{k}} \frac{1}{-\epsilon_{X0} + \bar{\epsilon}_{\mathbf{k}}} \right) \alpha_{\mathbf{0}} \simeq g \beta_{\mathbf{0}} \frac{1}{\mathcal{A}} \sum_{\mathbf{k}} \varphi_{1s\mathbf{k}}. \quad (1.66b)$$

Defining the dressed, i.e., renormalized, photon energy as

$$\omega_{C0} \equiv \epsilon_{C0} - \frac{g^2}{\mathcal{A}} \sum_{\mathbf{k}} \frac{1}{\varepsilon_X - E_g + \bar{\epsilon}_{\mathbf{k}}}, \quad (1.67)$$

the renormalized photon-exciton detuning at zero momentum as

$$\delta = \omega_{C0} - \epsilon_{X0}, \quad (1.68)$$

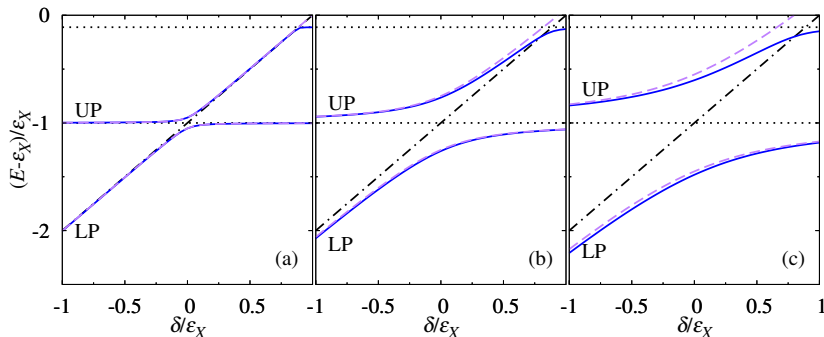


**Fig. 1.10:** Comparison between the lower and upper polariton energies obtained with the microscopic model (blue solid lines) and the coupled oscillator model (purple dashed lines), as a function of the exciton-photon detuning  $\delta = \omega_{C0} - \epsilon_{X0}$ . We set the Rabi coupling to  $\Omega = 0.1\epsilon_X$  (a),  $\Omega = 0.5\epsilon_X$  (b), and  $\Omega = 0.9\epsilon_X$  (c). The black dotted lines are the 1s and 2s exciton states energies, while the black dot-dashed line is the photon-exciton detuning  $\delta$ .

and the Rabi coupling as

$$\Omega \equiv \frac{2g}{\mathcal{A}} \sum_{\mathbf{k}} \varphi_{1s\mathbf{k}}, \quad (1.69)$$

Eqs. (1.66) recover exactly the coupled oscillator model (1.34).

The renormalization of the photon frequency (1.67) implies that when there is an active medium in the cavity, the photon energy  $\omega_{C0}$  shifts with respect to its bare value  $\epsilon_{C0}$ , which is instead the photon energy when there is no medium present in the cavity. The shift (1.67) is strongly dependent on the microscopic high-energy details of the problem that we are ignoring in our modelling. The red shift between the bare (empty) cavity energy and the dressed cavity energy when an active medium is instead present is something known in experiments and it has been measured [151]. TMD monolayer samples come in small flakes so that when embedded in a planar cavity offer the possibility to measure independently the renormalized photon energy  $\omega_{C0}$  and compare it to the bare value  $\epsilon_{C0}$ . Clearly, in a real system, the energy correction due to the dressing from the active medium is finite rather than divergent as our model predicts, as a cutoff associated with the nature of electronic states at large momenta does exist. The renormalization procedure just described allows us to obtain universal results independent of the microscopic details of the active.

We plot in Fig. 1.10 the polariton energies obtained as solutions of the coupled eigenvalue equations (1.61), where we have implemented the renormalization scheme by redefining the photon energy according to Eq. (1.67) and the Rabi coupling by Eq. (1.69) — the LP and UP energies are the first two eigenvalues of the problem. Here, we have defined the photon-exciton detuning

as

$$\delta = \omega_{C0} - \epsilon_{X0}, \quad (1.70)$$

which coincides with what is measured in experiments. The polariton energies are obtained for different values of the Rabi coupling: When  $\Omega = 0.1\epsilon_X$  (Fig. 1.10 (a)), we observe that the microscopic model coincides with the results of the coupled oscillator model (1.34) for all values of the detuning  $\delta$ , aside from when the UP crosses the value of the  $2s$  exciton state, which has not been included in the coupled oscillator model. For larger values of  $\Omega$  however, such as  $\Omega = 0.5\epsilon_X$  (Fig. 1.10 (b)) and  $\Omega = 0.9\epsilon_X$  (Fig. 1.10 (c)), the LP is still well described by the coupled oscillator model, while discrepancy between this and the microscopic model for the UP extends to a larger range of detunings.

### 1.5.3 Optical absorption and photoluminescence in weak and strong coupling

In this section, we want to define those observables such as optical absorption and emission that are measured experimentally. As already explained in Sec. 1.5.1, we differentiate between two separate experimental configurations: in one case the quantum well or the TMD monolayer is not embedded into a microcavity and it is probed by light, a regime we have labeled as *weak coupling* regime; in the other case, the active medium where excitons can be generated is embedded into a microcavity, the *strong coupling* regime.

In the weak coupling regime, the system's optical properties can be described starting from the retarded exciton Green's function. In order to use a notation that differentiates between the weak and strong coupling cases, we use  $G_X^{(0)}$  for the retarded exciton Green's function in weak coupling and  $G_X$  for the exciton Green's function in strong coupling. We restrict to the case where excitons have zero center of mass momentum and use the notation  $|\Psi_{\mathbf{Q}=0}\rangle = |\Psi\rangle$  for the exciton state defined in Eq. (1.23).

In the time domain, the exciton Green's function can be defined as the overlap between an appropriately chosen initial state and its forward time evolution with the system Hamiltonian (1.20):

$$G_X^{(0)}(t) = -i\Theta(t)\langle\Psi(0)|e^{-i\hat{H}t}|\Psi(0)\rangle. \quad (1.71)$$

The initial state  $|\Psi(0)\rangle$  is an electron-hole pair generated at the same spatial position following the absorption of a photon. This state, which is not an exciton state, can be written as:

$$|\Psi(0)\rangle = \frac{\mathcal{N}}{\sqrt{\mathcal{A}}} \sum_{\mathbf{k}} \hat{c}_{e\mathbf{k}}^\dagger \hat{c}_{h-\mathbf{k}}^\dagger |0\rangle. \quad (1.72)$$

We choose the parameter  $\mathcal{N} = (\frac{1}{\mathcal{A}} \sum_{\mathbf{k}} \Lambda)^{-1/2}$  so that this state is normalized  $\langle \Psi(0) | \Psi(0) \rangle = 1$ . This introduces a dependence on the cutoff  $\Lambda$  that we will remove later with a renormalization procedure. The exciton states  $|\Psi\rangle$  (1.23) are eigenstates of the Hamiltonian  $\hat{H}$  (1.20) with eigenvalues  $E_n$  and eigenvectors  $\varphi_{n\mathbf{k}}$  solutions of the Schrödinger equation (1.24). Note that, here, the eigenvalue index  $n$  does refer to the  $s$ -states only, because these are the only states that couple to light, however, not only to the bound Rydberg states (1.15a), i.e., we are also including electron-hole scattering states. As such, these states form a complete set of orthonormal states:

$$\begin{aligned} \hat{H} |\Psi_n\rangle &= E_n |\Psi_n\rangle & \sum_n |\Psi_n\rangle \langle \Psi_n| &= \mathbb{1} \\ & & \langle \Psi_n | \Psi_m \rangle &= \delta_{n,m}. \end{aligned} \quad (1.73)$$

Using this, we can write the exciton Green's function (1.71) as:

$$G_{X,\Lambda}^{(0)}(t) = -i\Theta(t) \sum_n |\langle \Psi(0) | \Psi_n \rangle|^2 e^{-iE_n t}, \quad (1.74)$$

where we have made explicit the dependence on  $\Lambda$  that we later eliminate. As  $\langle \Psi(0) | \Psi_n \rangle = \frac{\mathcal{N}}{\mathcal{A}} \sum_{\mathbf{k}} \varphi_{n\mathbf{k}}$ , in the frequency domain one has that:

$$G_{X,\Lambda}^{(0)}(\omega) = \sum_n \frac{|\frac{\mathcal{N}}{\mathcal{A}} \sum_{\mathbf{k}} \varphi_{n\mathbf{k}}|^2}{\omega - E_n + i\eta_X} = \sum_n \frac{|\mathcal{N}\varphi_n(0)|^2}{\omega - E_n + i\eta_X}, \quad (1.75)$$

where  $\varphi_n(\mathbf{r}) = \frac{1}{\mathcal{A}} \sum_{\mathbf{k}} e^{i\mathbf{k}\cdot\mathbf{r}} \varphi_{n\mathbf{k}}$ . Here, the frequency is shifted to the complex plane  $\omega \mapsto \omega + i\eta_X$ , with  $\eta_X > 0$ , so to guarantee that the retarded condition is satisfied. However, as already discussed in Sec. 1.5.1,  $\eta_X$  physically represents the sum of the exciton homogeneous and inhomogeneous broadening contributions.

The dependence on the cutoff introduced by the initial state (1.72) is inconvenient, as the normalization factor  $\mathcal{N} \rightarrow 0$  when  $\Lambda \rightarrow \infty$ .

As discussed in detail in Sec. 4.4 and App. B, it is possible to provide a renormalized expression of the exciton Green's function which is independent of the cutoff  $\Lambda$  and which provides a finite contribution from the bound  $ns$  states:

$$G_X^{(0)}(\omega) \equiv \left(\frac{2g}{\Omega}\right)^2 \frac{G_{X,\Lambda}^{(0)}(\omega)}{\mathcal{N}^2} = \sum_n \frac{\left| \frac{1}{\mathcal{A}} \sum_{\mathbf{k}} \varphi_{n\mathbf{k}} \left( \frac{1}{\mathcal{A}} \sum_{\mathbf{k}} \varphi_{1s\mathbf{k}} \right)^{-1} \right|^2}{\omega - E_n + i\eta_X}. \quad (1.76)$$

Here, the microscopic light-matter coupling constant  $g$  and the Rabi splitting  $\Omega$  are related by Eq. (1.69).

In linear response, the exciton spectral function coincides with the optical

absorption [175]. In order to show this, let us consider that the optical absorption corresponds to the transfer rate from an initial state containing no exciton  $|0\rangle$ , i.e., the vacuum state, to all the possible final states containing one exciton  $|\Psi_n\rangle$  (1.73) connected by the operator which describes the photo-generated electron-hole pair  $\mathcal{N}\sqrt{\mathcal{A}}\sum_{\mathbf{k}}^{\Lambda}\hat{c}_{e\mathbf{k}}^{\dagger}\hat{c}_{h-\mathbf{k}}^{\dagger}$ . Using Fermi's golden rule, one thus has that the optical absorption can be written as:

$$A_{X,\Lambda}(\omega) = \sum_n |\langle \Psi_n | \frac{\mathcal{N}}{\sqrt{\mathcal{A}}} \sum_{\mathbf{k}}^{\Lambda} \hat{c}_{e\mathbf{k}}^{\dagger} \hat{c}_{h-\mathbf{k}}^{\dagger} | 0 \rangle|^2 \delta(E_n - \omega). \quad (1.77)$$

Using the integral representation of the Dirac-delta function  $\delta(\omega) = \text{Re} \int_0^{\infty} \frac{dt}{\pi} e^{-i\omega t}$ , the definition of  $|\Psi(0)\rangle$  (1.72) and the completeness of the exciton states  $|\Psi_n\rangle$  (1.73) one finally gets:

$$A_{X,\Lambda}(\omega) = \text{Re} \int_0^{\infty} e^{i\omega t} \langle \Psi(0) | e^{-i\hat{H}t} | \Psi(0) \rangle = -\frac{1}{\pi} \text{Im} G_{X,\Lambda}^{(0)}(\omega). \quad (1.78)$$

In order to define an optical absorption that is cutoff independent, we can follow the renormalization procedure of Eq. (1.76) and obtain a cutoff independent absorption:

$$A_X(\omega) = -\frac{1}{\pi} \text{Im} G_X^{(0)}(\omega), \quad (1.79)$$

Note that  $A_{X,\Lambda}(\omega)$  and  $A_X(\omega)$  satisfy different sum-rules. For the cutoff dependent absorption  $A_{X,\Lambda}(\omega)$ , by definition one has that [175]

$$\int_{-\infty}^{\infty} d\omega A_{X,\Lambda}(\omega) = 1. \quad (1.80)$$

The cutoff independent absorption would instead give a divergent integral over all frequencies and it is normalized such that the oscillator strength of the 1s state (the area underneath) is set to 1.

Starting from absorption one can evaluate photoluminescence from the transfer rate from an initial state containing the photo-generated exciton  $|\Psi_n\rangle$  to a final state containing no exciton  $|0\rangle$ . It can be shown that, assuming that the population of excited states is thermalized to a Maxwell-Boltzmann distribution at a temperature  $T$  before emission and that they are otherwise uncorrelated, the absorption  $A_X(\omega)$  and photoluminescence  $P_X(\omega)$  are related by a detailed balanced condition [176–179]:

$$P_X(\omega) \propto e^{-\beta\omega} A_X(\omega), \quad (1.81)$$

where  $\beta = 1/k_B T$ . We will provide a rigorous derivation of this expression in Ch. 3.

The derivation of the optical absorption in the strong coupling regime follows the same steps given in Sec. 1.5.1. The photon Green's function can be derived by considering an initial state consisting of a single photon

$$|\Psi(0)\rangle = \alpha_0 \hat{a}_0^\dagger |0\rangle, \quad (1.82)$$

and a final state given by a polariton state (1.60), which is now an eigenstate of the Hamiltonian (1.59), with eigenvalues  $E_n$  and eigenvectors  $|\Psi_n\rangle$ . Using Eq. (1.73), we can write the photon Green's function as:

$$G_C(t) = -i\Theta(t) \sum_n |\langle \Psi(0) | \Psi_n \rangle|^2 e^{-iE_n t}. \quad (1.83)$$

As  $\langle \Psi(0) | \Psi_n \rangle = |\alpha_{n0}|^2$ , in the frequency domain, one has that:

$$G_C(\omega) = \sum_n \frac{|\alpha_{n0}|^2}{\omega - E_n + i\eta_C}, \quad (1.84)$$

As explained in Sec. 1.5.1, for good quality cavities,  $\eta_C \ll \Omega$ , one can use Fermi's golden rule to show that the photon spectral function coincides with the absorption spectrum:

$$A_C(\omega) = \text{Re} \int_0^\infty e^{i\omega t} \langle \Psi(0) | e^{-i\hat{H}t} | \Psi(0) \rangle = -\frac{1}{\pi} \text{Im} G_C(\omega). \quad (1.85)$$

## 1.5.4 Polariton condensation

To conclude this chapter, we dedicate this section to some of the major advances concerning the field of polaritons and the possibility they undergo a transition to condensed phases [180]. Since the first observation of exciton-polaritons a quarter of a century ago, the field has progressed at an extraordinary rate and exciton-polaritons have now emerged as novel driven-dissipative quantum fluids [138] and promising systems for exploring original properties of many-body non-equilibrium systems. Further, exciton-polariton structures have strong potential for quantum technologies, such as the possibility of room temperature operation, ultrafast dynamical response, easy tuning, and probing techniques, as well as relatively simple fabrication techniques. Although it is not possible to provide an exhaustive list of recent experimental achievements on polariton, in this final section, we summarise some of the most relevant experimental evidence of polariton condensation, and the relevant role played in the developing of novel all-optical devices.

The first experiment demonstrating spontaneous coherence in a polariton system involved coherent pumping of the cavity at a finite angle near the in-

flection point of the lower polariton dispersion [181, 182]. Upon exceeding a threshold value of the pump intensity, a parametric oscillation [183] ensues in the planar microcavity, resulting in the parametric luminescence on the signal and idler modes attaining a long-range coherence both in time and space. This phenomenon has been interpreted as an example of nonequilibrium BEC [184]. After some preliminary claims [185, 186], the realization of BEC condensation in a thermalized polariton gas was conclusively achieved for the first time in 2006 [159], using CdTe microcavities. As the pumping intensity was increased above a certain threshold, nonlinear emission at energies close to the bottom of the lower polariton branch was seen.

Since then, the field of polariton condensation has undergone rapid development. One intriguing development is the possibility of utilizing exciton polariton gases to investigate many-body physics and, specifically, superfluid hydrodynamics, as initially proposed in 2004 [187]. In 2009, the first experiment that explored the superfluidity properties of polariton fluids was published [188]. The authors employed a pulsed optical excitation technique to induce motion in a microcavity polariton condensate and observed distinct collective dynamics exhibiting superfluid characteristics, such as flow without resistance when passing through a defect. Subsequent experimental works expanded on this study to examine strong defects, demonstrating hydrodynamic nucleation of vortex-antivortex pairs [189, 190], and dark solitons [191, 192] in the flowing superfluid.

In the previous experiments we mentioned, only weak interactions between individual polaritons were studied, and the hydrodynamic behavior of the polariton condensate was examined as a result of the collective interactions of many coherent polaritons. Going beyond and into the regime of strongly correlated polaritons requires the observation of a photon blockade effect [193, 194] where interactions are strong enough to suppress double occupancy of a photonic lattice site. A convenient verification of the blockade phenomenon is provided by photon antibunching — a vanishing photon correlation function  $g^{(2)}(\tau)$  for delays  $\tau$  smaller than the polariton lifetime [195–197]. In Ref. [196] evidence of quantum correlations between polaritons spatially confined in a fiber cavity is reported. Photon correlation measurements show that careful tuning of the coupled system can lead to a modest reduction of simultaneous two-polariton generation probability by 5%. This modest reduction is related to the modest polariton interaction strength in neutral semiconductors. Recently a novel way to boost the optical nonlinearity of semiconductors has been reported [198]. This method involves a doped semiconductor structure in which the polariton is “dressed” by the surrounding charged medium, resulting in quasiparticles known as polaron-polaritons that can interact strongly with each other and extend over large spatial scales — see Sec. 2.3.1. The authors demonstrate that this dressing mechanism enhances the material’s optical non-

linearity by a factor of 50. In Ch. 2, this dressing mechanism will be described in detail.

The realization of quantum physical phenomena at macroscopic scale and room temperature offers significant opportunities for the development of innovative all-optical devices. For instance, polariton lasers exploit the coherent nature of Bose condensates of exciton-polaritons in semiconductors to achieve lasing with extremely low thresholds [199]. Although the concept of polariton lasers was introduced in 1996 [180], it was not until 2013 that electrical pumping of a polariton laser, a crucial aspect for practical use of polaritonic light sources, was demonstrated [200]. Other relevant applications include polariton switches and modulators [201], polariton lattices [202, 203], and networks [204, 205]. In the contest of device applications, 2D semiconductors structures like TMDs, thanks to their large oscillator strengths and exceptionally strong exciton binding energy with respect to quasi-2D organic and inorganic semiconductors, have been shown to be promising in the realization of photonic lasers [206–208] and robust exciton polaritons at room temperature [151, 209]. Very recently, the realization of polariton lasing was reported for the first time in a monolayer WS<sub>2</sub>-based planar microcavity at room temperature [210], showing great promise for their practical applications.

## Chapter 2

# Charged excitons and polaritons

*Recent advances in experimental techniques in 2D semiconductors have made it possible to investigate the interplay between electronic doping and strong light-matter coupling. This chapter focuses on those different phenomena that can be realized and studied in charged 2D light-matter systems, with a focus on the extremely imbalanced limit and the Fermi polaron problem. We will analyze in depth the Fermi polaron theory at zero temperature, while these results will be generalized to finite temperature in Ch. 3. Further, we will carry on a comparison with theories based on few-body excitations, i.e., excitons and trions. We will illustrate the broad recent experimental literature that studies this problem.*

## 2.1 Doped and gated 2D semiconductors

There are several experimental techniques that can be employed to load a gas of free carriers in a 2D quantum well or a TMD monolayer. Before focusing on the theoretical aspects concerning this configuration, we briefly review some of them here. We illustrate at the end of this section why this particular configuration has gained significant interest in recent years.

One of the most common techniques to charge a quantum well is gating the structure. Here, carriers are electrostatically accumulated using a field-effect transistor structure [106, 211, 212]. To achieve the desired carrier density, a gate electrode is placed on top of the quantum well, separated by a thin insulating layer. The gate voltage is used to control the number of charge carriers in the quantum well, by changing the electrostatic potential in the region near the quantum well. The gate voltage can attract or repel carriers from the quantum well, depending on its polarity. By applying a negative gate voltage, electrons are attracted from a nearby source and accumulate in

the quantum well, effectively doping it with electrons. Similarly, a positive gate voltage attracts holes and loads them into the quantum well. The carrier concentration can be controlled by varying the gate voltage, which affects the electrostatic potential in the region near the quantum well.

Another technique is modulation-doping [213, 214]. In this process, a dopant material is placed in the alloy barrier forming the quantum well. The energy difference between the dopant energy in the barrier and the ground state of the quantum well induces charge transfer. A finite excess of charge can also be induced in quantum well structures using optical excitation of specially crafted samples where quantum wells with different widths are coupled [215–218]. In particular, a wide and narrow quantum well are coupled together. When the narrow quantum well is photoexcited, the generated electrons quickly transfer toward the lower energy levels of the large quantum well. The holes, on the other hand, tunnel from the narrow to the wide quantum well at a much slower rate. An electron gas is thus formed in the large quantum well, the density of which is optically controlled.

TMD monolayers can be doped using field-effect transistors. Here, flakes of few-layer graphene serve as a contact and top/bottom gate electrodes. The carrier density is tuned by applying a gate voltage between the electrodes connected to the graphene flakes [219–221]. Other doping techniques commonly employed in TMD monolayers are substitutional and molecular doping. Substitutional doping means substituting atoms of the transitional metal or of the chalcogenide component with dopants [222–225]. However, control over doping with this technique is challenging. Molecular doping instead consists in modifying the electrical properties of a TMD monolayer by coating or depositing a film providing doping. This approach results in a heterostructure of the doping film and the TMD monolayer, where the electrical or optical properties of the monolayer can be tuned by either charge transfer from the dopant molecules [224, 226–228] or by dipole effects of the dopant molecules [229–231].

The net result of gating or doping techniques is to load a gas of excess charges into the 2D semiconductor. For a gas of non-interacting electrons or holes ( $\sigma = e, h$ ) the Fermi energy  $E_F$  is related to the gas density  $n_\sigma$  by

$$E_F = \frac{k_F^2}{2m_\sigma} \frac{1}{N} = \frac{2\pi}{m_\sigma} \frac{n_\sigma}{N}, \quad (2.1)$$

where  $k_F$  is the Fermi momentum and  $N = 2$  is the spin degeneracy. For a spin-polarised gas  $N = 1$ .

There are multiple reasons why generating a gas of excess charges in 2D semiconductors can be interesting both from fundamental and applied points of view. Injecting free carriers into a 2D semiconductor allows for modification of its optical response. One possibility is to create electrically injected polari-

ton devices, such as LEDs and lasers [200, 232–236]. Recently, the electrical injection has been employed to load polaritons into etched square and honeycomb lattices [237]. Here, the direct current injection has led to a laser-like emission from high-symmetry points, opening thus the possibility to generate electrically driven polariton lasers with topologically nontrivial properties. In Ref. [238], an external electric field is used to tune a microcavity between different lasing regimes, from a polariton condensate at strong coupling to a photon laser at weak coupling. Further, in a similar configuration [239], the polariton and photon lasing regimes have been identified by measuring the power dependence of the probed photocurrent between lateral contacts. Considering gated or doped 2D semiconductors allows tuning the semiconductor properties by changing the free carrier density. In effect, a band-gap renormalization is expected in this regime [240–243]. Further, the exciton binding energy and oscillator strength are modified by the screened Coulomb interaction, leading to a significant reduction in both binding energy and the oscillator strength [244].

These structures have also attracted noticeable interest because of the possibility of studying strongly correlated electron phases by optical means. One usually employs the dimensionless parameter  $r_s = m_e e^2 / (\epsilon \sqrt{\pi n_e}) = 1/k_F a_B$ , where  $a_B = \epsilon/m_e e^2$  is the Bohr radius and  $k_F$  the Fermi momentum, which is the ratio between the Coulomb interaction energy and the kinetic energy, to quantify the strongly interacting regime, when  $r_s$  becomes significantly greater than one. The dominance of Coulomb repulsion over kinetic energy can lead to the spontaneous formation of a crystal phase, i.e., to Wigner crystallization [245]. Here, electrons arrange themselves in configurations corresponding to the potential energy's absolute minima, thereby maximizing the distance between them. Recent quantum Monte Carlo calculations [246] have shown a critical value of  $r_s \gtrsim 30$  for Wigner crystallization. TMD monolayers are ideal candidates to achieve Wigner crystals, because of the large electron mass and small values of the dielectric constant. In these systems, a value of  $r_s \gtrsim 40$  can be reached for electron densities  $n_e \sim 10^{11} \text{ cm}^{-2}$  [247]. Optical probing of a Wigner crystal phase has been very recently reported in charge-tunable MoSe<sub>2</sub> monolayer [248] and bilayer [249]. It has been proposed that charged TMD monolayers are also expected to allow the study, by optical means, of the transition from a quantum liquid to a quantum solid phase, and the spontaneous appearance of intermediate charge density wave (CDW) phases [250–253]. The mechanisms behind the formation of a CDW phase in these systems are under debate [252]. Similarly, the competition or cooperation between CDW and superconducting phases is an open question [254]. The presence of numerous unresolved questions further enhances the interest in the field.

As discussed in Sec. 2.4 doped semiconductors provide an opportunity to investigate and characterize uncommon electron-hole pairing phenomena. In the extremely imbalanced limit, previous work has suggested that excitons can

acquire a finite center of mass momentum reminiscent of a roton minimum at large enough doping [255, 256]. Exciton pairing at finite center of mass momentum is related to the FFLO phase, which was first proposed for conventional superconductors [257, 258]. In Ch. 5, we expand upon these studies by examining how the strong coupling to light impacts the formation of this phase.

To conclude this section, let us comment that doped semiconductors have more recently attracted much interest because of the possibility of realizing a Fermi polaron or impurity problem. This question occupies a sizeable part of this thesis and its fundamental ideas will be analyzed in detail in Sec. 2.3. There, we will also connect the Fermi polaron formalism with those results that can be extracted from a few-body approach involving excitons and trions.

## 2.2 Distinguishable trions

Optical excitation of a doped or gated semiconductor can lead to the formation of charged few-body complexes such as trions. A trion is a bound state of either two conduction-band electrons and a valence-band hole (indicated as  $X^-$ ) or one electron and two holes ( $X^+$ ) and can be thought of as the semiconductor analog of either the hydrogen anion  $H^-$  or the molecular ion  $H_2^+$  [259], respectively. In this section, we will limit the discussion strictly to the three-body description, while, in Sec. 2.3, we will connect these results to those obtained for a finite density of excess charges within the polaron formalism. In particular, we will see in Sec. 2.3 that the polaron description allows describing the optical response of charged semiconductors from low to intermediate densities where the Fermi energy is of the order of the trion binding energy [260–265]. We will also see that, while the polaron description recovers some of the trion properties at low doping, such as its energy and oscillator strength [266], there are profound differences between the trion and polaron descriptions.

The first quantization Hamiltonian describing a three-body complex consisting of two electrons and one hole in 2D is given by [267]

$$\hat{\mathcal{H}} = -\frac{(\nabla_{e1}^2 + \nabla_{e2}^2)}{2m_e} - \frac{\nabla_h^2}{2m_h} + \frac{3}{2}E_g - V(\mathbf{r}_{e1}, \mathbf{r}_{e2}, \mathbf{r}_h), \quad (2.2)$$

where the factor  $3/2E_g$  comes from the fact that we have a three-body particle, and where  $\mathbf{r}_{e1,e2,h}$  denotes the position coordinates of the three carriers and  $V(\mathbf{r}_{e1}, \mathbf{r}_{e2}, \mathbf{r}_h)$  is the interaction potential which includes the electron-electron repulsion and the electrons-hole attraction. For unscreened Coulomb potential

one has

$$V(\mathbf{r}_{e1}, \mathbf{r}_{e2}, \mathbf{r}_h) = \frac{e^2}{\epsilon} \left( \frac{1}{|\mathbf{r}_{e1} - \mathbf{r}_h|} + \frac{1}{|\mathbf{r}_{e2} - \mathbf{r}_h|} - \frac{1}{|\mathbf{r}_{e1} - \mathbf{r}_{e2}|} \right), \quad (2.3)$$

where  $\epsilon$  is the dielectric constant. The Schrödinger equation for the trion wave function  $\Psi_{e1,e2,h}(\mathbf{r}_{e1}, \mathbf{r}_{e2}, \mathbf{r}_h)$  reads as

$$\hat{\mathcal{H}}\Psi_{e1,e2,h}(\mathbf{r}_{e1}, \mathbf{r}_{e2}, \mathbf{r}_h) = E\Psi_{e1,e2,h}(\mathbf{r}_{e1}, \mathbf{r}_{e2}, \mathbf{r}_h). \quad (2.4)$$

The trion binding energy  $\varepsilon_T$  (defined positive) is the energy difference between the energy of an exciton plus an electron  $\epsilon_{X0} + E_g/2 = -\varepsilon_X + 3/2E_g$  and the trion energy  $E_T$ :

$$\varepsilon_T \equiv \epsilon_{X0} + E_g/2 - E_T = -\varepsilon_X - (E_T - 3/2E_g). \quad (2.5)$$

As, introducing the trion binding energy  $\varepsilon_T$ , the energy gap  $E_g$  rescales out of the problem, we can measure energies with respect to it, i.e., we can set  $E_g = 0$ , which we carry on throughout the rest of this chapter. The trion wave function can be written as [268]

$$\Psi_{e1,e2,h}(\mathbf{r}_{e1}, \mathbf{r}_{e2}, \mathbf{r}_h) = e^{i\mathbf{QR}} \varphi(\mathbf{r}_{e1} - \mathbf{r}_h, \mathbf{r}_{e2} - \mathbf{r}_h) \mathcal{U}_{e1,e2}^{(2)}(\mathbf{r}_{e1}, \mathbf{r}_{e2}) \mathcal{U}_h^{(1)}(\mathbf{r}_h). \quad (2.6)$$

Here,  $\varphi(\mathbf{r}_{e1} - \mathbf{r}_h, \mathbf{r}_{e2} - \mathbf{r}_h)$  is the envelope function describing the in-plane relative motion of the two electrons with respect to the hole (we are considering explicitly the case of  $X^-$ ) and  $\mathcal{U}_{e1,e2}^{(2)}(\mathbf{r}_{e1}, \mathbf{r}_{e2})$  [ $\mathcal{U}_h^{(1)}(\mathbf{r}_h)$ ] is the two-particle [single-particle] Bloch function for the two electrons (the hole). The form of the trion wave function (2.6) is general and it implies that the trion as a whole is free to move in the in-plane space so that its envelope function can be written as a function of the center of mass  $\mathbf{R} = [m_e(\mathbf{r}_{e1} + \mathbf{r}_{e2}) + m_h\mathbf{r}_h]/(2m_e + m_h)$  and relative coordinates  $\mathbf{r}_{e1} - \mathbf{r}_h$  and  $\mathbf{r}_{e2} - \mathbf{r}_h$ .

Whether the trion wave function (2.6) has to satisfy symmetry constraints for the exchange of the two electrons  $\mathbf{r}_{e1} \leftrightarrow \mathbf{r}_{e2}$  depends on whether such electrons are indistinguishable or not [269]. For distinguishable electrons, i.e., electrons with different spin and/or valley indices, there are no restrictions on the symmetry and the system is free to choose the lowest energy configuration. One can show that this corresponds to a symmetric envelop function, i.e.,  $\varphi$  has an  $s$ -wave symmetry. However, if the electrons are indistinguishable, i.e., have the same spin and valley indices, the two-particle Bloch function must be symmetric when exchanging the two electrons ( $\mathbf{r}_{e1} \leftrightarrow \mathbf{r}_{e2}$ ), and therefore,  $\varphi(\mathbf{r}_{e1} - \mathbf{r}_h, \mathbf{r}_{e2} - \mathbf{r}_h)$  is an antisymmetric function, thus in the lowest energy solution has a  $p$ -wave symmetry. In III-V and II-VI quantum wells, where there are no valley degrees of freedom but only spin ones, indistinguishable

electrons mean they are in the same spin state and thus are in a spin-triplet state and the envelope wave function must be antisymmetric, while a symmetric envelope function occurs for a spin-singlet configuration, i.e., for an electron in two different spin states. In TMD monolayers, the additional valley degrees of freedom allows for a symmetric envelope trion wave function with a spin-triplet configuration. Note that, in contrast to distinguishable trions, the observation of indistinguishable one have been scarce, since for many materials this state is unbound due to Pauli repulsion. In general, it is known that positively charged indistinguishable trions  $X^+$  can become bound when the electron-to-hole mass ratio is sufficiently small [268] — see Ch. 4. For TMD monolayers, indistinguishable trions are always unbound [270]. For CdTe- and GaAs-based quantum wells indistinguishable  $X^+$  is expected to be bound [271, 272] but it has never been observed. However, a magnetic field perpendicular to the quantum well [273–277] does stabilize this solution, and indistinguishable trions have been observed experimentally [278–280]. There has also been evidence of indistinguishable trions in an electric field [281]. In this section, and more generally in this chapter, we only consider trion states formed out of two distinguishable majority carriers. The indistinguishable case will be discussed in detail in Ch. 4.

The Schrödinger equation for the relative motion is given by:

$$E\varphi(\mathbf{r}_{e1} - \mathbf{r}_h, \mathbf{r}_{e2} - \mathbf{r}_h) = \left[ -\frac{(\nabla_{e1h}^2 + \nabla_{e2h}^2)}{2\mu} - \frac{\nabla_{e1h} \cdot \nabla_{e2h}}{m_h} - V(\mathbf{r}_{e1}, \mathbf{r}_{e2}, \mathbf{r}_h) \right] \varphi(\mathbf{r}_{e1} - \mathbf{r}_h, \mathbf{r}_{e2} - \mathbf{r}_h), \quad (2.7)$$

where  $\mu = m_e m_h / (m_e + m_h)$  is the reduced exciton mass (1.6) and

$$\nabla_{e1h} = \frac{m_h}{m_e + m_h} \nabla_{e1} - \frac{m_e}{m_e + m_h} \nabla_h \quad (2.8a)$$

$$\nabla_{e2h} = \frac{m_h}{m_e + m_h} \nabla_{e2} - \frac{m_e}{m_e + m_h} \nabla_h. \quad (2.8b)$$

Some of the methods most commonly employed to solve the Schrödinger (2.7) and evaluate the trion binding energy  $\varepsilon_T$  are variational methods. Here, the result depends on the choice of the trial wave function. Ref. [282] employs a 22-parameter Hylleraas-type wave function [283]:

$$\Psi(s, t, u) = e^{-s/2} \sum_{i,j,k} c_{i,j,k} s^i t^j u^k, \quad (2.9)$$

where  $s = |\mathbf{r}_{e1} - \mathbf{r}_h| + |\mathbf{r}_{e2} - \mathbf{r}_h|$ ,  $t = |\mathbf{r}_{e1} - \mathbf{r}_h| - |\mathbf{r}_{e2} - \mathbf{r}_h|$ , and  $u = |\mathbf{r}_{e1} - \mathbf{r}_{e2}|$  are elliptic Hylleraas coordinates. Results from these calculations are plotted in Fig. 2.1 (a) and show that both positively and negatively charged trions are

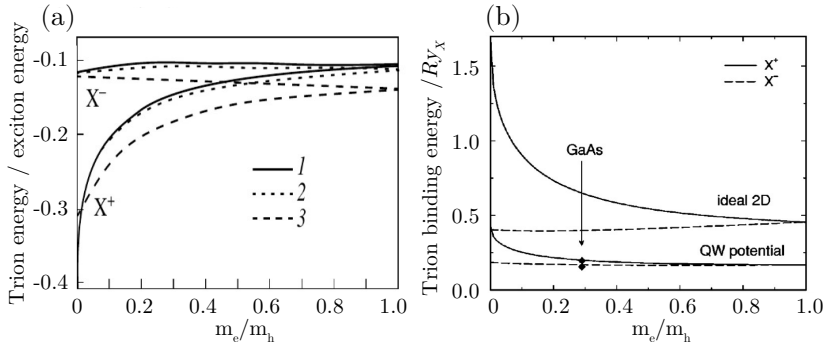


**Fig. 2.1:** Expected dependence of the energy (a) and binding energy (b) for distinguishable trions  $X^\pm$  on the electron-hole mass ratio obtained with different methods (see text). Panel (a) contains a comparison between the results obtained by Refs. [271, 272] (solid lines), Ref. [282] (dotted), and Ref. [267] (dashed). Here, the trion energy is rescaled with respect to the exciton energy in 2D. Adapted from Ref. [271]. Panel (b) are calculations for an ideal 2D quantum well and for a quasi-2D quantum well from Ref. [284]. Here the trion binding energy is rescaled with respect to the 3D exciton binding energy  $Ry_X$ .

bound for any value of the electron-hole mass ratio.

Quantitatively similar results have been obtained by employing much simpler trial wave functions [271, 272]. The trial wave function considered in Ref. [271] is one that interpolates between the trion wave function for two light charges and a heavy one and that one for two heavy charges and a light one. In the first case of two light charges and a heavy charge, one expects the trion to be well described by [285]

$$\Psi_{lh}(\mathbf{r}_1, \mathbf{r}_2) = (e^{-ar_1 - br_2} + e^{-br_1 - ar_2}) (1 + c|\mathbf{r}_1 - \mathbf{r}_2|), \quad (2.10)$$

where  $\mathbf{r}_{1,2}$  are the relative positions of the light particles from the heavy particle. Instead for the case of two heavy charges and a light charge, the trion is expected to be well described by

$$\Psi_{hhl}(\mathbf{r}_1, \mathbf{r}_2) = (e^{-ar_1} + e^{-ar_2}) \mathcal{R}(|\mathbf{r}_1 - \mathbf{r}_2|). \quad (2.11)$$

This wave function corresponds to the sum of two hydrogen-like wave functions [269], multiplied by the wave function of the relative motion  $\mathcal{R}(\rho)$ , where  $\rho = |\mathbf{r}_1 - \mathbf{r}_2|$ , which can be written as [271, 272]

$$\mathcal{R}(\rho) = \frac{e^{-s\rho}}{1 + d(\rho - \rho_0)^2}, \quad (2.12)$$

where  $s = \sqrt{-2m_h E}$  and  $E$  is the trion binding energy. Thus, Ref. [271]

suggests the use of the following trion wave function:

$$\Psi(\mathbf{r}_1, \mathbf{r}_2) = \Psi_{lh}(\mathbf{r}_1, \mathbf{r}_2)\mathcal{R}(\rho). \quad (2.13)$$

The clear advantage of this approach is that from 22 variational parameters of Ref. [282], one has only 6 variational parameters. Results for the trion binding energy evaluated this way are shown in Fig. 2.1 (a).

A completely different approach has been followed in Ref. [267] by using a mass-weighted coordinates system, where it was possible to obtain an analytical dependence of the trion binding energy from the electron-hole mass ratio  $\nu = m_e/m_h$ :

$$\frac{\varepsilon_{X^-}(\nu)}{Ry_X} = \frac{1}{1+\nu} \left[ \frac{9}{4} \left( 1 + \frac{2\nu+1}{\nu^2+4\nu+2} \right)^{-1} - 1 \right] \quad (2.14a)$$

$$\frac{\varepsilon_{X^+}(\nu)}{Ry_X} = \frac{1}{\nu} \frac{\varepsilon_{X^-}(1/\nu)}{Ry_X}. \quad (2.14b)$$

Here,  $Ry_X$  is the 3D exciton binding energy. These results are plotted in Fig. 2.1 (a), showing a reasonably good with the variational calculations of Refs. [271, 272, 282].

While the results previously discussed are valid for the strictly 2D limit, Ref. [284] has extended them to the quasi-2D geometry, by including the effective quantum well width. In particular, considering the specific case of  $X^-$  and assuming that the in-plane and perpendicular degrees of freedom factorize:

$$\Psi(\mathbf{r}_{\mathbf{r}_1}, \mathbf{r}_{e2}, \mathbf{r}_h, z_{e1}, z_{e2}, z_h) = \varphi(\mathbf{r}_{\mathbf{r}_1}, \mathbf{r}_{e2}, \mathbf{r}_h) \phi_e(z_{e1}) \phi_e(z_{e2}) \phi_h(z_h). \quad (2.15)$$

The effective 2D Coulomb potential is obtained from averaging the 3D potential over the particle densities in the quantum well confining direction:

$$V_{\sigma\sigma'}(\mathbf{r}_\sigma, \mathbf{r}_{\sigma'}) = \frac{e^2}{\epsilon} \int dz_\sigma dz_{\sigma'} \frac{\phi_\sigma^2(z_\sigma) \phi_{\sigma'}^2(z_{\sigma'})}{\sqrt{|\mathbf{r}_\sigma - \mathbf{r}_{\sigma'}|^2 + (z_\sigma - z_{\sigma'})^2}}, \quad (2.16)$$

where  $\sigma, \sigma' = e, h$ . One thus obtains a quasi-2D problem, which, in Ref. [284] is solved using a variational approach similar to the one employed in Ref. [286]. This work considers the specific case of a 25 nm GaAs quantum well and finds an agreement with the experimental results of [287]. Further, the authors compare their results with those obtained with a finite-difference technique [288], where the potential Eq. (2.16) is approximated as:

$$V_{\sigma\sigma'}(\mathbf{r}_\sigma, \mathbf{r}_{\sigma'}) \simeq \frac{e^2}{\epsilon} \frac{1}{\sqrt{|\mathbf{r}_\sigma - \mathbf{r}_{\sigma'}|^2 + (\alpha d_{QW})^2}}. \quad (2.17)$$

Here,  $\alpha$  is a fitting parameter that depends on the quantum well width  $d_{QW}$ . The results for the full potential (2.16) are shown as black symbols in Fig. 2.1 (b), while the trion binding energies obtained with the simplified potential (2.17) are shown as solid and dashed lines. It was found that the differences between the trion binding energies of positively and negatively charged excitons in quantum wells are less pronounced than in an ideal 2D case — see Fig. 2.1 (b).

The results discussed above can be applied to a quantum well in inorganic materials such as group III-V and II-VI compounds. More recently, variational approaches, similar to the ones used in Refs. [271, 272], have been applied to evaluate the trion binding energy in TMD monolayers [53, 268, 289]. Here, as discussed in Sec. 1.3, instead of a Coulomb potential, one has to use a Rytova-Keldish potential (1.29). In the calculations of Ref. [53, 289], microscopic details such as effective masses and screening length have been extracted from either density functional theory (DFT) and GW approximation or *ab initio* calculations. Similar to the quantum well case, also for TMD monolayers it has been found that for distinguishable majority charges both  $X^\pm$  are bound for any electron-hole mass ratio [268]. Path integral [290, 291] and diffusion Monte Carlo calculations [292] have given values for the trion binding energies in good agreement with those obtained from variational calculations. There have been also calculations not based on a parabolic band approximation, such as those based on stochastic approaches [293, 294], that have demonstrated a good agreement with effective mass models. Another computationally accurate method that does not rely on a parabolic band approximation is the one employing the Bethe-Salpeter equation [295], already used to describe excitonic properties [52, 57, 84]. Here, direct diagonalization of the corresponding three-particle Hamiltonian [270, 296–300] has led to results in reasonable agreement with those using a parabolic band approximation.

From the experimental point of view, there is a vast literature studying the signatures of (distinguishable) trions in optical spectra. The first detection of trions  $X^-$  in inorganic quantum wells can be found in Ref. [301] for a CdTe-based multiple quantum well structure using as doping source Indium planes placed inside the quantum well barriers. Analyzing absorption spectra, the authors found a trion binding energy of 2.7 meV. Later, a trion resonance has been observed in photoluminescence experiments in gated GaAs quantum wells, with trion binding energies in the range of 1.2 – 2 meV [278, 279, 302, 303]. These resonances can be attributed to three-body states in a spin-singlet state, while spin-triplet trions for  $X^-$  are unbound [271, 278, 286].

In TMD monolayers, researchers have recently observed trions in Mo-based [54, 297, 304, 306] and W-based [306–308] monolayers, with binding energies in the range of 20 – 40 meV, which is 10 or more times larger than in III-V and II-VI compound quantum wells. In Mo-based TMDs optical selection

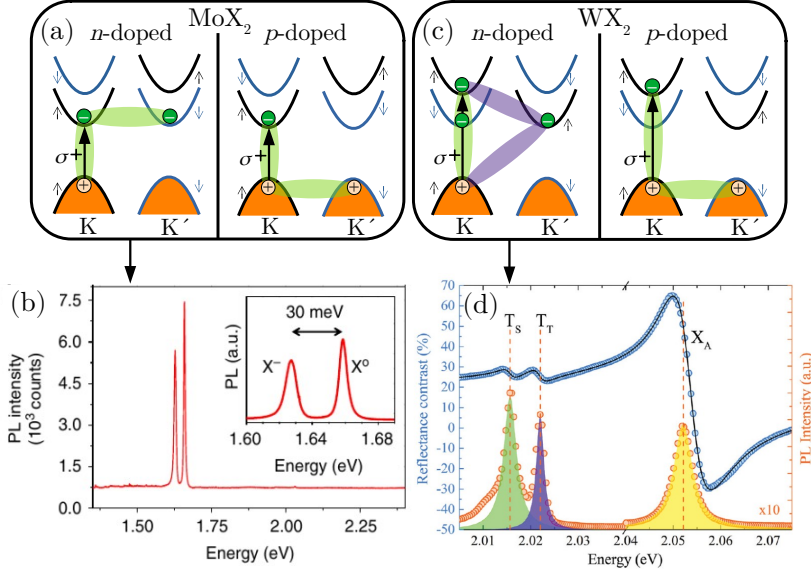


**Fig. 2.2:** (a) Schematic band structure of MoX<sub>2</sub> (a) and WX<sub>2</sub> (c) TMD monolayers with an extra charge. A  $\sigma^+$  polarised external laser generates a K-intervalley particle-hole pair. Green areas (purple area) indicate the spin-singlet intervalley trions (spin-triplet intravalley trion) that can form. In all cases are distinguishable trions. (b) Photoluminescence spectrum of a MoSe<sub>2</sub> TMD monolayer obtained in Ref. [304]. The inset shows the energy difference between the negatively charged trion and the neutral exciton. (d) Reflectance contrast (blue circles) and photoluminescence (orange circles) spectra of a WS<sub>2</sub> monolayer [305]. Green, purple, and yellow Lorentzian profiles are best fits for singlet trion, triplet trion, and neutral exciton, respectively.

rules establish that the lowest energy A-exciton is formed with an electron in the lowest conduction band and a hole in the highest valence band at the K and K' points. In presence of a moderate  $n$ -doping, the optically generated electron-hole pair can bind to an electron in the opposite valley with an opposite spin, thus forming a spin singlet intervalley trion. The same happens for moderate  $p$ -doping — see Figs. 2.2 (a,b). The triplet trion that can form from an extra charge in the same valley and band of either the electron or hole of the optically generated electron-hole pair is unbound for the values of electron and hole masses in TMD monolayers [270]. This indistinguishable trion state in fact displays a  $p$ -wave symmetry and thus it is always more weakly bound than the  $s$ -wave solution — we will discuss this aspect in detail in Ch. 4. In W-based TMD monolayers, the situation is similar for  $p$ -doping but changes drastically for  $n$ -doping. Here, in fact, the conduction bands are spin-inverted with respect to M-based TMD monolayers, and thus optical selection rules impose that the lowest energy A-exciton involves an electron in the upper conduction bands. For moderate  $n$ -doping, there are two different spin configurations for

distinguishable trions: an intravalley spin singlet trion configuration and an intervalley spin triplet configuration — see Fig. 2.2 (c). The trion spin doublet can be resolved because the singlet and triplet trions have different binding energies. Indeed, as predicted by Ref. [309], a repulsive electron-electron exchange energy affects the triplet trion but not the singlet one, giving a splitting of about 7 meV between these states. The trion doublet has been observed for WSe<sub>2</sub> [268, 310–312] and for WS<sub>2</sub> [313–315] — see Fig. 2.2 (d).

It is important to note that the fact that trions are observed in optical spectra such as PL and reflectance spectra means that trions have a finite oscillator strength, i.e., a finite coupling to light. However, as we will discuss in detail in Ch. 4 it is easy to show that in the strictly three-body limit, a trion has a vanishingly small oscillator strength [264, 266, 300, 316, 317]). The trion oscillator strength becomes however finite in presence of a finite density of majority carriers [266]. Here, depending if one considers distinguishable or indistinguishable trions, one has that the oscillator strength increases linearly [266, 317, 318] or quadratically with the Fermi sea energy [174]. In this regime, however, a more appropriate formalism describing the system’s optical properties is the one provided by the Fermi polaron model — see Sec. 2.3

There have been already in the past several authors questioning if the trion description is the most appropriate to describe the optical response of doped or gated two-dimensional semiconductors in presence of a finite density of excess carriers. It was already pointed out by Refs. [286, 318–320] that there are several experimental results that contrast with what is predicted by a three-body trion theory. For example, as we also discuss in Sec. 2.3, increasing the Fermi energy implies a transfer of oscillator strength from the exciton to the trion up to a point, when the Fermi energy is close to the trion binding energy, that all the oscillator strength is on the trion. This observation cannot be explained via a few-body description. Further, the distance between the exciton and trion energies measured in absorption or reflection, a quantity that should have the meaning of the trion binding energy, increases with growing electron density. However, the trion binding energy is expected to decrease with doping because of Pauli blocking effects and the reduction of Coulomb interaction due to screening [286]. It is therefore clear that beyond the very low-density regime, where the Fermi energy is much smaller than the trion binding energy, an alternative modelling to a few-body approach is necessary. Recent proposals [261, 264, 321, 322] have argued that the polaron description allows overcoming these limitations of the trion theory at finite doping and the experimental results can be interpreted in terms of the polaron model.

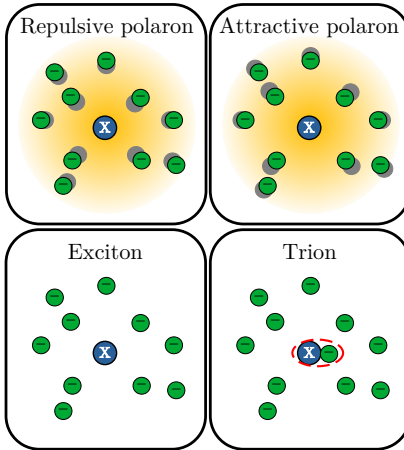


**Fig. 2.3:** Schematic representation of the possible states occurring in the “impurity problem”. In the many-body polaron description (top panels), the dressing of the impurity by excitations of the medium leads to the formation of repulsive and attractive polaron quasiparticles. In a few-body “mean-field”-like description (bottom panels), the interaction results in the formation of either an exciton or a trion surrounded by an inert Fermi sea.

## 2.3 Fermi polarons

The concept of “impurity problem” in quantum physics, i.e., a few particles surrounded by a quantum gas, goes back to 1933 when the Russian physicist Lev Landau [323] described the properties of conduction electrons in a dielectric medium<sup>1</sup>. Polarons are quasiparticles resulting from the dressing of the electrons by collective excitations of the dielectric medium. This idea was further elaborated by Fröhlich [325] who considered the properties of electrons in an ionic crystal, which were treated as a phonon bath. Here, polarons are electrons dressed by the phonon cloud in the crystal. The physical properties of a polaron, for instance, its mobility or its effective mass, can be very different from those of the bare electron, leading to strong modifications of the electrical and thermal transport properties of the material [326–328].

Polarons are ubiquitous in physics. Celebrated examples are the case of <sup>3</sup>He impurities in <sup>4</sup>He [329] and the Kondo effect generated by localized magnetic impurities in a metal [330]. Polarons also occur in nuclear [331, 332] and quark-gluon plasma [333] problems. Despite nearly a century of work, the polaron problem continues to attract significant interest [334–336] and research on this topic has expanded into new fundamental and applied areas.

Recent ground-breaking experiments in ultracold atomic gases have allowed exploring this regime [337–339] to a detailed level. Here, there is the unique possibility of considering a bath of different statistics (either fermionic or bosonic) and most importantly it is possible to tune the interaction strength between the impurity and the bath by using an external magnetic field via

<sup>1</sup> The name “polaron” was coined by Pekar in 1946 [324] to define the quasiparticle formed by an excess charge carrier localized within a potential well, generated by displacing the surrounding ions.

the Fano-Feshbach resonance [340]. Using this powerful tool, recent experiments have been able to vary the interaction between the impurity and the surrounding bath [341–343] allowing the study of polaron physics across the unitary regime of strong interactions. Differently from the semiconductor realizations, for ultracold 3D Fermi gases, it has been possible to gather evidence of a polaron-molecule transition [344]. We will discuss the Fermi polaron problem realization in ultracold atom set-ups in Sec. 2.3.7, while here we focus on the realization of this problem in 2D gated/doped semiconductors.

### 2.3.1 Experiments

Recently, the absorption and emission spectra of doped/gated 2D TMD monolayers [198, 220, 321, 345–349] have been interpreted in terms of a Fermi-polaron model [260–265]. As described in detail in the following section, this model implies that the optically generated exciton is dressed by excitations of the 2D Fermi gas of excess charge carriers (electrons or holes) induced by either gating or natural doping of the TMD monolayer. This leads to the formation of new quasiparticles named “attractive” and “repulsive” Fermi polarons. As schematically depicted in Fig. 2.3, in the repulsive polaron the exciton repels the surrounding charge carriers, while in the attractive polaron, the exciton attracts the carriers, leading to a local density enhancement or depletion of the medium. In this theory, the presence of an impurity implies a many-body response and dressing by the surrounding fermionic medium. This contrasts with a few-body “mean-field” like description where the effect of interaction ends up in the formation of an exciton or a trion but is not a collective many-body response of the whole system.

The characteristic reflectance spectra of gated TMD monolayers are presented in Fig. 2.4, for MoSe<sub>2</sub> [220] and for WSe<sub>2</sub> [221]. In both cases, the monolayers are encapsulated in hBN to reduce disorder effects and gated using graphene-based electric contacts. Varying the applied gate voltage  $V_g$  allows for modification of the density of excess electrons ( $n$ -doped side) or holes ( $p$ -doped side). The gate voltage applied in these experiments is such that  $E_F \in [0, 40]$  meV [321, 350, 351]. The spectra of Fig. 2.4 show that there is a range in the gate voltage where the monolayer is charge neutral. Here, the optical resonance coincides with the neutral exciton. When the gate voltage  $V_g$  is increased beyond the neutral region, electrons (holes) are injected into the monolayer. For MoSe<sub>2</sub>, Fig. 2.4 (a),  $n$ -doped and  $p$ -doped regions are almost symmetric and demonstrate the emergence of two resonances, one at higher energy continuously connected with the exciton energy and the one at lower energy recovering, at low doping, the distinguishable spin-singlet intervalley trion energy. However, for WSe<sub>2</sub>, Fig. 2.4 (b), while the  $p$ -doped spectrum is similar to the one of MoSe<sub>2</sub>, for  $n$ -doping, there are two resonances occur-

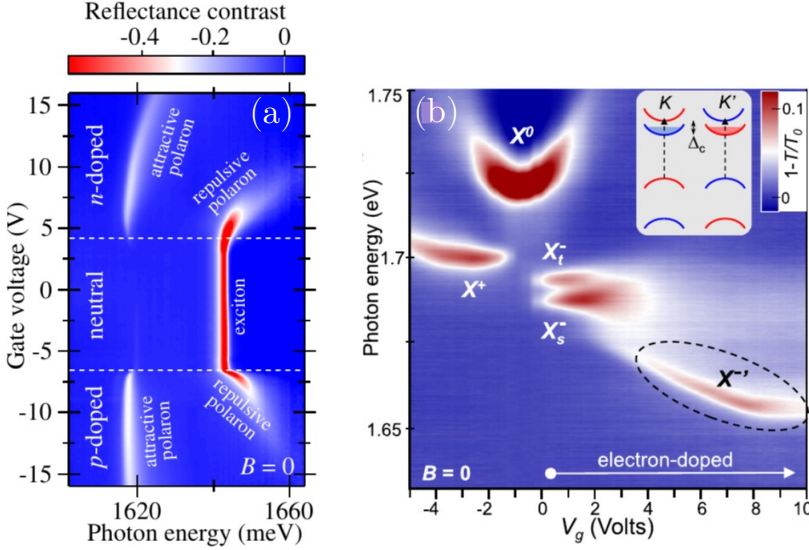


**Fig. 2.4:** Characteristic reflectance contrast (a) and absorption (b) spectra as a function of photon energy and gate voltage for MoSe<sub>2</sub> [220] (a) and WSe<sub>2</sub> [221] (b).

ring close to the trion energies which, at low doping, recover the energies of the spin-singlet intravalley distinguishable trion and that of the spin-triplet intervalley trion. Note that at third branch indicated as  $X^{-'}$  can be observed in the *n*-doped region of WSe<sub>2</sub>, whose nature is currently under debate and investigation [221, 312, 352–355].

As argued in detail in Sec. 2.3.2, it can be shown that the evolution of these resonances with the excess charge density is well described by a Fermi polaron theory [261, 265, 321, 356, 357]. The evolution of the attractive and repulsive polaron energies with density depends on several factors, among which are the number of Fermi seas involved in the problem and whether the exciton is affected by Pauli blocking mechanism or not. In the simplest case of a spin-polarised system, where the exciton is generated in a valley free of excess charges and the Fermi sea dressing occurs in a different valley, the attractive polaron is expected to red-shift in energy with doping, while the repulsive branch is expected to blue-shift. This case can be realized in presence of an external magnetic field. Indeed, the resulting Zeeman splitting effects lift the degeneracy of the two valleys, allowing one to selectively confine excess of charges in only one valley, to then optically excite an exciton in the opposite one — see Sec. 4.1 for further details on the role of Zeeman effects in TMD monolayers. Experimental results from Ref. [220] in this regime are shown in Fig. 4.12. Here, an out-of-plane magnetic field of  $B = 16$  T is applied to achieve a fully spin-polarized regime.

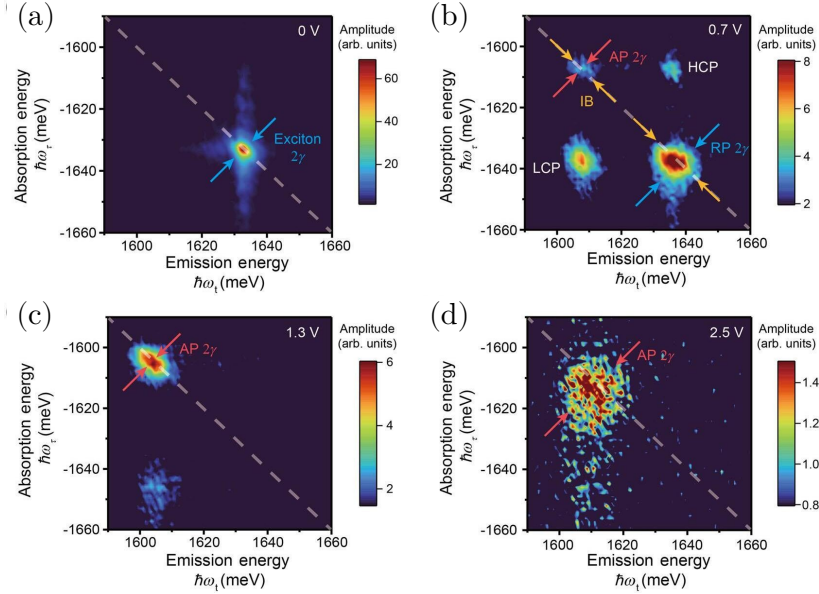


**Fig. 2.5:** One-quantum rephasing amplitude spectra of a MoSe<sub>2</sub> monolayer measured via 2D coherent electronic spectroscopy at different gate voltages (electron densities): (a)  $V_{TG} = 0\text{V}$  ( $n_e = 0$ ), (b)  $V_{TG} = 0.7\text{V}$  ( $n_e = 6.6 \times 10^{11}\text{cm}^{-2}$ ), (c)  $V_{TG} = 1.3\text{V}$  ( $n_e = 2.6 \times 10^{12}\text{cm}^{-2}$ ), and (d)  $V_{TG} = 2.5\text{V}$  ( $n_e = 6.6 \times 10^{12}\text{cm}^{-2}$ ). The homogeneous (inhomogeneous) linewidth of the exciton (a), attractive polaron (AP) (b-d), and repulsive polaron (RP) (b) are extracted from the cross-diagonal (diagonal) slices of the observed peaks. The two off-diagonal cross peaks, the lower (LCP) and higher cross peak (HCP) come from the electronic coupling between the attractive and repulsive polaron branches and have been previously studied in doped MoSe<sub>2</sub> monolayers [358]. Adapted from Ref. [351].

In the general case, while the repulsive branch always blue-shifts with doping, the attractive branch energy behavior is non-monotonic. If the exciton is generated in a valley with a finite density of free charges, the redshift due to the interaction with the Fermi sea in the opposite valley competes with the blueshift due to Pauli blocking effects on the fermionic components of the exciton. This effect simultaneously affects both the repulsive and attractive polaron behavior, meaning that their splitting is not affected. Thus attractive-repulsive polaron splitting originates solely from the polaronic dressing, and it increases linearly with  $E_F$  [54, 307], which can be considered as a hallmark of Fermi polaron physics as explained in the following section.

Another characteristic of the polaron problem is the oscillator strength transfer from the repulsive to the attractive branch. In the small doping regime, the attractive branch oscillator strength grows linearly with doping  $E_F$  [266], in agreement with the result obtained in a trion description. Increasing dop-

ing, the repulsive branch loses oscillator strength and its linewidth quickly broadens, while, at low temperatures, the attractive branch acquires oscillator strength but remains sharp. We will see in Ch. 3 that this feature is strongly dependent on temperature and, in the high temperature low doping regime, the attractive branch can significantly broaden and cease to be a well-defined quasiparticle [357, 359].

Homogeneous and inhomogeneous contributions to the polaron linewidths can be measured using two-dimensional coherent spectroscopy [360]. Very recently, this technique has been employed to a gated MoSe<sub>2</sub> monolayer — results are shown in Fig. 2.5. The inhomogeneous broadening is obtained by considering slices of the spectra in the diagonal direction (dashed lines), while the cross-diagonal direction gives information about the homogeneous broadening [360]. These experiments showed that the homogeneous broadening contribution to the repulsive polaron linewidth increases quadratically with  $E_F$ , while the attractive branch remains sharp and its homogeneous broadening is independent of doping [351]. While, as shown next in Sec. 2.3.2, a zero temperature polaron theory predicts a well-defined sharp attractive branch, whose broadening is doping independent, in agreement with these experiments, for the repulsive branch a zero temperature theory underestimates the broadening observed in experiments. Here, additional broadening mechanisms to those included in the polaron theory, such as non-radiative decay from the repulsive to the attractive branch enhanced by electron-electron interactions, have to be taken into account [351].

When the TMD monolayer is embedded in a microcavity, the strong coupling between light and matter can lead to the formation of Fermi polaron polaritons [244, 321, 345, 346, 361]. At finite doping, three polariton branches emerge, as shown in the reflectance spectra of Fig. 2.6 (a) [346]: the lower (LP), middle (MP), and upper (UP) polaritons branches are the result of strong coupling between the cavity photon and the attractive and repulsive polaron resonances. The polariton branch splitting is related to the polaron oscillator strength in the weak coupling regime to light. These splitting evolve thus with doping in a way described in detail in Sec. 2.3.4. Fig. 2.6 (b) shows the transmission spectrum of a MoSe<sub>2</sub> embedded into a fiber cavity is shown [321], revealing the dependence of the coupling to light of attractive and repulsive branches on the electron density. In order to do this, the authors of Ref. [321] have tuned the photon energy in resonance with either the attractive or the repulsive branch energies for each value of the gate voltage considered. One can observe that for the repulsive branch, the splitting between UP and MP diminishes with increasing doping because of the transfer of oscillator strength from the repulsive to the attractive branch. In contrast, while the attractive branch displays no splitting at neutrality, in agreement with the fact that the trion oscillator strength is negligible, a splitting first grows with doping and then eventually

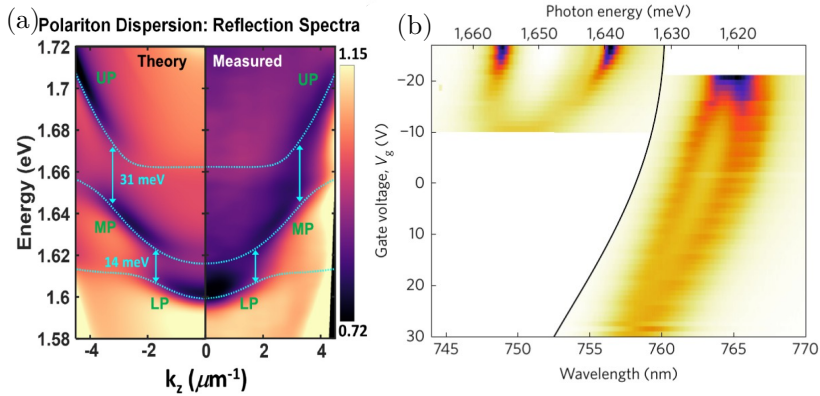


**Fig. 2.6:** (a) Reflection spectrum for a MoSe<sub>2</sub> monolayer embedded into an optical waveguide [346]. The light-blue dashed lines show the lower (LP), middle (MP), and upper polariton (UP). (b) Transmission spectrum of MoSe<sub>2</sub> embedded in a fibre cavity [321] as a function of photon frequency and gate voltage. On the left side of the solid black line, the photon is in resonance with the repulsive polariton branch, while on the right is in resonance with the attractive branch.

closes again.

There has been recently a rapidly increasing interest in the Fermi polaron regime in doped 2D semiconductors because of several reasons and because of fundamentally important implications that the study of this regime. One motivation lies in the fact that the dressing of polaritons by a Fermi gas can boost their non-linearities [198, 345, 362]. It has been recently found [198] that the effective polariton-polariton interaction strength can be enhanced by up to a factor of 50 compared to the charge-neutral regime when a MoSe<sub>2</sub> monolayer is electron-doped. Indeed, compared to a neutral polariton, the polaron-polariton is spatially much larger due to the local redistribution of electrons around the impurities [363]. This implies that polaritons are expected to interact at larger distances than polaritons. Note however that, even those these are extremely encouraging results, much larger polariton non-linearities are needed for quantum optics applications. Note also that the values reported in Ref. [198] are still inferior to those obtained with dipolar polaritons in coupled quantum well structures [364].

Reaching a regime of strongly interacting polaritons is relevant for exploring beyond mean-field effects, such as a polariton blockade regime. Note that recently, conventional and unconventional polariton blockade has been predicted for charged polaritons [365].

Another interesting prospect of considering charged exciton and polariton configurations lies in the possibility of manipulating these states by external electric and magnetic fields [220, 322, 366, 367]. Even though polaritons are

charge-neutral optical excitations, their interaction with the Fermi sea implies they respond to electric and magnetic fields.

Crucially, it has been recently shown that polaron states in charged 2D semiconductors can be employed to probe strongly correlated electron phases, such as a Wigner crystal phase [248, 368], a quantum Hall regime [220], fractional quantum Hall states in proximal graphene layers [369], and correlated Mott states of electrons in a moiré superlattice [370].

### 2.3.2 Zero temperature model

We dedicate this section to the description of a zero temperature Fermi polaron model tailored to describe the optical absorption spectra of gated/doped TMD monolayers at very low temperatures. The analysis of temperature effects will be carried on in Ch. 3. The model we use here is the one proposed in Refs. [261, 265, 321].

Let us consider the case of a low density of optically generated excitons in a doped TMD monolayer. The relevant energy scales of this problem are the exciton binding energy  $\varepsilon_X$ , the trion binding energy  $\varepsilon_T$ , and the Fermi sea energy  $E_F$ . As previously discussed, for TMD monolayers one has typically that  $\varepsilon_X \gg \varepsilon_T$ , with  $\varepsilon_X \sim 0.4 - 0.7$  eV [55, 72–74] and  $\varepsilon_T \sim 20 - 40$  meV [54, 297, 304, 306–308]. Further, we have seen in Sec. 2.3.1 that typically studied ranges of doping correspond to a Fermi energy  $E_F \sim 0 - 40$  meV. Thus, in these structures, one has that the exciton binding energy is the largest energy scale  $\varepsilon_X \gg \varepsilon_T, E_F$ . In this limit, approximating the exciton as a tightly bound structureless boson is a good approximation and a significant simplification as it reduces the problem degrees of freedom.

Further, we are going to focus on the spin-valley polarized case, where we ignore the spin and valley degrees of freedom by considering a polarized configuration. Here, the exciton is created in a valley different from the one of the Fermi electron gas. This configuration is motivated by the fact that, in those systems where the indistinguishable trion is not bound, the relevant dressing of the exciton occurs from those interband electron-hole pairs that belong to a different valley and thus that lead to the formation of a distinguishable trion — see Fig. 2.7. Note that in Mo-based TMD monolayers, Pauli blocking effects from the electron Fermi sea belonging to the same valley of the exciton can lead to a different doping dependence of the polaron energy shift from those predicted in our model see Fig. 2.7. This effect could be taken into account including a Fermi energy dependence on the exciton energy [321]. However, as we will see that neither this effect nor the bandgap renormalization affects the polaron energy splitting or other polaron properties such as the oscillator strength and the broadening, we will avoid it by considering the spin-valley polarised case.

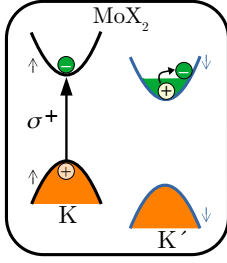


**Fig. 2.7:** The degeneracy between the K and K' valley can be lifted by applying a magnetic field perpendicular to the TMD monolayer — here is sketched a Mo-based monolayer. This allows for generating a spin-valley fully polarised configuration where the exciton is optically generated in one valley and is dressed by intravalley particle-hole excitations in the Fermi sea of the other valley.

The Hamiltonian employed is given by

$$\hat{H} = \hat{H}_0 + \hat{H}_{0X} + \hat{H}_{int} \quad (2.18a)$$

$$\hat{H}_0 = \sum_{\mathbf{k}} \epsilon_{\mathbf{k}} \hat{c}_{\mathbf{k}}^{\dagger} \hat{c}_{\mathbf{k}} \quad (2.18b)$$

$$\hat{H}_{0X} = \sum_{\mathbf{k}} \epsilon_{X\mathbf{k}} \hat{x}_{\mathbf{k}}^{\dagger} \hat{x}_{\mathbf{k}} \quad (2.18c)$$

$$\hat{H}_{int} = -\frac{v}{\mathcal{A}} \sum_{\mathbf{k}\mathbf{k}'\mathbf{q}} \hat{x}_{\mathbf{k}+\mathbf{q}}^{\dagger} \hat{c}_{\mathbf{k}'-\mathbf{q}}^{\dagger} \hat{c}_{\mathbf{k}'} \hat{x}_{\mathbf{k}}. \quad (2.18d)$$

Here, the fermionic operator  $\hat{c}_{\mathbf{k}}^{\dagger}$  creates a majority charged particle (either a conduction electron or a valence hole) with mass  $m$  and dispersion  $\epsilon_{\mathbf{k}} = \mathbf{k}^2/2m$ , while  $\hat{x}_{\mathbf{k}}^{\dagger}$  create an exciton with energy  $\epsilon_{X\mathbf{k}} = \epsilon_{X0} + \mathbf{k}^2/2m_X$ , where  $\epsilon_{X0} = -\epsilon_X$  — we are measuring energies with respect to the energy gap  $E_g$ , which is thus set to zero throughout this chapter. We consider the specific case of majority particles being electrons, but results can be easily extended to the case of hole doping. For simplicity, the model assumes that free charges are non-interacting.

If the Fermi sea is interacting, there are two possibilities to consider. The first is that it forms a strongly correlated phase at low density, in which case our current model can not be able to fully capture the physics of the system. The second possibility is that the free charges form a Fermi liquid at higher temperatures, where the excitations are quasiparticles analogous to particle-hole pairs. In this case, while quantitative deviations are still possible, we do not expect significant qualitative deviations from our theoretical model.

The  $\hat{H}_{int}$  term in Eq. (2.18d) describes the attractive interaction between electrons and excitons, which is approximated as short-range with a coupling strength of  $v > 0$ . Because a contact interaction leads to ultraviolet (UV) divergences [371], we introduce an UV cutoff  $\Lambda$  and renormalize the contact interaction by relating the bare parameter  $v$  to the trion binding energy  $\varepsilon_T$  (2.5) [372]:

$$\frac{1}{v} = \frac{1}{\mathcal{A}} \sum_{\mathbf{k}}^{\Lambda} \frac{1}{\varepsilon_T + \epsilon_{X\mathbf{k}} - \epsilon_{X0} + \epsilon_{\mathbf{k}}}. \quad (2.19)$$

By using this definition, we will find that all results will be cutoff independent

in the  $\Lambda \rightarrow \infty$  limit. As shown later, this equation can be derived from the Schrödinger equation (2.4) for the bound trion with energy  $E_T = \epsilon_{X\mathbf{0}} - \varepsilon_T$ . It has been recently demonstrated [265] that, when  $\varepsilon_X \gg \varepsilon_T, E_F$  approximating the exciton-electron interaction as short-range leads to essentially the same results for the polaron properties than those obtained by employing a microscopic finite-range potential. Note that, under the assumption of contact interaction, the Pauli exclusion principle suppresses  $s$ -wave interactions between the same species of fermion.

### 2.3.3 Simplified model for the distinguishable trion

Before moving on to describing the polaron formalism, we illustrate here the properties of the distinguishable trion within the simplified model Hamiltonian (2.18). As the attractive polaron recovers, in the low-doping regime, some of the trion properties, such as its energy and oscillator strength, it is useful to derive them first in this section.

At zero temperature, a trion with momentum  $\mathbf{Q}$  in the presence of a Fermi sea  $|FS\rangle = \prod_{|\mathbf{q}| < k_F} c_{\mathbf{q}}^\dagger |0\rangle$  is described as:

$$|T_2^{(\mathbf{Q})}\rangle = \frac{1}{\sqrt{\mathcal{A}}} \sum_{|\mathbf{k}| > k_F} \eta_{\mathbf{k}}^{(\mathbf{Q})} \hat{x}_{\mathbf{Q}-\mathbf{k}}^\dagger \hat{c}_{\mathbf{k}}^\dagger |FS\rangle. \quad (2.20)$$

The trion wave function  $\eta_{\mathbf{k}}^{(\mathbf{Q})}$  satisfies the Schrödinger equation [373]

$$E_T^{(\mathbf{Q}, E_F)} \eta_{\mathbf{k}}^{(\mathbf{Q})} = (\epsilon_{X\mathbf{Q}-\mathbf{k}} + \epsilon_{\mathbf{k}}) \eta_{\mathbf{k}}^{(\mathbf{Q})} - \frac{v}{\mathcal{A}} \sum_{|\mathbf{k}'| > k_F} \eta_{\mathbf{k}'}^{(\mathbf{Q})}, \quad (2.21)$$

and the trion energy can be evaluated by solving the implicit equation:

$$\frac{1}{v} = \frac{1}{\mathcal{A}} \sum_{|\mathbf{k}| > k_F} \frac{1}{-E_T^{(\mathbf{Q}, E_F)} + \epsilon_{X\mathbf{Q}-\mathbf{k}} + \epsilon_{\mathbf{k}}}. \quad (2.22)$$

For  $\mathbf{Q} = \mathbf{0}$  and  $E_F = 0$ , this equation coincides with Eq. (2.19), which admits the following solution in terms of the trion energy and wave function:

$$E_T^{(\mathbf{0}, 0)} = \epsilon_{X\mathbf{0}} - \varepsilon_T \quad (2.23a)$$

$$\eta_{\mathbf{k}}^{(\mathbf{0})} = \frac{\sqrt{Z_T}}{\varepsilon_T + \frac{\mathbf{k}^2}{2m_r}}, \quad (2.23b)$$

where  $m_r = mm_X/m_T$  is the trion reduced mass and  $Z_T = 2\pi\varepsilon_T/m_r$ .

Let us discuss the solution of Eq. (2.22) in different limits. When  $E_F = 0$ , it is profitable to introduce the relative momentum in the center of mass frame  $\mathbf{q}_r$ ,

so that the electron momentum becomes  $\mathbf{k} = \mathbf{q}_r + \mathbf{Q}_c$ , with  $\mathbf{Q}_c = \frac{m}{m_T} \mathbf{Q}$ , where  $m_T = m_X + m$  is the trion mass, and the exciton momentum becomes  $\mathbf{Q} - \mathbf{k} = \mathbf{Q}_X - \mathbf{q}_r$ , with  $\mathbf{Q}_X = \frac{m_X}{m_T} \mathbf{Q}$ . Now one has that relative and center of mass kinetic energies factorize,  $\epsilon_{X\mathbf{Q}-\mathbf{k}} + \epsilon_{\mathbf{k}} = \epsilon_{X\mathbf{Q}_X-\mathbf{q}_r} + \epsilon_{\mathbf{q}_r+\mathbf{Q}_c} = \epsilon_{X\mathbf{0}} + \epsilon_{r\mathbf{q}_r} + \epsilon_{T\mathbf{Q}}$ , where  $\epsilon_{r\mathbf{q}_r} = \frac{q_r^2}{2m_r}$  and  $\epsilon_{T\mathbf{Q}} = \frac{Q^2}{2m_T}$ . Thus, the trion energy and wave function are

$$E_T^{(\mathbf{Q}, E_F=0)} = -\varepsilon_T + \epsilon_{X\mathbf{0}} + \frac{Q^2}{2m_T} \quad (2.24a)$$

$$\tilde{\eta}_{\mathbf{q}_r}^{(\mathbf{Q})} = \frac{\sqrt{Z_T}}{\varepsilon_T + \epsilon_{r\mathbf{q}_r}} = \tilde{\eta}_{\mathbf{q}_r}^{(\mathbf{0})}, \quad (2.24b)$$

where  $\tilde{\eta}_{\mathbf{q}_r}^{(\mathbf{Q})} = \eta_{\mathbf{q}_r+\mathbf{Q}_c}^{(\mathbf{Q})}$ . At finite doping and zero momentum  $\mathbf{Q} = \mathbf{0}$ , Eqs. (2.21) and (2.22) can also be solved exactly to give

$$E_T^{(\mathbf{0}, E_F)} = -\varepsilon_T + \epsilon_{X\mathbf{0}} + \frac{m_T}{m_X} E_F \quad (2.25a)$$

$$\eta_{\mathbf{k}}^{(\mathbf{0})} = \frac{\sqrt{Z_T}}{-E_T^{(\mathbf{0}, E_F)} + \epsilon_{X\mathbf{0}} + \epsilon_{r\mathbf{k}}}. \quad (2.25b)$$

At finite doping and finite momentum, the integral in Eq. (2.22) can be solved analytically [374] and one gets an implicit equation for the trion energy:

$$2\varepsilon_T = -\tilde{E}_T^{(\mathbf{Q}, E_F)} - \frac{Q^2 m}{m_X m_T} + \sqrt{\left( \tilde{E}_T^{(\mathbf{Q}, E_F)} + \frac{Q k_F}{m_X} \right) \left( \tilde{E}_T^{(\mathbf{Q}, E_F)} - \frac{Q k_F}{m_X} \right)}, \quad (2.26)$$

where  $\tilde{E}_T^{(\mathbf{Q}, E_F)} = E_T^{(\mathbf{Q}, E_F)} - \frac{Q^2}{2m_X} - \frac{m_T}{m_X} E_F - \epsilon_{X\mathbf{0}}$ . This equation can be solved numerically and one finds that the trion acquires a finite momentum when  $E_F > \frac{m_X m_r}{m^2} \varepsilon_T$  [374].

Is it instructive to analyze the trion coupling strength to light in the simplified description of the Hamiltonian (1.34). It is very easy to understand why, at zero doping,  $E_F = 0$ , trions do not couple to light, and thus cannot be probed optically. This is because the matrix element between a trion state and a cavity photon plus a majority particle at zero momentum  $|C+1\rangle = \hat{a}_0^\dagger \hat{c}_0^\dagger |0\rangle$  of the light-matter interaction term  $\sum_{\mathbf{k}} \hat{x}_{\mathbf{k}}^\dagger \hat{a}_{\mathbf{k}}$  is given by

$$\langle T_2^{(0)} | \sum_{\mathbf{k}} \hat{x}_{\mathbf{k}}^\dagger \hat{a}_{\mathbf{k}} | C+1 \rangle = \frac{1}{\sqrt{\mathcal{A}}} \eta_{\mathbf{0}}^{(0)}. \quad (2.27)$$

Taking the squared amplitude of this matrix element, we see that the coupling

to light of a single trion scales as  $1/\mathcal{A}$ , which is vanishingly small. On the other hand, if one has  $N$  electrons within the area  $\mathcal{A}$ , then the coupling to light scales instead as  $N/\mathcal{A} = n \sim E_F$ . Thus, even though the coupling per electron vanishes, the net effect of having an electronic medium is to create a continuum of states, with a total spectral weight that scales as  $E_F$ , in agreement with Ref. [266].

### 2.3.4 Chevy ansatz and self-energy

In the limit of weak optical pumping which generates a low density of excitons, such that the excitons can be considered as independent, non-interacting impurities, the polaron ground state can be described by the following ansatz:

$$|P_3^{(\mathbf{Q})}\rangle = \varphi_0^{(\mathbf{Q})} \hat{x}_{\mathbf{Q}}^\dagger |FS\rangle + \frac{1}{\mathcal{A}} \sum_{\mathbf{k}, \mathbf{q}} \varphi_{\mathbf{k}\mathbf{q}}^{(\mathbf{Q})} \hat{x}_{\mathbf{Q}+\mathbf{q}-\mathbf{k}}^\dagger \hat{c}_{\mathbf{k}}^\dagger \hat{c}_{\mathbf{q}} |FS\rangle, \quad (2.28)$$

where the wave functions  $\varphi_0^{(\mathbf{Q})}$  and  $\varphi_{\mathbf{k}\mathbf{q}}^{(\mathbf{Q})}$  are to be found variationally. This is also known as Chevy's variational ansatz [375], originally formulated to describe the phase diagram of an interacting ultracold Fermi gas in the limit of extreme imbalance of the spin populations. Eq. (2.28) is a state which is a superposition of a bare exciton, and an exciton dressed by a single interband particle-hole excitation of the Fermi sea  $|FS\rangle$ . This involves exciting an electron from the Fermi sea to a momentum  $\mathbf{k} > \mathbf{k}_F$ , thus leaving behind a hole with momentum  $\mathbf{q} < \mathbf{k}_F$ . This exciton dressed by an electron-hole pair is also referred to as "trion-hole" state, even though is not a superposition of a bound trion plus a hole. This idea was already introduced to describe a doped semiconductor by Ref. [286]. We will discuss the comparison between the results obtained next within Chevy's ansatz (2.28) and those obtained in Ref. [286] in Sec. 2.3.5.

One might wonder why and in which limit truncating the expansion to a single interband particle-hole excitation in Eq. (2.28) is a good approximation for describing the impurity problem. For a contact interaction potential between the impurity and the Fermi sea as the one employed in Eq. (2.18d), it has been demonstrated that an almost exact cancellation of higher order contributions [376–378].

The energy of the polaron state is obtained by minimizing the expectation value  $\langle P_3^{(\mathbf{Q})} | \hat{H} - E | P_3^{(\mathbf{Q})} \rangle$  with respect to the variational parameters  $\varphi_0^{(\mathbf{Q})}$  and  $\varphi_{\mathbf{k}\mathbf{q}}^{(\mathbf{Q})}$ . This yields the equations:

$$E\varphi_0^{(\mathbf{Q})} = \epsilon_{X\mathbf{Q}}\varphi_0^{(\mathbf{Q})} - \frac{v}{\mathcal{A}^2} \sum_{\mathbf{k}\mathbf{q}} \varphi_{\mathbf{k}\mathbf{q}}^{(\mathbf{Q})}, \quad (2.29a)$$

$$E\varphi_{\mathbf{k}\mathbf{q}}^{(\mathbf{Q})} = E_{X\mathbf{k}\mathbf{q}\mathbf{Q}}\varphi_{\mathbf{k}\mathbf{q}}^{(\mathbf{Q})} - v\varphi_0^{(\mathbf{Q})} - \frac{v}{\mathcal{A}} \sum_{\mathbf{k}'} \varphi_{\mathbf{k}'\mathbf{q}}^{(\mathbf{Q})} + \frac{v}{\mathcal{A}} \sum_{\mathbf{q}'} \varphi_{\mathbf{k}\mathbf{q}'}^{(\mathbf{Q})}, \quad (2.29b)$$

where  $\epsilon_{X\mathbf{Q}} = \epsilon_{X\mathbf{0}} + \mathbf{Q}^2/2m_X$  and  $E_{X\mathbf{kqQ}} = \epsilon_{X\mathbf{Q+q-k}} + \epsilon_{\mathbf{k}} - \epsilon_{\mathbf{q}} = \epsilon_{X\mathbf{0}} + (\mathbf{Q} + \mathbf{q} - \mathbf{k})^2/2m_X + (\mathbf{k}^2 - \mathbf{q}^2)/2m$ . Since  $\varphi_{\mathbf{kq}}^{(\mathbf{Q})} \sim 1/k^2$  for large values of  $k$ , this implies that the last term on the r.h.s of Eq. (2.29b) vanishes when the cutoff  $\Lambda \rightarrow \infty$  and  $v \sim 1/\log \Lambda \rightarrow 0$  and can be therefore neglected. Note that the energy of an exciton at rest  $\epsilon_{X\mathbf{0}}$  can be rescaled out of Eqs (2.29),  $E \mapsto E - \epsilon_{X\mathbf{0}}$ , and we will therefore measure energies with respect to it from now onwards.

There are several equivalent ways of solving the eigenvalue problem (2.29) and evaluating optical observables such as the absorption spectrum. One direct way is to discretize the momenta  $\mathbf{k}$  and  $\mathbf{q}$  on a grid and to directly diagonalize the resulting matrix, obtaining the eigenvalues  $E_{n\mathbf{Q}}$  and eigenvectors  $\varphi_{n\mathbf{0}}^{(\mathbf{Q})}$  and  $\varphi_{n\mathbf{kq}}^{(\mathbf{Q})}$  — see App. A for further details. One can then evaluate the retarded exciton Green's function with the same procedure described in Sec. 1.5.3:

$$G_X(\omega, \mathbf{Q}) = \sum_n \frac{|\varphi_{n\mathbf{0}}^{(\mathbf{Q})}|^2}{\omega + i\eta_X - E_{n\mathbf{Q}}} . \quad (2.30)$$

Here, the positive imaginary component  $\eta_X > 0$  guarantees that the retarded condition is satisfied. At the same time, as already discussed in Sec. 1.5.1,  $\eta_X$  can be physically interpreted as the contribution of the homogeneous and inhomogeneous broadening to the exciton linewidth.

A more rigorous approach (that in an appropriate limit recovers the results obtained within the Chevy ansatz) is one that makes use of the concept of exciton self-energy  $\Sigma_X(\omega, \mathbf{Q})$  [141]

$$\Sigma_X(\omega, \mathbf{Q}) = \frac{1}{\mathcal{A}} \sum_{\mathbf{q}} \mathcal{J}(\omega, \mathbf{q}, \mathbf{Q}) , \quad (2.31)$$

where  $\mathcal{J}(\omega, \mathbf{q}, \mathbf{Q})$  is the  $T$  matrix describing the exciton-medium scattering. The self-energy describes the energy that a particle gains as a result of its interactions with the surrounding medium. Ideally, the self-energy should contain all contributions from the exciton-medium interaction, i.e.,

$$\Sigma_X(\omega, \mathbf{Q}) = \Sigma^{1ph}(\omega, \mathbf{Q}) + \Sigma^{2ph}(\omega, \mathbf{Q}) + \dots . \quad (2.32)$$

Nevertheless, if one includes a single particle-hole dressing of the Fermi cloud, the self-energy can be truncated at the first order. This approximation is referred to as the ladder approximation [379]. Within Chevy's ansatz, the exciton self-energy can be derived starting from the eigenvalue problem (2.29),

by rewriting it in an equivalent form by using the auxiliary function  $\chi_{\mathbf{q}}^{(\mathbf{Q})}$ :

$$\chi_{\mathbf{q}}^{(\mathbf{Q})} = \frac{v}{\mathcal{A}} \sum_{\mathbf{k}} \varphi_{\mathbf{kq}}^{(\mathbf{Q})} \quad (2.33a)$$

$$E\varphi_0^{(\mathbf{Q})} = \epsilon_{X\mathbf{Q}}\varphi_0^{(\mathbf{Q})} - \frac{1}{\mathcal{A}} \sum_{\mathbf{q}} \chi_{\mathbf{q}}^{(\mathbf{Q})} \quad (2.33b)$$

$$E\varphi_{\mathbf{kq}}^{(\mathbf{Q})} = E_{X\mathbf{kqQ}}\varphi_{\mathbf{kq}}^{(\mathbf{Q})} - v\varphi_0^{(\mathbf{Q})} - \chi_{\mathbf{q}}^{(\mathbf{Q})}. \quad (2.33c)$$

Introducing Eq. (2.33c) into Eq. (2.33a) and solving for  $\chi_{\mathbf{q}}^{(\mathbf{Q})}$  we obtain

$$\chi_{\mathbf{q}}^{(\mathbf{Q})} = \varphi_0^{(\mathbf{Q})} \left[ \frac{1}{v} + \frac{1}{\mathcal{A}} \sum_{\mathbf{k}} \frac{1}{E - E_{X\mathbf{kqQ}}} \right]^{-1}, \quad (2.34)$$

where we have used that  $(v/\mathcal{A}) \sum_{\mathbf{k}} 1/(E - E_{X\mathbf{kqQ}}) \rightarrow -1$  in the limit  $\Lambda \rightarrow \infty$ . Substituting (2.34) into Eq. (2.33b), one thus finally obtains an implicit equation for the energy  $E$ :

$$E - \epsilon_{X\mathbf{Q}} = \frac{1}{\mathcal{A}} \sum_{\mathbf{q}} \left[ \frac{1}{v} - \frac{1}{\mathcal{A}} \sum_{\mathbf{k}} \frac{1}{E - E_{X\mathbf{kqQ}}} \right]^{-1}. \quad (2.35)$$

This equation can be employed to self-consistently find the polaron energy  $E$ .

The implicit equation for the polaron energy  $E$  (2.35) can be used to deduce the exciton self-energy within the one particle-hole excitation approximation

$$\begin{aligned} \Sigma_X(\omega, \mathbf{Q}) &= \frac{1}{\mathcal{A}} \sum_{\mathbf{q}} \mathcal{J}(\omega + \epsilon_{\mathbf{q}}, \mathbf{Q} + \mathbf{q}) \\ &= \frac{1}{\mathcal{A}} \sum_{\mathbf{q}} \left[ \frac{1}{v} - \frac{1}{\mathcal{A}} \sum_{\mathbf{k}} \frac{1}{(\omega + \epsilon_{\mathbf{q}}) - \epsilon_{X\mathbf{Q}+\mathbf{q}-\mathbf{k}} - \epsilon_{\mathbf{k}}} \right]^{-1}. \end{aligned} \quad (2.36)$$

Thus, the retarded exciton Green's function  $G_X(\omega, \mathbf{Q})$  can be written in terms of the exciton self-energy

$$G_X(\omega, \mathbf{Q}) = \frac{1}{\omega + i\eta_X - \epsilon_{X\mathbf{Q}} - \Sigma_X(\omega, \mathbf{Q})}, \quad (2.37)$$

by making use of the Dyson equation [141]:

$$G_X(\omega, \mathbf{Q}) = G_X^{(0)}(\omega, \mathbf{Q}) + G_X^{(0)}(\omega, \mathbf{Q})\Sigma_X(\omega, \mathbf{Q})G_X(\omega, \mathbf{Q}), \quad (2.38)$$

where  $G_X^{(0)}(\omega, \mathbf{Q}) = 1/(\omega + i\eta_X - \epsilon_{X\mathbf{Q}})$ . Finally, as discussed in Sec. 1.5.3 the optical absorption coincides with the exciton spectral function (1.79). As in Eq. (2.30) we have added by hand a positive imaginary part  $\eta_X$  to guarantee the

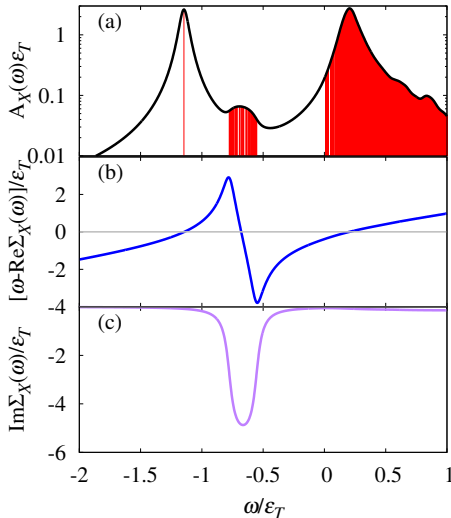


**Fig. 2.8:** (a) Exciton spectral function  $A_X(\omega)$  as a function of the photon frequency  $\omega$  (measured with respect to the exciton at rest energy  $\varepsilon_{X0}$ ), obtained by solving the matrix problem Eq. (2.29) or using the exciton Green’s function in terms of the self-energy  $\Sigma_X(\omega)$ . The red vertical lines are the eigenvalues  $E_n$ . Real (b) and imaginary (c) parts of the exciton self-energy  $\Sigma_X(\omega)$ . The electron density is fixed at  $E_F = 7.5$  meV, the exciton linewidth at  $\eta_X = 1$  meV, the trion binding energy  $\varepsilon_T = 25$  meV, and  $m_X = 2m_e$ .

retarded properties of the Green’s function, and that we can also interpret as the exciton broadening. Note that however calculations of the self-energy (2.36) can be carried on in the  $\eta_X = 0$  limit. This is essential if one wants to evaluate the system photoluminescence — see Sec. 3.2.3.

In the following, we are going to discuss the results that can be obtained by employing both approaches and show that they lead to exactly the same results. We are going to focus on the specific case of  $\mathbf{Q} = \mathbf{0}$  for the rest of this section and, thus, to lighten the notation we are going to drop the  $\mathbf{Q}$  dependence everywhere.

The zero temperature Fermi polaron formalism described in this section is applicable to any quantum impurity problem, i.e., an impurity surrounded by a 2D Fermi gas, including both ultracold atomic gases — which we will discuss in detail in Sec. 2.3.7 — and doped semiconductors. To be concrete, in the following, we will consider the experimentally relevant case of electron-doped MoSe<sub>2</sub> monolayers, where  $\varepsilon_T \simeq 25$  meV [321] and  $m_X/m = 2.05$  [59]. In this system one can readily achieve doping densities  $E_F$  in the range of 0–40 meV [321].

We plot in Fig. 2.8 (a) the spectral function  $A_X(\omega)$  (1.79), obtained by either solving the eigenvalue problem Eq. (2.29) or by evaluating the exciton self-energy  $\Sigma_X(\omega)$  (2.36). Both methods lead to exactly the same results. The exciton spectral function reveals thus that the spectrum is dominated by two resonances, the attractive and repulsive polaron branches. By evaluating the eigenvalues  $E_n$  obtained solving the matrix problem (2.29) we also find that the attractive branch coincides with the system lowest eigenvalue  $E_A = E_{n=1}$ , i.e., it is the polaron ground state, and that this eigenvalue is isolated and separated

from those that belong to the repulsive branch from a continuum, which we will identify with the trion-hole continuum. By contrast, the repulsive branch does not correspond to a specific eigenstate; rather it is composed of a continuum of eigenstates with closely spaced eigenvalues, resulting in a polaron quasiparticle with a finite lifetime, larger than the excitonic one  $\eta_X$ . The attractive and repulsive polaron energies, i.e., the energies of the spectral function peaks, can also be found by evaluating the real part of the exciton Green's function poles:

$$E_{A,R} = \text{Re}\Sigma(E_{A,R}) . \quad (2.39)$$

In Fig. 2.8 (b) we plot  $\omega - \text{Re}\Sigma_X(\omega)$ . One can easily show that the zeros of this function, i.e., the solutions of Eq. (2.35), always correspond to the maxima of the spectral function. However, there can be cases where Eq. (2.39) does not admit a solution but the spectral function continues to have a maximum. This occurs, at zero temperature, for example to the repulsive branch, that at large enough doping, ceases to be a well-defined quasiparticle, yet the spectral function still has a small and broad maximum. One can show that this occurs when  $E_F \gtrsim 3\varepsilon_T$  [380]. This large doping regime is not analyzed in this work. Note also that the Eq. (2.35) admits a third solution between the attractive and repulsive polaron energies which also corresponds to a weak and very broad maximum of the spectral function. This, as we will see next, is the trion-hole continuum, i.e., a continuum of scattering states between the bound trion and the Fermi sea hole.

Fig. 2.8 (a) shows that there is an intrinsic linewidth that can be associated with each polaron resonances and that is quantified by the imaginary part of the self-energy  $\text{Im}\Sigma_X(E_{A,R})$ . In the limit where the self-energy imaginary part is negligible  $\text{Im}\Sigma_X(E_{A,R}) \ll \text{Re}\Sigma_X(E_{A,R}) = E_{E,R}$ , the exciton Green's function can be approximated as [141]

$$G_X^{(0)}(\omega) \underset{\omega \approx E_{A,R}}{\simeq} \frac{Z_{A,R}}{\omega - E_{A,R} + i\Gamma_{A,R}} , \quad (2.40)$$

or in other words, the spectral function close to each resonance can be approximated with a Lorentzian with spectral weight

$$Z_{A,R} = \left( 1 - \left. \frac{\partial \text{Re}\Sigma_X(\omega)}{\partial \omega} \right|_{\omega_{A,R}} \right)^{-1} , \quad (2.41)$$

and Half Width at Half Maximum (HWHM)

$$\Gamma_{A,R} = -Z_{A,R} \text{Im}\Sigma_X(\omega_{A,R}) . \quad (2.42)$$

These quantities coincide with the polaron oscillator strength, i.e., its capacity

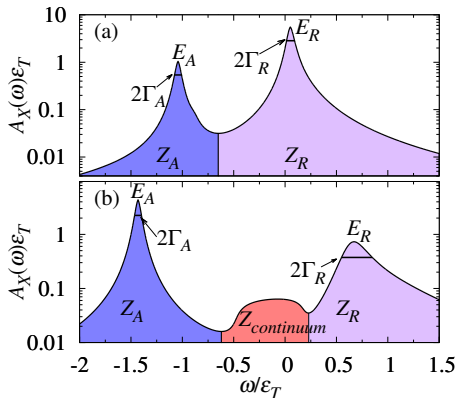


**Fig. 2.9:** Spectral function  $A_X(\omega)$  for (a)  $E_F = 0.1\epsilon_T$  and (b)  $E_F = 0.8\epsilon_T$ . We extract the polaron energies  $E_{A,R}$  as the peak positions, the linewidth  $2\Gamma_{A,R}$  as the peaks FWHM, and the polaron spectral weight  $Z_{A,R,continuum}$  as the area under the peaks. We fixed  $\eta_X = 0.04\epsilon_T$ . At low doping (a) the trion-hole continuum appears as merged with the attractive branch and  $Z_{continuum} = 0$  as an effect of broadening.

to couple to light, and the polaron inverse decay rate, respectively.

In Fig. 2.9 we explain how we extract the polaron properties from the spectral function profiles  $A_X(\omega)$ . The attractive and repulsive polaron energies  $E_{A,R}$  are evaluated as the peak positions, their linewidths  $2\Gamma_{A,R}$  as the peak FWHMs, and the polaron spectral weights  $Z_{A,R,continuum}$  as the area under the peak. We have used the location of the spectral function minima to establish the lower and upper bound of the continuum area providing  $Z_{continuum}$ . Note that in this figure we have fixed  $\eta_X = 0.04\epsilon_T$ . This implies that at low doping in panel (a) the trion-hole continuum appears as merged with the attractive branch and  $Z_{continuum} = 0$ . This is an artifact of imposing a broadening because we know that the attractive branch is a sharp separate eigenvalue of the problem at zero temperature.

We compare the polaron branch properties extracted from the spectral function with the results obtained by using a pole expansion, i.e., using Eqs. (2.39), (2.41), (2.42), in Fig. 2.10. We observe an extremely good agreement between the two approaches. It is not surprising that the pole expansion works extremely well for the attractive polaron branch, which, at zero temperature, coincides with the isolated ground state (we will see that this result changes dramatically at finite temperature). However, it is very surprising that it also works extremely accurately for the repulsive branch (see later Fig. 2.10) which is a continuum of states and its lineshape differs substantially from a Lorentzian. For this reason, the repulsive branch is also referred to as a “resonance continuum”.

To study the doping dependence of the polaron properties, we plot in Fig. 2.10 (a) the doping and energy dependence of the spectral function. As expected from the analysis at a fixed detuning done previously, the optical absorption is dominated by the polaron quasiparticle resonances: the attractive polaron branch at lower energy  $E_A$  and the repulsive polaron branch at higher energy  $E_R$ . In the limit of vanishing doping, the attractive branch energy re-

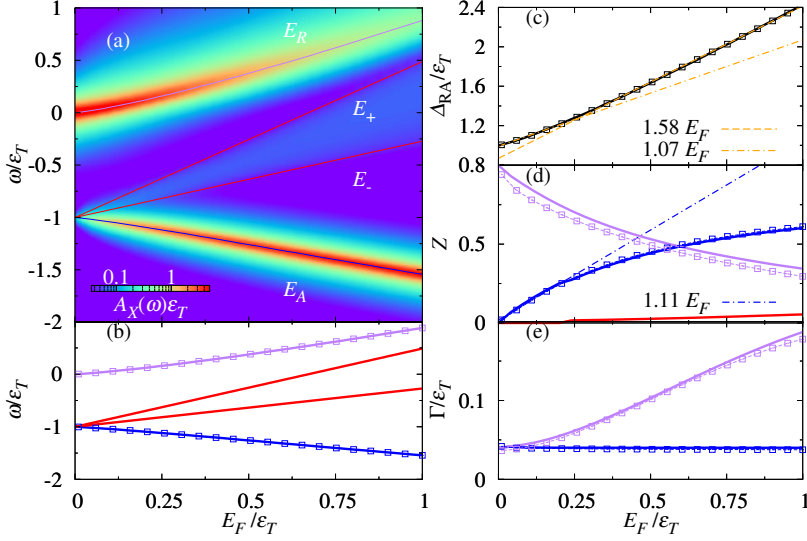


**Fig. 2.10:** (a) Exciton spectral function  $A_X(\omega)$  as a function of doping and energy. Blue and purple lines are the attractive ( $A$ ) and repulsive ( $R$ ) polaron energies, respectively, while the red lines are the boundaries of the trion-hole continuum  $E_\pm$  (see text). Doping dependence of the energy position  $E_A$ ,  $E_R$ ,  $E_\pm$  (b), energy splitting  $\Delta_{RA}$  (c), spectral weights  $Z_{A,R,continuum}$  (d), and half linewidths  $\Gamma_{A,R}$  (e) extracted from the spectral function. The solid lines have been extracted from properties of the spectral peaks — see text. The dashed lines with symbols have instead been extracted from the quasiparticle properties Eqs. (2.39), (2.41), (2.42). In panel (c), the orange dot-dashed line is a linear fit of the low doping dependence of the polaron branch splitting which is in agreement with a slope  $\sim 1$ , while the orange dashed line is a linear fit of the higher density region and gives a slope approximately  $\sim m_T/m_X$ . In panel (d), the blue dot-dashed line is a linear fit of the low-density dependence of the attractive branch spectral weight.

covers the trion energy  $E_A \rightarrow -\varepsilon_T$ , while the repulsive branch energy reduces to the exciton energy,  $E_R \rightarrow 0$  — we remind that we measure energies with respect to that of the exciton at rest. As pointed out in Ref. [381], while experimental absorption line shifts were found to be in relatively good agreement with the variational approach we have described here [321], at higher Fermi energies increasing deviations are found in particular for the attractive polaron branch. One possible source for discrepancies pointed out in Ref. [381] are finite-range corrections of the exciton-electron interaction.

We evaluate the energy splitting between repulsive and attractive branches  $\Delta_{RA} = E_R - E_A$  in Fig. 2.10(c) with both methods illustrated above, which show perfect agreement. By fitting the splitting at low and higher doping finding in both cases a linear dependence on the Fermi energy but with different slopes. At low doping, we find  $\Delta_{RA} \sim E_F$ , while for  $E_F \gtrsim \varepsilon_T/2$ , we find that

$\Delta_{RA} \sim m_T/m_X E_F$ . Note that in the literature [261, 265] the very small doping behavior has been overlooked, while the larger doping behavior  $\Delta_{RA} \sim m_T/m_X E_F$  that we find agrees with what previously found. It is important to note that extracting the splitting from the spectral function at a finite and large broadening can mask its precise behavior.

As far as the coupling to light properties of the polaron branches is concerned, at very low doping the repulsive branch retains all the spectral weight and the attractive branch is dark. However, when doping increases, there is a transfer of oscillator strength from the repulsive to the attractive branch. This is shown in Fig. 2.10 (d), where we plot the doping dependence of the spectral weights  $Z_{A,R}$  for each branch. At low doping  $E_F \ll \varepsilon_T$ ,  $Z_A$  grows linearly with  $E_F$ , in agreement with what is expected from a trion picture [266] (2.27) (blue dot-dashed line). The small discontinuity that we observe for the continuum spectral weight in Fig. 2.10 (d) derives from the fact that we are evaluating areas of the spectral function at a finite value of the broadening  $\eta_X$ .

There are important differences between the attractive and repulsive polaron branches, even though they both satisfy Eq. (2.39) for values of doping up to  $E_F \sim \varepsilon_T$  that we consider here. As already mentioned, the attractive polaron is always a sharp resonance, with a Lorentzian broadening coinciding with the intrinsic broadening  $2\Gamma_A = 2\eta_X$  — see Fig. 2.10 (e). As shown in Fig. 2.8 (a), the attractive branch energy coincides with the lowest eigenvalue energy,  $E_A = E^{(n=1)}$ , while the repulsive branch does not correspond to a specific eigenstate. As a consequence, its broadening  $2\Gamma_R$  grows monotonically with  $E_F$  and only coincides with  $2\eta_X$  at small doping — see Fig. 2.10 (e). Still, it can be well described by the quasiparticle properties Eq. (2.39), Eq. (2.41), and Eq. (2.42). This is shown in Fig. 2.10 (b,c,d,e), where we compare the results for  $E_{A,R}$ ,  $Z_{A,R}$ , and  $\Gamma_{A,R}$  obtained from both the peaks properties (solid lines) or the quasiparticle properties Eqs. (2.39), (2.41), (2.42) (squared symbols). We observe that the positions of the poles coincide with high accuracy with those of the spectral function maxima. In particular, for the repulsive branch, both the spectral weight and the broadening from the quasiparticle theory are in very good agreement with those evaluated from the spectral function, even when the linewidth is non-negligible. Previous theoretical analysis [265] predicts a linear behaviour of  $\Gamma_R$  with  $E_F$  at small doping which our analysis does not reveal.

Note that the polaron theory substantially underestimates the homogeneous broadening of the repulsive branch observed in experiments [351] as doping density increases. Experiments of Ref. [351] observe a quadratic behavior with  $E_F$ , which is not captured by Chevy's ansatz. This discrepancy suggests the existence of additional non-radiative transitions from the repulsive to the attractive branch. In Ref. [351], it has been shown that electron-electron interactions can enhance this non-radiative decay. By adding an extra particle-hole

excitation in the same valley as the exciton (and different from that of the Chevy ansatz), the authors of Ref. [351] find an additional increase of  $\Gamma_R$  which rescale quadratically with  $E_F$  and agrees with the experimental measurements of the homogeneous broadening of the repulsive peak.

In between the attractive and repulsive branches, we observe in Fig. 2.10 (a) a continuum of states that correspond to scattering states between a bound trion and an unbound Fermi-sea-hole states with a well-defined relative momentum  $\mathbf{q}$  in the variational function  $\varphi_{\mathbf{k}\mathbf{q}}$ . This continuum is also called in the literature as “trion-hole” continuum. The boundaries of this so-called trion-hole continuum can be evaluated analytically from the energy of a trion (see Sec 2.3.3) plus the kinetic energy of a hole. If the hole has zero momentum  $\mathbf{q} = \mathbf{0}$ , then, because of momentum conservation, the trion is also at zero momentum, and the upper boundary of the trion-hole continuum is (2.25a)

$$E_+ = E_T^{(\mathbf{0}, E_F)} = -\varepsilon_T + \frac{m_T}{m_X} E_F. \quad (2.43)$$

Conversely, the energy of the trion-hole lower bound is

$$E_- = E_T^{(\mathbf{k}_F, E_F)} - E_F, \quad (2.44)$$

where both the hole and trion are at  $\mathbf{q} = \mathbf{k}_F = k_F \hat{\mathbf{n}}$ , with  $\hat{\mathbf{n}}$  an arbitrary direction, and  $E_T^{(\mathbf{k}_F, E_F)}$  is the trion energy, which can be evaluated from Eq. (2.22).

Thus, at zero temperature, as soon as one has some doping, the attractive branch is separated from the trion-hole continuum by an energy gap. Note that, while this trion-hole continuum is a consequence of considering a single excitation of the medium, our results are consistent with those of diagrammatic quantum Monte Carlo [382] which demonstrated that there is a region of anomalously low spectral weight (a “dark continuum”) above the narrow attractive polaron branch. This situation can change drastically at finite temperatures, where the trion-hole continuum merges with the attractive branch at large enough temperature or at low enough dopings. This will be analyzed in detail in Ch. 3.

To conclude this section, we briefly discuss other polaron approaches that have been developed for the description of doped semiconductors. As already mentioned, the concept of polaron as a superposition between an exciton and a trion-hole state was originally introduced in Ref. [286] to describe the properties of doped II-VI compound quantum wells [383]. In Ref. [286], the authors consider an exciton mode mixed with a correlated state of a trion and a hole of the Fermi sea similar to what is done in Chevy’s ansatz. Using a diagrammatic approach to solve the problem, they were able to capture the typical oscillator strength transfer that can be observed in the optical response of doped semiconductors. They found that, in the small doping regime, the attractive polaron

oscillator strength increases linearly with doping, which agrees with the doping dependence of the trion oscillator strength described in Sec. 2.2 and with what we found with the previously described approach.

Recently, a polaron approach that does not rely on approximating the exciton as tightly bound and that includes unscreened Coulomb interactions between all carriers has been proposed in Refs. [262–264]. The authors propose a variational state similar to the state  $|P_3\rangle$  considered in Eq. (2.28), but where the exciton is described in terms of the intervalley electron and hole pair:

$$|M_4\rangle = \left( \sum_{\mathbf{k}_1} \frac{\varphi_{\mathbf{k}_1}}{\sqrt{\mathcal{A}}} \hat{c}_{h-\mathbf{k}_1}^\dagger \hat{c}_{e\mathbf{k}_1}^\dagger + \sum_{\mathbf{k}_1, \mathbf{k}_2, \mathbf{q}} \frac{\varphi_{\mathbf{k}_1 \mathbf{k}_2 \mathbf{q}}}{\sqrt{2\mathcal{A}^{3/2}}} \hat{c}_{h\mathbf{q}-\mathbf{k}_1-\mathbf{k}_2}^\dagger \hat{c}_{e\mathbf{k}_1}^\dagger \hat{c}_{e_{FS}\mathbf{k}_2}^\dagger \hat{c}_{e_{FS}\mathbf{q}} \right) |FS\rangle. \quad (2.45)$$

Here, the operators  $\hat{c}_{e\mathbf{k}}^\dagger$  and  $\hat{c}_{e_{FS}\mathbf{k}}^\dagger$  describe two distinguishable electrons. This state, similarly to the Chevy ansatz (2.29), includes only one electron-hole excitation of the Fermi sea and thus a maximum of four particles on top of the Fermi sea. We consider a similar ansatz in Sec. 4.4 in case of two indistinguishable electrons when we consider the impurity problem in the spin-valley polarized case. As explained there, the problem large Hilbert space hinders the possibility of directly diagonalizing the eigenvalue problem associated to (2.45). For this reason, the authors of Ref. [262] resort to some approximation. They factorize the four-body wave function into a “trion+hole” wave function

$$\varphi_{\mathbf{k}_1 \mathbf{k}_2 \mathbf{q}} = \phi_{\mathbf{k}_1 \mathbf{k}_2} \psi_{\mathbf{q}}. \quad (2.46)$$

Further, they assume a momentum dependence of the trion wave function  $\phi_{\mathbf{k}_1 \mathbf{k}_2}$  similar to that of Eq. (2.13). Note that this is a strong assumption, as it implies that there are no correlations between the trion and hole degrees of freedom. With these assumptions, the authors find the appearance of polaron branches that resemble those previously described in Ref. [286]. It stands out the absence of a trion-hole continuum in their results.

### 2.3.5 Connection to the trion theory

It is instructive to compare the results obtained within the polaron formalism with those that can be extracted from a mean-field few-body approach that describes the optical response of doped semiconductors in terms of few-body complexes such as excitons and trions. This subject has raised significant interest recently and it is interesting to analyze if there are conceptual differences and summarise differences in predictions.

As far as agreements between the two approaches, we have seen that the polaron description predicts that the polaron branch energies recover those of the exciton and trion at low doping and that the attractive oscillator strength grows linearly with  $E_F$  exactly as the trion plus an inert Fermi sea description predicts [266]. However, the energy of a trion in a Fermi sea blueshifts with doping due to the Pauli blocking with the surrounding electrons [373] — see Eq. (2.25a). In contrast, the attractive polaron energy in the spin-valley polarised configuration redshifts with doping. A blueshift can occur in the unpolarized case, where there is a Fermi sea also in the same valley where the exciton is created in Mo-based monolayers. This suggests that, at finite doping, the attractive and repulsive polaron quasiparticles differ from the trion and exciton states, respectively. Further, the transfer of oscillator strength from the repulsive to the attractive branch cannot be described by a few-body approach [346].

Note that within the single particle-hole-excitation ansatz (2.28), while the repulsive polaron effective mass recovers that of the exciton at low doping, the same does not occur for the repulsive polaron [374, 384] — see App. D. This is because the single particle-hole Chevy’s ansatz is not able to recover the polaron-trion (or polaron-molecule) transition that is expected to occur when doping decreases [373, 374]. In systems with contact interactions, this transition can be found by adding an additional particle-hole excitation to the  $|P_3\rangle$  ansatz and considering a polaron state  $|P_5\rangle$  at finite center of mass momentum as recently demonstrated in Ref. [385] — see App. D. It is currently an open question if this transition occurs if one includes a realistic description of Coulomb interaction effects in the polaron modelling.

The most striking difference between the attractive polaron state and the trion state is that the first is a composite boson (to the same extent the exciton is), while the trion is a composite fermion. Their different statistics are expected to lead to dramatically different interaction properties [362], something we had no time to analyze in this work but is an extremely interesting perspective of our work. A related issue is the different responses to an external electric field that are expected for polaron and trion states. Trions are expected to respond to an applied electric field similarly to other charged particles, exhibiting drag properties similar to that studied in Ref. [386]. In contrast, the drag behavior of polarons is more complex and was recently analyzed in Ref. [366]. Although polarons are charge-neutral optical excitations, they interact with the Fermi sea and follow the motion of charge carriers under an electric or magnetic field. The response of polarons to an applied electric field differs significantly from that of charged particles such as trions. Under equilibrium conditions with disorder and static electric fields, polarons do not respond to a force on the bath particles at zero temperature. However, in scenarios involving dynamical fields, where the field frequency is much greater than the inverse disorder lifetime

of the bath particles, or non-equilibrium setups where impurities have a finite lifetime, polaron response can be as significant as that of trions [366].

It is important to stress that while there is a net distinction between the attractive polaron branch and the trion-hole continuum at zero temperature, at high temperatures and low doping, the attractive ceases to be a well-defined quasiparticle because it merges with the trion-hole continuum. In this limit, it is possible to recover a “trion picture” to correctly describe the system response, yet aside from the trion bound state, one has also to include the electron-exciton scattering states. This is automatically carried on in the polaron formalism, as we will discuss in detail in Ch. 3.

To conclude this section, let us mention that there have been some attempts to include the effects of Fermi sea blocking on exact *ab initio* calculations of the three-body trion state [270, 300, 317]. Here, *ab initio* calculations are employed for the single-particle basis set that then are used to solve the three-body problem. In these works, doping effects are accounted for by discretizing the quasimomentum in the Brillouin zone and imposing an IR cutoff that represents the Fermi momentum blocking the occupation of the lower momenta states. The drawback of this simplistic approach is that it is not possible to discern between finite size and doping effects.

### 2.3.6 Strong light-matter coupling

We now extend the formalism of Sec. 2.3.2 to describe recent experiments where a doped TMD monolayer is embedded into a microcavity [244, 321, 345, 346, 361]. In this case, the strong coupling between light and matter can lead to the formation of Fermi polaron-polaritons [321, 387]. To describe the light-matter coupled system, we add to the Hamiltonian (2.18) two terms representing the cavity photons and the photon-exciton interaction:

$$\hat{H} = \hat{H}_0 + \hat{H}_{0X} + \hat{H}_{0C} + \hat{H}_{int} + \hat{H}_{XC} \quad (2.47a)$$

$$\hat{H}_{0C} = \sum_{\mathbf{k}} \epsilon_{C\mathbf{k}} \hat{a}_{\mathbf{k}}^\dagger \hat{a}_{\mathbf{k}} \quad (2.47b)$$

$$\hat{H}_{XC} = \frac{\Omega}{2} \sum_{\mathbf{k}} (\hat{x}_{\mathbf{k}}^\dagger \hat{a}_{\mathbf{k}} + \text{H.c.}) . \quad (2.47c)$$

Photons are described by the bosonic operators  $\hat{a}_{\mathbf{k}}^\dagger$  and have a dispersion  $\epsilon_{C\mathbf{k}} = \delta + \mathbf{k}^2/2m_C$ , where  $\delta$  is the exciton-photon detuning

$$\delta = \epsilon_{C0} - \epsilon_{X0} . \quad (2.48)$$

We remind the reader that, as before, we are measuring energies with respect to the one of the exciton at rest  $\epsilon_{X0}$ .

In order to derive the photon Green's function and the optical absorption in the strong coupling regime, one can follow the same procedure employed in Sec. 2.3. Similarly to what is done within Chevy's ansatz approach, the variational ansatz we employ is:

$$|P_3^{(\mathbf{Q})}\rangle = \alpha_0^{(\mathbf{Q})} \hat{a}_{\mathbf{Q}}^\dagger |FS\rangle + \varphi_0^{(\mathbf{Q})} \hat{x}_{\mathbf{Q}}^\dagger |FS\rangle + \frac{1}{\mathcal{A}} \sum_{\mathbf{k}, \mathbf{q}} \varphi_{\mathbf{k}\mathbf{q}}^{(\mathbf{Q})} \hat{x}_{\mathbf{Q}+\mathbf{q}-\mathbf{k}}^\dagger \hat{c}_{\mathbf{k}}^\dagger \hat{c}_{\mathbf{q}} |FS\rangle. \quad (2.49)$$

We neglect the dressing of the photon operator by a particle-hole excitation  $\frac{1}{\mathcal{A}} \sum_{\mathbf{k}, \mathbf{q}} \alpha_{\mathbf{k}\mathbf{q}}^{(\mathbf{Q})} \hat{a}_{\mathbf{Q}+\mathbf{q}-\mathbf{k}}^\dagger \hat{c}_{\mathbf{k}}^\dagger \hat{c}_{\mathbf{q}} |FS\rangle$ . This term involves photon recoil and therefore implies energies far off-resonance from the exciton and trion energies because of the extremely small mass of the photon [321].

The associated equations of motion are:

$$E\varphi_0^{(\mathbf{Q})} = \frac{\Omega}{2} \alpha_0^{(\mathbf{Q})} - \frac{v}{\mathcal{A}^2} \sum_{\mathbf{k}, \mathbf{q}} \varphi_{\mathbf{k}\mathbf{q}}^{(\mathbf{Q})} \quad (2.50a)$$

$$E\varphi_{\mathbf{k}\mathbf{q}}^{(\mathbf{Q})} = E_{X\mathbf{k}\mathbf{q}\mathbf{Q}} \varphi_{\mathbf{k}\mathbf{q}}^{(\mathbf{Q})} - v\varphi_0^{(\mathbf{Q})} - \frac{v}{\mathcal{A}} \sum_{\mathbf{k}'} \varphi_{\mathbf{k}'\mathbf{q}}^{(\mathbf{Q})} \quad (2.50b)$$

$$E\alpha_0^{(\mathbf{Q})} = \delta\alpha_0^{(\mathbf{Q})} + \frac{\Omega}{2} \varphi_0^{(\mathbf{Q})}, \quad (2.50c)$$

where we have neglected the terms that vanish in the limit  $\Lambda \rightarrow \infty$ .

By following an analogous derivation to that in Sec. 2.3.4, and focusing on the  $\mathbf{Q} = \mathbf{0}$  case, one can easily demonstrate that the retarded photon Green's function in the frequency domain is given by:

$$G_C(\omega) = \sum_n \frac{|\alpha_{n0}|^2}{\omega - E_n + i\eta_C}. \quad (2.51)$$

Note that, for the same reason that we can neglect the particle-hole dressing of the photon operator in the ansatz (2.49), the expressions for the exciton self-energy  $\Sigma_X(\omega)$  in Eq. (2.36) are not affected by the coupling to light. Therefore, we can derive the coupled exciton and photon Green's functions in the strong coupling regime by inverting the matrix (1.41)

$$\mathbb{G}(\omega) = \begin{pmatrix} \omega + i\bar{\eta}_X - \Sigma_X(\omega) & -\Omega/2 \\ -\Omega/2 & \omega + i\eta_C - \delta \end{pmatrix}^{-1}, \quad (2.52)$$

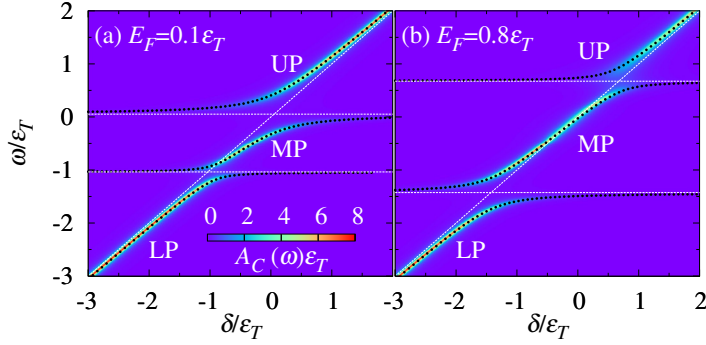


**Fig. 2.11:** Energy and detuning dependence of the photon spectral function  $A_C(\omega)$  in the light-matter strongly coupled system describing a TMD monolayer with an electron doping  $E_F = 0.1\epsilon_T$  (panel (a)) or  $E_F = 0.8\epsilon_T$  (panel (b)), embedded in a microcavity. The black dots are the LP, MP, and UP branches extracted from the three-coupled oscillator model (see text). The Rabi splitting is  $\Omega = 20\text{meV} \simeq 0.8\epsilon_T$ . Here, we have used a broadening of  $\eta_C = 1\text{meV} \simeq 0.04\epsilon_T$  for the photon and  $\bar{\eta}_X = 0.2\eta_C$  for the matter component.

and evaluating the diagonal elements, giving:

$$G_X(\omega) = \mathbb{G}_{11}(\omega) = \frac{1}{\omega + i\bar{\eta}_X - \Sigma_X(\omega) - \frac{(\Omega/2)^2}{\omega + i\eta_C - \delta}} \quad (2.53a)$$

$$G_C(\omega) = \mathbb{G}_{22}(\omega) = \frac{1}{\omega + i\eta_C - \delta - \frac{(\Omega/2)^2}{\omega + i\bar{\eta}_X - \Sigma_X(\omega)}}. \quad (2.53b)$$

Thus, the exciton Green's function is modified by both the effects of the electron-exciton scattering contained in the exciton self-energy and the strong coupling between the exciton and the photon modes. The optical absorption spectrum in a microcavity structure should be evaluated by making use of the input-output theory outlined in Sec. 1.5.1. However, in the limit of a “good” cavity, i.e., when the decay rate of a photon from the cavity is much smaller than the Rabi splitting  $\eta_C \ll \Omega$ , one has that

$$A_C(\omega) = -\frac{1}{\pi} \text{Im}G_C(\omega). \quad (2.54)$$

We plot in Fig. 2.11 the photon spectral function at normal incidence as a function of energy and detuning  $\delta$ . The strong coupling to light leads to three polariton branches, the LP, MP, and UP. We can capture the behavior of the Fermi polaron-polaritons by employing a three-coupled oscillator model, which

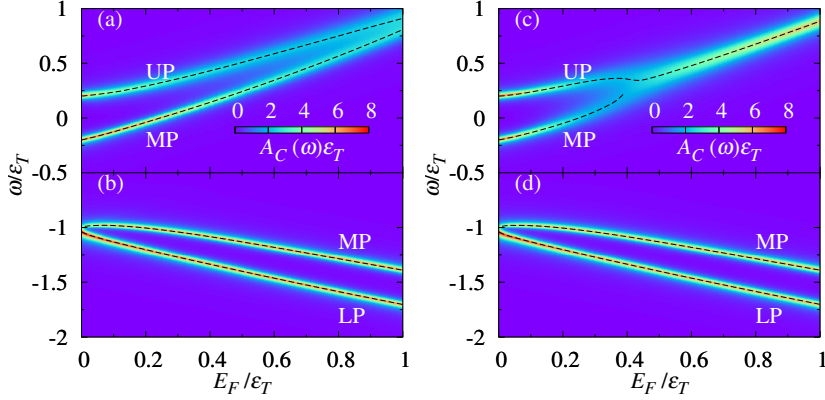


**Fig. 2.12:** (a,b) Doping dependence of the photon spectral function  $A_C(\omega)$  for a photon in resonance with either the repulsive branch  $\delta = E_R$  (a) or the attractive branch  $\delta = E_A$  (b). The black dashed lines are the LP, MP, and UP branches extracted from the three-coupled oscillator model — LP is not shown in panel (a) while UP is not shown in panel (b). (c,d) Doping dependence of the photon spectral function  $A_C(\omega)$  obtained with a three-coupled oscillator model (2.55b), where we have added an ad-hoc quadratic dependence on doping of the repulsive polaron broadening (see text). The Rabi splitting is  $\Omega = 0.4\epsilon_T$ .

yields the following simplified expression for the photon Green's function

$$\tilde{G}_C(\omega) = (\omega - \tilde{H})^{-1} \Big|_{11} \quad (2.55a)$$

$$\tilde{H} = \begin{pmatrix} \delta - i\eta_C & \Omega_A/2 & \Omega_R/2 \\ \Omega_A/2 & E_A - i\Gamma_A & 0 \\ \Omega_R/2 & 0 & E_R - i\Gamma_R \end{pmatrix}. \quad (2.55b)$$

Here, we have explicitly included a cavity photon lifetime  $1/\eta_C$  and we have used the extracted parameters for the exciton-polaron branches in the absence of coupling to light, namely the energies  $E_{A,R}$ , spectral weights  $Z_{A,R} = (\Omega_{A,R}/\Omega)^2$ , and half linewidths  $\Gamma_{A,R}$ . Note that we cannot evaluate the polariton branch energies as the (complex) eigenvalues of the matrix  $\tilde{H}$ , as discussed in Sec. 1.5.1. Rather, we have to evaluate first the photon spectral function and then determine the polariton energies from the photon spectral function peak positions, solutions of  $\text{Re}\tilde{G}_C^{-1}(\omega) = 0$ . The comparison in Fig. 2.11 between the LP, MP, and UP energies obtained in this way and the full calculation demonstrates essentially perfect agreement.

In order to compare the results of our model with the experimental results obtained in [321] in the strong coupling regime, the photon spectral function  $A_C(\omega)$  is plotted in Fig. 2.12 (a,b) as a function of doping, by changing the photon energy at each doping so that to be in resonance either with the repuls-

ive (Fig. 2.12 (a)) or the attractive branch (Fig. 2.12 (b)). The results indicate that if the photon is in resonance with the repulsive branch, then with increasing doping, the repulsive branch linewidth increases, leading to the closing of the UP and MP splitting. In Section 2.3.4, it was mentioned that while the polaron approach predicts a broadening of the repulsive branch which increases linearly with doping, recent experiments [351] have shown that the homogeneous contribution to the repulsive branch linewidth increases quadratically and that this can be explained in terms of electron-electron interactions. This implies that, when the photon mode is tuned in resonance with the repulsive branch, the MP-UP splitting is expected to close faster than what is predicted by the polaron theory. We thus include an ad-hoc quadratic dependence to  $\Gamma_R \mapsto \Gamma_R + (E_F/\varepsilon_T)^2$  and evaluate the resulting spectral function  $A_C(\omega)$  using the three-coupled oscillator model described in Eq. (2.55b). The result, shown in Fig. 2.6 (b), shows that while there are no consequences when the photon is in resonance with the attractive branch, when is instead in resonance with the repulsive branch the MP-UP splitting closes much faster, in agreement with the experimental results [321] shown in Fig. 2.6 (b). Note that experiments show that increasing  $E_F$  causes the LP-MP gap to also eventually close, though much slower than MP-UP, a behavior that is not predicted by the polaron description, which expects the attractive branch linewidth at low temperatures to stay sharp.

### 2.3.7 Ultracold atoms

In Section 2.3, it was discussed how impurity problems can be studied using a shared set of ideas and technical tools, even in seemingly distinct setups such as ultracold atomic mixtures. This has led to a significant amount of cross-disciplinary collaboration, with insights gained from one system informing the understanding of another. Ultracold atomic gases have provided valuable insights into polaron physics and have been particularly useful in gaining intuition into the behavior of polarons in other systems such as semiconductors. Indeed, species composition and densities, interaction strengths, and confining geometries can be precisely controlled in ultracold atomic gases [388].

In this section, we are going to focus on the uniform Fermi gas with short-range interactions, a set-up that has already been successfully realized experimentally in 3D [341, 389, 390], 2D [342, 343, 391–393], and 1D [394, 395] systems. It should be noted that although our focus is on impurities in a fermionic environment, Bose environments have also been achieved [396–398].

In the following, we give a brief overview of the experimental methods used to investigate Fermi polarons in ultracold atoms to see how they compare to the one employed to study Fermi polarons in semiconductors. In ultracold atomic mixtures, quasiparticle properties can be analyzed by radio-frequency

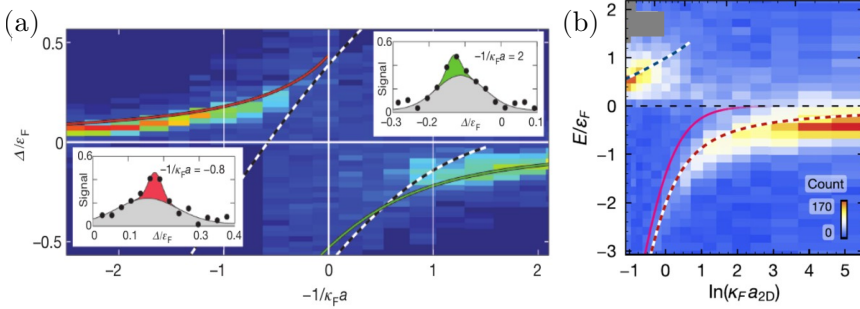


**Fig. 2.13:** (a) RF injection spectroscopy of impurities immersed in a 3D Fermi gas [341]. The impurity-medium interaction strength is contained in the dimensionless parameters  $1/k_F a$ , tuned via a narrow Feshbach resonance. Red and green solid lines are the repulsive and attractive polaron energies obtained using a polaron approach within Chevy's ansatz. Black and white dashed lines are the boundary of the dressed molecule — see text. (b) RF injection spectroscopy of impurities immersed in a 2D Fermi gas [343]. The impurity-medium interaction strength is given by the dimensionless parameters  $\ln k_F a_{2D}$ , tuned via an orbital Feshbach resonance. Blue-white and red-white dashed lines are the repulsive and attractive polaron energies obtained using a polaron approach. The red line is the molecule energy — see text.

(RF) spectroscopy [399]. This method involves using an oscillating RF field to couple two internal hyperfine states of the impurity atoms. Since the RF field has a long wavelength, it is essentially uniform over the sub-millimeter scale of atomic samples, and absorption of RF photons results in negligible momentum transfer to the atoms. The two hyperfine states are chosen to have different interaction strengths with the surrounding medium, which can be either a third hyperfine state of the same atomic species or a different atomic species.

In the case of injection spectroscopy, a weak RF pulse transfers impurities from a nearly non-interacting state to a state with strong interactions with the medium particles. Spectroscopy at varying interaction strengths can be performed by tuning the impurity-medium scattering length via a Feshbach resonance [340]. In the linear response regime, the injection RF signal  $I_{inj}(\omega)$  is proportional to the impurity spectral function  $A(\omega, \mathbf{q})$  [400, 401]

$$I_{inj}(\omega) \propto \sum_{\mathbf{q}} n_{\mathbf{q}} A(\omega, \mathbf{q}), \quad (2.56)$$

where  $n_{\mathbf{q}}$  is the initial momentum distribution of the impurities. To make a parallelism with experiments in 2D semiconductors, the injection signal is analogous to a momentum-averaged absorption spectrum, where one measures the response of the system to the creation of an impurity. Injection spectroscopy allows one to probe the entire many-body spectrum of strongly interacting impurities since it addresses both the ground and the excited states of the

system [341, 343].

The opposite protocol, known as ejection spectroscopy, involves flipping a strongly interacting state into a non-interacting state and has been widely used to probe the ground state of strongly interacting mixtures with arbitrary population imbalance [402]. While ejection spectroscopy generally depends on the initial occupation of states in the strongly interacting system, it simplifies when the impurity concentration is very low, and the impurities are uncorrelated, resulting in a Boltzmann distribution. In this case, the ejection and injection spectra are directly related by [179].

$$I_{ej}(\omega) = e^{\beta\omega} e^{\beta\Delta F} I_{inj}(-\omega), \quad (2.57)$$

where  $\Delta F$  is the difference in free energy between the interacting and the non-interacting impurity. The exponential prefactor suppresses the repulsive branch at positive energies, which clearly illustrates why ejection spectroscopy is ideally suited to investigations of ground-state properties [344, 403]. Note that the relation between ejection and injection signal is analogous to the detailed balanced condition (3.19) between photoluminescence and absorption in semiconductor physics derived in Sec. 1.5.3.

Let's discuss some experimental evidences of polaron physics in ultracold gases and confront them with the theoretical results. In Fig. 2.13, experimental RF injection spectroscopy of impurities immersed in a 3D Fermi gas [341] and a 2D Fermi gas [343] are shown. The interaction strength in the 3D and 2D scenarios is encoded by the dimensionless parameters  $1/k_F a_{3D}$  and  $\ln(k_F a_{2D})$ , respectively. These quantities can be tuned via Feshbach resonance mechanisms. In these plots, the zero of the energy corresponds to the frequency of the atomic RF transition in the absence of the medium. The repulsive polaron energy branch is clearly visible at positive RF detunings and loses oscillator strength when approaching the unitarity limit of strong interactions from the repulsive side, i.e., when  $a \rightarrow 0^+$  or  $\ln(k_F a_{2D}) < 0$ . When crossing over the attractive side, the oscillator strength is then transferred to the attractive polaron branch, visible in the negative RF detuning region, for values of the interaction away from the strongly interacting unitarity regime. In these plots, the lines corresponding to the theoretical predictions for  $E_{A,R}$  are obtained within the same polaron approach described in Sec. 2.3.2.

In 3D, it is known that, for increasing attraction and for equal masses [404–406], there is a transition from a polaron state to a molecular state, where the impurity is bound to a single atom of the surrounding medium [407]. For a sufficiently light impurity, it has been suggested that a dressed trimer can become energetically favourable [408]. In Fig. 2.13 (a), the energy boundaries of the molecule-hole continuum are shown as black-white dashed lines. The presence of a continuum is due to the removal of an atom with energy between 0 and

$E_F$  to form the molecule, i.e., which is equivalent to the trion-hole continuum boundaries described in Eqs. (2.43) and (2.44). In Fig. 2.13 (a), the energy of the attractive polaron becomes higher than the energy of a molecule at finite momentum for values of  $-1/k_F a \sim 0.6$  implying that the attractive polaron is not the system ground state any longer and can decay into a molecular state. Indeed, recently the transition between the polaron and molecular states has been observed in a spin-imbalanced ultracold gas of  $^{40}\text{K}$  atoms [344].

In 2D, theoretical work [373, 374] has predicted a transition for equal masses from a polaron to a dressed molecular state around  $-1.1 \leq \ln k_F a \leq -0.8$ . This transition has not been detected experimentally yet — aside from an early claim in Ref. [342]. In Fig. 2.13 (b) we report a recent RF injection spectroscopy of an impurity immersed in a 2D Fermi gas [343]. Here the authors do not see any direct signatures of this transition. However, they observe a reduction of contrast in the strongly interacting regime until the attractive branch completely vanishes around  $\ln k_F a \sim -0.5$ .

While a contact interaction model correctly describes the polaron properties in doped semiconductors, it is not clear yet whether the polaron-molecule (i.e., polaron-trion) transitions survive in that case if one takes into account the effects of a realistic long-range Coulomb interaction. There have been indications [262, 346] that, by including a realistic description of Coulomb interactions, a charge three-body bound is never the system ground state of a doped 2D material as it gets surrounded by a screening hole and forms instead an attractive polaron.

## 2.4 Pairing phenomena with charge imbalance

The focus of our analysis on doped 2D semiconductors in this chapter has been so far on the effects induced by charges on weak optical excitation of the system, i.e., with a low number of excitons. We conclude this chapter with a short overview of how the presence of charge imbalance modifies the collective pairing phenomena, because of frustration effects.

Intriguing questions about collective coherent phenomena in fermionic systems do arise in presence of population imbalance, i.e., when not every fermion can pair up. Pairing frustration mechanisms can be found in many areas of physics. For instance, in conventional superconducting thin films with an in-plane magnetic field, the Zeeman effect can generate a spin-imbalanced system, causing electron spins to point along the applied field and ultimately breaking superconductivity [409]. This leads the system to suffer a transition from a superconducting to a normal state. In quantum chromodynamics, differences in quark masses result in a mismatch among the Fermi surfaces between the species that could pair [410]. Atomic gases are of particular interest because

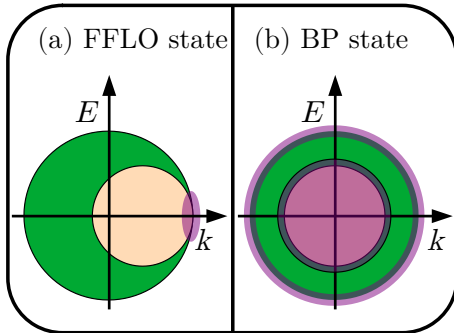


**Fig. 2.14:** Sketch of majority carrier (green) and minority carrier (light-orange) Fermi seas in presence of charge imbalance. (a) In the FFLO state pairing (purple area) occurs in a small sliver of the Fermi sea where nesting occurs. (b) In contrast, for the breached-pair (BP) state, pairing occurs isotropically, and it is optimized by emptying the majority species from a ring in momentum.

they offer an ideal testing ground for exploring the quest for superfluid behavior in imbalanced two-component Fermi systems, as the populations in two hyperfine states of the fermionic atoms can be easily controlled externally [411, 412].

In an imbalanced Fermi mixture, the system can adjust itself to remain partially coherent by maintaining a finite density of paired fermions and accommodating a finite density of unpaired fermions before reaching a normal state. In the 1960s, it was proposed [257, 258] that to accommodate the density difference while restoring some coherence, a simple uniform BCS state could be replaced by a state  $|\Phi_{\mathbf{Q}}\rangle$  with finite center-of-mass momentum Cooper-pairs and a finite density of unpaired fermions. The minority particle Fermi surface shifts to contact the larger one, and pairs are formed in the vicinity of the touching point — see Fig. 2.14 (a). If the energy gain due to pair formation exceeds the kinetic energy penalty, then the finite center of mass state has lower energy than the normal state and describes the ground state. This state with a single center-of-mass pair momentum is known as an FF state (Fulde Ferrel [257]) and a superposition of states with opposite momenta LO (Larkin Ovchinnikov [258]). Both states are commonly referred to as FFLO states. This state has been proposed as the ground state for imbalanced systems in various contexts, including superconductors and imbalanced quantum chromodynamic systems [410], cold atoms [413, 414], and semiconductors [255, 256]. However, there is no consensus on whether such a state has been observed in superconducting or cold atom systems, despite some evidence discussed in Ref. [415]. Weak attractive interaction in superconductors and ubiquitous phase separation accompanying the first-order phase transition from a zero- to a finite-momentum condensate in cold atoms are the main issues [414, 416]. In contrast, semiconductors do not face these problems since electrons and holes are charged particles, which prevents phase separation. Additionally, electron-hole interaction via long-range Coulomb potentials, as opposed to weak phonon-mediated potentials, makes the excitonic condensed state more resilient to external parameter variations.

Moreover, strong exciton-photon coupling in semiconductors with microcavities results in a much higher critical temperature of condensation, leading to room polariton condensation — see Sec. 1.5.4. Thus, semiconductors in microcavities provide an ideal platform for exploring the physics of imbalanced polaritonic condensates. In Ch. 5, we will discuss in detail the effects of light-matter coupling on the possible formation of an FFLO state in a semiconductor system with extreme imbalanced densities.

Although FFLO phases are common to imbalanced two-component fermions with attractive interactions, more exotic alternatives have been suggested in special cases. For example, a breached-pair [417] state, also called Sarma state [418] can occur, where the minority species pair up with the other species inside the majority Fermi sea, leaving fermions with higher energy unpaired — see Fig. 2.14 (b). This breached-pair state can also occur in an anisotropic manner where excess particles are squeezed out of a region in momentum space anisotropically. This mechanism was already proposed but always found energetically unfavorable [419]. However, it turns out that strong coupling to light and long-range Coulomb interaction favors this phase at moderate imbalances [420].

## Chapter 3

# Crossover from polarons to trions at finite temperature

*In this chapter, we study systematically the role of temperature in the optical response of doped two-dimensional semiconductors. By making use of a finite-temperature Fermi-polaron theory, we reveal a crossover from a quantum-degenerate regime with well-defined polaron quasiparticles to an incoherent regime at high temperature or low doping where the lowest energy attractive polaron quasiparticle is destroyed, becoming subsumed into a broad trion-hole continuum. We demonstrate that the crossover is accompanied by significant qualitative changes in both absorption and photoluminescence. With increasing temperature (or decreasing doping), the emission profile of the attractive branch evolves from a symmetric Lorentzian to an asymmetric peak with an exponential tail involving trions and recoil electrons at finite momentum. In the high-temperature low-doping regime we employ a quantum virial expansion to obtain exact analytic expressions for the photoluminescence and we predict new features such as a non-trivial shape of the attractive branch peak related to universal resonant exciton-electron scattering and an associated energy shift from the trion energy. Our theory allows us to formally unify the two distinct theoretical pictures that have been applied to this system, where we reveal that the predictions of the conventional trion picture correspond to a high-temperature and weak-interaction limit of Fermi-polaron theory. We compare our results to recent experiments on doped monolayer MoSe<sub>2</sub> finding excellent agreement.*

*The results discussed in this chapter have been reported in the following manuscripts, which have been recently submitted for the peer review process:*

[357] A. TIENE, B. C. MULKERIN, J. LEVINSEN, M. M. PARISH, and F. M. MARCHETTI:

Crossover from exciton polarons to trions in doped two-dimensional semiconductors at finite temperature,  
[10.48550/ARXIV.2212.05635](https://arxiv.org/abs/2212.05635) (2022).

[359] B. C. MULKERIN, A. TIENE, F. M. MARCHETTI, M. M. PARISH and J. LEVINSEN:

Virial expansion for the optical response of doped two-dimensional semiconductors,  
[10.48550/ARXIV.2212.05627](https://arxiv.org/abs/2212.05627) (2022).

## 3.1 Introduction

The theoretical analysis of the Fermi polaron problem in 2D doped/gated semiconductors has mainly focused on the zero-temperature limit [261, 265, 321]<sup>1</sup>. This theory has been analyzed in detail in Sec. 2.3.2. However, a natural question to ask is how the system changes with temperature since this has been shown to strongly modify the nature of the Fermi polaron quasiparticles in cold-atom experiments [403]. In particular, as illustrated in Ch. 2 there is a competing picture to that of the Fermi polaron based on few-body complexes such as excitons and trions, which provides a description for the photoluminescence of the attractive branch in doped semiconductors at finite temperature [300, 421, 422]. While at zero temperature there are profound differences between these two approaches, it is natural to ask whether the conclusions drawn in Ch. 2 hold also at finite temperature.

In this chapter, we use a finite-temperature variational approach developed in the context of cold atoms [423] to reveal the important role that temperature plays in the exciton-polaron problem. In particular, we demonstrate that, when the temperature becomes large compared to the Fermi energy of charge carriers, the attractive Fermi polaron merges with a continuum of states comprised of a bound trion and unbound Fermi-sea-hole, i.e., the trion-hole continuum. Here, the attractive branch ceases to be a well-defined quasiparticle and it crosses over into an incoherent regime dominated by the trion-hole continuum. We discuss the implications of this crossover for the existence of polariton quasiparticles when the semiconductor is strongly coupled to light in a microcavity. By contrast, we find that temperature does not qualitatively change the nature of the repulsive branch at typical doping levels, only its polaron properties.

<sup>1</sup> While the results in Refs. [262, 387] have been derived at finite temperature, the former only considered infinite exciton mass, while the latter did not analyze the consequences of temperature on the polaron description.

We find that the disappearance of the attractive polaron quasiparticle has little effect on its energy and spectral weight, but it strongly modifies the linewidth and the overall shape of the attractive peak in both absorption and photoluminescence. In particular, we observe that the attractive branch evolves from a symmetric Lorentzian shape to a strongly asymmetric profile with an exponential tail below the trion energy.

To describe the trion-dominated regime at low temperatures and high doping, we employ a quantum virial expansion [424] for the optical response, which is a perturbatively exact theory when the temperature  $T$  greatly exceeds the Fermi energy  $E_F$ , and is therefore applicable at high temperature and/or low doping. We show that this corresponds to a limit of the Fermi-polaron picture where the coherent dressing cloud of the attractive polaron quasiparticle is destroyed by thermal fluctuations in contrast to the situation at lower temperatures. We demonstrate that the virial expansion predicts hitherto unrecognized features in photoluminescence such as a non-trivial behavior of the attractive peak near the trion energy related to 2D resonant exciton-electron scattering. This in turn implies that the trion binding energy is likely to have been overestimated by about 10% in experiments. We compare our results to a recent experiment on a doped MoSe<sub>2</sub> monolayer [349] and find excellent agreement. Finally, we show analytically that the virial expansion reduces to the predictions of the trion picture in the limit where  $E_F \rightarrow 0$ .

Note that, even though our model is formulated to describe doped 2D semiconductors, our results can be easily generalized to 2D atomic Fermi gases [342, 343, 425], and they can straightforwardly be extended to the three-dimensional case.

## 3.2 Model

The model Hamiltonian we consider is the same one we have used to describe the spin-valley polarized quantum impurity problem at zero temperature in Sec.2.3.2. Here, a single and isolated exciton interacts with a fermionic gas of carriers:

$$\hat{H} = \hat{H}_0 + \hat{H}_{0X} + \hat{H}_{int} \quad (3.1a)$$

$$\hat{H}_0 = \sum_{\mathbf{k}} (\epsilon_{\mathbf{k}} - \mu) \hat{c}_{\mathbf{k}}^\dagger \hat{c}_{\mathbf{k}} \quad (3.1b)$$

$$\hat{H}_{0X} = \sum_{\mathbf{k}} \epsilon_{X\mathbf{k}} \hat{x}_{\mathbf{k}}^\dagger \hat{x}_{\mathbf{k}} \quad (3.1c)$$

$$\hat{H}_{int} = -\frac{v}{\mathcal{A}} \sum_{\mathbf{k}\mathbf{k}'\mathbf{q}} \hat{x}_{\mathbf{k}+\mathbf{q}}^\dagger \hat{c}_{\mathbf{k}'-\mathbf{q}}^\dagger \hat{c}_{\mathbf{k}'} \hat{x}_{\mathbf{k}}. \quad (3.1d)$$

The surrounding medium is described within the grand canonical ensemble [423]. Here the chemical potential  $\mu$  is related to the excess electron density  $n = N/\mathcal{A}$  by

$$\mu = T \ln(e^{\beta E_F} - 1) \quad E_F = \frac{2\pi}{m} n, \quad (3.2)$$

where  $E_F$  is the Fermi energy and  $\beta = T^{-1}$  the inverse temperature.

We assume the Fermi sea to be non-interacting, an assumption that becomes exact in the high-temperature, low-doping limit [359]. Further, the exciton-charge interaction is approximated as a contact interaction [265, 381] with coupling strength  $v > 0$  up to a high-momentum cutoff  $\Lambda$ . The validity of this approximation has been discussed in Sec. 2.3.2. The renormalization of the exciton-electron contact interaction is carried out by expressing the interaction strength in terms of the trion binding energy  $\varepsilon_T$  (2.5) [372]:

$$\frac{1}{v} = \frac{1}{\mathcal{A}} \sum_{\mathbf{k}}^{\Lambda} \frac{1}{\varepsilon_T + \epsilon_{X\mathbf{k}} + \epsilon_{\mathbf{k}}}. \quad (3.3)$$

As explained in Sec. 2.3.2, through this definition and by keeping  $\varepsilon_T$  finite, our results become independent of the cutoff once we consider the  $\Lambda \rightarrow \infty$  limit.

### 3.2.1 Variational approach

At finite temperature, one can employ the variational approach for impurity dynamics developed in Ref. [423] in the context of the Fermi polaron problem in ultracold atomic gases. This variational approach has been successfully used to model dynamical probes such as Ramsey spectroscopy [179, 390] and Rabi oscillations [426, 427], as well as static thermodynamic properties such as the impurity contact [403, 428]. We review the approach here, formulating it for the 2D semiconductor problem. We consider the case of zero impurity momentum, relevant for evaluating absorption and emission. The generalization to finite impurity momentum is discussed in Appendix C.

The starting point of the variational approach [423] is the time-dependent impurity operator that approximates the exact operator in the Heisenberg picture,  $\hat{x}_0(t) = e^{i\hat{H}t} \hat{x}_0 e^{-i\hat{H}t}$ . We choose the form

$$\hat{x}_0(t) \simeq \varphi_0(t) \hat{x}_0 + \frac{1}{\mathcal{A}} \sum_{\mathbf{k}, \mathbf{q}} \varphi_{\mathbf{k}\mathbf{q}}(t) \hat{c}_{\mathbf{q}}^\dagger \hat{c}_{\mathbf{k}} \hat{x}_{\mathbf{q}-\mathbf{k}}, \quad (3.4)$$

which is written in terms of the time-dependent variational coefficients  $\varphi_0(t)$  and  $\varphi_{\mathbf{k}\mathbf{q}}(t)$ . The truncated form of this operator is similar to that of the Chevy ansatz [375] Eq. (2.28) employed for the zero-temperature state — see Sec. 2.3.

The time-dependent exciton operator (3.4) does not coincide with the exact solution of the Heisenberg equation of motion, and thus we determine the variational coefficients by minimizing the error function

$$\Delta(t) = \langle \hat{e}(t) \hat{e}^\dagger(t) \rangle_\beta \equiv \text{Tr}[\hat{\rho}_0 \hat{e}(t) \hat{e}^\dagger(t)], \quad (3.5)$$

with respect to  $\varphi_0^*(t)$  and  $\varphi_{\mathbf{k}\mathbf{q}}^*(t)$ . Here, the trace is over medium-only states,  $\hat{e}(t) = i\partial_t \hat{x}_0(t) - [\hat{x}_0(t), \hat{H}]$  is an error operator, and  $\hat{\rho}_0 = e^{-\beta \hat{H}_0} / Z_0$  is the medium-only density matrix with  $Z_0 = \text{Tr}[e^{-\beta \hat{H}_0}]$  the medium partition function in the grand canonical ensemble. By considering the stationary solutions,  $\varphi_0(t) = \varphi_0 e^{-iEt}$  and  $\varphi_{\mathbf{k}\mathbf{q}}(t) = \varphi_{\mathbf{k}\mathbf{q}} e^{-iEt}$ , we obtain the following eigenvalue problem:

$$E\varphi_0 = -\frac{v}{\mathcal{A}^2} \sum_{\mathbf{k}, \mathbf{q}} f_{\mathbf{q}}(1 - f_{\mathbf{k}}) \varphi_{\mathbf{k}\mathbf{q}} \quad (3.6a)$$

$$E\varphi_{\mathbf{k}\mathbf{q}} = E_{X\mathbf{k}\mathbf{q}} \varphi_{\mathbf{k}\mathbf{q}} - v\varphi_0 - \frac{v}{\mathcal{A}} \sum_{\mathbf{k}'} (1 - f_{\mathbf{k}'}) \varphi_{\mathbf{k}'\mathbf{q}}. \quad (3.6b)$$

Here,  $E_{X\mathbf{k}\mathbf{q}} = \epsilon_{X\mathbf{q}-\mathbf{k}} + \epsilon_{\mathbf{k}} - \epsilon_{\mathbf{q}}$  and we have used the Fermi-Dirac distribution for the electron occupation,  $\langle \hat{c}_{\mathbf{k}}^\dagger \hat{c}_{\mathbf{k}'} \rangle_\beta = f_{\mathbf{k}} = [e^{\beta(\epsilon_{\mathbf{k}} - \mu)} + 1]^{-1}$ , and for the hole occupation,  $\langle \hat{c}_{\mathbf{k}} \hat{c}_{\mathbf{k}'}^\dagger \rangle_\beta = 1 - f_{\mathbf{k}}$ . Note that we have dropped terms that vanish when  $\Lambda \rightarrow \infty$ ; for instance, since  $v \sim 1/\ln \Lambda \rightarrow 0$ , terms like  $\frac{v}{\mathcal{A}} \sum_{\mathbf{q}'} f_{\mathbf{q}'} \varphi_{\mathbf{k}\mathbf{q}'}$  also go to zero as  $\Lambda \rightarrow \infty$ .

The set of equations in (3.6) constitutes an eigenvalue problem that can be solved to give a set of eigenvalues  $E_n$  and associated eigenvectors  $\varphi_{n0}$  and  $\varphi_{n\mathbf{k}\mathbf{q}}$ , with  $n$  a discrete index. We require that the corresponding stationary operators

$$\hat{x}_{n0} = \varphi_{n0} \hat{x}_0 + \frac{1}{\mathcal{A}} \sum_{\mathbf{k}, \mathbf{q}} \varphi_{n\mathbf{k}\mathbf{q}} \hat{c}_{\mathbf{q}}^\dagger \hat{c}_{\mathbf{k}} \hat{x}_{\mathbf{q}-\mathbf{k}},$$

are orthonormal under a thermal average,  $\langle \hat{x}_{n0} \hat{x}_{m0}^\dagger \rangle_\beta = \delta_{n,m}$ , implying that

$$\varphi_{n0} \varphi_{m0}^* + \frac{1}{\mathcal{A}^2} \sum_{\mathbf{k}, \mathbf{q}} f_{\mathbf{q}}(1 - f_{\mathbf{k}}) \varphi_{n\mathbf{k}\mathbf{q}} \varphi_{m\mathbf{k}\mathbf{q}}^* = \delta_{n,m}.$$

The stationary operators thus form a complete basis within which we can expand the approximate impurity operator (3.4), giving

$$\hat{x}_0(t) = \sum_n \varphi_{n0}^* \hat{x}_{n0} e^{-iE_n t}, \quad (3.7)$$

where  $\varphi_{n0}^* = \langle \hat{x}_0 \hat{x}_{n0}^\dagger \rangle_\beta$  and where we have used the boundary condition  $\hat{x}_0(0) = \hat{x}_0$ .

The exciton retarded Green's function in the time domain,

$$G_X(t) = -i\theta(t)\langle[\hat{x}_0(t), \hat{x}_0^\dagger]\rangle_\beta = -i\theta(t)\langle\hat{x}_0(t)\hat{x}_0^\dagger\rangle_\beta, \quad (3.8)$$

can be evaluated approximately within the variational ansatz (3.4) by using Eq. (3.7). By taking the Fourier transform into the frequency domain we obtain:

$$G_X(\omega) = \sum_n \frac{|\varphi_0^{(n)}|^2}{\omega - E_n + i0^+}, \quad (3.9)$$

where the small imaginary part originates from the Heaviside function  $\theta(t)$  in the retarded Green's function  $G_X(t)$ .

### 3.2.2 Exciton self-energy and $T$ matrix

As discussed above, solving the eigenvalue problem (3.6) allows us to evaluate the exciton Green's function. It turns out that it is numerically convenient to instead consider the exciton self-energy  $\Sigma_X(\omega)$ , which is related to the Green's function via

$$G_X(\omega) = \frac{1}{\omega - \Sigma_X(\omega)}. \quad (3.10)$$

The expression for the exciton self-energy can be derived by manipulating the eigenvalue problem (3.6) [423], following the same procedure valid at zero temperature, introducing an auxiliary function  $\chi_{\mathbf{q}} = \frac{v}{\mathcal{A}} \sum_{\mathbf{k}} (1 - f_{\mathbf{k}}) \varphi_{\mathbf{k}\mathbf{q}}$  — see Sec. 2.3.2. In this way, the exciton self-energy reads

$$\Sigma_X(\omega) = \frac{1}{\mathcal{A}} \sum_{\mathbf{q}} f_{\mathbf{q}} \mathcal{T}(\omega + \epsilon_{\mathbf{q}}, \mathbf{q}), \quad (3.11)$$

where the inverse of the  $T$  matrix is defined as

$$\mathcal{T}^{-1}(\omega, \mathbf{q}) = -\frac{1}{v} - \frac{1}{\mathcal{A}} \sum_{\mathbf{k}} \frac{1 - f_{\mathbf{k}}}{\omega - \epsilon_{\mathbf{k}} - \epsilon_{X\mathbf{k}-\mathbf{q}} + i0^+}. \quad (3.12)$$

The same expression (3.11) can also be derived by using a diagrammatic expansion within the ladder approximation [49, 379]. Thus, our variational approach provides an additional theoretical foundation for ladder diagrams.

It is profitable to separate the vacuum contribution to the  $T$  matrix, describing the electron-exciton scattering in the absence of a surrounding Fermi gas, from the many-body contribution. To this end, we note that the logarithmic divergence of the second term in (3.12) cancels with that of the inverse contact interaction constant  $v^{-1}$  (3.3), allowing the vacuum contribution  $\mathcal{T}_0$  to be calculated analytically [429] (Note that, throughout this chapter, energies

are measured with respect to that of the exciton at rest):

$$\mathcal{T}^{-1}(\omega, \mathbf{q}) = \mathcal{T}_0^{-1}(\omega, \mathbf{q}) - \Pi_{mb}(\omega, \mathbf{q}) \quad (3.13a)$$

$$\mathcal{T}_0^{-1}(\omega, \mathbf{q}) = \frac{m_r}{2\pi} \ln \left( \frac{-\varepsilon_T}{\omega - \frac{q^2}{2m_T} + i0^+} \right) \quad (3.13b)$$

$$\Pi_{mb}(\omega, \mathbf{q}) = -\frac{1}{\mathcal{A}} \sum_{\mathbf{k}} \frac{f_{\mathbf{k}}}{\omega - \epsilon_{\mathbf{k}} - \epsilon_{X\mathbf{k}-\mathbf{q}} + i0^+}, \quad (3.13c)$$

where  $m_T = m + m_X$  is the trion mass and  $m_r = mm_X/m_T$  is the exciton-electron reduced mass. Note that the vacuum  $T$  matrix (3.13b) has a pole at the bound state, i.e., the trion energy,  $\omega = -\varepsilon_T + \epsilon_{T\mathbf{q}}$ , where  $\epsilon_{T\mathbf{q}} = \frac{q^2}{2m_T}$  is the trion kinetic energy (for a summary of the trion properties at finite momentum and finite doping, see Sec 2.3.3). Differently from the vacuum  $T$  matrix (3.13b), the many-body correction in Eq. (3.13c) cannot be evaluated analytically. We describe in Sec. 3.2.4 the numerical procedure we follow to evaluate it.

The system's optical response, such as the optical absorption and photoluminescence, can be evaluated starting from the exciton Green's function, as we describe in the next section.

### 3.2.3 Optical absorption and photoluminescence

The optical absorption coincides with the exciton spectral function:

$$A_X(\omega) = -\frac{1}{\pi} \text{Im}G_X(\omega). \quad (3.14)$$

Indeed, in the linear-response regime, as already discussed in Sec. 1.5.3, the spectral function is equivalent to the transfer rate from an initial state  $|n\rangle$  containing no excitons (the impurity vacuum) to a final state  $|\nu\rangle$  containing a single exciton. Here, the impurity vacuum and single-impurity states are eigenstates of the Hamiltonian, i.e.,  $\hat{H}|n\rangle = \hat{H}_0|n\rangle = E_n|n\rangle$  and  $\hat{H}|\nu\rangle = E_\nu|\nu\rangle$ . Using Fermi's golden rule, we have

$$A_X(\omega) = \sum_{n,\nu} \langle n|\hat{\rho}_0|n\rangle |\langle \nu|\hat{x}_{\mathbf{0}}^\dagger|n\rangle|^2 \delta(E_\nu - E_n - \omega), \quad (3.15)$$

which satisfies the sum-rule:

$$\int_{-\infty}^{\infty} d\omega A_X(\omega) = 1. \quad (3.16)$$

In order to evaluate the photoluminescence, we instead consider the opposite situation, i.e., an initial state  $|\nu\rangle$  containing the medium and the exciton, and a final state  $|n\rangle$  after the exciton has recombined to emit a photon. Here, we

have assumed that the exciton density is low enough such that each exciton can be treated individually. The transfer rate at thermal equilibrium is then given by

$$P_X(\omega) = \sum_{n,\nu} \langle \nu | \hat{\rho} | \nu \rangle |\langle n | \hat{x}_{\mathbf{0}} | \nu \rangle|^2 \delta(E_\nu - E_n - \omega), \quad (3.17)$$

where  $\hat{\rho} = e^{-\beta \hat{H}} / Z_{int}$  is the density matrix associated with the interacting exciton and medium system (3.1) and  $Z_{int} = \sum_\nu \langle \nu | e^{-\beta \hat{H}} | \nu \rangle$  the associated partition function. It is straightforward to show that the photoluminescence satisfies the following sum rule

$$\int_{-\infty}^{\infty} d\omega P_X(\omega) = \text{Tr}[\hat{\rho} \hat{x}_{\mathbf{0}}^\dagger \hat{x}_{\mathbf{0}}]. \quad (3.18)$$

Using the properties of the delta function, the absorption  $A_X(\omega)$  and photoluminescence  $P_X(\omega)$  can be related by a detailed balanced condition [179]:

$$P_X(\omega) = \frac{Z_0}{Z_{int}} e^{-\beta \omega} A_X(\omega). \quad (3.19)$$

The thermodynamic, Boltzmann-type scaling between absorption and emission profiles (3.19) is also known as the Kubo-Martin-Schwinger relation [430, 431], the Kennard-Stepanov relation [432–434] or the van Roosbroeck-Shockley relation [435], depending on the context within which it has been studied, and it applies to a broad range of systems, including semiconductors [176–178]. It relies on the assumption that the population of excited states, here excitons, has thermalized at a temperature  $T$  before the emission and that they are otherwise uncorrelated. Note also that the thermalization temperature  $T$  can be different from the system lattice (cryostat) temperature.

### 3.2.4 Numerical implementation

Even though one only has to evaluate two momentum integrals to obtain the exciton Green's function in Eq. (3.10), namely the integrals in Eqs. (3.11) and (3.13c), some comments about the numerical procedure are necessary. For the optical absorption (3.14), the numerical convergence of the integrals is much improved by shifting the frequency to the complex plane,  $\omega \mapsto \omega + i\eta_X$ . Apart from helping with convergence, this shift provides a simplified description of the exciton's intrinsic broadening due to effects beyond those included in the Hamiltonian such as recombination and disorder. In the following, we have used the typical value  $\eta_X = 0.04\varepsilon_T \simeq 1$  meV.

Including  $\eta_X$  implies that the exciton spectral function decays as a Lorentzian at low and high energies. However, one cannot evaluate the photoluminescence using this procedure. Indeed, by using the detailed balance condi-

tion (3.19), the photoluminescence diverges at infinitely low frequencies if one uses a finite value of  $\eta_X$  to evaluate the absorption since the Boltzmann occupation increases more rapidly than the Lorentzian decay of absorption. This means that photoluminescence needs to be evaluated by first calculating absorption at  $\eta_X = 0$  and then multiplying by the Boltzmann occupation. In order to do this, it is useful to re-write the  $\mathbf{k}$  and  $\mathbf{q}$  integrals appearing in the exciton self-energy formula (3.13c) in a way that is numerically efficient when there is no broadening.

Let us start by rewriting (3.13c) in an equivalent form:

$$\begin{aligned} \Pi_{mb}(\omega, \mathbf{q}) &= -\frac{1}{\mathcal{A}} \sum_{\mathbf{k}} \frac{f_{\mathbf{k}+\frac{m}{m_T}\mathbf{q}}}{\omega - \epsilon_{\mathbf{k}+\frac{m}{m_T}\mathbf{q}} - \epsilon_{X\mathbf{k}-\frac{m_X}{m_T}\mathbf{q}} + i0^+} \\ &= -\int \frac{dkk}{2\pi} \frac{\int \frac{d\theta}{2\pi} f_{\mathbf{k}+\frac{m}{m_T}\mathbf{q}}}{\omega - \epsilon_{\mathbf{q}\frac{m}{m_T}} - \epsilon_{\mathbf{k}\frac{m_X}{m_T}} + i0^+}. \end{aligned} \quad (3.20)$$

The  $k$ -integral can then be evaluated numerically by applying the Sokhotski–Plemelj theorem

$$\int dx \frac{F(x)}{x + i0^+} = -i\pi F(0) + \mathcal{P} \int dx \frac{F(x)}{x}, \quad (3.21)$$

where  $\mathcal{P}[\dots]$  is the integral Cauchy principal part.

As far as the  $\mathbf{q}$ -integral for evaluating the exciton self-energy (3.11) is concerned, it can be re-written in the following equivalent form by defining  $y = q^2$ :

$$\Sigma_X(\omega) = \int \frac{dy}{4\pi} \frac{f_{\sqrt{y}}}{\mathcal{T}^{-1}(\omega + \epsilon_{\sqrt{y}}, \sqrt{y})}. \quad (3.22)$$

This integral has a pole when  $\text{Re}\mathcal{T}^{-1} = 0 = \text{Im}\mathcal{T}^{-1}$ . Using a model involving contact interactions in 2D means that such a pole always exists, and furthermore, it is a simple pole [436]. Thus, we define  $y^* = y^*(\omega)$  to be the pole of the  $T$  matrix.

In this case, we can apply the residue theorem to write:

$$\begin{aligned} \Sigma_X(\omega) &= \mathcal{P} \int \frac{dy}{4\pi} \frac{f_{\sqrt{y}}}{\text{Re}\mathcal{T}^{-1}(\omega + \epsilon_{\sqrt{y}}, \sqrt{y}) + i\text{Im}\mathcal{T}^{-1}(\omega + \epsilon_{\sqrt{y}}, \sqrt{y})} \\ &\quad - \frac{i\pi\Theta(y^*)}{4\pi} \text{sign} \left[ \text{Im}\mathcal{T}^{-1}(\omega + \epsilon_{\sqrt{y^*}}, \sqrt{y^*}) \right] \\ &\quad \times \text{Res}_{y^*} \left[ \frac{f_{\sqrt{y}}}{\text{Re} \left[ \mathcal{T}^{-1}(\omega + \epsilon_{\sqrt{y}}, \sqrt{y}) \right]} \right], \end{aligned} \quad (3.23)$$

where the principal part prescription is used in the vicinity of the pole at  $y^*$ ,

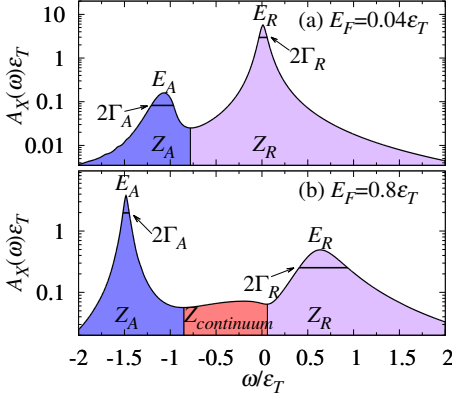


**Fig. 3.1:** Spectral function  $A_X(\omega)$  at temperature  $T = 50 \text{ K} \approx 0.17\epsilon_T$  for (a)  $E_F = 0.04\epsilon_T$  and (b)  $E_F = 0.8\epsilon_T$ . We extract the attractive and repulsive polaron energy  $E_{A,R}$  as the peak position, the linewidth  $2\Gamma_{A,R}$  as the peak FWHM, and the polaron spectral weight  $Z_{A,R,continuum}$  as the area under the peak. While at low doping (a) the trion-hole continuum is merged with the attractive branch and  $Z_{continuum} = 0$ .

and the residue can be evaluated as

$$\text{Res}_{y^*} \left[ \frac{f\sqrt{y}}{\text{Re}[\mathcal{T}^{-1}(\omega + \epsilon\sqrt{y}, \sqrt{y})]} \right] = \frac{f\sqrt{y^*}}{\left| \frac{\partial \text{Re}\mathcal{T}^{-1}(\omega + \epsilon\sqrt{y}, \sqrt{y})}{\partial y} \right|_{y^*}}. \quad (3.24)$$

From the expression of the exciton self-energy, we can get the exciton Green's function (3.10). These results allow us to evaluate the absorption and photoluminescence without any intrinsic homogeneous broadening for the exciton. For absorption alone, the integration method illustrated here is unnecessary, as one can conveniently shift the frequency to the complex plane,  $\omega \mapsto \omega + i\eta_X$ , where  $\eta_X$  is related to the exciton homogeneous and inhomogeneous broadening, giving well-converged results. However, as explained in Sec. 3.2.4, for the luminescence one has to resort to the integration method illustrated above.

The effects of the exciton intrinsic decay time can be re-introduced at the end of the calculation by convolving the photoluminescence with a Lorentzian profile with broadening  $2\eta_X$

$$\bar{P}_X(\omega') = \int_{-\infty}^{\infty} d\omega' P_X(\omega') \frac{1}{\pi} \frac{\eta_X}{(\omega - \omega')^2 + \eta_X^2}. \quad (3.25)$$

### 3.3 Weak coupling regime

We now discuss the effect of temperature on the optical response. Results about the zero temperature case can be found in Sec. 2.3.2. Fig. 3.2 (a,b,c) allows a comparison between the doping-dependent properties of optical absorption at zero and finite temperature. In this figure, the polaron energy  $E_{A,R}$  is evaluated

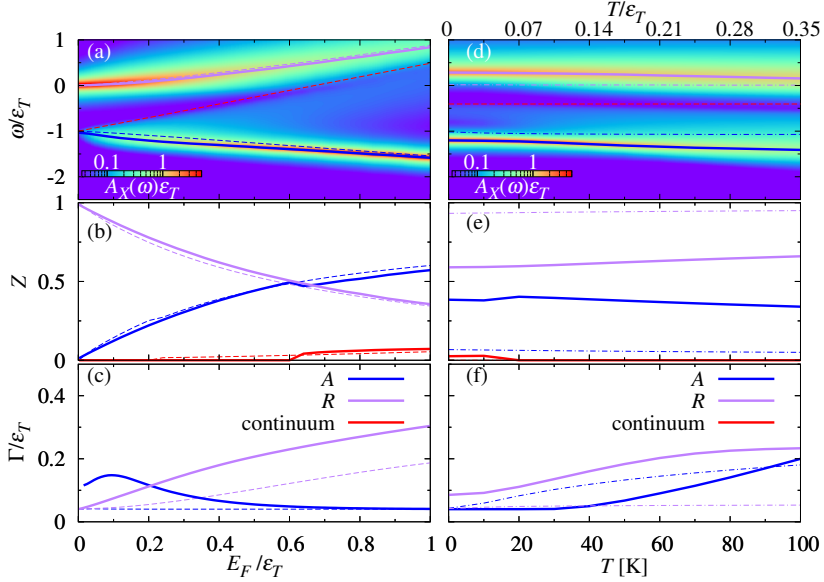


**Fig. 3.2:** (a) Spectral function  $A_X(\omega)$  for a fixed temperature  $T = 50 \text{ K} \approx 0.17\epsilon_T$ . Dashed lines are the zero-temperature energies — for the trion-hole continuum, we plot only the upper boundary  $E_+$  (2.43). Solid lines are the attractive (blue) and repulsive (purple) branch energies at finite temperature. (b,c) Doping dependence of the spectral weights  $Z$  and half linewidths  $\Gamma$  extracted from the spectral function at  $T = 0$  (dashed) and  $T = 50 \text{ K} \approx 0.17\epsilon_T$  (solid). (d,e,f) Same spectral properties, as a function of temperature, for fixed doping of  $E_F = 0.4\epsilon_T$  (solid lines and spectral function), and  $E_F = 0.04\epsilon_T$  (dot-dashed lines). In panels (c,f), the constant value of  $\Gamma_R$  at small doping or zero temperature is approximately given by the intrinsic broadening  $\eta_X$ .

as the spectral function peak position, the linewidth  $2\Gamma_{A,R}$  as the FWHM, and the spectral weight as the area under the peak. We have used the location of the spectral function minima as limits for the integrals evaluating the spectral weights: If there is only one minimum, this is the upper (lower) bound for evaluating  $Z_A$  ( $Z_R$ ), while if there are two minima, these are the limits for evaluating the trion-hole continuum spectral weight  $Z_{\text{continuum}}$  — see Fig. 3.1. This criterion is the origin of the small discontinuity in the residues shown in Figs. 3.2 and 3.6.

Both the energies and spectral weights of attractive and repulsive branches have a very weak dependence on temperature in the regime  $T \lesssim \epsilon_T$ . The branch energies are slightly redshifted, while  $Z_A$  ( $Z_R$ ) is slightly smaller (larger) compared to the zero-temperature case. This small variation with temperature is also observed in Fig. 3.2(d,e) for fixed doping. The most important difference at finite temperature is the behavior of the trion-hole continuum, which subsumes the attractive branch when  $T \gtrsim E_F$ , i.e., at sufficiently low doping

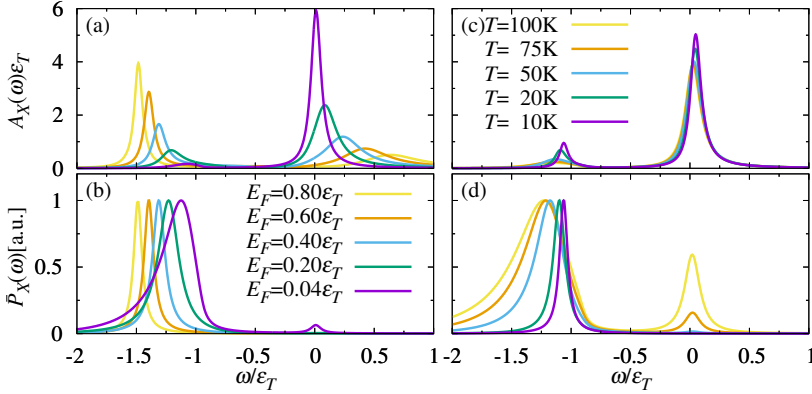


**Fig. 3.3:** Spectral function  $A_X(\omega)$  (a) for different dopings  $E_F$  and at a fixed temperature of  $T = 50 \text{ K} \approx 0.17\epsilon_T$  and (c) for different values of the temperature  $T$  and at a fixed doping  $E_F = 0.1\epsilon_T$ . Lorentzian convolved photoluminescence  $\bar{P}_X(\omega)$  (b) for different dopings  $E_F$  and at a fixed temperature of  $T = 50 \text{ K} \approx 0.17\epsilon_T$  and (d) for different values of the temperature  $T$  and at a fixed doping  $E_F = 0.1\epsilon_T$ . The attractive branch photoluminescence peaks are rescaled to unity.

or sufficiently high temperature. This can be clearly seen from Fig. 3.2 (a), where we no longer observe a sharp lower bound of the trion-hole continuum at low doping because, at finite temperature, the unbound hole belonging to the trion-hole continuum can thermally occupy any momentum state. However, the upper bound of the trion-hole continuum is still clearly visible and approximately follows the zero-temperature expression  $E_+$  (2.43). Similarly, for fixed doping in Fig. 3.2 (d), we observe that the trion-hole continuum is only well-separated from the attractive branch at low temperatures.

Since the spectral weight of the trion-hole continuum is small, its merging with the attractive branch only slightly affects the attractive peak energy. However, the disappearance of the attractive polaron quasiparticle strongly modifies the attractive-branch linewidth  $2\Gamma_A$ . In particular, we observe in Fig. 3.2 (c) that  $\Gamma_A$  has a striking non-monotonic dependence at low doping, while it decreases towards its zero-temperature value (corresponding to the intrinsic broadening  $\eta_X$ ) when  $E_F$  increases. Likewise, increasing the temperature at fixed doping can substantially increase  $\Gamma_A$  from  $\eta_X$ , as shown in Fig. 3.2 (f). As we will discuss in Sec. 3.3.1, this behavior signals a crossover from a coherent Fermi polaron regime to an incoherent trion-dominated regime, where there no longer exists a well-defined attractive quasiparticle that is separated from the trion-hole continuum. The repulsive branch, on the other hand, remains a polaron quasiparticle with a finite lifetime (broadening) for the dopings considered in this work ( $E_F \lesssim \epsilon_T$ ). In particular, we see that temperature does not change the nature of the repulsive branch in Figs. 3.2, but it can

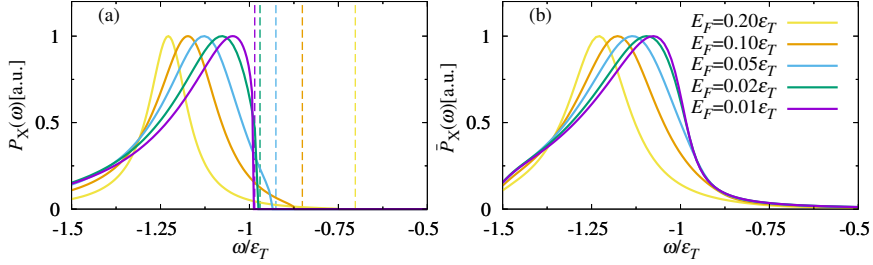


**Fig. 3.4:** (a) Unconvolved photoluminescence  $P_X(\omega)$  and (b) Lorentzian convolved photoluminescence  $\bar{P}_X(\omega)$  for different dopings  $E_F$ , at a fixed temperature of  $T = 50 \text{ K} \simeq 0.17\epsilon_T$ , and for a frequency range around the attractive branch only. The photoluminescence peaks are rescaled to unity. In panel (a) the vertical dashed lines are the upper boundary of the trion-hole continuum  $E_+$  at zero temperature (2.43).

lead to a faster increase of the half linewidth  $\Gamma_R$  with increasing doping — see Fig. 3.2 (c).

We now discuss the shape of the optical response profiles and how they evolve with either doping or temperature. Figs. 3.3 display both the absorption and the Lorentzian convolved photoluminescence (3.25) — at fixed temperature — Figs 3.3 (a,b) — and fixed doping — Figs 3.3 (c,d). The repulsive polaron quasiparticle shows up approximately as a Lorentzian symmetric profile in both absorption and photoluminescence spectra, with an FWHM that increases with increasing  $E_F$ . Note that the FWHM of the repulsive branch only has a weak dependence on temperature in Fig. 3.3 (c,d) since  $E_F$  has been fixed to a low value such that the intrinsic width  $2\eta_X$  dominates.

By contrast, the shape of the attractive branch is strongly modified by temperature: in the low-temperature (high-doping) regime  $E_F > T$ , it is described by a Lorentzian with FWHM  $2\eta_X$ , while for  $E_F < T$ , it develops a strongly asymmetric shape with an exponential tail below the trion energy. This evolution in the asymmetry of the attractive branch once again indicates a crossover from a Fermi-polaron quasiparticle to a continuum of trion states.

In Fig. 3.4 we further analyze the shape of the attractive peak at low doping  $E_F \lesssim T$ , comparing the Lorentzian convolved photoluminescence  $\bar{P}_X(\omega)$  with the “bare” photoluminescence  $P_X(\omega)$ , where we have removed the effects of any intrinsic exciton broadening. In Fig. 3.4 (a), we observe a sharp onset of the photoluminescence which approximately coincides with the upper boundary of the trion-hole continuum at zero temperature,  $E_+$ . Thus, according to Eq. (2.43), it blueshifts with increasing doping. As shown in Fig. 3.4 (b), any intrinsic broadening  $\eta_X$  only smooths out the sharp onset, while it has little effect on the position of the peak. When  $E_F$  increases, the sharp onset tends to disappear as the attractive peak redshifts and detaches from the trion-hole continuum.

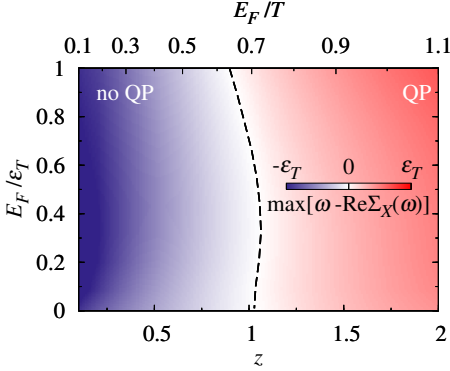


**Fig. 3.5:** Maximum value of  $\omega - \text{Re}\Sigma_X(\omega)$  for  $\omega < 0$  as a function of the Fermi gas fugacity  $z = e^{\beta\mu}$  and doping. The black dashed line describes the values of  $z$  and  $E_F$  at which this maximum is zero. On the left of this curve (blue area), the attractive branch is not a polaron quasiparticle (no QP), while on the right (red area) the attractive branch is a well-defined polaron quasiparticle (QP).

Our calculated profiles for the attractive branch are in excellent quantitative agreement with recent experiments in the high-temperature (low-doping) regime [349], as discussed in [359]. The exponential tail of the asymmetric attractive peak has previously been modelled within a trion picture for the case of photoluminescence [284, 304, 318, 437]. There, the tail is ascribed to the kinetic energy of remaining electrons after the exciton within each trion has decayed into a photon. This description in terms of electron recoil can be formally derived from our theory in the limit of weak interactions, as we will discuss in Sec. 3.3.2.

### 3.3.1 Loss of the attractive polaron quasiparticle: polaron to trion-hole continuum crossover

In this section, we use the pole condition

$$E_{A,R} = \text{Re}\Sigma_X(E_{A,R}), \quad (3.26)$$

to characterize the crossover from a well-defined polaron quasiparticle to a trion-hole continuum with increasing temperature (decreasing doping). In order to find the values of temperature and doping at which this crossover occurs, we plot in Fig. 3.5 the local maximum value of the function  $\omega - \text{Re}\Sigma_X(\omega)$  for  $\omega < 0$  and identify the curve of doping versus fugacity  $z = e^{\beta\mu} = e^{\beta E_F} - 1$  at which this maximum value is zero. For  $E_F \lesssim \varepsilon_T$ , we find that this occurs roughly when  $z \sim 1$  and thus  $E_F \sim 0.7T$ . On the left of this curve, we lose the attractive polaron quasiparticle, as the condition (3.26) cannot be satisfied, i.e.,  $E_A - \text{Re}\Sigma_X(E_A) \neq 0$ . On the right of this curve, instead, the system is in the polaron regime where (3.26) is satisfied.

In order to further illustrate this crossover, we compare the results for the polaron energies, spectral weights, and linewidths extracted from the spectral

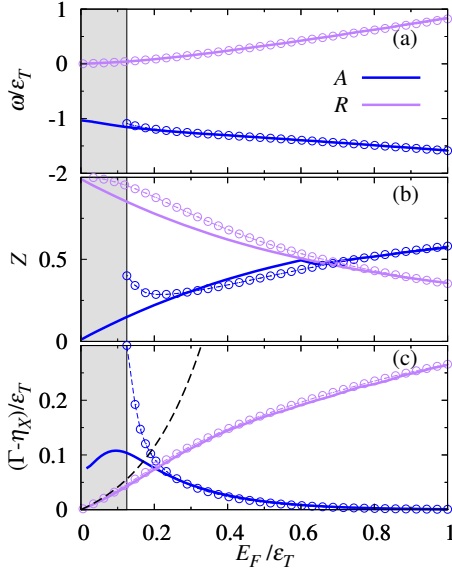


**Fig. 3.6:** (a) Polaron energies  $E_{A,R}$ , (b) spectral weights  $Z_{A,R}$ , and (c) half linewidths  $\Gamma_{A,R}$ , evaluated from the exciton spectral function (solid lines) and from quasiparticle expressions (symbols). The attractive branch stops to be a quasiparticle resonance in the gray region at low doping when  $E_F \lesssim 0.7T$ . In panel (c) we plot  $\Gamma_{A,R} - \eta_X$  in order to compare the numerical results with the analytical estimate of the repulsive branch broadening evaluated at  $\eta_X = 0$  at small doping (dashed line), derived within the virial expansion in Sec. 3.3.2. Temperature is fixed at  $T = 50 \text{ K} \simeq 0.17\epsilon_T$ .

function with those obtained by treating the polaron as a well-defined quasiparticle [141]. In the latter case, the polaron properties can be obtained directly from the expression of the impurity self-energy. The quasiparticle properties have already been discussed in Sec. 3.3.1, and are here proposed. Close to a quasiparticle resonance, the exciton Green's function can be approximated as

$$G_X(\omega) \underset{\omega \simeq E_j}{\simeq} \frac{Z_j}{\omega - E_j + i\Gamma_j}, \quad (3.27)$$

where  $j = A, R$  is the two-branch index, and the quasiparticle energy  $E_j$  is a solution of Eq. (3.26). The pole weight or residue  $Z_j$  is

$$Z_j = \left( 1 - \left. \frac{\partial \text{Re}\Sigma_X(\omega)}{\partial \omega} \right|_{E_j} \right)^{-1}, \quad (3.28)$$

and the polaron damping rate is

$$\Gamma_j = -Z_j \text{Im}\Sigma_X(E_j). \quad (3.29)$$

We compare the results for  $E_j$ ,  $Z_j$ , and  $\Gamma_j$  obtained with both methods in Fig. 3.6. We observe that the positions of the poles coincide to high accuracy with those of the spectral function maxima — see Fig. 3.6 (a). For the repulsive branch, both the spectral weight and the broadening from the quasiparticle theory are in good agreement with those evaluated from the spectral

function, even when the linewidth is non-negligible. By contrast, for the attractive branch, the results depart from one another when we approach the (gray) region  $E_F \lesssim 0.7T$  where there is no attractive quasiparticle, and the quasiparticle description breaks down since, according to Eq. (3.28),  $1/Z_A \rightarrow 0$  when  $\max[\omega - \text{Re}\Sigma_X(\omega)] = 0$ .

In the following section, we analyze the system properties well inside the trion-hole continuum (gray) regime, where the attractive branch is no longer a polaron quasiparticle. Here, for temperatures  $T \gtrsim E_F$ , we can apply a systematic quantum virial expansion.

### 3.3.2 Virial expansion and connection to the trion wave function at high temperature or low doping

As discussed, at high temperature or low doping such that the fugacity  $z = e^{\beta\mu} \lesssim 1$ , the attractive polaron quasiparticle disappears and the attractive branch only consists of a broad continuum. In this limit, one can formally apply a perturbatively exact quantum virial expansion in the fugacity [359]. We will now discuss how this expansion is related to the polaron theory, and how this allows us to demonstrate that the trion picture results of Refs. [284, 349] are contained within the polaron formalism.

The virial expansion corresponds to a systematic expansion in powers of the fugacity  $z = e^{\beta\mu}$ . In the high-temperature/low-doping regime  $T \gtrsim E_F$ , we have  $z \lesssim 1$ , allowing us to perform an exact perturbative expansion around the ideal Boltzmann gas limit of the medium (where  $z \simeq \beta E_F$ ). The virial expansion has been extensively used in other contexts. For instance, to obtain thermodynamic quantities and quantum corrections to the equation of state in condensed matter physics [438, 439], nuclear physics [440] and ultracold gases [424, 441]. It has also been used to calculate response functions for atomic gases [442–448], magnetic impurities [449], magnons [450] and Coulomb systems [451].

When  $T \gg E_F$  and  $z \simeq \beta E_F \ll 1$ , we can formally expand the Fermi occupation function which then coincides with the Boltzmann distribution  $f_{\mathbf{k}} \simeq z e^{-\beta\epsilon_{\mathbf{k}}}$ . Likewise, to leading order in  $z$  we have  $\mathcal{T} \simeq \mathcal{T}_0$ <sup>2</sup>. Within this expansion, the exciton self-energy in Eq. (3.11) becomes

$$\Sigma_X(\omega) \simeq \frac{z}{\mathcal{A}} \sum_{\mathbf{q}} e^{-\beta\epsilon_{\mathbf{q}}} \mathcal{T}_0(\omega + \epsilon_{\mathbf{q}}, \mathbf{q}). \quad (3.30)$$

<sup>2</sup> In principle, one can obtain the self-energy (3.11) for an arbitrary electron-exciton potential by determining the corresponding  $T$  matrix. However, since the relevant energy scales in TMDs (i.e.,  $T$ ,  $E_F$ , and the trion binding energy  $\epsilon_T$ ) are smaller than that set by the range of the potential, the  $T$  matrix is well approximated by its low-energy  $s$ -wave form [452], which does not depend on the nature of the potential.

In other words, to the leading order in the fugacity, the self-energy is determined by two-body interactions weighted by a Boltzmann distribution. Note that, at the lowest order in  $z$ , the assumption made in Chevy's ansatz of considering only a single particle-hole excitation becomes exact since a higher number of particle-hole excitations enter at higher order in  $z$  since they require multiple electrons to be scattered from the medium, where each medium excitation is weighted by  $z$  [447, 453]. This furthermore means that the assumption of neglecting electron-electron interactions, if we work at the lowest order in  $z$ , becomes also correct.

Focusing first on the attractive branch, in the regime  $T \lesssim \varepsilon_T$ , which is the situation in most current experiments, the dominant contribution to the self-energy arises from the pole of the  $T$  matrix at the trion energy. We, therefore, expand the  $T$  matrix for  $\omega \simeq -\varepsilon_T + \varepsilon_{T\mathbf{q}}$ , with the result

$$\mathcal{J}_0(\omega + \varepsilon_{\mathbf{q}}, \mathbf{q}) \simeq \frac{Z_T}{\omega + \varepsilon_{\mathbf{q}} - \varepsilon_{T\mathbf{q}} + \varepsilon_T + i0^+}, \quad (3.31)$$

where  $Z_T \equiv 2\pi\varepsilon_T/m_r$ . The  $T$  matrix can be expressed in terms of the vacuum ( $E_F = 0$ ) trion wave function  $\tilde{\eta}_{\mathbf{q}_r}^{(0)}$  for a contact electron-exciton interaction. In our case, the relative momentum is  $\mathbf{q}_r = \mathbf{q}m_X/m_T$ , and therefore the kinetic energy of the relative motion is  $\varepsilon_{r\mathbf{q}_r} = \varepsilon_{\mathbf{q}} - \varepsilon_{T\mathbf{q}}$ . Using the expression for the vacuum trion wave function in the center of mass frame,  $\tilde{\eta}_{\mathbf{q}_r}^{(0)} = \frac{\sqrt{Z_T}}{\varepsilon_T + \varepsilon_{r\mathbf{q}_r}}$  (see Sec 2.3.3), we have

$$\mathcal{J}_0(\omega + \varepsilon_{\mathbf{q}}, \mathbf{q}) \simeq \frac{|\varepsilon_T + \varepsilon_{r\mathbf{q}_r})\tilde{\eta}_{\mathbf{q}_r}^{(0)}|^2}{\omega + \varepsilon_{r\mathbf{q}_r} + \varepsilon_T + i0^+}. \quad (3.32)$$

Here, the numerator is derived by manipulating the relation between the trion wave function and  $Z_T$ , and is momentum independent. However, this is a special property of the contact electron-exciton interaction, and Eq. (3.32) in fact yields the correct generalization for an arbitrary electron-exciton interaction that leads to the formation of a trion. In other words, it can be applied for any realistic trion wave function. To see this, we note that the generalization of Eq. (3.30) to arbitrary two-body transition operator  $\hat{T}_0$  is

$$\Sigma_X(\omega) \simeq \frac{z}{\mathcal{A}} \sum_{\mathbf{q}} e^{-\beta\varepsilon_{\mathbf{q}}} \langle \mathbf{Q}, \mathbf{q}_r | \hat{T}_0(\omega + \varepsilon_{\mathbf{q}}) | \mathbf{Q}, \mathbf{q}_r \rangle. \quad (3.33)$$

We have defined the two-body state  $|\mathbf{Q}, \mathbf{q}_r\rangle \equiv \hat{c}_{\mathbf{q}}^\dagger x_0^\dagger |vac\rangle$  in terms of the relative momentum  $\mathbf{q}_r$  and the total momentum  $\mathbf{Q}$  which are related to the electron momentum via  $\mathbf{q}_r + \mathbf{Q}m/m_T = \mathbf{q}$  and the exciton momentum via  $-\mathbf{q}_r + \mathbf{Q}m_X/m_T = \mathbf{0}$ .

To evaluate the matrix element of the transition operator for an electron-exciton interaction that yields a trion bound state, we use the relationship between Green's operator and the transition operator at energy  $E$ :

$$\hat{G}(E) = \hat{G}_0(E) + \hat{G}_0(E)\hat{T}(E)\hat{G}_0(E). \quad (3.34)$$

Here,  $\hat{G}(E) = \frac{1}{E - \hat{H} + i0^+}$  and  $\hat{G}_0(E) = \frac{1}{E - \hat{H}_0 - \hat{H}_{0X} + i0^+}$  (which, for the two-body problem, should be evaluated in the canonical ensemble, effectively taking  $\mu = 0$ ). Close to the trion resonance, we can neglect the first term, and we, therefore, have the spectral representation

$$\begin{aligned} \langle \mathbf{Q}, \mathbf{q}_r | \hat{T}_0(E) | \mathbf{Q}, \mathbf{q}_r \rangle & \simeq \langle \mathbf{Q}, \mathbf{q}_r | \hat{G}_0^{-1}(E) \hat{G}(E) \hat{G}_0^{-1}(E) | \mathbf{Q}, \mathbf{q}_r \rangle \\ & = (E - \epsilon_{\mathbf{q}})^2 \langle \mathbf{Q}, \mathbf{q}_r | \hat{G}(E) | \mathbf{Q}, \mathbf{q}_r \rangle \\ & \simeq (E - \epsilon_{\mathbf{q}})^2 \frac{|\tilde{\eta}_{\mathbf{q}_r}^{(0)}|^2}{E + \epsilon_T - \epsilon_{T\mathbf{Q}} + i0^+} \\ & \simeq \frac{(-\epsilon_T + \epsilon_{T\mathbf{Q}} - \epsilon_{\mathbf{q}})^2 |\tilde{\eta}_{\mathbf{q}_r}^{(0)}|^2}{E + \epsilon_T - \epsilon_{T\mathbf{Q}} + i0^+}, \end{aligned} \quad (3.35)$$

where in the third step we approximated the expectation value by inserting the trion state, and in the last step we used the pole condition. Taking  $E = \omega + \epsilon_{\mathbf{q}}$  and using  $\mathbf{Q} = \mathbf{q}$  we see that Eq. (3.35) reduces to Eq. (3.32) which demonstrates that it holds for arbitrary electron-exciton interactions that lead to trion formation.

Using the approximation for the vacuum  $T$  matrix, Eq. (3.32), the self-energy in Eq. (3.30) becomes

$$\begin{aligned} \Sigma_A(\omega < -\epsilon_T) & \simeq \frac{z}{\mathcal{A}} \sum_{\mathbf{q}} e^{-\beta\epsilon_{\mathbf{q}}} |\tilde{\eta}_{\mathbf{q}_r}^{(0)}|^2 \\ & \times \left[ \mathcal{P} \frac{|\epsilon_{r\mathbf{q}_r} + \epsilon_T|^2}{\omega + \epsilon_{r\mathbf{q}_r} + \epsilon_T} - i\pi\omega^2 \delta(\omega + \epsilon_{r\mathbf{q}_r} + \epsilon_T) \right], \end{aligned} \quad (3.36)$$

where  $\mathcal{P}$  denotes the principal value. This explicitly relates the self-energy calculated within the polaron theory to the trion wave function in the regime where the fugacity is small, and importantly it applies for any realistic trion wave function. A similar approach involving trion wave functions has been used to calculate absorption [421]. Note that the real part diverges logarithmically when  $\omega + \epsilon_T \rightarrow 0^-$ , and therefore it cannot in general be neglected close to the onset of the attractive branch.

For the repulsive branch, we can again apply Eq. (3.30) to find the leading

contribution at small fugacity. In the regime where  $E_F \ll \varepsilon_T$ , the width of the repulsive branch is much smaller than the trion binding energy, and to the lowest order in the fugacity, we can simply evaluate the repulsive polaron self-energy within the repulsive branch by taking  $\omega = 0$ . We then use the fact that, to logarithmic accuracy, the logarithmic behavior at small momentum is generic for the vacuum  $T$  matrix for any short-range interaction [269, 452] and thus we have

$$\begin{aligned} \Sigma_R(0) &\simeq \frac{z}{\mathcal{A}} \frac{2\pi}{m_r} \sum_{\mathbf{q}} \frac{e^{-\beta\epsilon_{\mathbf{q}}}}{\ln(\varepsilon_T/\epsilon_{r\mathbf{q}_r}) + i\pi} \\ &\simeq \frac{z(m/m_r)T}{\pi^2 + \ln^2(e^{\gamma_E}\beta\varepsilon_T)} [\ln(e^{\gamma_E}\beta\varepsilon_T) - i\pi] , \end{aligned} \quad (3.37)$$

where  $\gamma_E \simeq 0.5772$  is the Euler-Mascheroni constant. Here, we have evaluated the integral by noting that the integral is dominated by  $\epsilon_{\mathbf{q}} \sim 1/\beta$  for small  $\beta\varepsilon_T$ , and the inclusion of  $\gamma_E$  originates from expanding the integral to the first subleading order in  $\beta\varepsilon_T$ .

The self-energies in Eqs. (3.36) and (3.37) can now be directly inserted into the Dyson equation (3.10) to yield the absorption in Eq. (3.14) or the photoluminescence in Eq. (3.19). To be explicit, within the virial expansion we have the exciton spectral function

$$A_X(\omega) = -\frac{1}{\pi} \text{Im} \left[ \frac{\Theta(-\omega - \varepsilon_T)}{\omega - \Sigma_A(\omega)} + \frac{1}{\omega - \Sigma_R(0)} \right]. \quad (3.38)$$

This yields a broad continuum for the attractive branch, where the spectral weight vanishes at  $\omega + \varepsilon_T \rightarrow 0^-$ , and when we are far below this onset, we have  $\Sigma_A(\omega)/\omega \rightarrow 0$ . Therefore we have an exponential tail modulated by the trion wave function:

$$A_X(\omega) \underset{\omega \rightarrow -\infty}{\simeq} z e^{\beta(\omega + \varepsilon_T) \frac{m_T}{m_X}} \left| \tilde{\eta}_{\sqrt{2m_r|\omega + \varepsilon_T|}}^{(0)} \right|^2. \quad (3.39)$$

The peak of the absorption is between the onset and the tail, and therefore it will not correspond to the vacuum trion energy. This can lead to an overestimate of the trion binding energy in experiments [349]. From Eq. (3.37), we find that the repulsive branch is a Lorentzian of width  $\Gamma_R = \pi(m/m_r)E_F/[\pi^2 + \ln^2(e^{\gamma_E}\beta\varepsilon_T)]$ . We have compared in Fig. 3.6(c) this expression against the numerical evaluation of the repulsive branch half linewidth  $\Gamma_R - \eta_X$  (where we have removed the effect of the intrinsic exciton lifetime), finding excellent agreement at low doping, inside the region of validity of the virial expansion.

For the photoluminescence, we find

$$P_X(\omega) \simeq -\frac{Z_0}{Z_{int}} \frac{1}{\pi} \text{Im} \left[ \frac{\Theta(-\omega - \varepsilon_T) e^{-\beta\omega}}{\omega - \Sigma_A(\omega)} + \frac{1}{\omega - \Sigma_R(0)} \right], \quad (3.40)$$

where we have used the fact that the width of the repulsive branch is much smaller than the temperature, and thus the repulsive branch is very weakly modified by the Boltzmann factor.

Equation (3.40) is a key result of this work. We see that the repulsive branch is a Lorentzian peak at  $\omega = \text{Re} \Sigma_R(0)$ , where both the width and position scale with  $E_F$ , similar to Fermi polaron theories [261, 380, 384]. However, for the attractive branch, we find that we cannot satisfy the condition  $\omega = \text{Re} \Sigma_A(\omega)$ , indicating that there is no attractive polaron quasiparticle in the limit  $z \ll 1$ , unlike for the quantum degenerate case  $z > 1$  — see Sec. 3.3.1. Instead, we have an asymmetric continuum of trion states, with a sharp onset at  $\omega = -\varepsilon_T$  and an exponential tail involving trions and recoil electrons at finite relative momentum, where

$$P_X(\omega) \propto e^{\beta\omega m/m_x} / \omega^2 \quad (3.41)$$

for  $-\omega \gg \varepsilon_T$  in agreement with Ref. [284]. Moreover, in the limit of an infinitely heavy exciton, we see that the tail in PL loses its exponential dependence, becoming a power law, unlike in the case of absorption. The shape of the onset is dictated by 2D resonant electron-exciton scattering at the trion energy, leading to a universal logarithmic divergence in the self-energy:

$$\Sigma_A(\omega \lesssim -\varepsilon_T) \simeq -z\varepsilon_T \left(\frac{m_T}{m_x}\right)^2 \left[ \ln \left( -e^{\gamma_E} \beta \frac{m_T}{m_x} (\omega + \varepsilon_T) \right) + i\pi \right]. \quad (3.42)$$

Previous trion theories of PL [284, 318, 349] focussed on the imaginary part of the self-energy, as we show below, and thus appear to have missed this divergence in the real part.

### 3.3.3 Comparison with experiments

Recently, the PL originating from a MoSe<sub>2</sub> monolayer was measured for the case of a hole doping (per valley) of  $n_h \simeq 0.5 \times 10^{11} \text{ cm}^{-2}$  and for lattice temperatures  $T = 5\text{--}50\text{K}$  [349], corresponding to fugacities in the range  $z \simeq 1\text{--}0.1$ . Therefore, apart from the very lowest temperatures explored, the experiment was well within the regime of validity of the virial expansion. To compare our spectra calculated using Eq. (3.40), we apply a Lorentzian broadening of 1 meV, matching the experimental linewidth [349]. We start by analyzing the distance between the peaks of the attractive and repulsive branches which, primarily due to the non-trivial shape of the attractive branch, does not correspond to  $\varepsilon_T$  even at very low doping. Fig. 3.7 (a) shows our theoretical result for two values

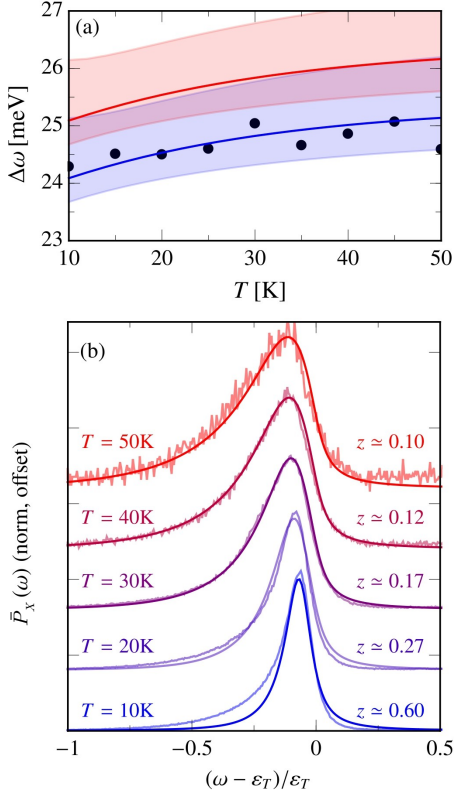


**Fig. 3.7:** (a) Frequency difference between attractive and repulsive peaks as a function of temperature. The black dots are the experimental peak positions of Ref. [349]. The blue and red shaded regions correspond to the results of the virial expansion using binding energies  $\varepsilon_T = 22.5$  meV and  $23.5$  meV. The solid lines correspond to the experimental hole density  $n_h = 0.5 \times 10^{11}$  cm $^{-2}$ , and the lower and upper bounds of each shaded region to densities of  $0.25 \times 10^{11}$  cm $^{-2}$  and  $10^{11}$  cm $^{-2}$ . (b) Comparison between theoretical (dark) and experimental [349] (light) PL spectra for the attractive branch at different lattice temperatures. The theoretical spectra were obtained by convolving Eq. (3.40) with a Lorentzian of width 1 meV [349] and using  $\varepsilon_T = 22.5$  meV,  $n_h = 0.5 \times 10^{11}$  cm $^{-2}$ , and  $m_X = 1.15m_0$  and  $m = 0.59m_0$ . The experimental PL has been shifted horizontally to match the peaks of the virial expansion.

of the trion binding energy,  $\varepsilon_T = 22.5$  meV and  $23.5$  meV, and for a range of densities. Even though this is noticeably below the quoted experimental value of  $25$  meV [321, 349], we see that the virial expansion correctly reproduces the splitting between the peaks when we take  $\varepsilon_T = 22.5$  meV. Thus, the fact that the attractive branch peak in PL does not correspond to the onset implies that the trion binding energy is likely to have been overestimated by as much as 10% in previous works<sup>3</sup>. We expect corrections to this result to be at most comparable to the Fermi energy [357] which for this experiment is  $0.4$  meV.

Fig. 3.7 (b) shows the comparison of our results for the attractive branch PL with experiments, using the extracted  $\varepsilon_T$ . We see that the agreement is essentially perfect at high temperature, with small discrepancies at lower temperatures. Since our theory is fully analytic and contains no free parameters, this is a remarkable agreement. The remaining discrepancy could potentially be due to the temperature of the system being different from that of the crystal

<sup>3</sup> This is also consistent with Ref. [437] which has shown that the extracted trion binding energy is sensitive to the shape of the trion peak.

lattice at low  $T$ .

### 3.3.4 Connection to the trion theory of electron recoil

Finally, we discuss how our theory relates to the calculation of electron recoil in previous trion-picture calculations such as in Refs. [284, 318]. As we shall demonstrate, that theory corresponds to a weak-interaction limit of the low doping/high-temperature version of our polaron theory. To see this, we take the limit of a small self-energy in the Dyson equation in Eq. (3.10) as follows:

$$G_X(\omega) \simeq \frac{1}{\omega} + \frac{1}{\omega^2} \Sigma_X(\omega). \quad (3.43)$$

Since the  $1/\omega$  terms only have a pole at  $\omega = 0$  (i.e., at the bare exciton energy), the attractive branch is obtained from the imaginary part of the self-energy. The detailed balance equation (3.19) then implies that the corresponding PL from the attractive branch is

$$\begin{aligned} P_A(\omega) &\simeq -\frac{1}{\pi} \frac{Z_0}{Z_{int}} \frac{e^{-\beta\omega}}{\omega^2} \text{Im} \Sigma_A(\omega) \\ &\simeq \frac{Z_0}{Z_{int}} \frac{z}{\mathcal{A}} \sum_{\mathbf{q}} e^{-\beta(\omega+\epsilon_{\mathbf{q}})} |\tilde{\eta}_{\mathbf{q}_r}^{(0)}|^2 \delta(\omega + \epsilon_{r\mathbf{q}_r} + \epsilon_T) \\ &\simeq \frac{Z_0}{Z_{int}} z e^{\frac{\beta(m\omega+m_T\epsilon_T)}{m_X}} \left| \tilde{\eta}_{\sqrt{2m_r|\omega+\epsilon_T|}}^{(0)} \right|^2 \Theta(-\omega - \epsilon_T), \end{aligned} \quad (3.44)$$

where we used Eq. (3.36). Up to frequency-independent prefactors, this precisely matches the result of Refs. [284, 318]. Thus, the trion-picture PL is already contained within the polaron picture. However, as we have already argued, the trion picture calculation assumes that we are in a weakly interacting limit where the self-energy is much smaller than the frequency. This assumption manifestly breaks down close to the onset of the attractive branch, where the real part of the self-energy diverges, and hence the previous trion picture calculation fails to correctly describe the onset and shape of the attractive branch. On the other hand, it correctly identifies the exponential tail of the PL, which is dominated by the imaginary part of the self-energy.

For the repulsive branch, the trion picture again uses the weak-interaction limit of the Dyson equation (3.43), this time neglecting even the second term on the right-hand side. This results in

$$P_R(\omega) \simeq \frac{Z_0}{Z_{int}} \delta(\omega), \quad (3.45)$$

with a small correction that counteracts the oscillator strength transferred to the attractive branch [318]. We see that the trion picture fails to describe

the Lorentzian shape of the repulsive polaron, which arises from the exciton-electron scattering states as well as the full Dyson series.

### 3.4 Strong light-matter coupling

As done in Sec. 2.3.6, to describe the light-matter coupled system, we add two terms describing cavity photons and the photon-exciton interaction to the Hamiltonian (3.1):

$$\hat{H} = \hat{H}_0 + \hat{H}_{0X} + \hat{H}_{0C} + \hat{H}_{int} + \hat{H}_{XC} \quad (3.46a)$$

$$\hat{H}_{0C} = \sum_{\mathbf{k}} \epsilon_{C\mathbf{k}} \hat{a}_{\mathbf{k}}^\dagger \hat{a}_{\mathbf{k}} \quad (3.46b)$$

$$\hat{H}_{XC} = \frac{\Omega}{2} \sum_{\mathbf{k}} (\hat{x}_{\mathbf{k}}^\dagger \hat{a}_{\mathbf{k}} + \text{H.c.}) . \quad (3.46c)$$

Photons are described by the bosonic creation operator  $\hat{a}_{\mathbf{k}}^\dagger$  with dispersion  $\epsilon_{C\mathbf{k}} = \delta + \mathbf{k}^2/2m_C$  (1.31), where  $\delta$  is the photon-exciton energy detuning (1.38). In order to derive the photon Green's function and the optical absorption in the strong coupling regime, one can follow the same procedure employed in Sec. 1.5.3. The difference is that now we formulate a variational ansatz for the time-dependent photon operator, with an analogous form to (3.4):

$$\hat{a}_{\mathbf{0}}(t) \simeq \alpha_0(t) \hat{a}_{\mathbf{0}} + \frac{1}{\mathcal{A}} \sum_{\mathbf{k}, \mathbf{q}} \varphi_{\mathbf{kq}}(t) \hat{c}_{\mathbf{q}}^\dagger \hat{c}_{\mathbf{k}} \hat{x}_{\mathbf{q}-\mathbf{k}} + \varphi_0(t) \hat{x}_{\mathbf{0}} . \quad (3.47)$$

We neglect the dressing of the photon operator by a particle-hole excitation  $\frac{1}{\mathcal{A}} \sum_{\mathbf{k}, \mathbf{q}} \alpha_{\mathbf{kq}}(t) \hat{c}_{\mathbf{q}}^\dagger \hat{c}_{\mathbf{k}} \hat{a}_{\mathbf{q}-\mathbf{k}}$ . This term involves photon recoil and therefore implies energies far off-resonance from the exciton and trion energies because of the extremely small mass of the photon.

To obtain the eigenvalue problem for the light-matter coupled system, we introduce the error operator corresponding to the photon  $\hat{e}(t) = i\partial_t \hat{a}_{\mathbf{0}}(t) - [\hat{a}_{\mathbf{0}}(t), \hat{H}]$  and minimize the error function, Eq. (3.5), with respect to the variational coefficients  $\alpha_0^*(t)$ ,  $\varphi_{\mathbf{kq}}^*(t)$ , and  $\varphi_0^*(t)$ . Considering the stationary solutions, we find

$$E\varphi_0 = \frac{\Omega}{2} \alpha_0 - \frac{v}{\mathcal{A}^2} \sum_{\mathbf{k}, \mathbf{q}} f_{\mathbf{q}} (1 - f_{\mathbf{k}}) \varphi_{\mathbf{kq}} \quad (3.48a)$$

$$E\varphi_{\mathbf{kq}} = E_{X\mathbf{kq}} \varphi_{\mathbf{kq}} - v\varphi_0 - \frac{v}{\mathcal{A}} \sum_{\mathbf{k}'} (1 - f_{\mathbf{k}'}) \varphi_{\mathbf{k}'\mathbf{q}} \quad (3.48b)$$

$$E\alpha_0 = \delta\alpha_0 + \frac{\Omega}{2} \varphi_0 , \quad (3.48c)$$

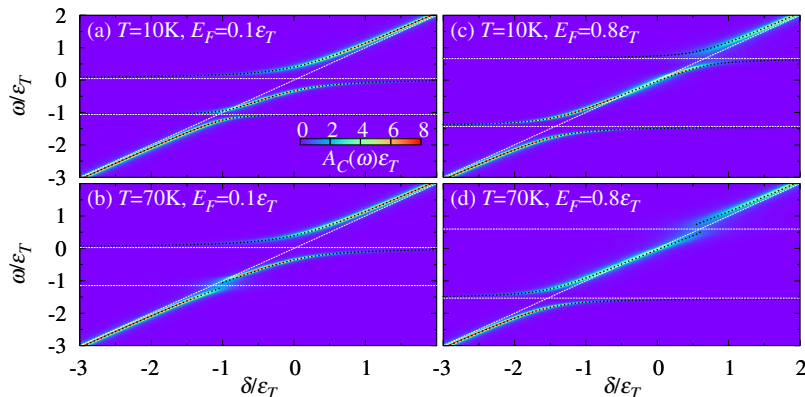


**Fig. 3.8:** Energy and detuning dependence of the photon spectral function  $A_C(\omega)$  in the light-matter strongly coupled system describing a TMD monolayer with an electron doping  $E_F = 0.1\epsilon_T$  (panel (a) and (b)) or  $E_F = 0.8\epsilon_T$  (panel (c) and (d)), embedded in a microcavity at a finite temperature  $T = 10K \simeq 0.034\epsilon_T$  (panel (a) and (c)) and  $T = 70K \simeq 0.24\epsilon_T$  (panel (b) and (d)). The black dots are the LP, MP, and UP branches extracted from the three-coupled oscillator model (see text). The Rabi splitting is  $\Omega = 20\text{meV} \simeq 0.8\epsilon_T$ . Here, we have used a broadening of  $\eta_C = 1\text{meV} \simeq 0.04\epsilon_T$  for the photon and  $\bar{\eta}_X = 0.2\eta_C$  for the matter component.

where we have again neglected terms that vanish in the limit  $\Lambda \rightarrow \infty$ . These equations reduce to those for the exciton polaron, Eq. (3.6), when we take  $\Omega = 0$  and  $\alpha_0 = 0$ .

We plot in Fig. 3.8 the finite-temperature photon spectral function at normal incidence as a function of energy and detuning  $\delta$ . When  $T \ll E_F \lesssim \Omega$ , the strong coupling to light leads to three polariton branches, LP, MP, and UP, as can be seen in Fig. 3.8 (a,c). Remarkably, we find that a strong enough light-matter coupling can produce well-defined polariton quasiparticles (where  $\text{Re}\tilde{G}_C^{-1}(\omega) = 0$ ) for the lower and middle branches even when there is no attractive polaron quasiparticle and Eq. (3.26) is not satisfied. However, once the linewidths  $2\Gamma_{A,R}$  approach  $\Omega_{A,R}$ , the energy splitting between branches closes, indicating a loss of strong coupling. We observe this in the low-doping regime for LP and MP (Fig. 3.8 (b)), and in the high-doping regime for MP and UP (Fig. 3.8 (c,d)). Within the three-coupled oscillator model (2.55b), this transition from weak to strong light-matter coupling approximately occurs when  $2\Gamma_{A,R} \gtrsim \Omega_{A,R}$ , as expected, though there are small deviations when the attractive branch is no longer a well-defined polaron quasiparticle. The effect of temperature on this transition can be easily accounted for by considering its effect on the quasiparticle linewidths and spectral weights.

The results shown in Fig. 3.9 illustrate that, when the photon is at resonance with the repulsive branch (Fig. 3.9 (a)), the increase of the repulsive branch

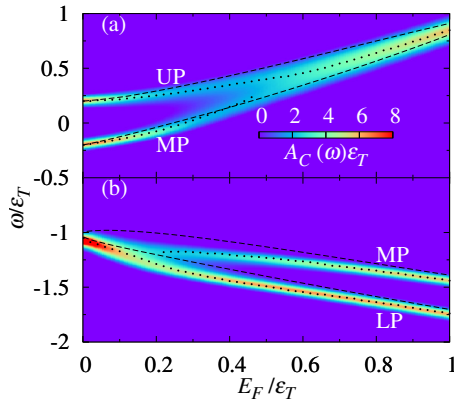


**Fig. 3.9:** Doping dependence of the photon spectral function  $A_C(\omega)$  at  $T = 50\text{K} \simeq 0.17\epsilon_T$  for a photon in resonance with either the repulsive branch  $E_R$  (a) or the attractive branch  $E_A$  (b). The black dashed lines are the polariton branches obtained with a three-coupled oscillator model at  $T = 0$  (see Fig. 2.12), while the black dotted lines at  $T = 50\text{K} \simeq 0.17\epsilon_T$ . The Rabi splitting is  $\Omega = 10\text{meV} \sim 0.4\epsilon_T$ . Here,  $\eta_C = 1\text{meV} \simeq 0.04\epsilon_T$  and  $\bar{\eta}_X = 0.2\eta_C$ .

linewidth with temperature leads to a faster closing between the UP and MP spitting with doping. On the contrary, when instead the photon is at resonance with the attractive branch (Fig. 3.9(a)), at finite temperature, the increase of doping sharpens the attractive branch absorption line towards a regime where the linewidth recovers the value of  $\bar{\eta}_X$ . Because of this, while at low doping the system can be in the weak coupling regime if the temperature is large enough and  $\Omega$  small enough, increasing the doping always leads to a finite splitting between the LP and MP.

### 3.5 Conclusions and perspectives

In this chapter, we have studied the optical properties of a doped two-dimensional semiconductor at a finite temperature using a Fermi-polaron approach involving a single excitation of the fermionic medium. Our results reveal that the attractive branch can experience a smooth transition from a regime where it is a well-defined quasiparticle to a regime where it is subsumed into a broad continuum of trion-hole scattering states. This crossover results in a strong change in the spectral lineshape and can be driven by either decreasing doping or increasing temperature, but it cannot occur at zero temperature. While the Fermi polaron theory is able to capture both limits, theories based on the trion wave function necessarily only apply in the limit where there is no well-defined quasiparticle. In particular, we formally show that the trion theory corresponds to a weak-interaction limit of our finite-temperature Fermi polaron theory.

In the high-temperature and low-density limit, we have applied a controlled virial expansion, which we show corresponds to a thermally incoherent limit of Fermi-polaron theory where the attractive polaron quasiparticle no longer exists. Our theory has the advantage of being fully analytic, and it yields

excellent agreement with experiments without the need for fitting parameters. Our approach is very generic and can potentially be applied to a broad range of systems, for instance emerging designer materials such as moiré superlattices where signatures of polaron physics have already been observed [454–456].

In the regime of strong light-matter coupling, we have shown how the temperature can modify the properties of the Fermi polaron-polaritons. We demonstrate that the strong-to-weak coupling crossover observed at finite temperature for the attractive branch at low enough doping and the repulsive branch in the high doping regime can be explained in terms of the linewidths and spectral weights of the two branches.

In future studies, it would be interesting to investigate how the quasiparticle transition of the attractive branch, driven by either temperature or doping, would affect the interactions between exciton impurities. In particular, common descriptions of polaron-polaron interactions use Landau’s theory of dilute solutions [457], which assumes well-defined quasiparticles. Such interactions could, for instance, be measured using coherent multidimensional spectroscopy on gated 2D materials, similar to recent experiments on intrinsically doped samples [458].

## Chapter 4

# Indistinguishable carrier polarons

*This chapter investigates the optical absorption spectrum of doped 2D semiconductors in the spin-valley polarized limit when the Fermi sea consists of carriers that are indistinguishable from those forming the exciton. This results in a three-body trion state with  $p$ -wave symmetry. To understand the implications of this, we use a polaron description to evaluate the system's optical properties across a range of densities. Our findings are compared to the scenario where the Fermi sea includes distinguishable carriers, resulting in an  $s$ -wave trion ground state. The results discussed in this chapter have been published in the following publication:*

- [356] A. TIENE, J. LEVINSEN, J. KEELING, M. M. PARISH and F. M. MARCHETTI:  
Effect of fermion indistinguishability on optical absorption of doped two-dimensional semiconductors,  
[Phys. Rev. B 105, 125404 \(2022\)](#).

## 4.1 Spin-valley polarized limit

In Chs. 2 and 3, we investigated how the optical spectrum of a doped semiconductor evolves when doping increases in the specific case where the optically excited exciton is dressed by the excitations of a distinguishable fermionic medium. We refer to this scenario as the *distinguishable carrier polaron* (DCP). In this chapter, we aim to study the opposite case, where the free carriers are indistinguishable from one of the carriers forming the exciton. We will refer to this scenario as the *indistinguishable carrier polaron* (ICP). In order to realize experimentally this limit it is necessary to reach a spin-valley fully polarized limit. Indeed, as discussed in Sec. 1.3, the two valley conduction and valence bands of TMD monolayers are energetically degenerate, thus leading to the

formation of two distinct Fermi seas when the material is doped — see Sec. 2.1. As discussed in Sec. 2.3.2, for Mo-based monolayers (and W-based monolayers at low doping), the experimental results [220, 321] can be interpreted in terms of the exciton dressing by a distinguishable Fermi sea, even if multiple Fermi seas are generated. For this reason, the DCP scenario has so far received most of the attention from theoretical studies [261, 264, 265, 321].

The valley energy degeneracy can be lifted by applying a small magnetic field, via the Zeeman effect. For TMD monolayers, there are three contributions to the Zeeman shift in [459–462]. One contribution comes from the spin magnetic moment, shifting the bands by a quantity  $\Delta_s = 2s_z\mu_B B$ , where  $\mu_B = e/2m_0$  is the Bohr magneton and  $s_z$  the spin component of the band. Note that, while this effect contributes to lifting the valley degeneracy, it does not affect the excitonic optical resonance since optical excitation preserves spin, and so the effect on the initial and final state is the same. On the other hand, the atomic orbital moment affects differently the valence and conduction bands. In particular, the orbital composition of the conduction band is mainly from  $d$ -orbitals with  $m = 0$  and differs from the composition of the edges of the valence bands, which are mainly composed by  $d$ -orbital with  $m = 2$  ( $m = -2$ ) for the K ( $K'$ ) valley. Thus, only the valence bands are shifted, by a quantity  $\Delta_m = m\tau\mu_B B$ , where  $\tau$  is the valley index,  $\tau = 1$  for K and  $\tau = -1$  for  $K'$ . Finally, the Zeeman shift due to the valley magnetic moment shifts the entire valley. This shift is given by  $\Delta_v = g_i\tau\mu_B B$ , where  $g_i = m_0/m_i$  is the valley  $g$ -factor for band  $i$  ( $i = c, v$ ). Taking this into account, the global effect of Zeeman splitting on the exciton resonance is

$$\Delta_X(B) = -\tau(2 - \Delta_g)\mu_B B, \quad (4.1)$$

where  $\Delta_g = g_c - g_v$ . In the limit of identical electron and hole effective masses  $\Delta_g = 0$  and thus, the total Zeeman shift between the K and  $K'$  exciton depends only on the orbital magnetic moment and increases linearly with the magnetic field at a rate approximately of  $-4\mu_B \approx -230\mu\text{eVT}^{-1}$  [459–463], i.e., typical effective  $g$ -factor is  $g \sim -4$ . This result is in agreement with both *ab initio* calculations and experimental findings — see Ref. [464] and references therein, which obtained a  $g$ -factor ranging between  $-3$  and  $-3.5$  in Mo- and W-based TMD monolayers.

Further, there are other effects induced by a perpendicular magnetic field that affect the optical response of a doped TMD monolayer. The presence of a magnetic field generates the quenching of the kinetic energy spectrum of electrons and holes to a set of degenerate Landau levels [465], separated by the Landau quantization energy  $\omega_B = eB/mc$  [322, 466], known as Larmor frequency. Owing to heavy effective carrier masses and reduced screening, the Larmor frequency in a TMD monolayer is much smaller than the binding ener-

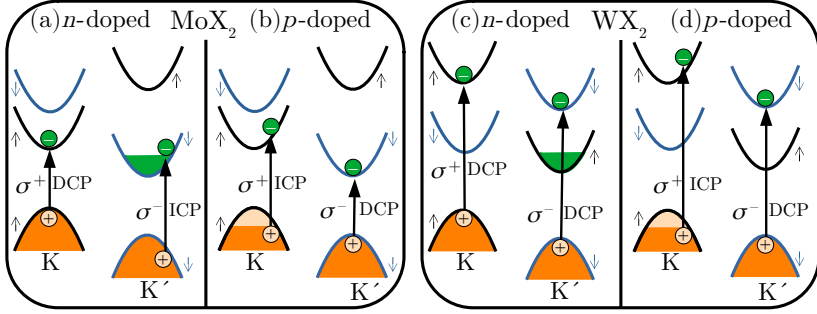


**Fig. 4.1:** Schematic representation of the band structure of doped  $\text{MoX}_2$  and  $\text{WX}_2$  monolayers in the presence of Zeeman splitting induced by a perpendicular magnetic field. The DCP and ICP configurations can be realized thanks to the optical selection rules. Note that while  $\text{MoX}_2$  monolayers allow DCP and ICP on both the  $n$ -doped and  $p$ -doped sides, for  $\text{WX}_2$  monolayers, ICP can only be realized with  $p$ -doping.

gies of the exciton even at high magnetic fields up to  $B \sim 10$  T [220]. In this regime, the magnetic field is too weak to alter the structure of excitons [322], and as such it only influences the free charges in the system. Still, the interplay between Coulomb interaction and magnetic field can influence the excitonic resonance inducing a diamagnetic shift, which is anticipated to increase quadratically with field  $\Delta E_{dia} = e^2 \langle r_{1s}^2 \rangle B^2 / 8\mu$  [463, 467], where  $\langle r_{1s}^2 \rangle$  is the mean squared radius of the  $1s$  exciton. The large reduced mass and small exciton radius in the TMD monolayer results in a small diamagnetic shift coefficient of about  $\sigma \approx 0.32 \mu\text{eV}\text{T}^{-2}$  [463], compared with the previously reported  $g$ -factor  $g = -4\mu_B \approx -230\mu\text{eV}\text{T}^{-1}$ . As such, in TMD monolayers, for moderate values of the magnetic field  $\omega_B \lesssim \varepsilon_T$ , the most relevant magnetic effect on the exciton resonance is the Zeeman splitting of the conduction and valence bands, while the Landau quantization of the electronic states mainly influences the excess charge. Lifting valley degeneracy enables to control of the valley polarization and allows for the unequivocal realization of either the ICP or DCP scenario described at the beginning of this section. At sufficiently small doping, it is possible to accommodate the excess charge entirely in the lowest conduction band, as illustrated in Fig. 4.1. Because of the optical selection rules, we can selectively create an exciton in one of the two valleys to reproduce either the ICP or DCP scenario — see Fig. 4.1. While both the DCP and ICP configurations can be achieved by  $n$ - and  $p$ -doping Mo-based TMD monolayers, in W-based monolayers, the ICP configuration is only possible on the  $p$ -doped side. Full spin valley polarisation has been achieved in both  $\text{WSe}_2$  [461, 462] and  $\text{MoSe}_2$  [459, 460] experiments. Indeed, a high degree of valley polarization has been realized at modest magnetic fields, up to an electron density  $n_1 \approx 1.6 \times 10^{12} \text{ cm}^{-2}$  [468] (corresponding to a Fermi energy  $E_F \approx 15$  meV).

For III-V and II-VI compound quantum wells, the Zeeman splitting is smaller than the one in TMD monolayers, i.e., here  $g$ -factors for GaAs quantum well are in the range  $g \in [-0.44 : 0.4]$  [469] — different values depend mostly on the quantum well width. Further, smaller carrier effective masses and a smaller exciton binding energy with respect to TMD monolayers result in a Larmor frequency that can be larger than the exciton binding energy even for small values of the magnetic field. In this regime, the excitonic spectra are dominated by Landau level-associated peaks [470]. In the opposite limit, when  $w_B < \varepsilon_X$ , large values of the exciton radius imply a large diamagnetic shift of the excitonic resonance [470] compared with the small Zeeman splitting. This means that it is difficult to achieve a spin-polarized regime without introducing other relevant orbital effects. Note that, in the strong magnetic field limit when the distance between Landau levels becomes large, all particles in the trion complex are confined to their lowest Landau levels and have their spins aligned with the magnetic field [276].

## 4.2 Model

We seek to model the spectral response of a doped semiconductor, where one of the two charges forming the exciton is identical to those forming the Fermi sea. As such, we write the following Hamiltonian, describing only two species of charges, each belonging to a single (spin-valley polarized) conduction and valence band :

$$\hat{H} = \hat{H}_0 + \hat{H}_{eh} + \hat{H}_{ehC} \quad (4.2a)$$

$$\hat{H}_0 = \sum_{\mathbf{k}\sigma} \epsilon_{\sigma\mathbf{k}} \hat{c}_{\sigma\mathbf{k}}^\dagger \hat{c}_{\sigma\mathbf{k}} + \sum_{\mathbf{k}} \epsilon_{C\mathbf{k}} \hat{a}_{\mathbf{k}}^\dagger \hat{a}_{\mathbf{k}} \quad (4.2b)$$

$$\hat{H}_{eh} = -\frac{v}{\mathcal{A}} \sum_{\mathbf{k}\mathbf{k}'\mathbf{q}} \hat{c}_{1\mathbf{k}}^\dagger \hat{c}_{2\mathbf{k}'}^\dagger \hat{c}_{2\mathbf{k}'+\mathbf{q}} \hat{c}_{1\mathbf{k}-\mathbf{q}} \quad (4.2c)$$

$$\hat{H}_{ehC} = \frac{g}{\sqrt{\mathcal{A}}} \sum_{\mathbf{k}\mathbf{q}} \left( \hat{c}_{1\frac{\mathbf{q}}{2}+\mathbf{k}}^\dagger \hat{c}_{2\frac{\mathbf{q}}{2}-\mathbf{k}}^\dagger \hat{a}_{\mathbf{q}} + \text{h.c.} \right) . \quad (4.2d)$$

Here,  $\hat{c}_{\sigma=1,2\mathbf{k}}$  and  $\hat{c}_{\sigma=1,2\mathbf{k}}^\dagger$  are the majority ( $\sigma = 1$ ) and minority ( $\sigma = 2$ ) species annihilation and creation operators, respectively. These have a dispersion  $\epsilon_{\sigma\mathbf{k}} = \mathbf{k}^2/2m_\sigma$  (1.1), where  $m_\sigma$  is the effective mass and  $\mathbf{k}$  is the 2D momentum. Note that, throughout this chapter, energies are measured with respect to the band-gap energy. We denote the density of the majority species as  $n_1$  and thus the Fermi energy is (2.1),

$$E_F = \frac{k_F^2}{2m_1} = \frac{2\pi}{m_1} n_1 , \quad (4.3)$$

where  $k_F$  is the Fermi momentum. For electron doping,  $\sigma = 1$  are conduction electrons and  $\sigma = 2$  are valence holes. For hole doping,  $\sigma = 1$  are valence holes and  $\sigma = 2$  are conduction electrons. The only distinction between these two cases is the assignment of masses  $m_{1,2}$ , so we can swap between the two by interchanging  $m_1 \leftrightarrow m_2$ .

In order to considerably simplify our calculations, in  $\hat{H}_{eh}$  (4.2c) we approximate the electron-hole Coulomb interaction as a contact interaction of strength  $v > 0$ . This limit describes the case where interactions between charges are strongly screened. In such a case, intraspecies interactions vanish since the relative wave function between identical fermions must have a node at zero separation. One may wonder whether the use of contact interactions — in place of Coulomb (1.22b), or screened Coulomb (1.29) interactions — significantly changes when a  $p$ -wave trion state exists. However, as we show in Sec. 4.3, in the zero-density limit, our model predicts nearly the same critical mass ratio for trion formation [374, 471] as found for the Coulomb problem [271, 272]. As such, we expect that the use of contact interactions will allow us to faithfully capture the qualitative features of the ICP scenario. Because our model does not include same species interactions, we are neglecting band-gap renormalization effects induced by doping [240–243]. However, our predictions for the energy difference between repulsive and attractive branches are accurate [265].

The operators  $\hat{a}_{\mathbf{k}}$  and  $\hat{a}_{\mathbf{k}}^\dagger$  describe the cavity photon mode with a dispersion  $\epsilon_{C\mathbf{k}} = \epsilon_{C0} + \mathbf{k}^2/2m_C$  (1.31), where  $m_C$  is the photon mass (1.32) and  $\mathbf{k}$  is the in-plane momentum. These photons couple to the matter excitations via the term  $\hat{H}_{ehC}$  in Eq. (4.2d). We have taken the strength  $g$  of the coupling to be independent of momentum and applied the rotating wave approximation. These approximations are appropriate when the band-gap energy greatly exceeds the other energy scales in the problem.

### 4.2.1 Renormalization of contact interactions

The use of contact interactions and momentum-independent light-matter coupling introduces UV divergences — see, e.g., Ref [371]. These can be regularized by introducing a UV cutoff  $\Lambda$ , i.e., assuming that  $v$  and  $g$  are non-zero only up to a momentum  $\Lambda$ , which is typically set by the electronic band structure. As already discussed in Sec. 1.5.2 and Sec. 2.3.2, results independent of the short-distance physics can be obtained by then renormalizing both coupling strengths  $v$  and  $g$  so that observable quantities do not depend on the cutoff, as also shown in recent calculations employing this same model to study polariton-electron scattering [472, 473].

The electron-hole interaction strength  $v$  can be renormalized by relating it

to the physically measurable exciton binding energy,  $\varepsilon_X > 0$ , via [429]:

$$\frac{1}{v} = \frac{1}{\mathcal{A}} \sum_{\mathbf{k}}^{\Lambda} \frac{1}{\varepsilon_X + \bar{\epsilon}_{\mathbf{k}}}, \quad (4.4)$$

where  $\bar{\epsilon}_{\mathbf{k}} = \epsilon_{1\mathbf{k}} + \epsilon_{2\mathbf{k}} = \mathbf{k}^2/2\mu$ , with  $\mu = (1/m_1 + 1/m_2)^{-1}$  being the reduced mass. When  $\Lambda \rightarrow \infty$ ,  $v^{-1} \sim \ln \Lambda \rightarrow \infty$  and thus  $v \rightarrow 0$ . Note that the right-hand side of Eq. (4.4) is related to the normalized  $1s$  exciton wave function at zero electron-hole separation (evaluated in the absence of coupling to light), since in momentum space this wave function is given by

$$\Phi_{\mathbf{k}}^{1s} = \sqrt{\frac{2\pi\varepsilon_X}{\mu}} \frac{1}{\varepsilon_X + \bar{\epsilon}_{\mathbf{k}}}. \quad (4.5)$$

The light-matter coupling strength  $g$  can be renormalized by considering the single-polariton problem at zero doping and matching the eigenvalues of the microscopic problem to the experimental observables — see Sec. 1.5.2. Experiments typically fit the LP and UP polaritons to a coupled oscillator model (1.34) (describing a tightly bound exciton and a photon):

$$\hat{H} = \begin{pmatrix} -\varepsilon_X + \delta & \Omega/2 \\ \Omega/2 & -\varepsilon_X \end{pmatrix} \quad (4.6a)$$

$$\epsilon_{LP,UP} = -\varepsilon_X + \frac{\delta \mp \sqrt{\delta^2 + \Omega^2}}{2}. \quad (4.6b)$$

Here,  $\delta = \epsilon_{C0} + \varepsilon_X$  is the photon-exciton detuning and  $\Omega$  the Rabi splitting (1.35). As such, the procedure we follow is to write the finite (renormalized) Rabi splitting  $\Omega$  in terms of the bare coupling  $g$  and the relative  $1s$  exciton wave function at zero electron-hole separation, which describes the amplitude for electron and hole to overlap (see [472] or Sec. 1.5.2 for details):

$$\Omega = \frac{2g}{\mathcal{A}} \sum_{\mathbf{k}}^{\Lambda} \Phi_{\mathbf{k}}^{1s} = \frac{2g}{v} \sqrt{\frac{2\pi\varepsilon_X}{\mu}}. \quad (4.7)$$

Because  $1/v$  diverges logarithmically with the cutoff,  $g \sim 1/\ln \Lambda \rightarrow 0$  when  $\Lambda \rightarrow \infty$ , in such a way that the physically meaningful parameter  $\Omega$  is finite.

We finally turn to the photon-exciton detuning  $\delta$ . Here, Ref. [473] found that to match the coupled-oscillator model, there is a shift from the bare detuning  $\epsilon_{C0} + \varepsilon_X$  associated with our Hamiltonian. Specifically, one has that

$$\delta = \epsilon_{C0} + \varepsilon_X - \frac{\Omega^2}{8\varepsilon_X}. \quad (4.8)$$

In summary, we take the finite (renormalized) energy scales in our problem

to be the exciton binding energy  $\varepsilon_X$ , and the zero doping Rabi splitting  $\Omega$ . Further, the other relevant parameters are the photon-exciton detuning  $\delta$ , the Fermi energy  $E_F$ , and the mass ratio  $m_2/m_1$ .

### 4.3 Distinguishable and indistinguishable trions

In this section, we demonstrate that when the trion contains two indistinguishable excess majority particles, i.e., two particles with identical spin and valley indices, the lowest energy is the one with one unit of angular momentum, i.e., it is a  $p$ -wave state. By contrast, for distinguishable particles, because there is not a particular symmetry property that the trion wave function has to satisfy, the ground state is free to choose the lowest energy solution and the wave function is  $s$ -wave.

In this section, we summarize the relevant results for the ICP trion. We start by considering the particular limit of large mass imbalance, where the problem can be solved analytically, thus providing insight into the nature of the trion state. We then present the numerically exact solution for a general mass ratio. We considered the simplified description where the electron-hole interaction is a contact interaction, and where the same species repulsion is neglected. While our model overestimates the trion binding energy, we show how it predicts correctly where the unbinding transition occurs. Our results are consistent with the behavior of the ICP in Sec. 4.4, where we find that the three-particle component of the polaron ground state always has  $p$ -wave orbital character in the low-doping limit.

#### 4.3.1 Limit of large mass imbalance

The Hamiltonian in Eq. (4.2) is rotationally symmetric, and consequently, the trion states have definite angular momentum. In the following, we consider both the case of distinguishable and indistinguishable fermions and identify the differences between these cases. To clearly illustrate the role played by exchange symmetry in determining the angular momentum, it is instructive to first consider the limit of a small minority over majority mass ratio,  $m_2/m_1 \ll 1$ , where we can use the Born-Oppenheimer approximation [269, 474]. This consists of assuming that the light particle at position  $\mathbf{r}$  adiabatically adjusts its wave function to the positions of the two heavy particles at  $\pm\mathbf{R}/2$ , as illustrated in Fig. 4.2 (a). Within this approximation, the total wave function takes the form of a product

$$\Psi(\boldsymbol{\rho}_1, \boldsymbol{\rho}_2) = \phi(\mathbf{R})\psi_{\mathbf{R}}(\mathbf{r}), \quad (4.9)$$

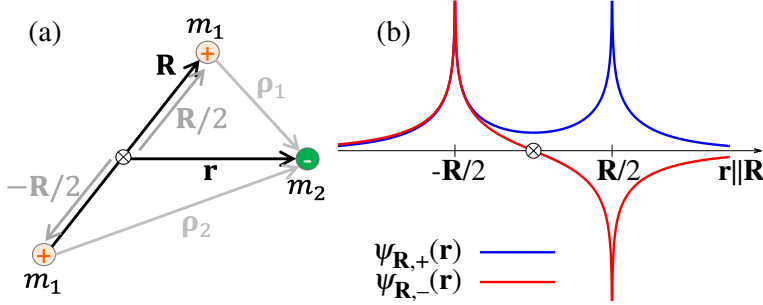


**Fig. 4.2:** Sketches for the Born-Oppenheimer approximation. (a) Coordinate definitions. The light minority particle (with mass  $m_2$ ) at  $\mathbf{r}$  adiabatically adjusts its motion to the heavy majority particles (with masses  $m_1$ ) at  $\pm\mathbf{R}/2$ . (b) Wave function of the light particle  $\psi_{\mathbf{R},\pm}(\mathbf{r})$ , Eq. (4.10) along the axis separating the heavy particles.

where  $\boldsymbol{\rho}_{1,2} = \mathbf{r} \mp \mathbf{R}/2$  are the relative positions of the light particle with respect to the heavy particles. Here,  $\Psi_{\mathbf{R}}(\mathbf{r})$  is the wave function of the light particle, and  $\phi(\mathbf{R})$  governs the motion of the heavy particles.

The wave function of the light particle is obtained by solving the Schrödinger equation for fixed positions of the heavy particles. This can be shown [475] to have a solution in terms of the modified Bessel function of the second kind,  $K_0(\kappa r)$ . Since the solution must be a parity eigenstate under  $\mathbf{R} \rightarrow -\mathbf{R}$ , there are two possibilities for  $\psi_{\mathbf{R}}(\mathbf{r})$  [475]

$$\psi_{\mathbf{R},\pm}(\mathbf{r}) = \mathcal{N}_{\pm}(R) [K_0(\kappa_{\pm}(R) |\mathbf{r} + \mathbf{R}/2|) \pm K_0(\kappa_{\pm}(R) |\mathbf{r} - \mathbf{R}/2|)], \quad (4.10)$$

where  $\mathcal{N}_{\pm}(R)$  is an overall normalization. These two wave functions are illustrated in Fig. 4.2 (b). As argued in Ref. [475], the momentum scale  $\kappa_{\pm}(R)$  associated with the motion of the light particle is obtained by solving the equation  $\ln(\kappa_{\pm} a_X) = \pm K_0(\kappa_{\pm} R)$  with  $a_X \equiv 1/\sqrt{2\mu\varepsilon_X^{-1}}$ .

Having solved for the motion of the light particle at a fixed separation of the heavy particles, one considers the motion of the heavy particles in the presence of the effective potential  $E_{\pm}(R) = -\kappa_{\pm}^2(R)/2\mu^2$  mediated by the light particle. Here, we should note that only  $E_+(R)$  corresponds to a potential energy surface below the exciton at  $-\varepsilon_X$  — see Fig. 4.3 (a), and hence only this wave function can lead to trion formation.

In the case of distinguishable heavy particles, there are no restrictions on the overall symmetry under the exchange of these particles, and so the symmetry

<sup>1</sup> This condition is obtained by applying the Bethe-Peierls boundary condition when the light particle approaches one of the heavy particles:  $\lim_{\tilde{r} \rightarrow 0} [\tilde{r}(\psi)_{\tilde{r}}^{\pm}/\psi] = 1/\ln(\tilde{r}e^{\gamma}/2a_{2D})$  with  $\tilde{\mathbf{r}} \equiv \mathbf{r} \pm \mathbf{R}/2$  [475], and  $\gamma \approx 0.577$  is the Euler gamma.

<sup>2</sup> Here we use the reduced mass rather than the light particle mass [476], and hence the energy surface corresponds to the energy of the relative motion of the light particle relative to one of the heavy particles.

of  $\psi_{\mathbf{R},+}(\mathbf{r})$  does not impose any restrictions on the symmetry of  $\phi(\mathbf{R})$ . As such, the ground state trion is the lowest energy solution, which is in the  $s$ -wave angular momentum channel. By contrast, if the two heavy particles are identical fermions, the overall wave function must be antisymmetric under  $\mathbf{R} \rightarrow -\mathbf{R}$ . Since the attractive potential corresponds to the function  $\psi_{\mathbf{R},+}(\mathbf{r})$  which is symmetric under exchange, and since the total wave function  $\Psi$  is antisymmetric,  $\phi(\mathbf{R})$  must then be antisymmetric under exchange. This, in turn, implies that  $\phi(\mathbf{R})$  has odd angular momentum, and therefore the ground state trion forms in the  $p$ -wave channel.

The effective potential

$$V_{\text{eff},\pm}^{(\ell)}(R) = E_{\pm}(R) + \frac{\ell^2}{m_1 R^2}, \quad (4.11)$$

including the centrifugal barrier for angular momentum  $\ell$  is illustrated in Fig. 4.3 (a) for  $\ell = 0, 1$  and the two symmetries  $\pm$ . We see that the bare mediated potential  $E_+(R) = V_{\text{eff},+}^{(\ell=0)}(R)$  (corresponding to the  $s$ -wave case) is purely attractive, while the  $p$ -wave potential  $V_{\text{eff},+}^{(\ell=1)}(R)$  has an attractive well when  $R \sim a_X$ , within which the trion forms, and a centrifugal barrier at small  $R$ . We also find that the attractive well and bound state only exist when the mass ratio  $m_2/m_1$  is sufficiently small. The form of the potential and in particular the short-range repulsion provided by the centrifugal barrier means that the critical mass ratio for trion binding is relatively insensitive to the precise form of the interaction potential between heavy particles.

In the limit of a large mass imbalance,  $m_2/m_1 \rightarrow 0$ , the trion energy  $E_{T_3}$  in the Born-Oppenheimer approximation takes the known form [475]:

$$\frac{|E_{T_3}| - \varepsilon_X}{\varepsilon_X} \simeq \frac{m_1}{m_2} \frac{2e^{-2\gamma}}{9}, \quad (4.12)$$

where  $\gamma \simeq 0.577$  is the Euler constant. We will now compare these results with an exact calculation within our model (4.2).

### 4.3.2 Trion binding energy

Having gained insight into the trion state at a large mass ratio, we next discuss the range of mass ratios for which this state is bound [374, 471]. We thus consider a trion state in a vacuum with zero center of mass momentum, which is described by the following state

$$|T_3\rangle = \frac{1}{\sqrt{2\mathcal{A}}} \sum_{\mathbf{k}_1 \neq \mathbf{k}_2} \gamma_{\mathbf{k}_1 \mathbf{k}_2} \hat{c}_{2-\mathbf{k}_1-\mathbf{k}_2}^\dagger \hat{c}_{1\mathbf{k}_1}^\dagger \hat{c}_{1\mathbf{k}_2}^\dagger |0\rangle, \quad (4.13)$$

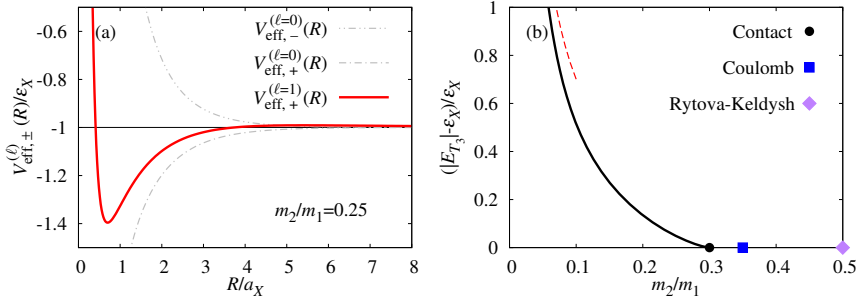


**Fig. 4.3:** (a) Effective potential  $V_{\text{eff},\pm}^{(\ell)}(R)$  (4.11) determining the motion of the majority heavy particle within the Born-Oppenheimer approximation for  $m_2/m_1 = 0.25$ . The solid (red) line is  $V_{\text{eff},+}^{(\ell=1)}(R)$  for the  $p$ -wave trion, while gray dot-dashed and dot-dot-dashed lines are the bare mediated potentials  $E_{\pm}(R) = V_{\text{eff},\pm}^{(\ell=0)}(R)$  respectively. (b) Lowest-energy  $p$ -wave trion binding energy (solid black line), evaluated by numerically solving the eigenvalue problem (4.14), as a function of the minority over majority mass ratio  $m_2/m_1$ . At a small mass ratio, the binding energy diverges according to Eq. (4.12) (dashed red line). Squared (blue) and rhombus (purple) symbols indicate the critical mass ratios obtained for bare Coulomb [271, 272] and Rytova-Keldysh effective interactions [268].

where we must obey  $\gamma_{\mathbf{k}_2\mathbf{k}_1} = -\gamma_{\mathbf{k}_1\mathbf{k}_2}$ . The trion wave function in momentum space  $\gamma_{\mathbf{k}_1\mathbf{k}_2}$  is the Fourier transform of the wave function in real space, Eq. (4.9),  $\gamma_{\mathbf{k}_1\mathbf{k}_2} = \int d\boldsymbol{\rho}_1 \int d\boldsymbol{\rho}_2 e^{i\mathbf{k}_1 \cdot \boldsymbol{\rho}_1 + i\mathbf{k}_2 \cdot \boldsymbol{\rho}_2} \Psi(\boldsymbol{\rho}_1, \boldsymbol{\rho}_2)$ . We can also argue that the trion ground state is  $p$ -wave in this general case if we consider the configuration where one of the light particles is placed on top of the heavy particle. This is equivalent to taking one of the positions,  $\boldsymbol{\rho}_1$ , to zero in the wave function. We thus obtain a wave function that only depends on the position  $\boldsymbol{\rho}_2$  of the remaining light particle, while still having the same definite angular momentum. We then note that this wave function must go to zero when  $\boldsymbol{\rho}_2 \rightarrow \mathbf{0}$  since there cannot be two (fermionic) light particles at the same position. This condition is most easily satisfied by placing the remaining light particle in a  $p$ -wave state. Hence the ground-state trion is  $p$ -wave.

To test whether this trion state is bound, we calculate its energy and compare it with the exciton energy. The trion energy can be found by minimizing  $\langle T_3 | (\hat{H} - E) | T_3 \rangle$  with respect to the complex wave function  $\gamma_{\mathbf{k}_1\mathbf{k}_2}^*$  to obtain the following eigenvalue equation

$$E\gamma_{\mathbf{k}_1\mathbf{k}_2} = \mathcal{E}_{\mathbf{k}_1\mathbf{k}_2}\gamma_{\mathbf{k}_1\mathbf{k}_2} - \frac{v}{\mathcal{A}} \sum_{\mathbf{k}'} (\gamma_{\mathbf{k}'\mathbf{k}_2} + \gamma_{\mathbf{k}_1\mathbf{k}'}) , \quad (4.14)$$

where  $\mathcal{E}_{\mathbf{k}_1\mathbf{k}_2} = \epsilon_{1\mathbf{k}_1} + \epsilon_{1\mathbf{k}_2} + \epsilon_{2\mathbf{k}_1+\mathbf{k}_2}$ . Equation (4.14) corresponds to a Fredholm integral equation of the second kind and its solution is obtained using Gauss-Legendre quadrature for the numerical integrals [477].

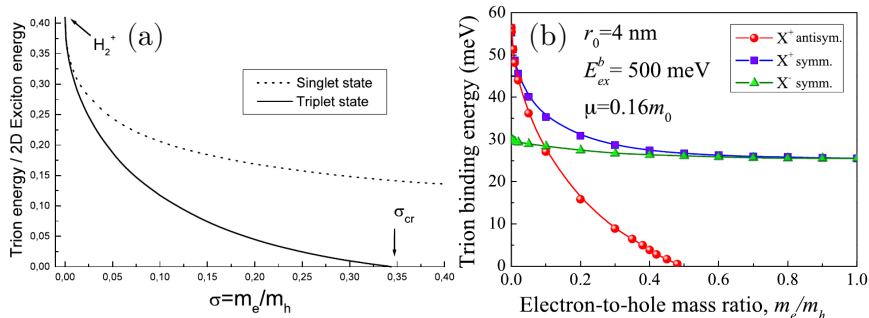


**Fig. 4.4:** (a) Binding energies of the  $p$ -wave spin-triplet (solid line) and  $s$ -wave spin-singlet (dashed line) trion  $X^+$  as a function of the electron-hole mass ratio for a 2D GaAs quantum well and unscreened Coulomb interactions (1.22b) — adapted from Ref. [272]. (b) Binding energies for the  $p$ -wave (antisymmetric)  $X^+$  trion (red), the  $s$ -wave symmetric  $X^+$  (blue), and  $X^-$  (green) trions as a function of the electron-hole mass ratio. The parameters used are for a WSe<sub>2</sub> monolayer described by a RK interaction potential (1.29), with a screening radius  $r_0 = 4$  nm and a fixed reduced mass  $\mu = 0.16m_0$  — adapted from Ref. [268].

As argued above, the ground state must have overall angular momentum  $\ell = \pm 1$  (i.e., it is  $p$ -wave), so we may consider the following ansatz:

$$\gamma_{\mathbf{k}_1\mathbf{k}_2} = e^{i\theta_1} \gamma_{k_1k_2(\theta_2-\theta_1)}. \quad (4.15)$$

We have numerically checked that the ground state of Eq. (4.14) always satisfies this condition. In agreement with Refs. [374, 471], we find that the  $p$ -wave trion binds for a mass ratio  $m_2/m_1 \lesssim 0.3$  — see Fig. 4.3 (b). We see that our calculated binding energy closely matches that obtained within the Born-Oppenheimer approximation in the limit of a large mass ratio, Eq. (4.12), see the dashed (red) line in Fig. 4.3 (b).

In typical semiconductors, the hole’s effective mass is larger than the electron mass. As such, the critical mass ratio obtained above implies that a  $p$ -wave trion bound state can exist only if the majority particles are holes, meaning that it is an  $X^+$  trion. By contrast, for distinguishable particles, the  $s$ -wave bound state exists for all mass ratios [471], and both  $X^+$  and  $X^-$  trions are possible.

As noted in Sec. 4.2, we approximate the interaction between charges as a contact interaction, which can be considered as assuming that interactions between charges are strongly screened. This overestimates the  $p$ -wave trion binding energy when  $m_2/m_1 \rightarrow 0$ . In fact, the contact interaction causes the binding energy to diverge according to Eq. (4.12), which is a well-known feature of contact interactions [478]. An interaction that decays at large momentum transfer (like a screened Coulomb interaction) would instead result in a finite

binding energy [268, 271, 272]. Nevertheless, the contact interaction approximation correctly describes the existence of a critical mass ratio. Furthermore, the critical ratio found for contact interactions,  $m_2/m_1 \lesssim 0.3$  agrees well with that found for bare Coulomb interactions [271, 272],  $m_2/m_1 \lesssim 0.35$ , as well as for Rytova-Keldysh effective interactions describing TMD monolayers [268],  $m_2/m_1 \lesssim 0.5$  — see Fig. 4.4. These critical mass ratios are marked by symbols in Fig. 4.3 (b).

### 4.3.3 Coupling to light

The dipole matrix element for the transition between a single isolated trion and a single carrier vanishes—i.e., the isolated trion does not couple to light. Here we are showing it explicitly, for both DCP and ICP, by considering the matrix element of the light-matter interaction term  $\hat{H}_{ehC}$  (4.2d) between the trion state in Eq. (4.13) and a cavity photon plus a majority particle state at zero momentum  $|C+1\rangle = \hat{a}_0^\dagger \hat{c}_{10}^\dagger |0\rangle$  [266]:

$$\langle T_3 | \hat{H}_{ehC} | C+1 \rangle = \frac{\sqrt{2}}{\sqrt{\mathcal{A}}} \eta_{\mathbf{0}}^* . \quad (4.16)$$

Here,  $\eta_{\mathbf{k}} = \frac{g}{\mathcal{A}} \sum_{\mathbf{k}'} \gamma_{\mathbf{k}'\mathbf{k}}$  describes the recombination probability amplitude of an electron and hole in the trion with total momentum  $\mathbf{k}^3$ . The term in Eq. (4.16) is in general vanishingly small due to the prefactor of order  $1/\sqrt{\mathcal{A}}$  [479]; such suppression is present for both  $s$ - and  $p$ -wave trions. Additionally, in the  $p$ -wave case we have  $\eta_{\mathbf{k}} \rightarrow 0$  as  $k \rightarrow 0$  due to Eq. (4.15), i.e., the  $p$ -wave transition is further forbidden by symmetry.

Now let us discuss how these results lead to a non-zero oscillator strength in experiments carried out at small but finite doping. In the  $s$ -wave case, the oscillator strength of the trion branch is proportional to the square of the matrix element in Eq. (4.16) multiplied by the number of particles within the area  $\mathcal{A}$ , i.e., the oscillator strength scales as the majority particle density  $\sim n_1$ . This estimate is smaller than the exciton oscillator strength by a factor proportional to  $n_1$ , in agreement with results based on the trion [266, 317, 318] and the polaron [261, 321, 479] pictures.

In order to estimate the finite-density trion oscillator strength in the  $p$ -wave case, we need to consider adding the correction to the sum appearing in Eq. (4.16) since this is identically zero at  $k_F = 0$ . For  $k_F \ll \sqrt{2\mu|E_{T_3}|}$ , we therefore instead calculate the matrix element between a final-state trion at a typical center of mass momentum  $\mathbf{k}_F \equiv k_F \hat{\mathbf{n}}$  (where  $\hat{\mathbf{n}}$  is a unit vector in

<sup>3</sup> This is in principle equivalent to taking the limit  $\rho_1 \rightarrow 0$  in  $\int d\boldsymbol{\rho}_2 e^{i\mathbf{k}\cdot\boldsymbol{\rho}_2} \Psi(\boldsymbol{\rho}_1, \boldsymbol{\rho}_2)$ , as in Ref. [266]. However, care must be exercised in the case of contact interactions since  $\lim_{\rho_1 \rightarrow 0} \Psi(\boldsymbol{\rho}_1, \boldsymbol{\rho}_2)$  is formally divergent. Thus, one must also include the coupling  $g$  to cancel the logarithmic divergence at short distances.

an arbitrary direction), and an initial state with a photon at normal incidence and a carrier at momentum  $\mathbf{k}_F$ . To leading order, the matrix element becomes  $\sqrt{2/\mathcal{A}} \eta_{\mathbf{k}_F}^*$ . It is straightforward to show that, in the  $p$ -wave case,  $\eta_{\mathbf{k}_F}$  scales linearly with  $k_F \propto \sqrt{n_1}$ . To see this, we can rewrite Eq. (4.14) in terms of  $\eta_{\mathbf{k}}$ <sup>4</sup>:

$$\left( \frac{1}{v} + \frac{1}{\mathcal{A}} \sum_{\mathbf{k}_1} \frac{1}{E - \mathcal{E}_{\mathbf{k}_1 \mathbf{k}_2}} \right) \eta_{\mathbf{k}_2} = \frac{1}{\mathcal{A}} \sum_{\mathbf{k}_1} \frac{\eta_{\mathbf{k}_1}}{E - \mathcal{E}_{\mathbf{k}_1 \mathbf{k}_2}}. \quad (4.17)$$

Like  $\gamma$ ,  $\eta$  satisfies the  $p$ -wave symmetry  $\eta_{\mathbf{k}} = e^{i\theta} \eta_k$ . Therefore, the right-hand side is identically zero at  $\mathbf{k}_2 = \mathbf{0}$ , and thus  $\eta_{\mathbf{0}} = 0$  and the matrix element in Eq. (4.16) vanishes. At finite doping, instead, we want to estimate  $\eta_{\mathbf{k}_F}$  at small  $k_F$ . Expanding the kinetic energy  $\mathcal{E}_{\mathbf{k}_1 \mathbf{k}_F}$  for small  $\mathbf{k}_F$  to linear order, and using the  $p$ -wave condition, we then find the first non-zero term scales as  $k_F$ , multiplied by a  $k_F$ -independent integral. Taking the square amplitude of the matrix element and multiplying by the number of majority particles within the area  $\mathcal{A}$ , we thus find that in the  $p$ -wave case the trion oscillator strength  $\sim n_1^2$ . This estimate agrees with the numerical results obtained within the polaron picture, as analyzed below in Sec. 4.4.3.

## 4.4 Polaron state

In this section, we present a wave function ansatz describing exciton-polaron (polariton) states with indistinguishable carriers. We first present the ansatz, which we use to describe both ground and excited states, and then discuss how we may efficiently calculate the absorption spectrum within this ansatz. We consider the following ansatz describing a superposition of a bare photon and an exciton with a dressing cloud of electron-hole excitations of the Fermi sea, all with zero center of mass momentum:

$$|\widetilde{M}_4\rangle = \left( \alpha \hat{a}_{\mathbf{0}}^\dagger + \sum_{\mathbf{k}_1} \frac{\varphi_{\mathbf{k}_1}}{\sqrt{\mathcal{A}}} \hat{c}_{2-\mathbf{k}_1}^\dagger \hat{c}_{1\mathbf{k}_1}^\dagger + \sum_{\mathbf{k}_1, \mathbf{k}_2, \mathbf{q}} \frac{\varphi_{\mathbf{k}_1 \mathbf{k}_2 \mathbf{q}}}{\sqrt{2\mathcal{A}^{3/2}}} \hat{c}_{2\mathbf{q}-\mathbf{k}_1-\mathbf{k}_2}^\dagger \hat{c}_{1\mathbf{k}_1}^\dagger \hat{c}_{1\mathbf{k}_2}^\dagger \hat{c}_{1\mathbf{q}}^\dagger \right) |FS\rangle, \quad (4.18)$$

normalized so that

$$1 = \langle \widetilde{M}_4 | \widetilde{M}_4 \rangle = |\alpha|^2 + \frac{1}{\mathcal{A}} \sum_{\mathbf{k}_1} |\varphi_{\mathbf{k}_1}|^2 + \frac{1}{\mathcal{A}^3} \sum_{\mathbf{k}_1, \mathbf{k}_2, \mathbf{q}} |\varphi_{\mathbf{k}_1 \mathbf{k}_2 \mathbf{q}}|^2. \quad (4.19)$$

---

<sup>4</sup> In practice, having a Fermi sea restricts the momentum  $\mathbf{k}_1$  appearing in the sums to be above the Fermi surface. However, due to the  $p$ -wave symmetry, such corrections are higher order in  $k_F$  and may be neglected here.

In Eq. (4.18),  $|FS\rangle = \prod_{\mathbf{q}} \hat{c}_{1\mathbf{q}}^\dagger |0\rangle$  describes the Fermi sea of majority particles, and we use the convention that momenta labeled  $\mathbf{k}_i$  represent states above the Fermi sea ( $k_i > k_F$ ), while momenta labeled  $\mathbf{q}$  refer to states below ( $q < k_F$ ). We denote the state in Eq. (4.18) by  $\widetilde{M}_4$  [374] to indicate it is a molecular (i.e., excitonic) state with up to four-body correlations. The first two terms in  $|\widetilde{M}_4\rangle$  are, respectively, a photon with amplitude  $\alpha$ , and an electron-hole pair (undressed exciton) with wave function  $\varphi_{\mathbf{k}}$  in terms of the relative electron-hole momentum  $\mathbf{k}$ . The final term describes a scattered exciton and a single intra-band particle-hole excitation of the majority particle Fermi sea. The associated four-body wave function  $\varphi_{\mathbf{k}_1\mathbf{k}_2\mathbf{q}}$  can be viewed as a trion-like (three-particle) complex plus a hole of the Fermi sea. Indeed, this term reduces to the trion wave function (4.13) in the limit of vanishing doping. Thus, we will refer to this term as the “trion-hole” state for brevity, although it should be understood that the “trion” in this complex is not necessarily a well-defined three-particle bound state. Because the majority particles are indistinguishable, the trion-hole wave function  $\varphi_{\mathbf{k}_1\mathbf{k}_2\mathbf{q}}$  must be antisymmetric under the exchange  $\mathbf{k}_1$  and  $\mathbf{k}_2$ , i.e.,  $\varphi_{\mathbf{k}_1\mathbf{k}_2\mathbf{q}} = -\varphi_{\mathbf{k}_2\mathbf{k}_1\mathbf{q}}$ , which is satisfied by all our numerical results in the following.

In our variational state, Eq. (4.18), we consider only the states where the photon is at zero momentum, as these are experimentally accessible by a probe at normal incidence. Furthermore, we do not include the contribution of the particle-hole-dressed photon state,

$$\sum_{\mathbf{k}\mathbf{q}} \frac{\alpha_{\mathbf{k}\mathbf{q}}}{\mathcal{A}} \hat{a}_{\mathbf{q}-\mathbf{k}}^\dagger \hat{c}_{1\mathbf{k}}^\dagger \hat{c}_{1\mathbf{q}} |FS\rangle. \quad (4.20)$$

If present, this term would lead to a broadening of the photon, because a photon at  $\mathbf{Q} = \mathbf{0}$  could scatter to a different momentum  $\mathbf{q} - \mathbf{k}$ , which is typically non-zero because  $q < k_F$  and  $k > k_F$ . However, due to the photon mass  $m_C$  being approximately five orders of magnitude smaller than the bare electron mass ( $m_C \simeq 10^{-5}m_0$ ), finite-momentum photons have energies far off-resonance with both trion and exciton energies. As such, their contribution is negligible [480].

The ICP energy can be obtained minimizing the expectation value  $\langle \widetilde{M}_4 | (\hat{H} - E) | \widetilde{M}_4 \rangle$  with respect to the complex variational parameters  $\alpha^*$ ,  $\varphi_{\mathbf{k}_1}^*$ , and  $\varphi_{\mathbf{k}_1\mathbf{k}_2\mathbf{q}}^*$

to obtain the following eigenvalue equations:

$$E\alpha = \epsilon_{C0}\alpha - \frac{g}{\mathcal{A}} \sum_{\mathbf{k}'_1} \varphi_{\mathbf{k}'_1} \quad (4.21a)$$

$$E\varphi_{\mathbf{k}_1} = \bar{\epsilon}_{\mathbf{k}_1} \varphi_{\mathbf{k}_1} - \frac{v}{\mathcal{A}} \sum_{\mathbf{k}'_1} \varphi_{\mathbf{k}'_1} - g\alpha - \frac{\sqrt{2}v}{\mathcal{A}^2} \sum_{\mathbf{k}'_2 \mathbf{q}'} \varphi_{\mathbf{k}_1 \mathbf{k}'_2 \mathbf{q}'} \quad (4.21b)$$

$$\begin{aligned} E\varphi_{\mathbf{k}_1 \mathbf{k}_2 \mathbf{q}} &= \mathcal{E}_{\mathbf{k}_1 \mathbf{k}_2 \mathbf{q}} \varphi_{\mathbf{k}_1 \mathbf{k}_2 \mathbf{q}} + \frac{v}{\mathcal{A}} \sum_{\mathbf{q}'} \varphi_{\mathbf{k}_1 \mathbf{k}_2 \mathbf{q}'} - \frac{v}{\mathcal{A}} \sum_{\mathbf{k}'_1} \varphi_{\mathbf{k}'_1 \mathbf{k}_2 \mathbf{q}} \\ &\quad - \frac{v}{\mathcal{A}} \sum_{\mathbf{k}'_2} \varphi_{\mathbf{k}_1 \mathbf{k}'_2 \mathbf{q}} - \frac{v}{\sqrt{2}} (\varphi_{\mathbf{k}_1} - \varphi_{\mathbf{k}_2}), \end{aligned} \quad (4.21c)$$

where, as in Eq. (4.4),  $\bar{\epsilon}_{\mathbf{k}_1} = \epsilon_{1\mathbf{k}_1} + \epsilon_{2\mathbf{k}_1} = \mathbf{k}_1^2/2\mu$ , while  $\mathcal{E}_{\mathbf{k}_1 \mathbf{k}_2 \mathbf{q}} = \epsilon_{1\mathbf{k}_1} + \epsilon_{1\mathbf{k}_2} - \epsilon_{1\mathbf{q}} + \epsilon_{2\mathbf{q}-\mathbf{k}_1-\mathbf{k}_2}$ . By solving the coupled linear equations (4.21) we gain direct access to the energies of both the ground and excited states, as well as the corresponding wave functions. This includes information about the photon, exciton, and dressed exciton amplitudes.

Equations (4.21) show that the photon mode couples only to the bare exciton part of the state. However, the bare exciton and trion-hole terms are not system eigenstates in the presence of doping; they couple via the electron-hole interaction. As such—when the  $p$ -wave trion state is bound, i.e., for  $m_2/m_1 \lesssim 0.3$ —the eigenstates are hybridized to form attractive and repulsive polaron resonances, as well as an incoherent continuum of many-body states. Because of this hybridization, the photon couples to all of these eigenstates, leading to a transfer of oscillator strength from the repulsive branch—which, at low doping, is exciton-like—to the attractive branch—which, at low doping, is trion-like.

Even though for indistinguishable particles the symmetry of the (three-body) trion state is  $p$ -wave (4.15), the lowest energy wave functions of both the (two-body) exciton and (four-body) trion-hole contributions have an overall  $s$ -wave symmetry:

$$\varphi_{\mathbf{k}_1} = \varphi_{k_1} \quad (4.22a)$$

$$\varphi_{\mathbf{k}_1 \mathbf{k}_2 \mathbf{q}} = \varphi_{k_1 k_2 q(\theta_1 - \theta_q)(\theta_2 - \theta_q)}. \quad (4.22b)$$

Indeed, within our model Hamiltonian (4.2), all other angular momentum states are completely uncoupled to light, and hence we will be making this  $s$ -wave ansatz in the following. Clearly, in the case of the trion-hole wave function  $\varphi_{\mathbf{k}_1 \mathbf{k}_2 \mathbf{q}}$ , Eq. (4.22b) implies that we can equivalently choose as reference angle either the angle of the Fermi sea hole  $\theta_q$ , as in Eq. (4.22b), or the angle of any of the two majority species particles, e.g.,  $\varphi_{\mathbf{k}_1 \mathbf{k}_2 \mathbf{q}} = \varphi_{k_1 k_2 q(\theta_2 - \theta_1)(\theta_q - \theta_1)}$ . Note that, at low doping, the trion sub-space within the trion-hole complex of those

states corresponding to the attractive branch still has an angular momentum  $\ell = \pm 1$ , while the hole component has  $\ell = \mp 1$ , as shown later in Fig. 4.10. Yet, as we discuss below, the orbital character of both attractive and repulsive branches evolves with doping.

In solving the system of equations in (4.21), we want to consider the limit where the UV cutoff  $\Lambda \rightarrow \infty$ , and replace the bare parameters  $v, g, \epsilon_{C0}$  with the renormalized parameters, as discussed in Sec. 4.2.1. Our results will then be independent of microscopic physics and can be expressed in terms of the exciton binding energy  $\varepsilon_X$ , the photon-exciton detuning  $\delta$ , and the Rabi splitting  $\Omega$ . In addition to these, the other relevant parameters are the Fermi energy  $E_F$  and the mass ratio  $m_2/m_1$ . By considering the limit  $\Lambda \rightarrow \infty$ ,  $v \rightarrow 0$ , we may also simplify the form of Eq. (4.21c). Since the large- $k$  behavior of both exciton and trion-hole wave functions is  $\varphi_{\mathbf{k}_{1,2}} \sim \varphi_{\mathbf{k}_1\mathbf{k}_2\mathbf{q}} \sim 1/k_{1,2}^2$ , we can neglect the term  $\frac{v}{A} \sum_{\mathbf{q}'} \varphi_{\mathbf{k}_1\mathbf{k}_2\mathbf{q}'}$  in Eq. (4.21c) when  $\Lambda \rightarrow \infty$ .

#### 4.4.1 Numerical implementation

If one were working with a finite UV cutoff,  $\Lambda$ , then the discrete form of the Hamiltonian describing the eigenvalue problem (4.21) could be obtained by considering a grid for momenta  $k \in [k_F, \Lambda]$ . However, as we wish to consider the renormalized problem,  $\Lambda \rightarrow \infty$ , the grid for  $k$ -integrals has to extend up to infinity. We thus apply a transformation  $\beta = \tan k$ , with  $\beta \in [\arctan(k_F), \pi/2)$ . We then consider a Gauss-Legendre quadrature in  $\beta$  with  $N_k$  points, in  $q$  with  $N_q$  points, and in  $\theta$  with  $N_\theta$  points. Note that, in this way, by sending the number of points  $N_k \rightarrow \infty$ , we automatically consider the  $\Lambda \rightarrow \infty$  limit. For efficiency, we use a grid in polar coordinates that exploit the symmetry of the system.

This approach is only possible because of our use of contact interactions. If we had used full Coulomb interactions, this inevitably also requires intraspecies interactions (which vanish in the contact case). Such intraspecies interactions lead to the appearance of terms in the eigenvalue equations that involve differences of momenta, and, as such, do not lie on the original momentum grid.

By studying the dependence of the spectral functions on the number of points,  $N_k$ ,  $N_q$ , and  $N_\theta$ , we find that the convergence with respect to  $N_q$  and  $N_\theta$  is reached easily (already for  $N_q = 4$ ,  $N_\theta = 7$ ), while the details of the spectra strongly depend on  $N_k$ , as shown in Fig. 4.5. To be concrete, we observe that the two pronounced peaks corresponding to the attractive and repulsive polaron branches converge quickly with  $N_k$ . By contrast, the set of states that eventually will form a continuum continues to vary with  $N_k$ . This distinct behavior as a function of  $N_k$  allows us to distinguish the attractive and repulsive branches from the continuum. Note that we have checked that our results match between the direct diagonalization of Eqs. (4.21) and the

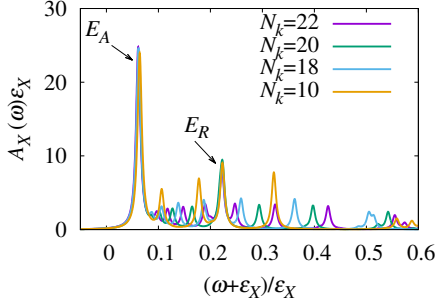


**Fig. 4.5:** Exciton spectral function profiles  $A_X(\omega)$  in the weak coupling regime for the same system parameters as Fig. 4.6 (a) ( $m_2/m_1 = 0.25$ , and  $\eta_X = 5 \times 10^{-3} \epsilon_X$ ), at  $E_F = 0.064 \epsilon_X$ , for different values of  $N_k$  and for  $N_q = 4$  and  $N_\theta = 8$ .

Haydock iteration method — see App. B. The recursive method however allows us to consider a larger number of grid points (up to  $N_k = 22$ ) than the direct diagonalization method (restricted to  $N_k = 10$ ) because it only involves matrix-vector operations and thus requires less memory.

Even though the recursive method allows us to reach larger values of  $N_k$  than exact diagonalization, at the maximum value we can reach,  $N_k = 22$ , the form of the continuum has still not converged. We observe in Fig. 4.5 that, by increasing  $N_k$ , the states associated with the continuum reduce in frequency and accumulate in the region between the attractive and repulsive branches. During this evolution, there are specific values of  $N_k$  where a given continuum state becomes resonant with the repulsive branch. In the  $N_k \rightarrow \infty$  limit, the continuum states would become dense, and so there would not be distinct resonances. Since the coupling between continuum and repulsive modes is small, the repulsive branch does not notably shift in energy at these resonances, but it does change its spectral weight. These resonances result in a slightly “noisy” behavior of the spectral weight of the repulsive branch and the continuum shown in Fig. 4.7 (c). The corresponding data points are plotted with empty rather than filled symbols.

Figs. 4.6, 4.7, 4.8, and 4.11 are obtained with the recursive method with  $N_k = 20$ ,  $N_q = 4$ , and  $N_\theta = 8$ .

Finally, we note that while Eq. (4.21) is written allowing for strong light-matter coupling,  $g$ , it can also be considered in the limit  $g \rightarrow 0$ . This therefore allows us to explore two distinct regimes: In the strong coupling regime, the 2D semiconductor is embedded in a microcavity and the coupling to light explicitly modifies the excitonic states resulting in the formation of polaron-polaritons. Conversely, in the weak coupling regime, the 2D semiconductor is probed by light in the absence of a cavity, and the probe light does not change the form of the spectrum. Technically, in our formulation, the latter case corresponds to removing the photonic part of the variational state in Eq. (4.18) (corresponding to removing Eq. (4.21a)) and taking  $g = 0$  in Eq. (4.21b), and thus this procedure will be implicit in the following whenever we discuss results obtained

in the weak coupling limit.

#### 4.4.2 Spectral functions

A natural probe of trion states is optical absorption which can be calculated, in both strong and weak coupling regimes, starting from the photon and exciton Green's functions respectively. We can follow a procedure similar to the one employed in Sec. 1.5.3. We here briefly summarize the main steps.

In the time domain, the photon and exciton Green's functions are defined as

$$G_{C,X}(t) = \langle \Psi_0^{C,X} | e^{-i\hat{H}t} | \Psi_0^{C,X} \rangle. \quad (4.23)$$

Here,  $|\Psi_0^{C,X}\rangle$  denotes the initial state within the space spanned by our ansatz. The choice of this state varies depending on which Green's function we seek to calculate. For the photon Green's function ( $C$ ) we consider an initial state with a single photon

$$|\Psi_0^C\rangle = \hat{a}_0^\dagger |FS\rangle. \quad (4.24)$$

The exciton Green's function ( $X$ ) is instead chosen to describe the response of the material to optical excitation, and thus the initial state we use is that of an electron-hole pair at the same spatial position — note that this state is *not* an exciton. We will nonetheless refer to this as the exciton Green's function in the following since this name is commonly used in the literature. We thus write

$$|\Psi_0^X\rangle = \frac{\mathcal{N}}{\sqrt{\mathcal{A}}} \sum_{\mathbf{k}} \hat{c}_{2-\mathbf{k}}^\dagger \hat{c}_{1\mathbf{k}}^\dagger |FS\rangle, \quad (4.25)$$

where the normalization  $\mathcal{N} = (\frac{1}{\mathcal{A}} \sum_{\mathbf{k}})^{-1/2}$  is chosen so that  $\langle \Psi_0^X | \Psi_0^X \rangle = 1$ .

Both Green's functions can be written in the frequency domain in terms of the complete set of eigenstates of Eqs. (4.21), described by eigenvalues  $E_n$ , and photonic  $\alpha_n$  and excitonic  $\varphi_{n\mathbf{k}}$  components of the eigenvectors:

$$G_C(\omega) = \sum_n \frac{|\alpha_n|^2}{\omega - E_n + i\eta} \quad (4.26a)$$

$$G_{X,\Lambda}(\omega) = \sum_n \frac{\left| \frac{\mathcal{N}}{\mathcal{A}} \sum_{\mathbf{k}} \varphi_{n\mathbf{k}} \right|^2}{\omega - E_n + i\eta}, \quad (4.26b)$$

where  $\eta$  denotes a Lorentzian linewidth which we add by hand. We note that the exciton Green's function  $G_{X,\Lambda}$  defined in Eq. (4.26b) depends on the UV cutoff  $\Lambda$  and needs to be renormalized in order to obtain a physical quantity that is cutoff independent. This is because as  $\Lambda \rightarrow \infty$ ,  $\mathcal{N} \sim \Lambda^{-1} \rightarrow 0$  while  $\frac{1}{\mathcal{A}} \sum_{\mathbf{k}} \varphi_{\mathbf{k}}^{(n)} \sim \log \Lambda \rightarrow \infty$ . As discussed in App. B, a cutoff independent form

can be obtained by considering the following rescaling

$$G_X(\omega) = \left(\frac{2g}{\Omega}\right)^2 \frac{G_{X,\Lambda}(\omega)}{\mathcal{N}^2} = \sum_n \frac{\left|\frac{1}{\Lambda} \sum_{\mathbf{k}} \varphi_{n\mathbf{k}} / \frac{1}{\Lambda} \sum_{\mathbf{k}} \Phi_{1s\mathbf{k}}\right|^2}{\omega - E_n + i\eta}, \quad (4.27)$$

where the microscopic light-matter coupling constant  $g$  and the Rabi splitting  $\Omega$  are related by Eq. (4.7), and  $\Phi_{1s\mathbf{k}}$  denotes the wave function of the  $1s$  exciton (4.5).

Because the photon mass is orders of magnitude smaller than that of the exciton, we can neglect the electron-hole photon dressing term in Eq. (4.20). This simplifies the problem considerably, in particular, we find that the strong coupling photon Green's function in Eq. (4.26a) is related to the exciton Green's function in the weak light-matter coupling regime  $G_X^{(0)}(\omega)$ , via (1.43):

$$G_C(\omega) = \frac{1}{\omega - \delta + \varepsilon_X - (\Omega/2)^2 G_X^{(0)}(\omega) + i\eta}. \quad (4.28)$$

Note however that  $G_X^{(0)}(\omega)$  is not the free exciton Green's function, because of the electron-hole dressing by the Fermi sea.

If we try to evaluate the exciton and photon Green's functions by first finding the complete set of eigenvalues and eigenvectors of Eqs. (4.21), this places significant constraints on the number of degrees of freedom we may consider, and thus on the precision of the calculation. We thus also employ a recursive method, originally developed by Haydock and collaborators [481], which allows one to consider a larger number of basis states, and thus reach a higher numerical precision. Here, one seeks to transform the eigenvalue problem (4.21) into a tridiagonal form, with the top left element corresponding to the expectation value on the initial state  $|\Psi_0^{C,X}\rangle$ . Truncating this recursive scheme at some order provides a basis for those states which are most relevant in terms of their contribution to the associated Green's function. The Green's function can then be conveniently evaluated by continued-fraction. Further details can be found in App. B. For our problem we can simultaneously evaluate both the photon Green's function  $G_C(\omega)$ , as well as the renormalized exciton Green function in the weak coupling limit to light  $G_X^{(0)}(\omega)$ , which are related by Eq. (4.28).

Finally, the exciton and photon spectral functions to describe the optical absorption in the weak and strong coupling regimes, respectively, are defined as in Eqs. (1.45) (1.47):

$$A_{X,C}(\omega) = -\frac{1}{\pi} \text{Im} G_{X,C}^{(0)}(\omega). \quad (4.29)$$

As discussed in Sec. 1.5.1, while the exciton spectral function  $A_X(\omega)$  corresponds to the absorption by the semiconductor (TMD monolayer or quantum

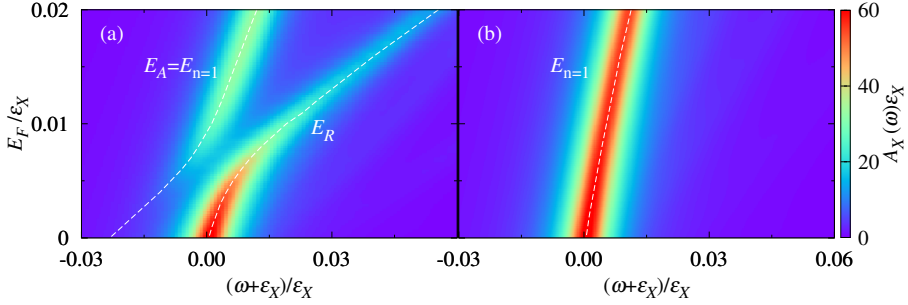


**Fig. 4.6:** Colormap of the exciton spectral function  $A_X(\omega)$  for the ICP case, in the weak coupling regime as a function of the frequency  $\omega$  and the majority particle Fermi energy  $E_F$ . (a) For  $m_2/m_1 = 0.25$ , the spectrum displays two Lorentzian resonances corresponding to attractive ( $\omega = E_A$ ) and repulsive ( $\omega = E_R$ ) polaron branches (indicated by dashed white lines). At  $E_F \rightarrow 0$ , these approach the trion ( $E_A \rightarrow E_{T_3}$ ) and exciton ( $E_R \rightarrow -\varepsilon_X$ ) energies, respectively. At  $m_2/m_1 = 0.25$ , the  $p$ -wave trion binding energy is  $(|E_{T_3}| - \varepsilon_X)/\varepsilon_X \simeq 0.022$  — see Fig. 4.3 (b). (b) For  $m_2/m_1 = 1$ , the  $p$ -wave trion is unbound and the spectrum has a single Lorentzian resonance, which continuously connects with the exciton mode at zero doping,  $\omega = E_{n=1} \rightarrow -\varepsilon_X$ . The linewidth in both panels is  $\eta = 5 \times 10^{-3} \varepsilon_X$ .

well), in the absence of any optical microcavity, the relation between the photon spectral function  $A_C(\omega)$  and optical absorption is more subtle. This spectral function does correspond to the absorption of light by an optical microcavity containing the semiconductor, but only in the limit where the cavity linewidth is much smaller than that of the excitons — see Sec. 1.5.1.

### 4.4.3 Weak coupling

We first present our results in the weak coupling regime. This corresponds to the absence of a cavity, and therefore we consider the exciton spectral function  $A_X(\omega)$ . This function shows distinct behavior depending on whether the  $p$ -wave trion state is bound ( $m_2/m_1 \lesssim 0.3$ ) or not ( $m_2/m_1 > 0.3$ ) — see Sec. 4.3.2. Note that mass ratios relevant to current experiments are  $m_2/m_1 \sim 1$ , typical for a TMD monolayer [59], and  $m_2/m_1 \sim 0.25$ , for a GaAs quantum well [482] (when hole-doped). We note also that the effective mass ratio in TMD monolayers can be tuned by application of strain [483, 484].

When the  $p$ -wave trion state is bound, the spectral function is characterized by two peaks, as shown in Fig. 4.6 (a). We identify these as the attractive branch at  $\omega = E_A$  and the repulsive branch at  $\omega = E_R$  (the location of these peaks are indicated by dashed white lines in Fig. 4.6 (a)). In the limit of zero doping  $E_F \rightarrow 0$ , the attractive mode continuously connects with the  $p$ -wave trion state ( $E_A \rightarrow E_{T_3}$ ), while the repulsive mode tends toward the exciton

state ( $E_A \rightarrow -\varepsilon_X$ ). As anticipated, in this limit, the trion has a vanishing spectral weight, and the spectral function has a single peak at the exciton energy with spectral weight (i.e., integrated area) equal to one. Upon increasing the doping, we see that there is a transfer of spectral weight from the repulsive (exciton) to the attractive (trion) branch.

The energy of the attractive branch peak coincides with the lowest eigenvalue of Eqs. (4.21),  $E_A = E_{n=1}$ , and we find that there is a strong suppression of spectral weight immediately above this value. As such, the attractive branch at finite doping retains a Lorentzian shape, which mirrors the DCP case — see e.g., Ref. [382] for a detailed discussion in the three-dimensional case. Conversely, the repulsive branch does not coincide with a single eigenvalue, because of the presence of a continuum between the attractive and repulsive modes. Despite this, we find that the repulsive branch also has a Lorentzian shape with a constant width  $\eta_X$  for all values of doping  $E_F$ . As such, we conclude that, for dressing by indistinguishable carriers, the shape of the repulsive branch is not affected by the continuum. We explain this result below by showing that at large enough doping the repulsive branch and the continuum have distinct symmetries and, as such, do not hybridize. Note that the ICP and DCP cases are very different in this regard, as we later discussed.

We next explore how the attractive and repulsive peak positions and weights evolve with doping. To do this, we fit the weak coupling exciton spectral function  $A_X(\omega)$  with two Lorentzians centered at  $E_{A,R}$  and with quasiparticle weights  $Z_{A,R}$ :

$$A_X(\omega) \simeq -\frac{1}{\pi} \text{Im} \left[ \frac{Z_A}{\omega - E_A + i\eta_X} + \frac{Z_R}{\omega - E_R + i\eta_X} \right]. \quad (4.30)$$

The weights  $Z_{A,R}$  correspond to the areas underneath the peaks. We have checked that these peaks fit this Lorentzian form extremely well for the entire range of doping considered.

In addition to the Lorentzian peaks, the spectral function also includes the continuum of many-body states. We denote the weight of this continuum as  $Z_{\text{continuum}}$ , and we estimate its value from a sum rule on the exciton Green's function. In fact, numerically we find that the exciton Green's function satisfies:

$$-\frac{1}{\pi} \int_{-\infty}^{E_N^0} d\omega \text{Im} G_X^{(0)}(\omega) = 1, \quad (4.31)$$

where the integral is up to the energy  $E_N^0 = k_F^2/2\mu$  of an unbound majority-minority pair on top of a Fermi sea with zero center of mass motion  $\mathbf{Q} = \mathbf{0}$ . Because of this, one can write that:

$$Z_A + Z_R + Z_{\text{continuum}} = 1. \quad (4.32)$$

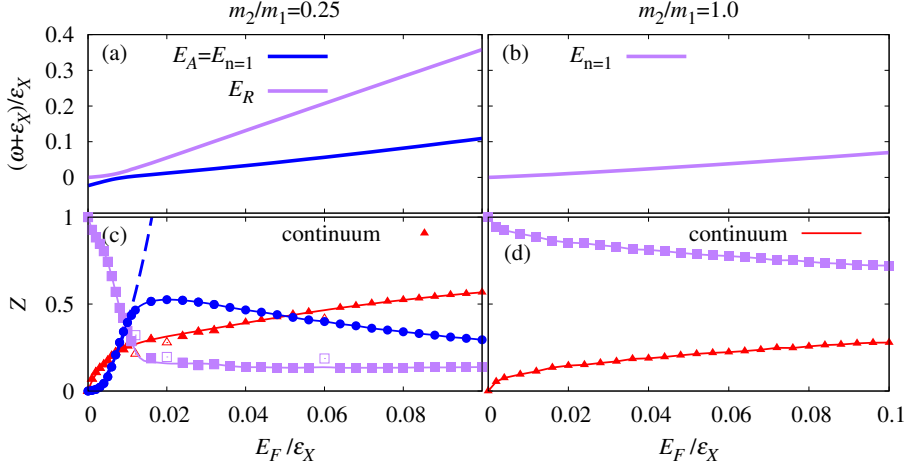


**Fig. 4.7:** Doping dependence of the branch energies (a,b) and spectral weights (c,d) of the exciton spectral function  $A_X(\omega)$  in the weak coupling regime. For mass ratio  $m_2/m_1 = 0.25$  (a,c), the spectrum has two peaks: the attractive branch at  $\omega = E_A = E_{n=1}$ , which coincides with the lowest eigenvalue of Eqs. (4.21), and the repulsive branch at  $\omega = E_R$  branch. For  $m_2/m_1 = 1$  (b,d), the spectrum is characterized by a single peak at  $\omega = E_{n=1}$ . The symbols in panels (c) and (d) correspond to the spectral weights found by integrating the peak areas for the R and A branches and using  $Z_{\text{continuum}} = 1 - Z_R - Z_A$  for the continuum weight. In panel (c), the dashed blue line shows a fit to the attractive branch weight with  $Z_A \sim (E_F/\varepsilon_X)^{1.92}$ . For the (purple) squares of panel (c), the empty symbols indicate a point where a resonance occurs with one of the continuum states, due to finite-size effects — see Sec. 4.4.1; solid lines are a guide to the eye, excluding these points.

Figure 4.7 shows the doping dependence of the energies of attractive and repulsive branches  $\omega = E_{A,R}$ , and of the weights  $Z_{A,R}$ , and  $Z_{\text{continuum}}$ , plotted for the same two mass ratios as shown in Fig. 4.6. We observe that both attractive and repulsive branches are blue-shifted when  $E_F$  increases. The blueshift of the upper (repulsive) branch can naturally be understood from the repulsion between the levels. The blueshift of the attractive branch can be understood as arising from the Pauli exclusion experienced by the optically generated majority particle. Note, however, that our model does not include interaction between same species charges and, as such, does not include band-gap renormalization effects [240–243] which can affect the absolute energy shift of attractive and repulsive branches with  $E_F$ . Our prediction for the energy difference between repulsive and attractive branches remains however accurate [265].

As doping first increases, the spectral weight of the repulsive branch is transferred to both the continuum and the attractive branch. However, initially, the attractive branch weight grows more slowly. Eventually, for  $E_F \gtrsim 0.02\varepsilon_X$ , both attractive and repulsive branches transfer their weights to the continuum.

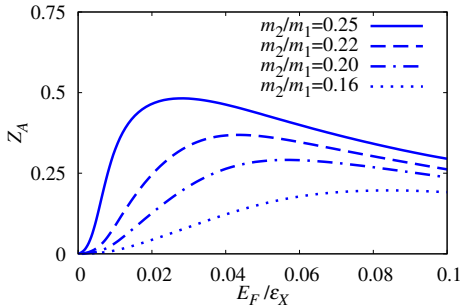


**Fig. 4.8:** Spectral weight of the attractive branch  $Z_A$  as a function of the Fermi energy  $E_F$  for different values of the minority over majority mass ratios  $m_2/m_1$  for the ICP case.

Note that the weights  $Z_{A,R}$  coincide with the oscillator strengths of attractive and repulsive modes, and thus, in the strong coupling regime, determine the Rabi splittings  $\Omega_{A,R} = \sqrt{Z_{A,R}}\Omega$  of the polariton modes, as discussed further in Sec. 4.4.5. Note also that the repulsive and continuum spectral weights have a slightly noisy behavior for a few specific values of  $E_F$ . As explained in Appendix 4.4.1, this is due to the finite-size effects of the numerical calculation and the lack of convergence of the continuum states. This leads to occasional resonances between continuum states and the repulsive branch, causing a reduction in oscillator strength (empty points in Fig. 4.7 (c)).

We find that the growth of the attractive branch spectral weight with doping is consistent with quadratic, with a fit to our numerical results giving  $Z_A \sim (E_F/\varepsilon_X)^{1.92}$  (dashed blue line in Fig. 4.7 (c)). This is quite different from the behavior known for the DCP case, where the growth is linear [266, 317]. This different power-law dependence of  $Z_A$  on  $E_F$  can be understood directly from the difference of  $s$ -wave and  $p$ -wave symmetry of the trion state belonging to the trion-hole complex. In both cases, one factor of  $E_F$  dependence arises to account for the relative probability of creating a majority electron-hole pair, as discussed in Ref. [266]. In the  $p$ -wave case, an extra factor arises since, as discussed in Sec. 4.3.3, the matrix element to create a trion from an electron at  $\mathbf{k} = \mathbf{0}$  vanishes by symmetry. As such, the amplitude for the transition to a trion-hole state depends not only on the density of carriers but on a momentum-weighted density, giving a higher power of  $E_F$ .

The dependence of  $Z_A$  on  $E_F$  varies with the mass ratio. This is shown in Fig. 4.8, where we plot the spectral weight of the attractive branch  $Z_A$  vs  $E_F$  for a variety of mass ratios  $m_2/m_1 < 0.3$ . The transfer of spectral weight is reduced at a larger mass imbalance when the  $p$ -wave trion is more strongly bound.

For  $m_2/m_1 > 0.3$ , the  $p$ -wave trion is unbound and, as noted above, the spectral function displays a single peak. This single branch continuously connects, at zero doping, with the exciton mode  $E_{n=1} \rightarrow -\varepsilon_X$ , as illustrated in Fig. 4.7 (b). The weights of the  $E_{n=1}$  state and the continuum are plotted

in Fig. 4.7 (d), showing a gradual weight transfer from the single branch to the continuum when  $E_F$  increases. This transfer to the continuum is slower than when the trion  $p$ -wave state is bound. We have also analyzed the case where the trion is unbound at zero doping and becomes bound by increasing  $E_F$  [374]. Surprisingly, we find that the spectral function displays two branches exclusively when the trion state is already bound at  $E_F = 0$  and otherwise is characterized by the repulsive branch only.

It is instructive to compare the results found for the ICP scenario with the DCP case, studied previously in Sec. 2.3.2 and which results are resumed in Fig. 2.10. In the DCP case, the  $s$ -wave trion is always bound, i.e.,  $|E_{T_3}| - \varepsilon_X > 0$ , for any mass ratio [268, 271, 272]. Therefore, the spectrum is always characterized by attractive and repulsive branches which continuously connect to the  $s$ -wave trion and exciton states, respectively. As in the ICP case, the attractive branch is well separated from the continuum and thus has a Lorentzian shape. However, the repulsive branch is in this case hybridized with the continuum and so its shape is not Lorentzian. Instead, the repulsive branch is characterized by an asymmetric shape and a linewidth that grows with  $E_F$  [265, 321]. From the energy peak positions Fig. 2.10 (b) one sees that the attractive branch in the DCP case red-shifts with doping; this difference is because, for distinguishable carriers, there is no effect of Pauli blocking on the exciton. From the spectral weights Fig. 2.10 (d), one sees that the transfer to the continuum is negligible in the DCP scenario. Further, at small densities, the attractive branch spectral weight has a linear dependence on density, as already predicted by Refs. [266, 317], in contrast with the quadratic dependence found in the ICP scenario.

#### 4.4.4 Hole angular momentum in the trion-hole complex

As noted previously, the four-body complex described by the wave function  $\varphi_{\mathbf{k}_1 \mathbf{k}_2 \mathbf{q}}$  in the ansatz (4.18) always has an overall  $s$ -wave symmetry,  $\ell = 0$ . The three-particle (trion) and Fermi sea hole subspaces within the complex can, however, have any orbital character consistent with this, i.e., the overall state can be a superposition of states where the trion and hole have opposite angular momenta  $\ell_{\text{trion}} = -\ell_{\text{hole}}$ ; in practice, we find that components with  $\ell_{\text{hole}} = 0, \pm 1$  dominate the state. In order to evaluate the hole (and, consequently, the trion) angular momentum in the trion-hole complex, we consider the probability  $P_\ell^{(n)}$  for the hole in a given eigenstate  $n$  to have an angular momentum  $\ell$ , which we define as

$$P_\ell^{(n)} = \frac{\frac{1}{\mathcal{A}^3} \sum_{\mathbf{k}_1 \mathbf{k}_2 \mathbf{q} \mathbf{q}'} e^{i\ell(\theta_{\mathbf{q}} - \theta_{\mathbf{q}'})} \varphi_{n\mathbf{k}_1 \mathbf{k}_2 \mathbf{q}}^* \varphi_{n\mathbf{k}_1 \mathbf{k}_2 \mathbf{q}'} \delta_{\mathbf{q} \mathbf{q}'}}{\frac{1}{\mathcal{A}^3} \sum_{\mathbf{k}_1 \mathbf{k}_2 \mathbf{q}} |\varphi_{n\mathbf{k}_1 \mathbf{k}_2 \mathbf{q}}|^2} . \quad (4.33)$$

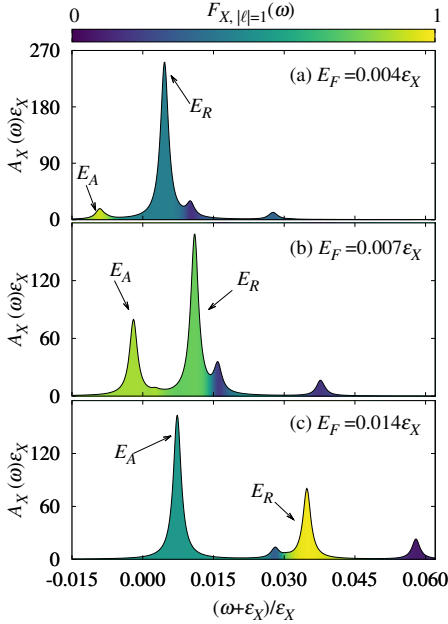


**Fig. 4.9:** Exciton spectral function  $A_X(\omega)$  and angular momentum character for the ICP case, in the weak coupling regime, plotted for different values of  $E_F$ , for  $m_2/m_1 = 0.25$ , and for  $N_k = 10$ ,  $N_q = 4$ ,  $N_\theta = 7$ . The colored area indicates the fraction of states with hole angular momentum  $|\ell| = 1$  in the trion-hole complex,  $F_{X,|\ell|=1}(\omega)$  defined in Eq. (4.37). The line width is fixed to  $\eta = 10^{-3}\varepsilon_X$ .

Here,  $\theta_q$  is the angle of the majority hole momentum variable  $\mathbf{q} = (q, \theta_q)$ , see Eq. (4.18). Due to time-reversal symmetry, the probability satisfies  $P_{-\ell}^{(n)} = P_\ell^{(n)}$  and it is normalized such that  $\sum_{\ell \in \mathbb{Z}} P_\ell^{(n)} = 1$ . We observe that, for eigenvalues up to the repulsive branch,  $E_n \lesssim E_R$ , the  $|\ell| \geq 2$  components have a negligible probability, so that the hole angular momentum is either  $\ell = 0$  or  $|\ell| = 1$ . Thus, in this energy interval,  $P_{\ell=0}^{(n)} \simeq 1 - 2P_{\ell=1}^{(n)}$ .

In order to relate this probability to frequency  $\omega$ , and to focus attention on those states which are optically active, it is convenient to define the angular-momentum-weighted exciton Green function as:

$$G_{X,\ell}(\omega) = \left(\frac{2g}{\Omega}\right)^2 \sum_n P_\ell^{(n)} \frac{\left|\frac{1}{\mathcal{A}} \sum_{\mathbf{k}} \varphi_{n\mathbf{k}}\right|^2}{\omega - E_n + i\eta_X}, \quad (4.34)$$

from which we can evaluate the angular-momentum-weighted spectral function as usual:

$$A_{X,\ell}(\omega) = -\frac{1}{\pi} \text{Im} G_{X,\ell}(\omega). \quad (4.35)$$

For  $\omega \lesssim E_R$ , we have

$$A_X(\omega) = \sum_{\ell \in \mathbb{Z}} A_{X,\ell}(\omega) \simeq A_{X,0}(\omega) + 2A_{X,1}(\omega), \quad (4.36)$$

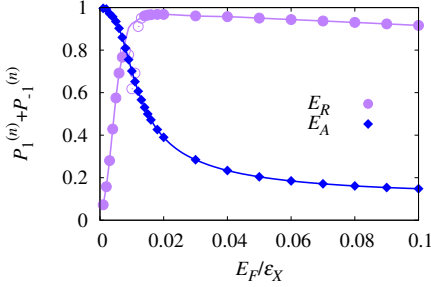


**Fig. 4.10:** Doping dependence of the  $p$ -wave orbital character ( $P_{\ell=1}^{(n)} + P_{\ell=-1}^{(n)}$ ) (4.33) of the eigenstate  $n$  closest to the attractive  $E_A$  and repulsive  $E_R$  branches of the ICP case at  $m_2/m_1 = 0.25$ . Symbols denote the values found from exact diagonalization. Empty symbols indicate values where a resonance with one of the continuum states occurs. Solid lines are a guide to the eye.

because the  $|\ell| \geq 2$  hole angular momentum components are suppressed. As such, we may define the fraction of the spectral function with angular momentum  $|\ell| = 1$  as

$$F_{X,|\ell|=1}(\omega) \equiv \frac{2A_{X,1}(\omega)}{A_X(\omega)}. \quad (4.37)$$

When this quantity is close to zero, the hole in the trion-hole complex is predominantly  $s$ -wave, while a value close to one means that it is nearly all  $p$ -wave. We show this in Fig. 4.9 by the colored area. Note that this plot is obtained at a low resolution ( $N_k = 10$ ) because evaluating the angular momentum character  $F_{X,|\ell|=1}(\omega)$  requires knowing the eigenstate in full, so we have to use a direct diagonalization routine rather than the iterative method. Nonetheless, we can still identify the attractive and repulsive branches by comparing these results with the spectral functions evaluated with a higher number of points via the iterative method, which establishes which peak positions are independent of  $N_k$ , and may thus be identified as the attractive and repulsive branches (see Fig. 4.5).

We observe that the symmetry of the peaks that we have previously identified as attractive and repulsive branches evolves as a function of doping. In particular, at very low doping — see Fig. 4.9 (a) — as expected, the hole (and thus the trion) of the trion-hole complex in the attractive branch has a  $p$ -wave symmetry, while the hole in the repulsive branch has  $s$ -wave symmetry. However, as  $E_F$  increases, the symmetries cross over so that at larger doping — see Fig. 4.9 (c) — the attractive branch becomes  $s$ -wave and the repulsive branch  $p$ -wave. Those states associated with the continuum do not change symmetry and remain  $s$ -wave at all dopings.

Note that, because attractive and repulsive peaks in Fig. 4.9 have constant values of the state fraction  $F_{X,1}(\omega)$  within their linewidth, we can characterize this symmetry in Fig. 4.10 by plotting the doping dependence of the probability  $P_{\ell=1}^{(n)} + P_{\ell=-1}^{(n)} = 2P_{\ell=1}^{(n)}$  for the eigenvalue  $E_n$  closest to the attractive  $E_A$  and repulsive  $E_R$  branches. When this quantity is zero, the hole (and trion) in the

trion-hole term is  $s$ -wave, while when it is one the hole and trion are  $p$ -wave. We observe that, as expected, at zero doping the attractive branch hole (and thus trion) has a  $p$ -wave symmetry, consistent with earlier arguments about the ground state of the trion for indistinguishable carriers. In the same limit, the repulsive branch hole (and thus trion) has an  $s$ -wave symmetry. At very low doping, when the attractive branch spectral weight  $Z_A$  has a quadratic dependence on  $E_F$ , the attractive branch is primarily  $p$ -wave and the repulsive branch  $s$ -wave. However, at larger doping, this switches to a regime where the attractive branch becomes instead  $s$ -wave and the repulsive branch  $p$ -wave. As noted previously the optically active continuum always retains the  $s$ -wave symmetry. When the continuum has the same or larger spectral weight of the repulsive branch, as seen at  $E_F \gtrsim 0.02\varepsilon_X$ , the repulsive branch is full  $p$ -wave. The different symmetry of the repulsive branch versus the continuum explains why the repulsive branch retains its Lorentzian shape with constant width  $\eta_X$ , and does not hybridize with the continuum. This behavior for the ICP case is very different than that seen for the DCP case — see Sec. 2.3.4.

Note that, in Fig. 4.10, while the orbital character of the attractive branch is smooth, the orbital character of the repulsive branch has a kink in a small interval of  $E_F$ . This is due to the coupling, at finite  $N_k$ , between the repulsive branch and one of the continuum states, as previously explained. For this reason, we plot these data points with empty rather than filled symbols.

#### 4.4.5 Strong coupling

We finally discuss how the above results obtained for the ICP case affect the spectrum in the regime of strong light-matter coupling. In Fig. 4.11 we plot the photon spectral function  $A_C(\omega)$  as a function of the photon-exciton detuning  $\delta$  and the frequency  $\omega$ , for two different values of  $E_F$ , for a Rabi splitting  $\Omega = 0.1\varepsilon_X$ , and for a mass ratio  $m_2/m_1 = 0.25$  at which the zero doping  $p$ -wave trion is bound—the same conditions as Figs. 4.6 (a) and 4.7 (a,c). This figure has been obtained by considering a Gaussian convolution of the exciton Green's function:

$$\frac{1}{\sqrt{2\pi}\sigma} \int d\omega' G_X^{(0)}(\omega') e^{-\frac{(\omega-\omega')^2}{2\sigma^2}}. \quad (4.38)$$

This convolution is used to reduce finite-size effects.

In Fig. 4.11 (a), we observe that, at low doping, the attractive branch has a negligible spectral weight and the attractive and repulsive branches are very close to each other, and therefore we only see two polariton branches. At larger  $E_F$  (panel (b)), we instead see three polariton branches, the LP, MP, and UP polariton. This occurs because the oscillator strength transfer from the repulsive to the attractive branch allows for anticrossings of the photon with both branches.

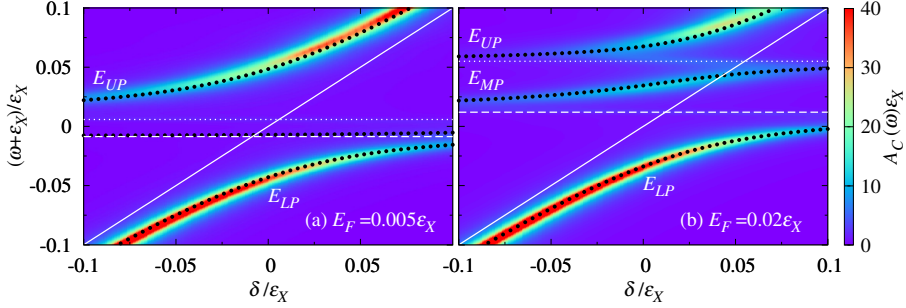


**Fig. 4.11:** Photon spectral function  $A_C(\omega)$  for the ICP case in the strong light-matter coupling regime, as a function of the photon-exciton, detuning  $\delta$  and the frequency  $\omega$ , for two different values of  $E_F$ . Attractive ( $\omega = E_A$ ) and repulsive ( $\omega = E_R$ ) branches evaluated in the weak coupling regime are plotted as dashed and dotted (white) lines, respectively. The black dots are the eigenvalues of the three-coupled oscillator model, Eq. (4.39), with parameters  $E_A$ ,  $E_R$ , and  $\Omega_{A,R} = \sqrt{Z_{A,R}}\Omega$  extracted from the weak coupling regime results (see panels (a) and (c) of Fig. 4.7). The mass ratio is  $m_2/m_1 = 0.25$ , the Rabi splitting  $\Omega = 0.1\epsilon_X$ , and the linewidth  $\eta = 5 \times 10^{-3}\epsilon_X$ . The exciton Green's function has been evaluated by applying a Gaussian convolution (4.38), with width  $\sigma = \eta$ .

In order to see the relation between the results in the strong coupling regime with those previously obtained in the weak coupling regime, we plot in Fig. 4.11 as (black) solid lines the eigenvalues of a three-coupled oscillator model:

$$\mathcal{H}_{3o} = \begin{pmatrix} -\epsilon_X + \delta & \Omega_A/2 & \Omega_R/2 \\ \Omega_A/2 & E_A & 0 \\ \Omega_R/2 & 0 & E_R \end{pmatrix}, \quad (4.39)$$

Here,  $E_{A,R}$  are the energies of the attractive and repulsive peaks obtained in Fig. 4.7 (a), while the effective Rabi splittings of attractive and repulsive branches are related to the branch spectral weights of Fig. 4.7 (b) via  $\Omega_{A,R} = \sqrt{Z_{A,R}}\Omega$  [341]. As Fig. 4.7 shows, there is perfect agreement between the polariton branches evaluated from the strong coupling spectral function and the eigenvalues of the three-coupled oscillator model (4.39)

## 4.5 Experiments

In order to observe the predictions of the work presented in the previous sections requires the  $p$ -wave trion state to be bound. As we have shown in Sec. 4.3, the positively charged trion  $X^+$  can bind when the ratio between the electron and the hole mass is sufficiently small [268, 272], i.e., for sufficiently more massive holes than the electron — see Fig. 4.4. For TMD monolayers, calculations for

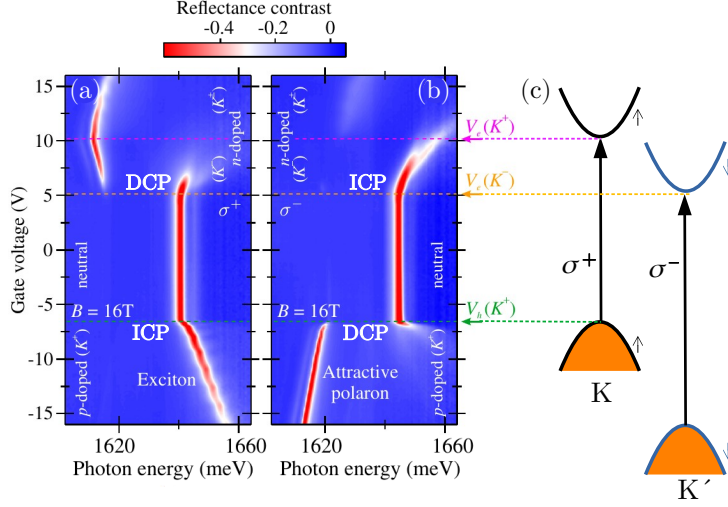


**Fig. 4.12:** Panels (a) and (b): Reflectance contrast spectra of a MoSe<sub>2</sub> TMD monolayer measured as a function of the gate voltage at a magnetic field  $B = 16$  T and probed for  $\sigma^+$  (a) and  $\sigma^-$  (b) circular polarization. The horizontal dashed lines indicate the positions of the bottoms (tops) of the conduction (valence) bands in panel (c). Adapted from Ref. [220].

MoX<sub>2</sub> (X=Se, S) indicate that the intravalley  $p$ -wave trion is unbound [270] because the electron-hole mass ratio is around one.

In Fig. 4.12 it is plotted the reflectance spectra for a MoSe<sub>2</sub> monolayer at a large enough magnetic field to reach full spin-valley polarisation — see Fig. 4.12 (c) — on the  $n$ -doped side up to voltages of around  $V_g \lesssim 10$  V and at all voltages on the  $n$ -side. Because of this, when the gate voltage reaches the minimum of the conduction band of the  $K'$  valley, the monolayer is doped with electrons with spin  $\downarrow$  ( $n$ -doped region). If the exciton is created in the  $K$  valley with a  $\sigma^+$  polarized light, we are in the DCP scenario and the optical response is dominated by the attractive and repulsive polaron branches. The attractive polaron branch energy redshifts at increasing doping, in contrast to the zero magnetic field case shown in Fig. 2.4 (a). This is because, in the fully spin-valley polarized regime shown here for voltages  $V_g \lesssim 10$  V, the exciton is not affected by Pauli blocking effects. For  $V_g \gtrsim 10$  V, the conduction band in the  $K$  valley starts to be populated as well and the gate dependence of the attractive branch now changes, showing instead a blueshift. By still using a  $\sigma^+$  polarised light and on the  $p$ -doped side the hole forming the exciton is identical to the holes that constitute the Fermi sea. This leads to the ICP scenario, where no attractive polaron branch is visible in the optical response, in agreement with the prediction that at these mass ratios the indistinguishable  $X^+$  trion is not bound. Here, only the repulsive branch is visible, in agreement with our

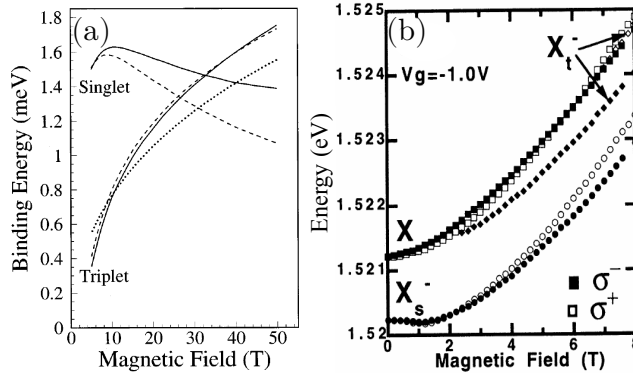


**Fig. 4.13:** (a) Prediction [277] for the symmetric singlet and antisymmetric triplet trion binding energies dependence on the magnetic field (solid lines), for a GaAs quantum well. Dashed lines are results obtained using the lowest subband approximation, while the dotted lines correspond to the lowest-Landau-level approximation. (b) Experimental results of Ref. [278] obtained from photoluminescence measurements for the trion and exciton energies for a GaAs quantum well in a perpendicular magnetic field.

predictions. The opposite situation arises when the exciton is generated in the  $K'$ -valley by a  $\sigma^-$  polarized light, as shown in Fig. 4.12 (b).

While in presence of electron doping the optical transitions evolve smoothly with the gate voltage, in the hole doping region they exhibit a pronounced oscillatory behavior. The oscillations visible in the spectra are due to the influence of the Landau levels quantization of the Fermi medium. While the attractive exciton-polaron branch is only weakly influenced by the magnetic field, the repulsive branch splits into a number of peaks separated by the Larmor frequency  $\omega_B$  [322, 466]. In Ref. [220], the authors speculated that the asymmetry between  $n$ - and  $p$ -doped region may be a consequence of the electron-hole effective mass ratio that exceeds unity (with a value around 2 [82, 485]), in contrast to *ab initio* calculations which predict both masses to be similar.

While the experimental detection of ICP is forbidden in TMD monolayers, due to electron and hole effective masses being too similar, some *ab initio* calculations [483, 484] has shown that the mass ratio of TMD monolayers is tunable, within a narrow range, by application of strain, either epitaxially or externally. Another way to potentially achieve ICP is by applying a stronger external magnetic field, which, in quantum well systems, has been predicted [273–277, 486] and demonstrated [278–280, 487] to increase the binding energies of charged excitons. Indeed calculations in this direction would be desirable.

As discussed in Sec.4.3.2, both  $X^-$  [278] and  $X^+$  [487]  $s$ -wave singlet trions are bound in GaAs quantum wells at zero magnetic field. Note that the terms triplet and singlet trions are commonly used in the literature to refer to  $p$ -wave

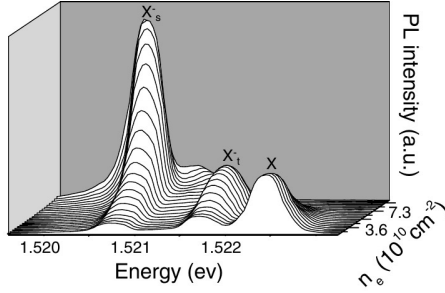


**Fig. 4.14:** Photoluminescence spectra of exciton ( $X$ ), triplet ( $X_t^-$ ), and singlet ( $X_s^-$ ) trions at  $B = 8$  T, as a function of doping [280].

and  $s$ -wave trions in quantum wells, respectively. This is because, unlike TMD monolayers, the particles involved possess only the spin degree of freedom. The electron-hole mass ratio for a GaAs is typically around  $m_e/m_h = 0.25$  [482], though there is not an exact value for this parameter, as it depends on various factors such as quantum well width and barrier composition [488]. For instance, the mass ratio reported in Ref. [487] is  $m_e/m_h = 0.58$ . The specific value of 0.25 is below the critical mass ratio of  $\sim 0.35$  discussed in Sec. 4.3.2 (see Fig. 4.4 (a)) and, as such, allows the existence of a weakly bound  $p$ -wave trion even at zero magnetic field. Yet, there has been not so far experimental evidence of the triplet trion  $X^+$  in absence of a magnetic field.

There has been however experimental evidence of bidding of the  $p$ -wave triplet trion  $X^+$  when a magnetic field is applied perpendicularly to the GaAs quantum well for a sufficiently high magnetic field [278–280, 487]. This is shown in Fig. 4.13 (b) where the experimental measurements for a negatively charged exciton in a GaAs quantum well obtained in Ref. [278] are reported. Fig. 4.13 (a) shows that, while for small values of the magnetic field, the singlet negatively charged exciton is the ground state, the triplet one eventually becomes the lowest energy one in the presence of a strong magnetic field, as evaluated in Ref. [277]. Similar results have also been obtained in CdTe quantum wells [489, 490].

Results from Ref. [280] have also indicated that, in the presence of a magnetic field and by increasing doping, the exciton oscillator strength can transfer to the triplet trion state. Fig. 4.14 (a) shows the effects of doping on the trion formation in a magnetic field of 8 T, as calculated in Ref. [280]. The exciton dominates the PL spectrum at low doping ( $\sim 3 \times 10^{10} \text{ cm}^{-2}$ ), but an increase of doping enhances the trion formation rate, reducing the exciton PL intensity and strengthening both singlet and triplet trion one. Ref. [280] extracted oscillator strength from the inverse decay rate obtained with photoluminescence experiments revealing an almost cubic dependence on the electron concentration, contrary to the quadratic behavior predicted by our calculations. Nonetheless, a more accurate estimation of the optical oscillator strength with respect to electron concentration is achievable by conducting reflectance or absorption

experiments. These experiments would provide a better assessment of our calculations' predictions.

## 4.6 Conclusions and perspectives

We have studied the optical properties of a doped 2D semiconductor, where one of the two charges forming the exciton is indistinguishable from those forming the Fermi sea induced by doping — a case we referred to as the ICP case. We have calculated the optical absorption, which describes transitions between the system ground state and states with an inter-band particle-hole pair (exciton). To describe the effects of the Fermi sea, we employed a polaron description where the exciton is dressed by a single intra-band particle-hole excitation of the Fermi sea.

The polaron formalism allows us to recover, at low doping, the properties of few-body complexes, i.e., the exciton and the trion. At the same time, this formalism allows one to describe the higher density many-body regime. From the comparison of our results with those obtained in the distinguishable (or DCP) case, we conclude that, while for the DCP case, the spectral function is always characterized by attractive and repulsive branches (because the associated  $s$ -wave trion is always bound), for the ICP case there are two branches only when the  $p$ -wave trion is bound, which requires sufficiently small minority to majority mass ratio.

Both the ICP and DCP cases show a transfer of oscillator strength from the repulsive to the attractive branch as one increases doping. Such a transfer of weight is possible because, in both cases, it is not the trion state itself which must couple to light, but rather a trion-hole complex (a complex consisting of three particles and a Fermi-sea hole) that indirectly couples to light via its coupling to the exciton. The spectral weight of the attractive branch has a different dependence on doping for the ICP and DCP cases: at low doping, in the DCP case it grows linearly with the Fermi sea density [266, 317], while in the ICP case, we find that it grows quadratically as a consequence of the  $p$ -wave nature of the trion state. In the regime of strong light-matter coupling, the transfer of oscillator strength to the attractive branch furthermore leads to the appearance of three polariton modes resulting from the anticrossing of the photon with both the attractive and repulsive branches. We have discussed how the Rabi splittings in the strong coupling polariton spectrum allow one to effectively measure the weak coupling quasiparticle weights.

The attractive polaron energy recovers, at low doping, the  $p$ -wave ( $s$ -wave) trion energy for the ICP (DCP) case. In both cases, this branch is a sharp Lorentzian-like peak of the spectral function, with a linewidth that does not change with doping. The repulsive polaron branch continuously connects at

low doping with the exciton energy. Because attractive and repulsive branches are separated by a continuum, the repulsive branch never coincides precisely with a system eigenstate. However, for the ICP case, the repulsive branch is, like the attractive branch, a sharp peak with a Lorentzian shape and a doping-independent broadening. This is in stark contrast with the DCP case, where the repulsive peak is a broad feature, involving multiple eigenstates, and has an asymmetric shape and a linewidth that increases with doping [265, 321]. The origin of the different nature of the repulsive branch in the ICP and DCP cases comes from the orbital character of the states involved. We show this by calculating the angular momentum of the three-particle (trion) and Fermi-sea hole components of the polaronic state, both for the repulsive branch and for the continuum. For the ICP case, at large enough doping, the repulsive branch and continuum states have different orbital characters and, thus, do not mix. For the DCP case, we also observe that the orbital characters of attractive and repulsive branches swap as one increases doping so that the Fermi-sea hole in the attractive branch has  $s$ -wave symmetry at high doping.

There are several directions in which this work can be generalized and extended. To start this, we have considered a simplified description of interactions, neglecting majority particle interactions and approximating the interaction between opposite charges as contact. We have seen that this is accurate to describe the binding-unbinding transition of the  $p$ -wave trion and, at the same time allows us to obtain the major qualitative results for the ICP polaron. In order to obtain quantitatively accurate results it would be interesting to include the effects of the long-range Coulomb interaction, something we plan for future work.

Moreover, we saw that to observe the results of our work, it is necessary to have a bound  $p$ -wave trion state, which can be achieved with a strong out-of-plane magnetic field. Our initial findings suggest that increasing doping in the presence of a magnetic field can lead to the transfer of the exciton oscillator strength to the  $p$ -wave trion state. Future studies may explore extending these results by including the effects of Landau quantization in the Fermi polaron regime of the ICP case. In this regime, one should be able to describe the spin-polarized case for a quantum well, where electrons occupy a single spin-polarized Landau level, allowing the description of the magnetic field-induced oscillator strength transfer from the exciton to the  $p$ -wave trion. This should also allow us to describe the magnetic oscillation which characterizes the polaron branches in TMD monolayer at small magnetic fields and to explore the possible enhancement of the  $p$ -wave trion binding energy in TMD, where the unitary electron-hole mass ratio forbids this state.

Another intriguing direction that would be extremely interesting to investigate as a future perspective of this work is how the different orbital characteristics of the ICP can affect the strength of polaron-polaron interactions. We

plan to analyze this scenario for both attractive and repulsive polarons as a function of charge density in future work.

## Chapter 5

# Pairing at extreme imbalance

*In this chapter we focus on pairing effects between a conduction band electron and a valence band hole and how this is modified by the presence of a Fermi sea of majority charges as well as the strong coupling to a microcavity photon field. We consider a microscopic theory that allows the modification of the electron-hole wave function by both the light-matter interaction and the Fermi sea. Using variational wave functions, we examine the competition between different electron-hole paired states for the specific cases of semiconducting III-V single quantum wells, electron-hole bilayers, and transition metal dichalcogenide monolayers embedded in a planar microcavity. We show how the Fermi sea of excess charges modifies both the electron-hole bound state (exciton) properties and the dielectric constant of the cavity active medium, which in turn affects the photon component of the polariton ground state. On the one hand, long-range Coulomb interactions and Pauli blocking of the Fermi sea promote electron-hole pairing with finite center-of-mass momentum, corresponding to an excitonic roton minimum. On the other hand, the strong coupling to the ultra-low-mass cavity photon mode favors zero-momentum pairs. We discuss the prospect of observing different types of electron-hole pairing in the photon spectrum.*

*The results discussed in this chapter have been published in the following publication:*

- [174] A. TIENE, J. LEVINSSEN, M. M. PARISH, A. H. MACDONALD, J. KEELING, and F. M. MARCHETTI:  
Extremely imbalanced 2D electron-hole-photon systems,  
[Phys. Rev. Research \*\*2\*\*, 023089 \(2020\)](#).

## 5.1 Introduction

We have discussed at length in Ch. 2 how recent technological progress has opened up the possibility to study the interplay between strong light-matter coupling and electronic doping in semiconductor structures [214, 217, 218, 321, 345, 350, 491, 492]. In this chapter, we will focus on pairing effects, i.e., on the two-body problem of a conduction band electron and a valence band hole, and we will determine the consequences on pairing of Pauli blocking from the Fermi sea, Coulomb interaction, and strong coupling to light.

Electron-hole systems with charge imbalance are expected to display exotic pairing phenomena such as the spontaneous appearance of excitons with finite center-of-mass (CoM) momentum [255, 256, 419, 493]. This finite CoM paired state is equivalent to the FFLO phase [257, 258], a spatially modulated paired phase first proposed in the context of spin-imbalanced conventional superconductors — see Sec. 2.4. The study of this inhomogeneous superfluid phase has attracted noticeable interest over the past five decades in a wide range of physical systems — see, e.g., the recent reviews [410, 413, 494]. However, a conclusive experimental observation of the FFLO state remains a challenge. Signatures and indirect evidence of the FFLO phase have been reported in heavy-fermion systems [495], layered organic superconductors [496–500], and iron-based superconductors [501]. There has also been related work on ultracold gases in 1D optical lattices, paving the way toward studying FFLO states in such systems [502]. It is therefore of particular interest to understand how such a state in an electron-hole system might be probed and controlled with light.

In this chapter, we discuss pairing effects in strongly carrier density imbalanced electron-hole 2D structures strongly coupled to a microcavity photon field. In the absence of light, it was previously shown that a sufficiently high density of excess charge causes the exciton energy to develop a roton minimum at finite CoM momentum [255, 256] that is related to the FFLO phase — see Sec. 5.3 for a detailed discussion. We discuss how strong coupling to light affects this excitonic FFLO roton minimum. While long-range Coulomb interactions and Pauli blocking promote the formation of a finite CoM momentum bound state, the strong coupling to low mass cavity photons tends to suppress such a phase. Conversely, the formation of an FFLO phase suppresses the coupling to light. We study the competition between these processes by deriving the phase diagram of the equilibrium extremely imbalanced electron-hole-photon system, focusing solely on pairing phenomena. We show that the exciton mode is affected not only by the presence of the majority species Fermi sea, but, at the same time, the excess charge modifies the dielectric constant of the active medium and, thus, it also affects the energy of the cavity photon mode. Con-

sequences of this predicted energy shift of the photon mode in the presence of a Fermi sea can be observed by comparing structures with different light-matter coupling, e.g., by embedding a different number of quantum wells into the planar cavity and thus in effect changing the Rabi splitting.

## 5.2 Model

We are going to make use of the fully microscopic model introduced in Ch. 1 describing an electron-hole system, interacting via Coulomb potential between all charges, and coupling via a photon field. We consider the fully spin polarized case, where electrons and holes are in a single spin state. In Sec. 4.1 we discussed how this can be achieved by introducing an external magnetic field. The system Hamiltonian reads as:

$$\hat{H} = \hat{H}_0 + \hat{H}_C + \hat{H}_{eh} + \hat{H}_{ehC} \quad (5.1a)$$

$$\hat{H}_0 = \sum_{\mathbf{k}, \sigma=1,2} \epsilon_{\sigma\mathbf{k}} \hat{c}_{\sigma\mathbf{k}}^\dagger \hat{c}_{\sigma\mathbf{k}} \quad (5.1b)$$

$$\hat{H}_C = \sum_{\mathbf{k}} \epsilon_{C\mathbf{k}} \hat{a}_{\mathbf{k}}^\dagger \hat{a}_{\mathbf{k}} \quad (5.1c)$$

$$\hat{H}_{eh} = \sum_{\sigma\sigma'} \sum_{\mathbf{k}\mathbf{k}'\mathbf{q}} \frac{W_{\mathbf{q}}^{\sigma\sigma'}}{2\mathcal{A}} \hat{c}_{\sigma\mathbf{k}}^\dagger \hat{c}_{\sigma'\mathbf{k}'}^\dagger \hat{c}_{\sigma'\mathbf{k}'+\mathbf{q}} \hat{c}_{\sigma\mathbf{k}-\mathbf{q}} \quad (5.1d)$$

$$\hat{H}_{ehC} = \frac{g}{\sqrt{\mathcal{A}}} \sum_{\mathbf{k}\mathbf{q}} \left( \hat{c}_{1\frac{\mathbf{q}}{2}+\mathbf{k}}^\dagger \hat{c}_{2\frac{\mathbf{q}}{2}-\mathbf{k}}^\dagger \hat{a}_{\mathbf{q}} + \text{h.c.} \right) . \quad (5.1e)$$

Here,  $\hat{c}_{\sigma\mathbf{k}}^\dagger$  ( $\hat{c}_{\sigma\mathbf{k}}$ ) and  $\hat{a}_{\mathbf{k}}^\dagger$  ( $\hat{a}_{\mathbf{k}}$ ) are the creation (destruction) electron-hole and cavity photon operators, and  $\epsilon_{\sigma\mathbf{k}} = \mathbf{k}^2/2m_\sigma$  (1.1) and  $\epsilon_{C\mathbf{k}} = \mathbf{k}^2/2m_C$  (1.31) are the electron-hole and cavity photon kinetic energies. We are measuring energies with respect to the energy gap  $E_g$ , which is thus set to zero throughout this chapter. The index  $\sigma, \sigma' = 1, 2$  is the electron-hole index — we use a notation where 1 stands for the majority particles and 2 for the minority one; which ones are electrons or holes is established by the value of the mass ratio  $m_2/m_1$ . For example,  $m_2/m_1 \sim 4$  [482] is the typical mass ratio between hole (minority) and electron (majority) particles in a GaAs quantum well. If instead, we consider  $\alpha = m_2/m_1 = 0.25$  it means that the electrons are the minority particles and the holes the majority ones.

As far as the Coulomb interaction terms between charges are concerned, we are going to consider two opposite situations. As explained later, the screening of Coulomb interaction induced by the majority carriers causes, in the absence of photons, a transition from bound to unbound excitonic states when the majority species density increases [255]. With the aim of including the possibility

of describing the binding-unbinding transition, we will present results for both the unscreened case, and for screened Coulomb interactions within the static random phase approximation (RPA). In RPA, the intraspecies potential reads as

$$V_{\mathbf{q}}^{sc} = \frac{V_{\mathbf{q}}}{1 - V_{\mathbf{q}}\Pi_1(\mathbf{q})} \quad (5.2a)$$

$$\Pi_1(\mathbf{q}) = \frac{N_s m_1}{2\pi} \left[ \frac{\sqrt{q^2 - 4\mathbf{k}_F^2}}{q} \theta(q - 2\mathbf{k}_F) - 1 \right], \quad (5.2b)$$

with  $N_s = 1$  for the spin polarized case and where  $V_{\mathbf{q}} = 2\pi e^2/\epsilon\mathbf{q}$  is the unscreened intraspecies potential (1.22a). In this chapter, we are also considering the possibility of electron and hole confinement in two separate wells. The bare potentials we consider are

$$W_{\mathbf{q}}^{11} = W_{\mathbf{q}}^{22} = V_{\mathbf{q}} \quad (5.3a)$$

$$W_{\mathbf{q}}^{12} = W_{\mathbf{q}}^{21} = -V_{\mathbf{q}}e^{-qd}, \quad (5.3b)$$

where  $d$  is the bilayers separation<sup>1</sup> In the screened case, the bare Coulomb interaction  $V_{\mathbf{q}}$  is substituted by the RPA screened potential  $V_{\mathbf{q}}^{sc}$ .

Considering screened interactions within RPA corresponds to effectively “dressing” the particles forming the exciton with density fluctuations, i.e., an infinite number of particle-hole pairs. RPA is expected to overestimate screening and provides a good approximation when the exciton Bohr radius greatly exceeds the interparticle spacing of the majority species, i.e.,  $a_X^2 n_1 \gg 1$ . RPA should be also reliable for sufficiently large bilayer distance  $d$ , since it removes the short-range interactions between electrons and holes where RPA has problems [503]. In the opposite limit,  $a_X^2 n_1 \ll 1$ , screening is negligible. With this in mind, unscreened and RPA screened interactions represent extreme limiting cases, thus allowing us to place a bound on the effect of screening in realistic materials.

### 5.2.1 Renormalization of the cavity photon energy

We have already seen in Ch. 1 that, modelling the electron-hole-photon coupling as a contact interaction as in  $\hat{H}_{\text{e-h-C}}$  (5.1), leads to an ultraviolet logarithmic divergence of the ground-state energy [140]. Since the details of the high-momentum physics, such as the band curvature due to the crystal lattice structure, are not included in our low-energy model, we will renormalize the ultraviolet divergence via the procedure described in Sec. 1.5.2. This allows to

<sup>1</sup> The single layer limit can be recovered by taking  $d \rightarrow 0$ .

deduce universal properties of our system that are independent of microscopic details.

We propose here an equivalent description of the renormalization procedure described in Sec. 1.5.2 by using, instead of a variational approach, Feynman diagrams [140]. The spectrum can be obtained from the poles of the photon Green's function, dressed to include the effects of the matter-light interaction. In this case, the retarded photon Green's function can be defined in terms of the photon self-energy as:

$$G_C(\omega) = \frac{1}{\omega - \epsilon_{C0} - \Sigma_C(\omega)}. \quad (5.4)$$

The photon self-energy  $\Sigma_C(\omega)$  includes the scattering effects because of electron-hole pair generation and it can thus be written in terms of the electron-hole Green's function as:

$$\Sigma_C(\omega) = \frac{g^2}{\mathcal{A}^2} \sum_{\mathbf{k}\mathbf{k}'} G(\omega, \mathbf{k}, \mathbf{k}'), \quad (5.5)$$

where  $G(\omega, \mathbf{k}, \mathbf{k}')$  is the electron-hole Green's function. This satisfies the Lippman-Schwinger equation [141]

$$G(\omega, \mathbf{k}, \mathbf{k}') = \frac{\delta_{\mathbf{k},\mathbf{k}'}}{\omega - \bar{\epsilon}_{\mathbf{k}}} - \frac{1}{\mathcal{A}} \sum_{\mathbf{k}''} \frac{V_{\mathbf{k}-\mathbf{k}''} G(\omega, \mathbf{k}'', \mathbf{k}')}{\omega - \bar{\epsilon}_{\mathbf{k}''}}, \quad (5.6)$$

where  $\bar{\epsilon}_{\mathbf{k}} = \epsilon_{1\mathbf{k}} + \epsilon_{2\mathbf{k}}$ . The first term on the right-hand side of Eq. (5.6) is the bare electron-hole pair retarded Green's function, while the second term accounts for all the possible repeated Coulomb interactions between the electron and the hole forming the exciton. The poles of Eq. (5.4) can thus be found solving

$$\omega - \epsilon_{C0} + \frac{g^2}{\mathcal{A}} \sum_{\mathbf{k}} \frac{1}{-\omega + \bar{\epsilon}_{\mathbf{k}}} = \frac{g^2}{\mathcal{A}^3} \sum_{\mathbf{k}\mathbf{k}'\mathbf{k}''} \frac{V_{\mathbf{k}-\mathbf{k}''} G(\omega, \mathbf{k}'', \mathbf{k}')}{\omega - \bar{\epsilon}_{\mathbf{k}''}} \quad (5.7)$$

As demonstrated in Ref. [140], while the right-hand side of this equation is convergent, the sum on the left depends logarithmically on the UV cutoff, making necessary the redefinition of the cavity photon frequency.

By carrying on the renormalization procedure at zero doping (see Sec. 1.5.2) in the weak coupling limit  $g \ll a_X \epsilon_X$ , the renormalized photon exciton detuning can be written as

$$\delta = \omega_{C0} - \epsilon_{X0}, \quad (5.8)$$

where  $\omega_{C\mathbf{0}}$  is the renormalized (finite and measurable) photon energy:

$$\omega_{C\mathbf{0}} \equiv \epsilon_{C\mathbf{0}} - \frac{g^2}{\mathcal{A}} \sum_{\mathbf{k}} \frac{1}{\varepsilon_X + \bar{\epsilon}_{\mathbf{k}}} . \quad (5.9)$$

In this limit, the Rabi coupling can be written as:

$$\Omega \equiv \frac{2g}{\mathcal{A}} \sum_{\mathbf{k}} \varphi_{1s\mathbf{k}} , \quad (5.10)$$

The definitions of the effective detuning, Eq. (5.8), and Rabi splitting, Eq. (5.10), represent a first-order approximation in the expansion parameter  $g \ll a_X \varepsilon_X$  to the experimentally measured detuning and Rabi splitting. An effort to obtain a better estimate of both parameters and a comparison with the approximation carried out here is discussed in App. E. There, we employ a definition of detuning and Rabi splitting which is similar to a possible experimental procedure. In this way, we find that the differences between the fitted parameters and those defined in Eqs. (5.8) and (5.10) are small. This implies only small quantitative changes in our results below when we push our results beyond the  $g \ll a_X \varepsilon_X$  validity regime of Eqs. (5.8) and (5.10).

## 5.2.2 Variational ansatz: FF, SF, and normal states

Because we want to describe how strong light-matter coupling affects the transition from having an exciton with zero CoM momentum to having one at finite CoM momentum, as doping increases, we focus on the extremely imbalanced limit, where there is a single minority particle  $\sigma = 2$  interacting with a Fermi liquid of majority particles  $\sigma = 1$ . To determine the mean-field zero temperature phase diagram, we find the ground state by a variational approach. The variational state we consider describes a superposition of a photon and an electron-hole pair, on top of a Fermi sea of majority particles,  $|FS\rangle = |FS\rangle_1 \otimes |0\rangle_2 \otimes |0\rangle_C$ :

$$|\Psi_{\mathbf{Q}}\rangle = \left( \sum_{\mathbf{k} > \mathbf{k}_F} \frac{\varphi_{\mathbf{k}}^{(\mathbf{Q})}}{\sqrt{\mathcal{A}}} \hat{c}_{1\mathbf{k}}^\dagger \hat{c}_{2\mathbf{Q}-\mathbf{k}}^\dagger + \alpha_0^{(\mathbf{Q})} \hat{a}_{\mathbf{Q}}^\dagger \right) |FS\rangle . \quad (5.11)$$

Here,  $\varphi_{\mathbf{k}}^{(\mathbf{Q})}$  and  $\alpha_0^{(\mathbf{Q})}$  are the excitonic and photonic variational parameters, respectively, and the normalization condition requires that

$$\langle \Psi_{\mathbf{Q}} | \Psi_{\mathbf{Q}} \rangle = \mathcal{A}^{-1} \sum_{\mathbf{k} > \mathbf{k}_F} |\varphi_{\mathbf{k}}^{(\mathbf{Q})}|^2 + |\alpha_0^{(\mathbf{Q})}|^2 = 1 . \quad (5.12)$$

The momentum  $\mathbf{Q}$  is the CoM momentum of the polaritonic bound state, while the label  $\mathbf{k}$  denotes the relative electron-hole momentum. Pauli blocking forbids occupation of all majority particle states below the Fermi momentum  $\mathbf{k}_F$ , and

we use the notation  $\sum_{\mathbf{k}>\mathbf{k}_F}$  to indicate summation over allowed states.

In the following, we will refer to the polaritonic bound state with finite CoM momentum  $|\Psi_{\mathbf{Q}\neq\mathbf{0}}\rangle$  as the Fulde-Ferrel (FF) state. Note that we use the notation FF rather than FFLO because the pairing wave function we consider is a single plane-wave, and thus it does not have any spatial modulation of density [257]. If we would consider increasing the density of minority particles, we expect a smooth evolution from the finite  $\mathbf{Q}$  bound state we describe here to a modulated coherent FFLO paired phase [419]. In the absence of cavity photons, the finite  $\mathbf{Q}$  bound state for a single impurity has already been analyzed for GaAs [255] and TMD [256] structures, where it was predicted to occupy a sizeable region of the phase diagram. For an imbalanced state of electron-hole bilayers, with a non-vanishing density of minority particles, an FFLO phase was also described in Refs. [419, 493].

Also by analogy to the terminology used to describe the states at non-zero minority density, we refer to the zero CoM momentum bound state  $|\Psi_{\mathbf{0}}\rangle$  as the superfluid (SF) state. For a finite minority particle density, the SF state is an excitonic condensate where pairing occurs for a balanced fraction of electrons and holes at zero CoM momentum (but finite relative momentum), while the excess majority species occupies a Fermi sea around  $\mathbf{k} = \mathbf{0}$ .

To find which state occurs in the presence of coupling to photons, we minimize  $\langle\Psi_{\mathbf{Q}}|\hat{H} - E|\Psi_{\mathbf{Q}}\rangle$  with respect to the complex amplitudes  $\varphi_{\mathbf{k}}^{(\mathbf{Q})}$  and  $\alpha_0^{(\mathbf{Q})}$  (5.11). This gives the coupled eigenvalue equations

$$(E - \xi_{\mathbf{k}\mathbf{Q}}) \varphi_{\mathbf{k}}^{(\mathbf{Q})} = - \sum_{\mathbf{k}'>\mathbf{k}_F} \frac{V_{\mathbf{k}-\mathbf{k}'}}{\mathcal{A}} \varphi_{\mathbf{k}'}^{(\mathbf{Q})} + g\alpha_0^{(\mathbf{Q})} \quad (5.13a)$$

$$(E - \nu_{C\mathbf{Q}}) \alpha_0^{(\mathbf{Q})} = \frac{g}{\mathcal{A}} \sum_{\mathbf{k}>\mathbf{k}_F} \varphi_{\mathbf{k}}^{(\mathbf{Q})} . \quad (5.13b)$$

The lowest energy eigenvalue  $E$  represents the energy of a bound lower polariton state in the presence of a Fermi sea, accounting for the modification of the exciton wave function both by light-matter coupling and by Pauli blocking. Here,  $\xi_{\mathbf{k}\mathbf{Q}} = \epsilon_{2\mathbf{Q}-\mathbf{k}} + \epsilon_{1\mathbf{k}} - \frac{1}{\mathcal{A}} \sum_{\mathbf{k}'<\mathbf{k}_F} U_{\mathbf{k}-\mathbf{k}'}$  includes the exchange correction to the electron dispersion. We neglect the energy of the interacting Fermi sea  $|FS\rangle$ ,  $\mathcal{E}_{FS} = \sum_{\mathbf{k}<\mathbf{k}_F} [\epsilon_{1\mathbf{k}} - \sum_{\mathbf{k}'<\mathbf{k}_F} U_{\mathbf{k}-\mathbf{k}'}/(2\mathcal{A})]$ , because we are interested in comparing  $E$  with that of the normal state, which also includes  $\mathcal{E}_{FS}$ .

Indeed, we find that at large majority particle density, the finite CoM momentum exciton can undergo an unbinding transition to the normal (N) state. This comprises an unbound minority particle on top of a Fermi sea of majority particles:

$$|\Psi_N\rangle = \hat{c}_{20}^\dagger \hat{c}_{1\mathbf{k}_F}^\dagger |FS\rangle , \quad (5.14)$$

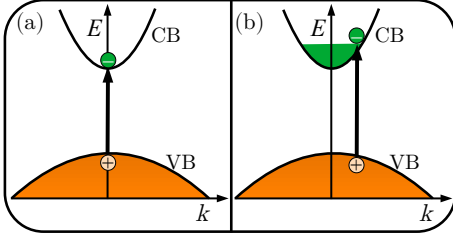


**Fig. 5.1:** Particle-hole excitation process following the absorption of a photon in absence (a) and with (b) a Fermi sea.

where  $\hat{\mathbf{k}}$  is an arbitrary direction, and this state has energy

$$E_N = E_F - \frac{1}{\mathcal{A}} \sum_{\mathbf{k}' < \mathbf{k}_F} U_{\mathbf{k}_F - \mathbf{k}'}, \quad (5.15)$$

where, as for  $E$ , we neglect the energy of the interacting Fermi sea,  $\mathcal{E}_{FS}$ . The excitonic FF state  $|\Psi_{\mathbf{Q}}\rangle$  (5.11) would reduce to the normal state  $|\Psi_N\rangle$  when we take  $\mathbf{Q} = \mathbf{k}_F$  and the exciton wave function takes the form,  $\varphi_{\mathbf{k}}^{(\mathbf{Q})} = \sqrt{\mathcal{A}}\delta_{\mathbf{k}, \mathbf{k}_F}$ . This corresponds to a wave function that has weight only when relative and CoM momenta are equal, and match the Fermi momentum  $\mathbf{k}_F$ .

It is worth noting that when this state occurs, the only possible normal state is purely electronic — i.e., it has zero photon fraction and is thus given by Eq. (5.14). This can be seen from the renormalization scheme of the photon energy (5.9), which has the consequence that any non-zero photon fraction always implies a bound state between minority and majority particles. That is to say, the presence of light can bind an otherwise unbound electron-hole pair.

### 5.2.3 Effective photon energy in presence of a Fermi gas

In order to understand how the ground state evolves with doping, it is instructive to consider how the effective photon energy changes as the majority density increases, due to a modification of the dielectric constant of the quantum well. As described in Sec. 1.5.2, in order to reproduce the experimental protocol for measurements, we have defined the renormalization of the photon energy using a procedure defined at zero gating/doping  $E_F = 0$ . This means that we define the renormalized photon energy  $\omega_{C\mathbf{Q}}$  (or equivalently the photon-exciton detuning  $\delta$ ) in such a way that it approximately matches what would be experimentally measured at  $E_F = 0$ . As illustrated in Fig. 5.1, the available particle-hole excitations contributing to the dressing of the photon propagator depend on  $E_F$ . As such, at a finite density of majority species, the effective photon energy  $\omega_{C\mathbf{Q}}^{(E_F)}$  differs from  $\omega_{C\mathbf{Q}}$  defined at  $E_F = 0$ . In this section, we want to identify and estimate the photon energy renormalization in the presence of doping.

We start by rewriting the eigenvalue equations (5.13a) and (5.13b) in an

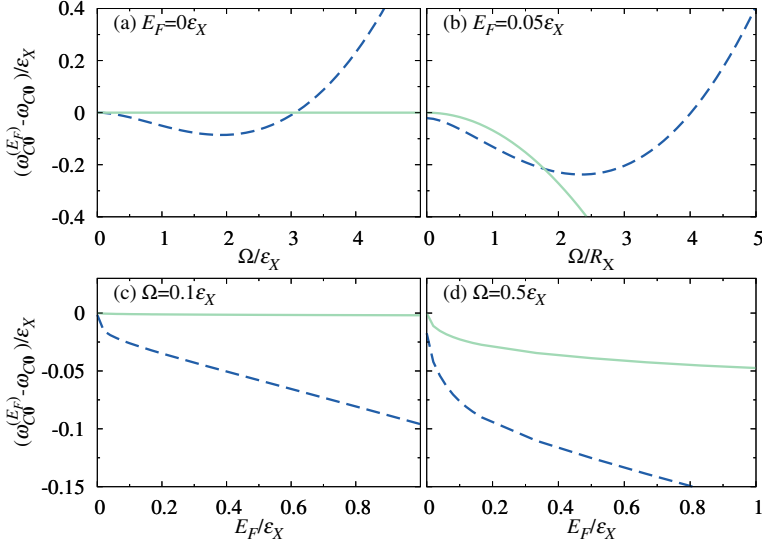


**Fig. 5.2:** Photon energy shift in presence of a Fermi gas  $\omega_{C0}^{(E_F)} - \omega_{C0}$  as estimated from Eq. (5.18) (solid line) and from Eq. (5.20) (dashed line) for either fixed Fermi energy  $E_F$  and varying Rabi splitting  $\Omega$  (a, b) or conversely fixed  $\Omega$  and varying  $E_F$  (c, d). Parameters are for a GaAs single quantum well ( $d = 0$ ), mass ratio  $m_2/m_1 = 0.25$ , and screened interactions  $N_s = 1$ .

equivalent form by inserting Eq. (5.13a) in (5.13b) and defining the new wave function  $\beta_{\mathbf{k}}^{(\mathbf{Q})} = \frac{1}{\mathcal{A}} \sum_{\mathbf{k}' > \mathbf{k}_F} V_{\mathbf{k}-\mathbf{k}'} \varphi_{\mathbf{k}'}^{(\mathbf{Q})} / (-E + \xi_{\mathbf{k}\mathbf{Q}})$ :

$$\left( E - \epsilon_{C\mathbf{Q}} + \frac{g^2}{\mathcal{A}} \sum_{\mathbf{k} > \mathbf{k}_F} \frac{1}{-E + \xi_{\mathbf{k}\mathbf{Q}}} \right) \alpha_0^{(\mathbf{Q})} = \frac{g}{\mathcal{A}} \sum_{\mathbf{k} > \mathbf{k}_F} \beta_{\mathbf{k}}^{(\mathbf{Q})}. \quad (5.16)$$

The divergence of the sum on the left-hand side of Eq. (5.16) is exactly canceled by the renormalization of the bare photon energy  $\epsilon_{C\mathbf{Q}}$  by particle-hole excitations, as described in Sec. 1.5.2. The form of Eq. (5.16) suggests that, in the presence of a Fermi sea, the effective renormalized photon energy can be estimated as

$$\omega_{C\mathbf{Q}}^{(E_F)} \simeq \epsilon_{C\mathbf{Q}} - \frac{g^2}{\mathcal{A}} \sum_{\mathbf{k} > \mathbf{k}_F} \frac{1}{-E + \xi_{\mathbf{k}\mathbf{Q}}}. \quad (5.17)$$

This estimate is expected to be valid in the limit of small light-matter coupling and sufficiently small density, where there is a well-defined exciton bound state with energy  $E_{X\mathbf{Q}}^{(E_F)}$  that is only weakly perturbed by light. In this limit, one can approximate  $E \simeq E_{X\mathbf{Q}}^{(E_F)}$ <sup>2</sup>. Taking the CoM momentum to be zero, we

<sup>2</sup>  $E_{X\mathbf{Q}}^{(E_F)}$  is the exciton energy at finite doping and CoM momentum.

then estimate the difference between  $\omega_{C\mathbf{0}}^{(E_F)}$  and the photon energy  $\omega_{C\mathbf{0}}$  at zero doping (5.9) as<sup>3</sup>

$$\omega_{C\mathbf{0}}^{(E_F)} - \omega_{C\mathbf{0}} \simeq -\frac{g^2}{\mathcal{A}} \left[ \sum_{\mathbf{k} > \mathbf{k}_F} \frac{1}{-E_{X\mathbf{0}}^{(E_F)} + \xi_{\mathbf{k}\mathbf{0}}} - \sum_{\mathbf{k}} \frac{1}{-E_{X\mathbf{0}} + \epsilon_{1\mathbf{k}} + \epsilon_{2\mathbf{k}}} \right]. \quad (5.18)$$

This energy difference is clearly finite because the logarithmic divergence of the first sum cancels with the one of the second sum. Thus, we see that the photon energy shift with doping depends quadratically on the light-matter coupling strength  $g$ , provided  $\Omega \ll |E_{X\mathbf{0}}^{(E_F)} - E_N|$ . By numerically evaluating the density dependence of the exciton energy at  $\mathbf{Q} = \mathbf{0}$ ,  $E_{X\mathbf{0}}^{(E_F)}$ , as well as the exchange correction to the electron dispersion, we find that, in the small  $\Omega$  and  $E_F$  limit, the photon energy shift  $\omega_{C\mathbf{0}}^{(E_F)} - \omega_{C\mathbf{0}}$  is always negative — see the solid line of Fig. 5.2). Such a shift could be observed in experiments by either comparing structures with different Rabi splittings or by changing the doping.

An alternative way of estimating the photon energy shift  $\omega_{C\mathbf{0}}^{(E_F)} - \omega_{C\mathbf{0}}$  in presence of a Fermi sea, is by identifying the detuning  $\delta_{50\%}$  at which the  $\mathbf{Q} = \mathbf{0}$  exciton state and the cavity photon are at resonance:

$$\omega_{C\mathbf{0}}^{(E_F)} = E_{X\mathbf{0}}^{(E_F)}. \quad (5.19)$$

We assume that this condition is satisfied when the photon fraction  $|\alpha_0^{(0)}|^2$  is 1/2. We can rewrite the condition (5.19), which defines the detuning at resonance,  $\delta_{50\%}$ , by subtracting the energy of the photon mode at zero doping/gating  $\omega_{C\mathbf{0}}$  (5.9) from both sides. Then using the definition  $\delta = \omega_{C\mathbf{0}} - E_{X\mathbf{0}}$  on the right-hand side gives:

$$\omega_{C\mathbf{0}}^{(E_F)} - \omega_{C\mathbf{0}} = E_{X\mathbf{0}}^{(E_F)} - E_{X\mathbf{0}} - \delta_{50\%}. \quad (5.20)$$

We can thus estimate the photon shift  $\omega_{C\mathbf{0}}^{(E_F)} - \omega_{C\mathbf{0}}$  at a fixed value of  $E_F$  and  $\Omega$  by evaluating  $E_{X\mathbf{0}}^{(E_F)} - E_{X\mathbf{0}}$ , i.e., by solving Eq. (5.21), and by numerically estimating the value of detuning  $\delta_{50\%}$  at which the photon fraction is exactly 1/2. The results of this estimate are plotted in Fig. 5.2 and compared with those obtained from Eq. (5.18). Note that, even at  $E_F = 0$ , this estimate predicts a photon energy shift because, beyond the weak coupling regime  $g \ll a_X \epsilon_X$ , the exciton wave function is strongly modified by light-matter coupling, affecting the definition of detuning  $\delta$  given in Eq. (1.38) (see discussion in App. E and Fig. E.1). At small and finite  $E_F$ , the estimates given by Eqs. (5.18) and (5.20) agree for small  $\Omega$  giving a negative shift of the photon energy, while, when  $\Omega$

<sup>3</sup>  $E_{X\mathbf{0}}$  is the exciton energy at  $E_F = 0$  and  $\mathbf{Q} = \mathbf{0}$ . In the specific case of single layer geometry and bare Coulomb interaction it can be related to the 1s exciton binding energy Eq. (1.17), i.e.,  $E_{X\mathbf{0}} = \epsilon_{X\mathbf{0}} = -\epsilon_X$ .

increases, Eq. (5.20) predicts an upturn of the shift to positive values.

Predicting the exact behavior of  $\omega_{C\mathbf{0}}^{(E_F)} - \omega_{C\mathbf{0}}$  with either  $\Omega$  or  $E_F$  is non-trivial, since both estimates of Eqs. (5.18) and (5.20) are based on the assumption that the system does behave like a two-level coupled oscillator model, an hypothesis which loses validity when either  $\Omega$  or  $E_F$  increases. As we will see in Sec. 5.4, the shift of the photon energy with doping has little consequence for the phase diagram at fixed Rabi splitting  $\Omega$ , while the implications are larger when we fix  $E_F$  and change  $\Omega$ .

### 5.3 Weak coupling regime

In absence of a microcavity confining the photon field, it was previously shown for an electron-hole bilayer [255] that a sufficiently high density of excess charge causes the exciton to develop a minimum at finite center of mass momentum, analogous to a roton minimum, which, as explained in Sec. 2.4, is also analogous of the FF [257] phase. These results have been recently extended to consider the interaction potential relevant for TMD monolayers in Ref. [256]. We are going to review briefly these results in this section.

The weak coupling regime means the system is probed in absence of the microcavity; so to all effects, it is described by the Hamiltonian (5.1) with  $g = 0$  and by the ansatz (5.11) with  $\alpha_0^{(\mathbf{Q})} = 0$ . The ground state energy of an exciton state in presence of a Fermi sea can be obtained by solving the following Schrödinger equation:

$$(E - \xi_{\mathbf{k}\mathbf{Q}}) \varphi_{\mathbf{k}}^{(\mathbf{Q})} = - \sum_{\mathbf{k}' > k_F} \frac{V_{\mathbf{k}-\mathbf{k}'}}{\mathcal{A}} \varphi_{\mathbf{k}'}^{(\mathbf{Q})}. \quad (5.21)$$

Note that the eigenvalue equation (5.21) coincides, in the limit of extreme imbalance, with the mean-field gap equation employed to describe the BEC-BCS crossover in imbalanced electron-hole bilayers [493, 504, 505]. To see this, we neglect the intra-layer Coulomb repulsion and rewrite Eq. (5.21) in terms of the gap  $\Delta_{\mathbf{k}}^{(\mathbf{Q})} \equiv 1/\mathcal{A} \sum_{\mathbf{k}' > k_F} V_{\mathbf{k}-\mathbf{k}'} \varphi_{\mathbf{k}'}^{(\mathbf{Q})}$ :

$$\Delta_{\mathbf{k}}^{(\mathbf{Q})} = \frac{1}{\mathcal{A}} \sum_{\mathbf{k}' > k_F} \frac{V_{\mathbf{k}-\mathbf{k}'}}{\mathcal{A}} \frac{\Delta_{\mathbf{k}'}^{(\mathbf{Q})}}{-E + \epsilon_{2\mathbf{Q}-\mathbf{k}'} + \epsilon_{1\mathbf{k}'}}. \quad (5.22)$$

It is easy to show that this equation is the linearized version of the mean-field gap equation for a balanced electron-hole condensate at zero temperature. Indeed, for balanced electron and hole populations, even a small attractive interaction can lead to an instability of the normal state to a condensed state, similar to what occurs to conventional superconductors within the BCS the-

ory [116]. Here, the ground state can be described by a coherent superposition of electron-hole pairs:

$$|\Phi\rangle = \prod_{\mathbf{k}} (u_{\mathbf{k}} + v_{\mathbf{k}} \hat{c}_{1\mathbf{k}}^\dagger \hat{c}_{2-\mathbf{k}}^\dagger) |0\rangle, \quad (5.23)$$

where  $|u_{\mathbf{k}}|^2 + |v_{\mathbf{k}}|^2 = 1$ . This state is able to describe exciton condensation in both the low and high density regimes, in what is referred to as the BEC-BCS crossover [506]. In the small density limit,  $n \ll a_X^{-2}$ , excitons do not overlap and they can be treated as tightly bound bosons so that they undergo Bose-Einstein condensation [104, 133]. In the opposite regime of large densities,  $n \gg a_X^{-2}$ , the Coulomb attraction is screened and condensation of loosely bound excitons resembles the same description as the BCS formulation of superconductivity. However, being excitons neutral objects, this limit is known as the exciton insulator state [507]. By minimizing the expectation value of the Hamiltonian (5.1) in the grand canonical ensemble,  $\langle \Phi | \hat{H} - \mu \hat{N} | \Phi \rangle$ , where  $\mu$  is the chemical potential fixing a balanced mean number of electrons and holes  $N = \langle \Phi | \hat{N} | \Phi \rangle$ , one gets a BCS-like set of equations [508] that have to be solved self-consistently:

$$\chi_{\mathbf{k}} = \epsilon_{e\mathbf{k}} + \epsilon_{h\mathbf{k}} - \mu - \sum_{\mathbf{k}'} W_{\mathbf{k}-\mathbf{k}'}^{11} \left( 1 - \frac{\chi_{\mathbf{k}'}}{E_{\mathbf{k}'}} \right) \quad (5.24a)$$

$$\Delta_{\mathbf{k}} = \sum_{\mathbf{k}'} W_{\mathbf{k}-\mathbf{k}'}^{12} \langle \hat{c}_{1\mathbf{k}'}^\dagger \hat{c}_{2-\mathbf{k}'}^\dagger \rangle = \sum_{\mathbf{k}'} W_{\mathbf{k}-\mathbf{k}'}^{12} \frac{\Delta_{\mathbf{k}'}}{E_{\mathbf{k}'}} \quad (5.24b)$$

$$N = \sum_{\mathbf{k}} \left( 1 - \frac{\chi_{\mathbf{k}}}{E_{\mathbf{k}}} \right) \quad (5.24c)$$

where

$$E_{\mathbf{k}} = \sqrt{\chi_{\mathbf{k}}^2 + |\Delta_{\mathbf{k}}|^2}, \quad (5.25)$$

is the quasiparticle excitation spectrum, i.e., the energy cost of taking one pair out of the condensate and adding either an electron or removing a hole. Eq. (5.24a) is the renormalized single particle kinetic energy of the relative degree of freedom. Eq. (5.24b) is the gap equation and Eq. (5.24c) fixes the mean number of particles in the system.

To complete the correspondence between Eq. (5.21) and the linearised mean-field gap equation, we require that the chemical potential of the minority particles is  $\mu_2 = E - k_F^2/2m_1$  and the chemical potential of the majority particles is  $\mu_1 = k_F^2/2m_1$ . Thus, the conditions for a bound state outlined above require that  $\mu_2 < 0$ , implying that  $\mu_2$  gives the exciton binding energy in this limit, which also matches with the mean-field theory.

In Ref. [255] the eigenvalue problem in Eq. (5.21) has been solved for parameters relevant for GaAs electron-hole bilayers and for both unscreened and

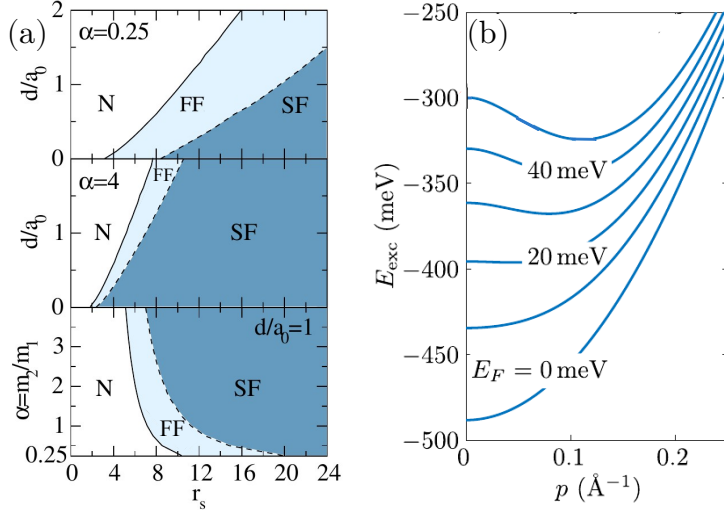


**Fig. 5.3:** (a) Phase diagram for mean-field pairing in the extremely imbalanced limit as a function of the interaction parameter  $r_s$ , as obtained in Ref. [255]. In the top two panels, the bilayer distance  $d$  varies while the mass ratio  $\alpha = m_2/m_1$  is fixed. In the bottom panel,  $\alpha$  varies and  $d$  is fixed. The inter- and intra-layer interactions have been screened using the RPA approximation in all cases. The region of SF corresponds to excitons with CoM momentum  $Q = 0$ , while the FF excitons have their lowest energy when  $Q \neq 0$ . The N region is where there are no bound excitons. (b) Exciton dispersion as a function of the CoM momentum  $p$  at different Fermi energies  $E_F$  in a doped MoSe<sub>2</sub> monolayer. Adapted from Ref. [256].

RPA screened inter- and intra-layer Coulomb interactions. In Fig. 5.3(a) results regarding the latter are shown. The interaction parameter utilized here is the dimensionless parameter  $r_s$ , given by  $r_s = \frac{m_1 e^2}{\epsilon \sqrt{\pi n_1}} = \frac{2}{k_F a_X}$ . This represents the ratio between the Coulomb interaction and the kinetic energy of the majority particle. The electron-hole mass ratios considered are those relevant to GaAs bilayers, with  $\alpha = \frac{m_2}{m_1} = [0.25, 4]$  [482]. In the low-density limit, as  $r_s \rightarrow \infty$ , the two-body limit is recovered, and it is expected that a bound exciton with  $Q = 0$ , i.e., an SF phase, will emerge. In contrast, in the opposite limit, where  $r_s$  is small, the screened interactions cause the exciton to eventually unbind and enter the N phase.

It should be noted that, as discovered in Ref. [255], the presence of the normal phase is a result of using a screened Coulomb interaction, as the bare Coulomb interaction always allows for a bound state. Indeed, looking at the gap equation (5.22) in presence of a bare Coulomb potential

$$\Delta_{\mathbf{k}}^{(\mathbf{Q})} = - \int_{\mathbf{k}' > k_F} \frac{d^2 \mathbf{k}'}{2\pi} \frac{e^{-d|\mathbf{k}-\mathbf{k}'|}}{|\mathbf{k}-\mathbf{k}'|} \frac{\Delta_{\mathbf{k}'}^{(\mathbf{Q})}}{-E + \epsilon_{2\mathbf{Q}-\mathbf{k}'} + \epsilon_{1\mathbf{k}'}} , \quad (5.26)$$

at the unbinding transition  $E = E_N = E_F$ , the integral is logarithmically divergent for  $\mathbf{Q} = \mathbf{k} = \mathbf{k}' = \mathbf{k}_F$  and so one must take  $\mathbf{k}_F = \infty$  for the equation to be satisfied. This implies that for the bare Coulomb inter-layer interaction the exciton with momentum  $\mathbf{Q} = \mathbf{k}_F$  for large  $\mathbf{k}_F$  is always bound. This is not the case for screened interaction, since the singularity at  $\mathbf{k} = \mathbf{k}'$  is removed, leaving an integrable singularity at  $\mathbf{Q} = \mathbf{k}' = \mathbf{k}_F$ .

The key point to note in Fig. 5.3 (a) is that for intermediate densities in a significant area of the phase diagram, the ground state of the system is a bound exciton with a finite momentum  $\mathbf{Q}$ , labeled as FF. The size of the FF region is largest when the minority particle is an electron ( $\alpha = 0.25$ ), rather than a hole ( $\alpha = 4$ ). The region is generally enhanced (and shifted to larger  $r_s$ ) when the minority particle is lighter, as shown in the lower panel of Fig. 5.3 (a). The reason for this is straightforward: An exciton with  $\mathbf{Q} = \mathbf{0}$  requires the minority particle to be above the Fermi sea, but a small mass ratio  $\alpha$  increases the kinetic energy cost for this, thus promoting the formation of an FF exciton, where the minority particle can sit below the Fermi surface. The FF region is also enlarged by increasing the distance between the bilayers,  $d$ . For large  $d$ , scattering with large momentum  $|\mathbf{k} - \mathbf{k}'| > 1/d$  is suppressed in  $V_{\mathbf{k}-\mathbf{k}'}^{sc}$ , which favors the FF state, where the wave function  $\varphi_{\mathbf{k}}^{(\mathbf{Q})}$  is peaked in the direction of  $\mathbf{Q}$ , over the SF state. However, a larger  $d$  requires a larger  $r_s$  to achieve FF, and Wigner crystallization is expected to eventually destroy FF. Quantum Monte Carlo calculations estimate that Wigner crystallization occurs when  $r_s \sim 70\alpha/(1 + \alpha)$  [246]. Therefore, the distance  $d$  required to observe FF sensitively depends on  $\alpha$ , for instance, for  $\alpha = 0.25$ , a distance of  $d/a_X \sim 1$  is desirable.

Recently, the appearance when increasing doping of an FF phase was also predicted in TMD monolayers. Ref. [256] investigated the elementary optical excitations, in the extreme imbalanced fully polarized scenario, for a MoSe<sub>2</sub> monolayer. In Ref. [256] the eigenvalue problem Eq. (5.21) is solved by employing the Rytova-Keldish electron-hole interaction (1.29), and fixing a mass ratio  $\alpha = 1.05$  ( $m_e = 0.56m_0$  and  $m_h = 0.59m_0$ ). The exciton dispersion they obtained is shown in Fig. 5.3 (b) for Fermi energies ranging from  $E_F = 0$  meV to  $E_F = 50$  meV. A roton minimum appears in the elementary optical excitations when the electron density is increased, which arises from the interplay between Pauli exclusion of excitons and the electron Fermi sea, and the long-range Coulomb interaction and the nonlocal dielectric screening, which are distinctive features of monolayers.

## 5.4 Strong coupling regime

We obtain the ground-state phase diagram in the strong coupling regime by numerically diagonalizing the coupled equations (5.13) and analyzing the nature of the lowest energy state, while comparing it with the energy of the normal state (5.15). We use a non-linear grid in the relative momentum  $\mathbf{k}$ -space — see App.A, and evaluate, at a given value of the CoM momentum  $\mathbf{Q}$ , the lowest eigenvalue  $E$  and the associated excitonic  $\varphi_{\mathbf{k}}^{(\mathbf{Q})}$  and photonic  $\alpha_0^{(\mathbf{Q})}$  eigenvectors, with  $|\alpha_0^{(\mathbf{Q})}|^2$  representing the state photon fraction. The results we show are numerically converged with respect to the number of points employed in the momentum grid. We then minimize the energy  $E$  with respect to  $Q \equiv |\mathbf{Q}|$ , and indicate the momentum at which the energy is minimized by  $Q_{\min}$ .

In the following we rescale energies by the 2D exciton binding energy  $\varepsilon_X$  (1.17) and lengths by the exciton Bohr radius  $a_X$  (1.16). Hence, only a few independent dimensionless parameters are left to characterize the system properties and phase diagram, namely, the mass ratio between minority and majority particles  $m_2/m_1$ , the rescaled bilayer distance  $d/a_X$ , the dimensionless majority particle density  $E_F/\varepsilon_X$ , the photon-exciton detuning  $\delta/\varepsilon_X$  (5.8), and the Rabi splitting  $\Omega/\varepsilon_X$  (5.10).

### 5.4.1 Quantum wells in planar microcavities

We first consider the case of a GaAs quantum well system embedded in a microcavity. In Fig. 5.4 we show our calculated phase diagram as a function of majority particle density and detuning, keeping the Rabi splitting fixed. We compare the results for both screened and unscreened Coulomb interactions, for a single quantum well ( $d = 0$ ) and a bilayer geometry ( $d = a_X$ ), and for one electron in a Fermi sea of holes ( $m_2/m_1 = 0.25$ ) and one hole in a Fermi sea of electrons ( $m_2/m_1 = 4$ ). In all cases, we see that the coupling to cavity light modes suppresses the formation of the finite momentum FF state as compared to the case without light-matter coupling. In particular, a strong coupling to light favors the  $\mathbf{Q} = \mathbf{0}$  state, since the photon mode at non-zero  $\mathbf{Q}$  is at high energy, due to the small photon mass. As such, strong coupling to light imposes that for detunings below a minimal value,  $\delta < \delta_{\min}$ , only the  $\mathbf{Q} = \mathbf{0}$  SF phase is allowed.

Fixing the detuning  $\delta > \delta_{\min}$  and increasing  $E_F$ , one first finds an SF-FF transition between a  $\mathbf{Q} = \mathbf{0}$  mixed polariton state and a  $Q_{\min} \neq 0$  FF state weakly coupled to light. This occurs because the energy gained by forming a finite  $\mathbf{Q}$  exciton state is larger than that obtained by dressing the  $\mathbf{Q} = \mathbf{0}$  exciton with a zero momentum photon. For screened interactions, the transition can be directly to the unbound N state, while for unscreened interactions there is

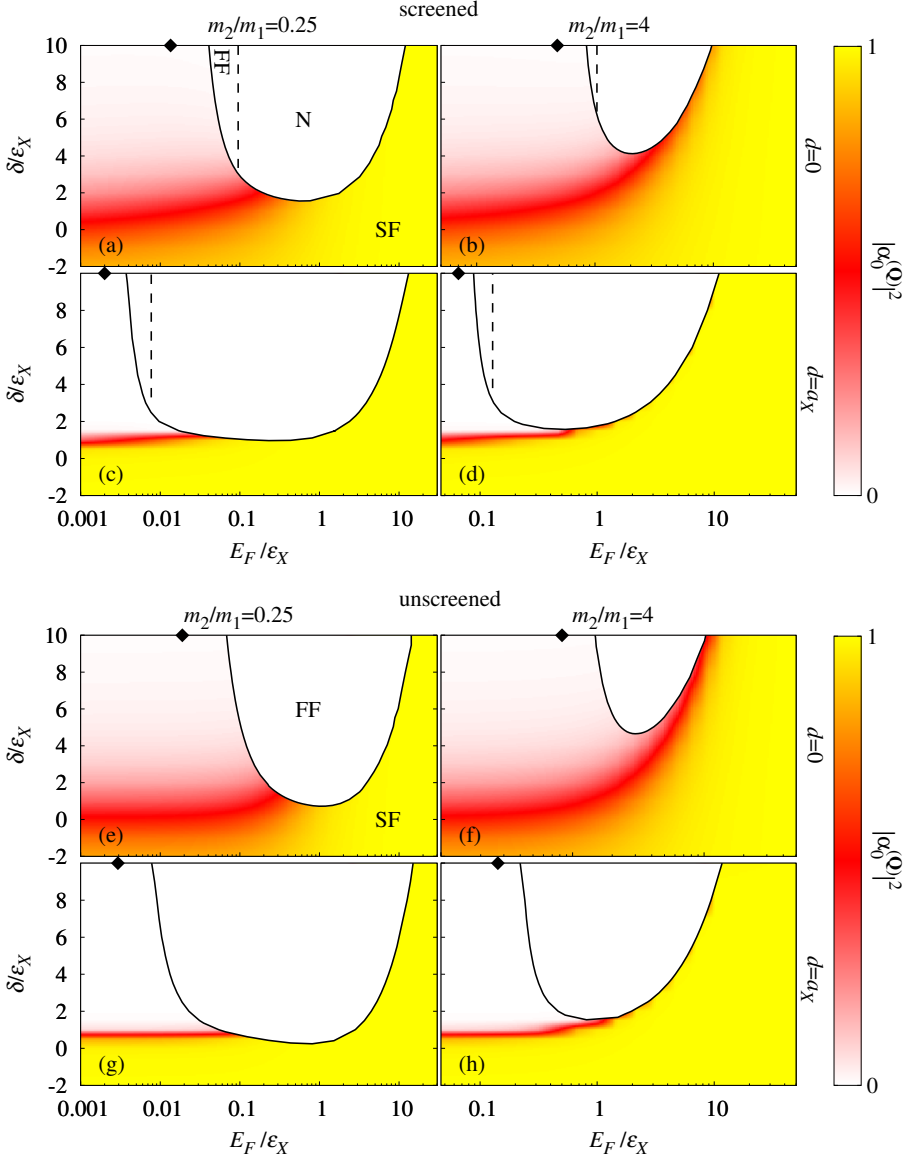


**Fig. 5.4:** Phase diagram of photon-exciton detuning  $\delta$  and majority particle Fermi energy  $E_F$  for a GaAs heterostructure with either a single quantum well ( $d = 0$ ) or a bilayer geometry at a distance  $d = a_X$ . The Rabi splitting is fixed to  $\Omega = 2\epsilon_X$  for the bilayer at  $d = a_X$  case. Solid lines are 1<sup>st</sup>-order transitions (SF-FF and SF-N). The dashed almost vertical line is the 2<sup>nd</sup>-order FF-N transition occurring for screened interactions. 1<sup>st</sup>- and 2<sup>nd</sup>-order transitions meet at a critical end-point. The diamond symbols indicate the value of the density,  $E_{F0}$ , at which the SF-FF transition occurs in the absence of the cavity field  $\Omega = 0 = \alpha_0^{(Q)}$ . The color map represents the photon fraction  $|\alpha_0^{(Q)}|^2$ .

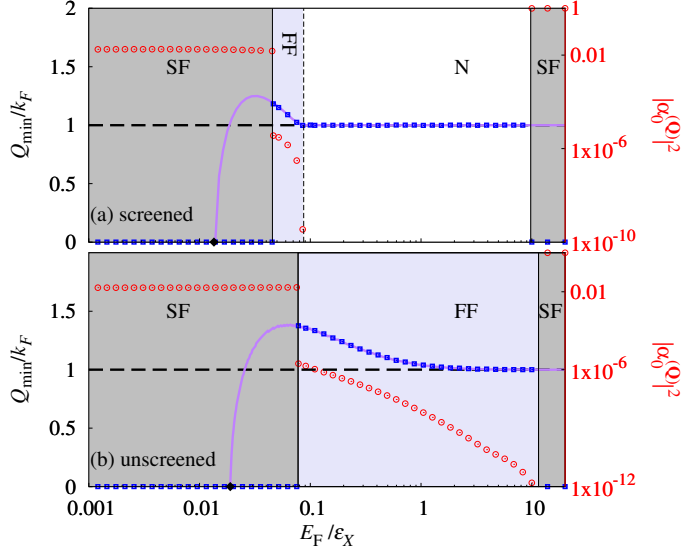


**Fig. 5.5:** Momentum  $Q_{\min}$  (blue squares) minimizing the polaritonic energy  $E$  as a function of the majority Fermi energy  $E_F$  for a single quantum well  $d = 0$ , mass ratio  $m_2/m_1 = 0.25$ , Rabi splitting  $\Omega = 2\varepsilon_X$  and detuning  $\delta = 8\varepsilon_X$ . Interactions are (a) RPA screened ( $N_s = 1$ ), and (b) unscreened ( $N_s = 0$ ). Solid (purple) lines represent the value of  $Q_{\min}$  in the absence of light-matter coupling ( $\Omega = 0$ ), while the thick dashed (black) line is the Fermi momentum  $\mathbf{k}_F$ . The corresponding photon fraction  $|\alpha_Q|^2$  is plotted with red circles and the corresponding axes are on the right side of each panel.

no normal phase, just as in the absence of photons [255].

As shown in Ref. [255], in the absence of the photon field, the excitonic SF-FF transition is always second order. In Fig. 5.5 we show this by plotting the momentum  $Q_{\min}$  — which minimizes the exciton energy  $E = E_{X\mathbf{Q}}^{(E_F)}$  solution of Eq. (5.21) — as a function of the Fermi energy of the majority species in absence of coupling to light (purple lines). We see that the transition from the SF  $\mathbf{Q} = \mathbf{0}$  to the finite momentum FF phase is continuous. In addition, for screened interactions, when increasing the density further,  $Q_{\min}$  locks to precisely  $\mathbf{k}_F$  at the FF-N transition.

In the presence of a cavity field, both the SF-FF and SF-N transitions become first order, with  $Q_{\min}$  changing discontinuously from  $Q_{\min} = 0$  to a finite value, as shown in Fig. 5.5 and Fig. 5.6. Because of the small cavity photon mass, the finite  $Q_{\min}$  FF phase has a small photon fraction, that decreases further on increasing  $E_F$  (see Fig. 5.5). Thus, the value of  $Q_{\min}$  almost coincides with that in the absence of the cavity field, and in particular  $Q_{\min}$  locks to  $\mathbf{k}_F$  at the FF-N transition. In contrast, for unscreened interactions,  $Q_{\min}$  asymptotically tends to  $\mathbf{k}_F$  in the FF region only for large values of  $E_F$ . In addition,

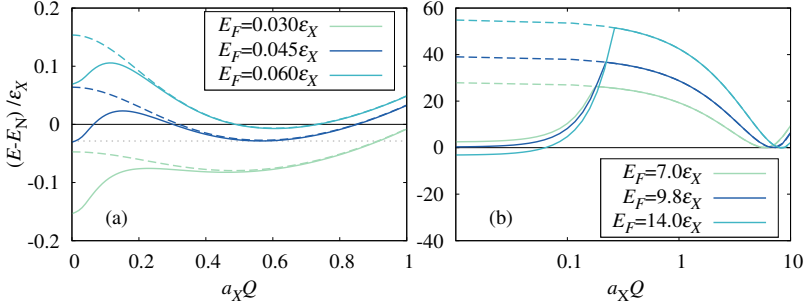


**Fig. 5.6:** Polariton ground state energy  $E$  with respect to the normal state energy  $E_N$  (solid lines) versus momentum  $Q$ . Parameters are for a GaAs heterostructure with a single quantum well ( $d = 0$ ), mass ratio  $m_2/m_1 = 0.25$ , Rabi splitting  $\Omega = 2\varepsilon_X$ , detuning  $\delta = 8\varepsilon_X$  and screened interactions ( $N_s = 1$ ). Dashed colored lines are the exciton energies  $E_{X\mathbf{Q}}^{(E_F)}$  evaluated in absence of the light-matter coupling,  $\Omega = 0$ . The gray dotted line indicates where the minima at  $Q = 0$  and  $Q \neq 0$  are equal. Panel (a) shows the 1<sup>st</sup> order SF-FF transition when increasing the system density, while panel (b) shows the N-SF 1<sup>st</sup> order transition.

the FF-N transition is always second order and it is only weakly affected by the coupling to light — thus it is approximately independent of both  $\delta$  and  $\Omega$ .

The SF-FF transition is strongly affected by the coupling to a cavity field. In particular, the exciton at  $\mathbf{Q} = \mathbf{0}$  strongly couples to the cavity photon when both energies are comparable, resulting in a half-matter half-light polariton state. In Fig. 5.4, the red region of the color map indicates where the photon fraction is around 50%, corresponding to resonance between the cavity photon and the exciton. The value of the detuning  $\delta$  for which resonance occurs is seen to grow with the majority density. This is mostly due to the  $\mathbf{Q} = \mathbf{0}$  exciton energy  $E_{X\mathbf{0}}^{(E_F)}$  growing with  $E_F$  due to Pauli blocking. Indeed, one can show that  $E_{X\mathbf{0}}^{(E_F)}$  grows sub-linearly for  $E_F \ll \varepsilon_X$  and screened interaction, while it grows linearly  $\sim E_F$  for  $E_F > \varepsilon_X$ .

This is shown in Fig. 5.7, where we compare the density dependence behavior of the rescaled energies  $E_{X\mathbf{Q}}^{(E_F)} - E_{X\mathbf{0}}$  of the exciton state in the weak coupling regime at  $\mathbf{Q} = \mathbf{0}$  (solid line) and at  $Q_{\min}$  (dashed line) for different mass ratios  $m_2/m_1 = 0.25, 4$  and for both screened and unscreened interactions. In Fig. 5.8 we plot  $E_{X\mathbf{Q}}^{(E_F)} - E_{X\mathbf{0}}$  as a function of density for a specific choice of parameters and superimpose a color map of the photon fraction  $|\alpha_0^{\mathbf{0}}|^2$  of the  $\mathbf{Q} = \mathbf{0}$  polariton state, as a function of  $E_F$  and detuning  $\delta$ . The red region shows where the photon fraction is around 50% indicating that the cavity photon energy is resonant with the  $\mathbf{Q} = \mathbf{0}$  exciton state — see Eqs. (5.19) and (5.20). As discussed in Sec. 5.2.3, the photon energy shift at  $\mathbf{Q} = \mathbf{0}$ ,  $\omega_{C\mathbf{0}}^{(E_F)} - \omega_{C\mathbf{0}}$ , depends only weakly on  $E_F$ . In particular, for the small value of  $\Omega$  used in Fig. 5.8 ( $\Omega = 0.2\varepsilon_X$ ), we expect that the  $E_F$  dependence of

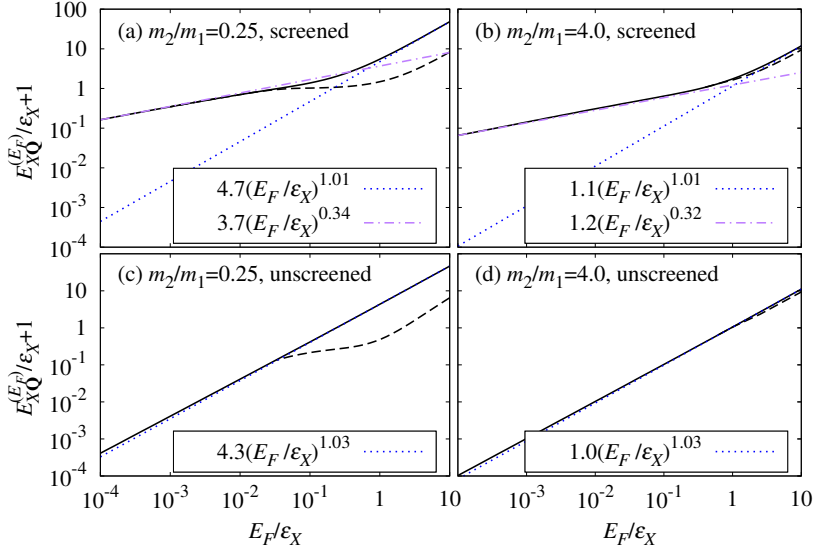


**Fig. 5.7:** Rescaled shift of exciton energies  $E_{X\mathbf{Q}}^{(E_F)} - E_{X\mathbf{0}}$  at  $\mathbf{Q} = \mathbf{0}$  (solid) and  $Q_{\min}$  (dashed) as a function of density, in the weak coupling regime. Parameters are for a GaAs single quantum well ( $d = 0$ ,  $E_{X\mathbf{0}} = -\varepsilon_X$ ), two different mass ratios  $m_2/m_1 = 0.25$  and  $m_2/m_1 = 4$ , and for both screened (a,b) and unscreened (c,d) interactions. Dot-dashed and dotted lines show the low- and high-density fittings, respectively.

the effective photon energy is negligible with respect to that of the exciton energy,  $|\omega_{C\mathbf{0}}^{(E_F)} - \omega_{C\mathbf{0}}| \ll |E_{X\mathbf{0}}^{(E_F)} - E_{X\mathbf{0}}|$ . Thus, in this case, we expect that  $\delta_{50\%} \simeq E_{X\mathbf{0}}^{(E_F)} - E_{X\mathbf{0}}$ , which matches what is observed in Fig. 5.8: The detuning  $\delta$  at which resonance occurs (red region) coincides with the energy shift of the exciton,  $E_{X\mathbf{0}}^{(E_F)} - E_{X\mathbf{0}}$  (solid line).

At large positive detunings, we recover, as expected, the results obtained in Ref. [255] for GaAs single wells and bilayers in the absence of light-matter coupling. Here, as one increases the majority particle density, Pauli blocking causes the exciton energy  $E = E_{X\mathbf{Q}}^{(E_F)}$  obtained by solving Eq. (5.21) to develop a minimum at finite CoM momentum  $Q_{\min}$ , as this reduces the kinetic energy cost of the minority particle. We denote the Fermi energy at which this transition occurs in the excitonic limit by  $E_{F0}$ , and, in the figures, this is illustrated by a diamond symbol.

By further increasing the density at fixed (large positive) photon-exciton detuning, there is eventually an additional first-order transition to an almost completely photon-like  $\mathbf{Q} = \mathbf{0}$  SF state. This is because the energy of the FF and N states is pushed up by Pauli blocking such that they exceed the photon energy at a sufficiently large density. As such, larger values of the detuning

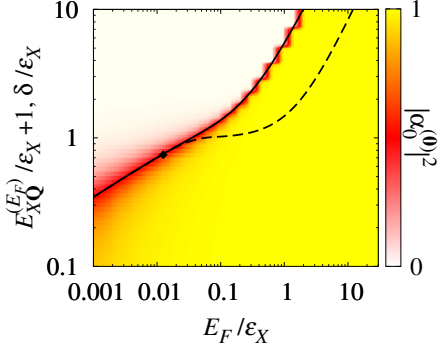


**Fig. 5.8:** Rescaled shift of exciton energies at  $\mathbf{Q} = \mathbf{0}$  (solid) and  $Q_{\min}$  (dashed) as a function of the density, for a GaAs single quantum well ( $d = 0$ ,  $E_{X\mathbf{0}} = -\varepsilon_X$ ),  $m_2/m_1 = 0.25$ , and screened interactions  $N_s = 1$ , in the weak coupling regime. The color map is the photon fraction  $|\alpha_0^{(0)}|^2$  of the polariton state at  $\mathbf{Q} = \mathbf{0}$  in the strong coupling regime, for  $\Omega = 0.2\varepsilon_X$ . The color map is plotted against  $E_F/\varepsilon_X$  ( $x$ -axis) and detuning  $\delta/\varepsilon_X$  ( $y$ -axis).

require larger values of density for this second transition to occur. Since this transition only weakly depends on the light-matter coupling, the FF-SF (N-SF) boundary essentially occurs when  $\delta \simeq E_{XQ_{\min}}^{(E_F)} - E_{X\mathbf{0}}$  ( $\delta \simeq E_N - E_{X\mathbf{0}}$ ), where  $E_{XQ_{\min}}^{(E_F)}$  is the FF exciton energy at Fermi energy  $E_F$  in the absence of the photon field – see Eq. (5.21).

From the study of the phase diagram at fixed Rabi splitting, we can draw similar conclusions about the mechanisms promoting the existence of a FF phase to those known in the absence of the cavity photon [255]: the FF phase is favored by unscreened Coulomb interactions and by a small minority particle mass. In addition, considering the unscreened case, a finite bilayer distance also favors FF. This is because the inter-layer interaction suppresses large momentum scattering and promotes an exciton wave function  $\varphi_{\mathbf{k}}^{(\mathbf{Q})}$  peaked at the  $\mathbf{k} \sim \mathbf{Q}$  direction, and also because a finite inter-layer distance reduces the effective electron-hole coupling to light. While our results demonstrate that embedding the quantum well structure into a cavity reduces the parameter region where FF can occur, this phase is still weakly coupled to light. Thus, the FF ground state should be visible in the photon momentum distribution, in an experiment with sufficient sensitivity. Note that for our simplified scenario in Eq. (5.11) of a single minority particle and thus a single photon in the cavity, the system photoluminescence is peaked at the energy  $E$ , with a weight given by the corresponding photon fraction  $|\alpha_0^{(\mathbf{Q})}|^2$ . Because, as shown in Fig. 5.5, this photon fraction is very small, it would require a very sensitive experimental probe. Even when (in presence of strong coupling to light) the lowest energy state is a  $\mathbf{Q} = \mathbf{0}$  polariton state, it has been suggested that the formation of a FF state could drastically change photoluminescence, due to the bottleneck effect of high momentum excitons relaxing to the true lowest energy polariton state [509].

It is possible to study the evolution of the FF phase with changing Rabi

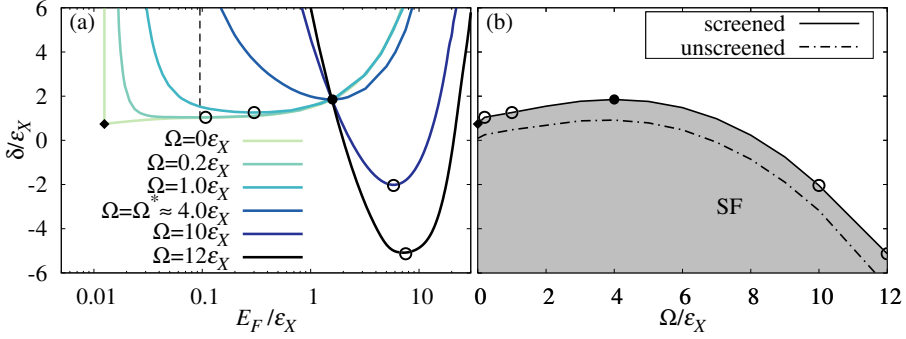


**Fig. 5.9:** (a) Solid lines are SF-FF (or SF-N) phase boundaries for different values of the Rabi splitting  $\Omega$ , for a single quantum well with hole doping,  $d = 0$ ,  $m_2/m_1 = 0.25$ , and for screened interactions  $N_s = 1$ . In particular, the region above a solid line is either FF (on the left of the dashed line) or N (on the right). The almost vertical dashed line is the approximately  $\Omega$ -independent FF-N boundary (see Fig. 5.4). Below each solid line, the phase is SF. Each symbol represents the minimal detunings  $\delta_{\min}$  of the boundaries — special values are  $\Omega = 0$  (filled diamond) and the  $\Omega$  at which  $\delta_{\min} = \delta^*$  (filled circle). A special value common to all boundaries is  $(\delta^*, E_F^*)$  (filled circle). (b) The solid line and symbols give the behavior of  $\delta_{\min}$  as a function of  $\Omega$  for screened  $N_s = 1$  interactions, while the dot-dashed line represents  $\delta_{\min}$  for unscreened  $N_s = 0$  interactions.

splitting by considering a sequence of cavities that have different numbers  $N_{QW}$  of embedded quantum wells, since  $\Omega \sim \sqrt{N_{QW}}$  [156, 158]. In particular, in Ref. [157], two structures with either 1 or 28 quantum wells stacked at the antinodes of the cavity field have been compared, allowing one to study the change of the Rabi splitting in the range  $0.3\epsilon_X \lesssim \Omega \lesssim 1.3\epsilon_X$ . Studying the evolution of the phase diagram with increasing Rabi splitting should in principle directly show how the introduction of light-matter coupling modifies the phase diagram.

With this motivation, in the left panel of Fig. 5.9, we compare the boundaries between the SF and the FF (SF and N) phases for different values of  $\Omega$ . Screened and unscreened interactions give qualitatively the same results, with the only difference being the absence of the N phase for unscreened interactions. The boundaries are also quantitatively similar in the two cases. In the absence of light-matter coupling, the SF-FF boundary is given by  $(E_F > E_{F0})$ :

$$\delta = E_{XQ_{\min}}^{(E_F)} - E_{X0}. \quad (5.27)$$

For the SF-N boundary at  $\Omega = 0$ , this expression becomes  $\delta = E_N - E_{X0}$ . We observe an evolution of the minimal photon-exciton detuning  $\delta_{\min}$  with  $\Omega$  (right panel of Fig. 5.9) which, starting from the value  $\delta_0 = E_{XQ_{\min}}^{(E_{F0})} - E_{X0}$  at  $\Omega = 0$ , grows up to a maximum value  $\delta^*$ , and then decreases again. Consequently,

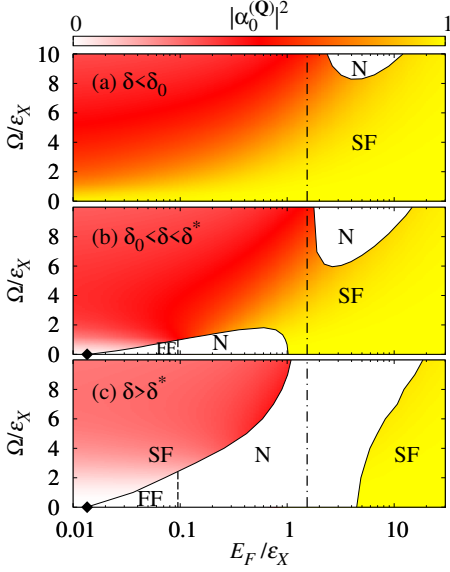


**Fig. 5.10:** Different possible topologies of the phase diagram as a function of the Rabi splitting  $\Omega$  and the majority particle Fermi energy  $E_F$  for a GaAs heterostructure with a single quantum well ( $d = 0$ ),  $m_2/m_1 = 0.25$ , and screened interactions  $N_s = 1$ . The detuning has been fixed to  $\delta = 0 < \delta_0$  (left panel),  $\delta_0 < \delta = 1.5\epsilon_X < \delta^*$  (middle panel), and  $\delta = 4\epsilon_X > \delta^*$  (right panel). In all panels, the vertical dot-dashed line is the value of  $E_F^*$  (see Fig. 5.9), while all other lines and labels are as in Fig. 5.4.

the light-matter coupling is detrimental to the formation of a finite momentum phase for small values of  $\Omega$ , while it favors finite  $\mathbf{Q}$  at  $\Omega \gtrsim 4\epsilon_X$ .

There is a special point  $(\delta^*, E_F^*)$  which is common to all SF-FF (SF-N) boundaries as one varies  $\Omega$ , i.e., one observes in the left panel of Fig. 5.9 that all lines appear to cross at a single point. At this particular value of the photon-exciton detuning and density, all the dependence on the Rabi splitting and thus the light-matter coupling is lost. Here, the decrease in energy due to forming a polariton is exactly counterbalanced by doping-induced changes to the cavity dielectric constant discussed in Sec. 5.2.3. Note that this behavior is not accurately captured by the estimated photon shift in Eq. (5.18), since this is not valid in the regime  $E_F > \epsilon_X$ . However, we can determine  $(\delta^*, E_F^*)$  once we account for all the electron-hole scattering processes, as shown in App. F. We have checked that the existence of the special point  $(\delta^*, E_F^*)$  is common to both structures with a single well and bilayer geometry, and it is also independent of whether interactions are screened or unscreened.

To further illustrate the special role played by the detuning  $\delta^*$  and Fermi energy  $E_F^*$ , we plot in Fig. 5.10 the three different types of phase diagrams at fixed detuning  $\delta$  that arise by varying  $\Omega$  and  $E_F$ . A common feature for all three cases is that, for  $E_F < E_F^*$ , the FF and N phases are suppressed on increasing  $\Omega$ , in favor of a strongly mixed light-matter polaritonic SF phase with  $|\alpha_0^{(0)}|^2 \sim 0.5$ . Note also that for  $E_F < E_F^*$  the FF (N) phase occurs only for  $\delta > \delta_0$ . In this small  $E_F$  case, the lowering of energy of the strongly mixed  $\mathbf{Q} = \mathbf{0}$  LP state with  $\Omega$  dominates over any change of the cavity dielectric constant because of gating/doping. Note that the phase diagram we see in this

small  $E_F$  case illustrates the idea that increasing light-matter coupling can stabilize a polaritonic ground state even when the purely excitonic system is unbound.

For  $E_F > E_F^*$ , we see quite a different behavior — a finite momentum FF or N phase is favored at larger values of the Rabi splitting  $\Omega$ , regardless of the value of the detuning. In this large  $E_F$  case, the SF-FF (SF-N) transition typically occurs from an almost purely photonic SF phase  $|\alpha_0^{(0)}|^2 \sim 1$  to an almost purely excitonic FF (N) phase with  $|\alpha_0^{(0)}|^2 \ll 1$  ( $|\alpha_0^{(0)}|^2 = 0$ ). This transition occurs because the shift in the cavity dielectric constant at finite  $E_F$  increases with  $\Omega$ , while the excitonic or normal state energy is  $\Omega$  independent, so that eventually, increasing  $\Omega$  to large enough values, one favors the excitonic phase over the polaritonic.

Note that for GaAs heterostructures with a single quantum well and  $m_2/m_1 = 0.25$ , we find that  $E_F^* \simeq 1.55\varepsilon_X$  ( $E_F^* \simeq 1.95\varepsilon_X$ ) for screened  $N_s = 1$  (unscreened  $N_s = 0$ ) interactions respectively — see App. F. This value of the Fermi energy is well below typical energies at which band curvature and structure start being important, so it lies within the range of the validity of our model. Indeed, from the GaAs lattice constant  $a \simeq 0.56$  nm, we can estimate that  $1/(2\mu a^2) \simeq 150\varepsilon_X \gg E_F^*$ .

## 5.4.2 TMD monolayer in planar microcavities

We derive here the phase diagram for the specific case of doped MoSe<sub>2</sub>, see Fig. 5.11. In particular, we consider the case of a single hole in a Fermi sea of electrons, with all electrons being spin and valley polarized, a regime that can be experimentally realized by applying a magnetic field [468]. Further, we have assumed a large enough spin-orbit splitting, so that only the lowest energy conduction band is considered.

Due to the fact that most of the dielectric screening takes place within the 2D layer, TMD materials require a separate analysis from the case of III-V semiconductor heterostructures. Specifically, we consider the same model Hamiltonian as before, Eq. (5.1), with Rytova-Keldish potential, Eq. (1.29). The electron and hole masses are  $m_1 \equiv m_e = 0.56m_0$  and  $m_2 \equiv m_h = 0.59m_0$  [53, 510], where  $m_0$  is the free electron mass. Because  $m_e$  and  $m_h$  have very similar values, little difference is expected whether the minority species is a hole — as explicitly considered here — or an electron.

Following Ref. [256], we neglect electron exchange; furthermore, we neglect screening by the electron gas on the basis that, for these materials, the plasma frequency,  $\omega_{\text{pl}}(\mathbf{k}_F) \simeq \sqrt{n_1 \mathbf{k}_F^2 V_{\text{RKK}_F}}/m_1 \sim 90$  meV (for  $E_F = 20$  meV), is much smaller than the exciton binding energy  $|\varepsilon_X| = 485$  meV [53, 510, 511]. We fix the cavity photon mass to  $m_C = 10^{-5}m_0$  and the Rabi splitting to

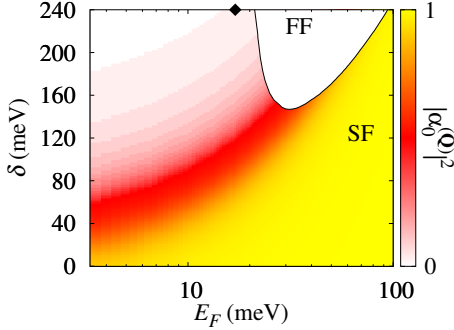


**Fig. 5.11:** Phase diagram for a  $\text{MoSe}_2$  monolayer embedded into a planar cavity as a function of photon-exciton detuning  $\delta$  and electron Fermi energy  $E_F$ . We take the Rabi splitting  $\Omega = 40\text{meV}$ . The solid line is the 1<sup>st</sup>-order SF-FF transition, while the diamond symbol indicates the value at which the SF-FF transition occurs in the absence of the cavity field [256].

$\Omega = 40\text{ meV}$  [151]. Importantly for our analysis, the renormalization scheme of the photon energy described in Sec. 1.5.2 is unchanged.

By considering the same variational polariton state as in Eq. (5.11) we derive the phase diagram versus detuning  $\delta$  and electron Fermi energy  $E_F$ . The resulting phase diagram is shown in Fig. 5.11, and is seen to qualitatively agree with the unscreened case of GaAs presented in Fig. 5.4. Because the long-range unscreened Coulomb interaction promotes the finite momentum bound FF phase, it is not surprising that the system never transitions to the normal state N for the potential in Eq. (1.29). As shown in Ref. [255], the bare Coulomb interaction always implies a bound exciton state for any density of majority particles. In the absence of the cavity photon mode, we recover the results of Ref. [256], which predicted an SF-FF transition at  $E_F = 20\text{ meV}$  — as before, this value is labeled with a diamond symbol in Fig. 5.11. Because of the large value of  $\varepsilon_X$  relative to  $\Omega$ , the minimal photon-exciton detuning for observing FF is found to be rather large,  $\delta_{\min} \simeq 147\text{ meV}$ . However, we expect this value to eventually decrease for  $\Omega \gtrsim \varepsilon_X$  in a manner similar to that shown in Fig. 5.9.

## 5.5 Conclusions and perspectives

We have studied pairing effects in an extremely charge imbalanced electron-hole mixture in either a single quantum well, a bilayer, or TMD monolayers embedded into a planar cavity. In particular, we have analyzed the competition between the formation of an FF-like [257] bound excitonic pair at finite CoM momentum, which is promoted by both long-range Coulomb interactions and the Pauli blocking of the Fermi sea [255, 256], and the formation of a strongly coupled polariton state at zero momentum, which is promoted by the strong coupling to the cavity field. By fixing the light-matter coupling, i.e., the Rabi splitting, we find that, as expected, strong coupling to a cavity photon mode competes against the formation of the finite momentum FF state, and so re-

duces the parameter range of majority species density where this phase occurs. Note that the FF phase does weakly couple to light to allow its detection in photoluminescence experiments with enough sensitivity. For large photon-exciton detunings, the photon becomes less relevant, and so the FF phase occupies a sizeable region at finite density of the majority species. At small densities, the FF phase is replaced by bound polariton states with zero CoM momentum, which lowers their energy through strong light-matter coupling. At large densities, one instead finds an almost purely photonic state (with zero momentum) because, due to Pauli blocking, the exciton energy grows roughly linearly with the density. As already known for the case without photons, a bound state always exists for unscreened Coulomb interactions, whereas with screening, an unbound state can replace the excitonic FF state.

To understand the topology of the phase diagram, we note that it is important that the presence of a Fermi sea not only changes the energy of the exciton but also the background cavity dielectric constant of the active medium, i.e., the gated/doped quantum well, the bilayer, or the TMD monolayer. This change has little consequences for the phase diagram at fixed Rabi splitting because the exciton energy shift with density dominates over the shift of the photon energy. However, the photon energy shift increases for sufficiently large values of the Rabi splitting and consequently does have a significant effect on the phase diagram at fixed detuning. In particular, we find that increasing the Rabi splitting at low enough doping/gating densities always promotes the formation of a zero momentum strongly bound polariton state. However, surprisingly, at large enough densities, this behavior is reversed, and increasing the coupling to light promotes the formation of finite momentum excitonic states weakly mixed with light.

The results in this chapter focus entirely on the regime of extreme imbalance, where there is only a single minority species particle. It is of course interesting to consider the behavior of the many-body state with a larger minority particle density as carried on in a recent work in Ref. [420]. Another important question concerns the possibility of more complex pairing states, even in the extreme imbalance state. The Ansatz we use in this chapter assumes that the pairing state has no effect on the majority Fermi sea, however, Coulomb interactions between majority particles mean this assumption will not necessarily hold. Relaxing this assumption allows the excitonic state to be dressed by electron-hole pairs of the majority band — similar to what happens in the polaron case. Understanding the interplay of this dressing with the internal structure of pairing, the coupling to light, and the crossover from the behavior we discuss here to the Fermi-edge polariton regime is a topic for future work.



# General conclusions and future perspectives

In this thesis, we explore the optical excitations of two-dimensional semiconductors and how their behavior is altered when an excess of free charges is introduced into the medium. We address several topics of interest regarding the extreme imbalanced limit regime, resulting in a combination of theoretical advancement and crucial explanations of experimental findings.

Chapter 3 explores the optical properties of doped semiconductors at finite temperatures by means of a finite-temperature Fermi-polaron approach. Through this technique, we unveil a smooth transition from a regime where the attractive branch behaves as a well-defined quasiparticle to a regime where it merges into a broad continuum of trion-hole scattering states. This crossover results in a dramatic change in the spectral lineshape and can be triggered by decreasing doping or increasing temperature, but it cannot occur at zero temperature. Interestingly, while the Fermi polaron theory successfully describes both limits, theories based on the trion wave function only apply when a well-defined quasiparticle is absent. In fact, we show that by introducing a perturbatively exact quantum virial expansion in the high-temperature or low-doping regime, the trion theory corresponds to a weak-interaction limit of our finite-temperature Fermi polaron theory. Recent experiments on doped monolayer  $\text{MoSe}_2$  have confirmed our results, indicating that previous measurements may have overestimated the trion binding energy. Moreover, in the realm of strong light-matter coupling, we discover that temperature can substantially alter the properties of Fermi polaron-polaritons. Specifically, we identify that the strong-to-weak coupling crossover observed at finite temperature for the attractive branch at low doping and the repulsive branch in the high doping regime can be explained by analyzing the linewidths and spectral weights of the two branches.

One of the main limitations of our finite-temperature approach is that our theory incorporates radiative broadening, disorder, and incoherence effects due to phonons in a phenomenological manner, by introducing experimentally rel-

evant values of homogeneous and inhomogeneous broadening as Lorentzian and Gaussian linewidths. However, a separate analysis of these effects would be beneficial. It is worth noting that phonon effects are not significant for monolayer TMDs at low temperatures, but as the temperature increases, they become more relevant. It would be desirable to examine these effects separately to gain a better understanding of their contribution to the system's behavior. Therefore, the inclusion of phonons in the analysis should not be overlooked, as they can significantly impact the system's overall behavior at higher temperatures.

Looking ahead, our research opens up exciting new avenues for future investigations. For instance, it would be fascinating to explore how the quasiparticle transition of the attractive branch, induced by either temperature or doping, affects the polaron-polaron interaction properties, and how they affect the optical nonlinearities of doped semiconductors. Nonlinear effects are crucial for the development of optical quantum information platforms, as they allow different information-carrying photons to interact and perform basic tasks such as changing the photons' color, modifying their statistics, and inducing entanglement between them. Such interactions could be measured using cutting-edge techniques like coherent multidimensional spectroscopy on gated two-dimensional materials.

In chapter 4 we consider the spin-valley polarized limit. This particular configuration assumes that the excess carriers forming the Fermi sea are identical to one of the two carriers that form the exciton. As a result, the three-body trion state in this system has  $p$ -wave symmetry. Using a zero temperature polaron description, we manage to extrapolate from few-body bound states to many-body states in the high-density regime, discovering that the optical spectrum exhibits an attractive quasiparticle branch, a repulsive branch, and a many-body continuum only in the parameter range where the  $p$ -wave trion is bound. We also evaluate the doping dependence of the corresponding energies and spectral weights. Notably, our results show that at low doping, the oscillator strength of the attractive branch scales with the square of the Fermi energy due to the trion's  $p$ -wave symmetry. As we increase the density, we discover that both the repulsive and attractive branches blueshift and that the orbital character associated with these branches interchange, making us wonder if the different orbital characteristics of the *indistinguishable carrier polaron* could enhance the polaron-polaron interaction strength. This represents one of the main focus of our future research activity.

To deepen our research in this field, we also plan to analyze the ICP scenario moving away from our current assumption of contact interaction and considering a proper Coulomb interaction, achieving more accurate and precise quantitative results. In order to observe the outcomes of our work, a bound  $p$ -wave trion state is necessary. We believe that a sufficiently strong out-of-

plane magnetic field could achieve this state, where the carrier orbital motion undergoes Landau-level quantization. Preliminary results have shown that in the presence of a magnetic field, increasing doping can cause the exciton oscillator strength to transfer to the  $p$ -wave trion state, opening up a world of possibilities for future studies in the Landau quantized regime. Last but not least, we are also keen to explore temperature effects on the properties of the *indistinguishable carrier polaron*, as done for the *distinguishable carrier polaron* in chapter 4.

In Chapter 5, we explore the behavior of two-dimensional electron-hole systems embedded in optical microcavities under extreme charge imbalance conditions. Our research focuses on the competition between different electron-hole paired states for specific cases of semi-conducting III-V single quantum wells, electron-hole bilayers, and transition metal dichalcogenide monolayers embedded in a planar microcavity. Using variational wave functions, we investigate the complex interplay between electron-hole pairing and photon modes in the many-body polariton ground state. Our findings shed light on the ways that the Fermi sea of excess charges modifies both the exciton properties and the dielectric constant of the cavity active medium, affecting the photon component of the many-body polariton ground state. We show that long-range Coulomb interactions and Pauli blocking of the Fermi sea promote electron-hole pairing with finite center-of-mass momentum, corresponding to an excitonic roton minimum. On the contrary, the strong coupling to the ultra-low-mass cavity photon mode favors zero-momentum pairs.

Our research is limited to the regime of extreme imbalance, where there is only one minority species particle. The behavior of the many-body state with a higher minority particle density could be equally intriguing. Furthermore, we're curious about the possibility of more complex pairing states, even in extreme imbalance scenarios. Our Ansatz assumes that the pairing state does not impact the majority Fermi sea, but we recognize that Coulomb interactions between the majority particles may challenge this assumption. Relaxing this assumption could open up new possibilities for the excitonic state and its interaction with electron-hole pairs of the majority band.

Recent years have witnessed a considerable surge of interest in the realization of charged polariton configurations in doped two-dimensional semiconductors, leading to a wealth of fascinating results. This thesis addresses fundamental questions about the physics of doped 2D semiconductors embedded in optical microcavities, taking a step forward towards the development of next-generation electronic and optoelectronic devices.



# Conclusiones generales y perspectivas futuras

En esta tesis, exploramos las excitaciones ópticas de semiconductores bidimensionales y cómo se altera su comportamiento cuando se introduce un exceso de cargas libres en el medio. Abordamos varios temas de interés en relación con el régimen límite de desequilibrio extremo, lo que resulta en una combinación de avances teóricos y explicaciones cruciales de hallazgos experimentales.

El capítulo 3 explora las propiedades ópticas de semiconductores dopados a temperaturas finitas mediante una aproximación Fermi-polarón a temperatura finita. Mediante esta técnica, desvelamos una transición suave desde un régimen en el que la rama atractiva se comporta como una cuasipartícula bien definida a un régimen en el que se funde en un amplio continuo de estados de dispersión trión-hueco. Este cruce da lugar a un cambio drástico en la forma de las líneas espectrales y puede desencadenarse al disminuir el dopaje o aumentar la temperatura, pero no puede producirse a temperatura cero. Curiosamente, mientras que la teoría del polaron de Fermi describe con éxito ambos límites, las teorías basadas en la función de onda del trión sólo se aplican cuando no existe una cuasipartícula bien definida. De hecho, mostramos que al introducir una expansión cuántica virial perturbativamente exacta en el régimen de alta temperatura o bajo dopado, la teoría de triones corresponde a un límite de interacción débil de nuestra teoría de Fermi polaron de temperatura finita. Experimentos recientes en una monocapa de  $\text{MoSe}_2$  dopada han confirmado nuestros resultados, indicando que las mediciones anteriores pueden haber sobrestimado la energía de enlace del trión. Además, en el ámbito del fuerte acoplamiento luz-materia, descubrimos que la temperatura puede alterar sustancialmente las propiedades de los polaron-polaritones de Fermi. En concreto, identificamos que el cruce de acoplamiento fuerte a débil observado a temperatura finita para la rama atractiva a bajo dopaje y la rama repulsiva en el régimen de alto dopaje puede explicarse analizando los anchos de línea y los pesos espectrales de las dos ramas.

Una de las principales limitaciones de nuestro enfoque de temperatura fi-

nita es que nuestra teoría incorpora los efectos de ensanchamiento radiativo, desorden e incoherencia debidos a los fonones de manera fenomenológica, introduciendo valores experimentalmente relevantes de ensanchamiento homogéneo e inhomogéneo como anchos de línea lorentziano y gaussiano. Sin embargo, un análisis separado de estos efectos sería beneficioso. Cabe señalar que los efectos fonónicos no son significativos para los TMD monocapa a bajas temperaturas, pero a medida que aumenta la temperatura, se vuelven más relevantes. Sería conveniente examinar estos efectos por separado para comprender mejor su contribución al comportamiento del sistema. Por tanto, no debe pasarse por alto la inclusión de los fonones en el análisis, ya que pueden influir significativamente en el comportamiento general del sistema a temperaturas más elevadas.

De cara al futuro, nuestra investigación abre nuevas e interesantes vías de investigación. Por ejemplo, sería fascinante explorar cómo la transición de cuasipartículas de la rama atractiva, inducida por la temperatura o el dopaje, afecta a las propiedades de interacción polaron-polaron, y cómo afectan a las no linealidades ópticas de los semiconductores dopados. Los efectos no lineales son cruciales para el desarrollo de plataformas ópticas de información cuántica, ya que permiten que diferentes fotones portadores de información interactúen y realicen tareas básicas como cambiar el color de los fotones, modificar sus estadísticas e inducir entrelazamiento entre ellos. Estas interacciones podrían medirse utilizando técnicas de vanguardia como la espectroscopia multidimensional coherente en materiales bidimensionales con compuerta.

En el capítulo 4 consideramos el límite polarizado espín-valle. Esta configuración particular supone que los portadores en exceso que forman el mar de Fermi son idénticos a uno de los dos portadores que forman el excitón. Como resultado, el estado triónico de tres cuerpos en este sistema tiene simetría de onda  $p$ . Utilizando una descripción de polaron a temperatura cero, conseguimos extrapolar desde estados ligados de pocos cuerpos a estados de muchos cuerpos en el régimen de alta densidad, descubriendo que el espectro óptico exhibe una rama de cuasipartículas atractiva, una rama repulsiva y un continuo de muchos cuerpos sólo en el rango de parámetros donde el trión de onda  $p$  está ligado. También evaluamos la dependencia del dopaje de las energías y pesos espectrales correspondientes. En particular, nuestros resultados muestran que a bajo dopaje, la fuerza oscilatoria de la rama atractiva escala con el cuadrado de la energía de Fermi debido a la simetría de onda  $p$  del trión. A medida que aumentamos la densidad, descubrimos que tanto la rama repulsiva como la atractiva se desplazan hacia el azul y que el carácter orbital asociado a estas ramas se intercambia, lo que nos hace preguntarnos si las diferentes características orbitales del *indistinguishable carrier polaron* podrían aumentar la fuerza de interacción polaron-polaron. Esto representa uno de los principales focos de nuestra futura actividad investigadora.

Para profundizar nuestra investigación en este campo, también planeamos

analizar el escenario ICP alejándonos de nuestra suposición actual de interacción de contacto y considerando una interacción de Coulomb adecuada, logrando resultados cuantitativos más exactos y precisos. Para observar los resultados de nuestro trabajo, es necesario un estado de trión de onda  $p$  ligada. Creemos que un campo magnético fuera del plano suficientemente intenso podría alcanzar este estado, en el que el movimiento orbital del portador experimenta una cuantización a nivel de Landau. Los resultados preliminares han demostrado que, en presencia de un campo magnético, el aumento del dopaje puede hacer que la fuerza oscilatoria del excitón se transfiera al estado de trión de onda  $p$ , lo que abre un mundo de posibilidades para futuros estudios en el régimen cuantizado de Landau. Por último, pero no por ello menos importante, también estamos interesados en explorar los efectos de la temperatura sobre las propiedades del emphpolaron de portador indistinguible, como se hizo para el emphpolaron de portador indistinguible en el capítulo 4.

En Chapter 5, exploramos el comportamiento de sistemas bidimensionales electrón-hueco embebidos en microcavidades ópticas bajo condiciones extremas de desequilibrio de carga. Nuestra investigación se centra en la competencia entre los diferentes estados emparejados electrón-hueco para casos específicos de pozos cuánticos simples semiconductores III-V, bicapas electrón-hueco y monocapas de dicalcogenuro de metales de transición embebidas en una microcavidad planar. Utilizando funciones de onda variacionales, investigamos la compleja interacción entre el emparejamiento electrón-hueco y los modos fotónicos en el estado básico polaritón de muchos cuerpos. Nuestros descubrimientos arrojan luz sobre las formas en que el mar de Fermi de cargas en exceso modifica tanto las propiedades del excitón como la constante dieléctrica del medio activo de la cavidad, afectando al componente fotónico del estado fundamental del polaritón de muchos cuerpos. Demostramos que las interacciones de Coulomb de largo alcance y el bloqueo de Pauli del mar de Fermi promueven el emparejamiento electrón-hueco con momento de centro de masa finito, correspondiente a un mínimo excitónico roton. Por el contrario, el fuerte acoplamiento al modo de fotones de la cavidad de masa ultrabaja favorece los emparejamientos de momento cero.

Nuestra investigación se limita al régimen de desequilibrio extremo, en el que sólo hay una partícula de especie minoritaria. El comportamiento del estado de muchos cuerpos con una mayor densidad de partículas minoritarias podría ser igualmente intrigante. Además, tenemos curiosidad por la posibilidad de estados de emparejamiento más complejos, incluso en escenarios de desequilibrio extremo. Nuestro Ansatz asume que el estado de emparejamiento no afecta al mar de Fermi mayoritario, pero reconocemos que las interacciones de coulombio entre las partículas mayoritarias pueden desafiar esta suposición. Relajar esta suposición podría abrir nuevas posibilidades para el estado excitónico y su interacción con pares electrón-hueco de la banda mayoritaria.

Los polaritones cargados en semiconductores bidimensionales dopados se han convertido en un área de investigación apasionante en las últimas décadas, ofreciendo resultados fascinantes. Esta tesis aborda cuestiones fundamentales sobre la física de los semiconductores bidimensionales dopados embebidos en microcavidades ópticas, dando un paso adelante en el desarrollo de dispositivos electrónicos y optoelectrónicos de nueva generación.

# Appendices

## A Momentum discretization and matrix diagonalization

In the numerical implementation of the eigenvalue problems encountered during this work, we have to discretize momenta and symmetrize the eigenvalue problem by taking into account the normalization condition of the problem considered. In this appendix, we briefly review the numerical implementation used to solve specifically the eigenvalue problem (1.24) — the same procedure applies to any other scenario.

Using 2D polar coordinates, to solve Eq. (1.24) we have to discretize 2 variables,  $k$  and  $\theta$ , where the angle  $\theta$  is measured with respect to the reference angle of  $\mathbf{Q}$ . We measure energies, length, and mass scales in units of  $\varepsilon_X$ ,  $a_X$ , and  $\mu$ , respectively, defined in (1.17), (1.16), and (1.6). Thus, in the following, we use the simplified notation:

$$\mathbf{k}a_X \mapsto \mathbf{k} \quad \frac{\epsilon_{e\mathbf{k}} + \epsilon_{h\mathbf{Q}-\mathbf{k}}}{\varepsilon_X} \mapsto \mathbf{k}^2 + \frac{\mathbf{Q}^2}{m_X} + E_g \quad (\text{A.1a})$$

$$\frac{m_X}{\mu} \mapsto m_X \quad \frac{V_{\mathbf{q}}}{\varepsilon_X a_X^2} \mapsto \frac{2\pi}{q} \quad (\text{A.1b})$$

$$\frac{\mathcal{A}}{a_X^2} \mapsto \mathcal{A} \quad \frac{a_X^2}{\mathcal{A}} \sum_{\mathbf{k}} \mapsto \frac{1}{\mathcal{A}} \sum_{\mathbf{k}} = \int \frac{d\mathbf{k}}{(2\pi)^2} = \int D_k^2 D_\theta^2 . \quad (\text{A.1c})$$

For integrals we use a Gauss-Legendre (GL) quadrature:

$$\int_{-1}^1 f(x)dx \simeq \sum_{i=1}^N w_i f(x_i) , \quad (\text{A.2})$$

where  $N$  are the number of sample points,  $w_i$  the weights, and  $x_i$  are the abscissae, i.e., the roots of the  $n$ -th Legendre polynomial. The generalization

to an arbitrary interval  $[a, b]$  is straightforward

$$\int_a^b f(x)dx \approx \sum_{i=1}^n w_i f\left(\frac{b-a}{2}x_i + \frac{b+a}{2}\right). \quad (\text{A.3})$$

In the specific case of an unlimited momentum variable  $k \in [0, \infty)$ , the change of integration variable  $k \mapsto \tan \beta$  results in a new finite interval  $\beta \in [0, \frac{\pi}{2})$  which can be discretized by GL quadrature, obtaining

$$k_i = \tan \beta_i \quad w_{k_i} = \frac{w_{\beta_i}}{\cos^2 \beta_i}. \quad (\text{A.4})$$

The normalization condition becomes:

$$1 = \sum_k^{N_k} \sum_{\theta}^{N_{\theta}} |\tilde{\varphi}_{k\theta}^{(\mathbf{0})}|^2, \quad (\text{A.5})$$

where

$$\tilde{\varphi}_{k\theta}^{(\mathbf{0})} = D_k D_{\theta} \varphi_{k\theta}^{(\mathbf{0})} \quad D_k^2 = \frac{dkk}{2\pi} = \frac{d\beta \tan \beta}{2\pi \cos^2 \beta} \quad D_{\theta}^2 = \frac{d\theta}{2\pi}. \quad (\text{A.6})$$

We can rewrite Eq. (1.24) as (we set  $V_0 = 0$ ):

$$(E - E_g) \tilde{\varphi}_{k\theta}^{(\mathbf{Q})} = \left(k^2 + \frac{Q^2}{m_X}\right) \tilde{\varphi}_{k\theta}^{(\mathbf{Q})} - \sum_{N_k N_{\theta}} D_k D_{k'} D_{\theta} D_{\theta'} \frac{2\pi}{\sqrt{k^2 + k'^2 - 2kk' \cos(\theta - \theta')}} \tilde{\varphi}_{k'\theta'}^{(\mathbf{Q})}, \quad (\text{A.7})$$

which can be easily diagonalized.

## B Iterative method

This method has been developed in 1972 by Roger Haydock and collaborators [481] to recursively solve an eigenvalue problem

$$\mathbb{H}_{\ell\ell'} \phi_{\ell'} = E \phi_{\ell},$$

by transforming the Hamiltonian  $\mathbb{H}_{\ell\ell'}$  in a tridiagonal matrix. Once this is done, the associated Green's function can be evaluated exactly by continued-fraction.

The idea is to start from an initial state  $\mathbf{u}_0$ , which represents the system physical initial conditions. For example, if we want to evaluate the photon Green's function, the initial state will be the state with a photon, i.e.,  $\mathbf{u}_0 = (1, 0, 0, \dots)$ . The complete Hilbert space is build considering all possible states

orthogonal to the initial state.

**Step  $n = 0$ .** Let us assume that  $\mathbf{u}_0$  is normalised, i.e.,  $\mathbf{u}_0^\dagger \mathbf{u}_0 = 1$ , then the next step is

$$\mathbf{u}_1 = \frac{\mathbb{H}\mathbf{u}_0 - a_0\mathbf{u}_0}{b_1} = \frac{\tilde{\mathbf{u}}_1}{b_1} \quad a_0 = \mathbf{u}_0^\dagger \mathbb{H}\mathbf{u}_0 \quad b_1^2 = \tilde{\mathbf{u}}_1^\dagger \tilde{\mathbf{u}}_1, \quad (\text{B.1})$$

which guarantees the normalisation of  $\mathbf{u}_1$  as well as its orthogonality to  $\mathbf{u}_0$ .

**Step  $n = 1$ .** The next step requires two coefficients, i.e.,  $a_1$  and  $b_2$ :

$$\mathbf{u}_2 = \frac{\mathbb{H}\mathbf{u}_1 - a_1\mathbf{u}_1 - b_1\mathbf{u}_0}{b_2} = \frac{\tilde{\mathbf{u}}_2}{b_2} \quad a_1 = \mathbf{u}_1^\dagger \mathbb{H}\mathbf{u}_1 \quad b_2^2 = \tilde{\mathbf{u}}_2^\dagger \tilde{\mathbf{u}}_2. \quad (\text{B.2})$$

It is easy to show that

$$b_2 = \mathbf{u}_1^\dagger \mathbb{H}\mathbf{u}_2. \quad (\text{B.3})$$

We can thus write the general step  $n$  as

$$\mathbf{u}_{n+1} = \frac{\mathbb{H}\mathbf{u}_n - a_n\mathbf{u}_n - b_n\mathbf{u}_{n-1}}{b_{n+1}} = \frac{\tilde{\mathbf{u}}_{n+1}}{b_{n+1}} \quad (\text{B.4a})$$

$$a_n = \mathbf{u}_n^\dagger \mathbb{H}\mathbf{u}_n \quad (\text{B.4b})$$

$$b_{n+1} = \sqrt{\tilde{\mathbf{u}}_{n+1}^\dagger \tilde{\mathbf{u}}_{n+1}} = \mathbf{u}_n^\dagger \mathbb{H}\mathbf{u}_{n+1}. \quad (\text{B.4c})$$

This means that on the basis  $\mathbf{u}_n$ , the Hamiltonian has a tridiagonal form

$$\mathbb{H} = \begin{pmatrix} a_0 & b_1 & 0 & 0 & \cdots & 0 \\ b_1 & a_1 & b_2 & 0 & \cdots & 0 \\ 0 & b_2 & a_2 & b_3 & \cdots & 0 \\ 0 & 0 & b_3 & a_3 & \ddots & \vdots \\ \vdots & \vdots & \vdots & \ddots & \ddots & b_n \\ 0 & 0 & 0 & \cdots & b_n & a_n \end{pmatrix} \quad (\text{B.5})$$

The photon Green's function is defined as

$$\mathbb{G} = (E + i\epsilon - \mathbb{H})^{-1}, \quad (\text{B.6})$$

and can be evaluated using the continued-fraction representation:

$$\begin{aligned} G_C(E) &= \mathbf{u}_0^\dagger (E + i\epsilon - \mathbb{H})^{-1} \mathbf{u}_0 \\ &= (\mathbb{G})_{00} = \frac{1}{E + i\epsilon - a_0 - \frac{b_1^2}{E + i\epsilon - a_1 - \frac{b_2^2}{E + i\epsilon - a_2 - \cdots}}} \end{aligned} \quad (\text{B.7})$$

This can also be rewritten in a simpler form to implement:

$$G_C(E) = \frac{1}{E + i\epsilon - a_0 - b_1^2 g_1(E)} \quad (\text{B.8a})$$

$$g_1(E) = \frac{1}{E + i\epsilon - a_1 - b_2^2 g_2(E)} \quad (\text{B.8b})$$

$$g_n(E) = \frac{1}{E + i\epsilon - a_n - b_{n+1}^2 g_{n+1}(E)}. \quad (\text{B.8c})$$

In the trivial case of the coupled oscillator model (1.34), where the matrix is already tridiagonal,

$$\hat{H} = \begin{pmatrix} \epsilon_{C\mathbf{q}} & \frac{\Omega}{2} \\ \frac{\Omega}{2} & \epsilon_{X\mathbf{q}} \end{pmatrix} \quad (\text{B.9})$$

one recovers the known results, where  $a_0 = \epsilon_{C\mathbf{q}}$ ,  $a_1 = \epsilon_{X\mathbf{q}}$ , and  $b_1 = \frac{\Omega}{2}$ , and:

$$G_C(\omega, \mathbf{q}) = \frac{1}{(\omega - \epsilon_{C\mathbf{q}} + i\eta) - \frac{(\Omega/2)^2}{\omega - \epsilon_{X\mathbf{q}} + i\eta}}. \quad (\text{B.10})$$

In the case where the exciton is composite, we can identify in the expression (B.8a) the exciton Green's function in the  $g = 0$  weak coupling limit. To do that, we consider the simplified case of  $|M_2\rangle$  (no electron-hole dressing) and then generalize the result to  $|\tilde{M}_4\rangle$  (4.18).

If we organize the vector

$$\phi = \left( \alpha_0 \quad \tilde{\varphi}_{k_1} \quad \tilde{\varphi}_{k_2} \quad \dots \quad \tilde{\varphi}_{k_{N_k}} \right)^T, \quad (\text{B.11})$$

where  $k_{i=1,2,\dots,N_k}$  are the discretized momenta and  $D_{k_{i=1,2,\dots,N_k}}^2$  the discretized weights — see Sec. A, then  $\mathbb{H}_{\ell\ell'}$  takes the following form

$$\mathbb{H}_{\ell\ell'} = \begin{pmatrix} \nu_{C\mathbf{0}} - E_g & -gD_{k_1} & -gD_{k_2} & \dots & -gD_{k_{N_k}} \\ -gD_{k_1} & \omega_{X,k_1} & vD_{k_1}D_{k_2} & \dots & \dots \\ -gD_{k_2} & vD_{k_1}D_{k_2} & \omega_{X,k_2} & \dots & \dots \\ \dots & \dots & \dots & \dots & \dots \\ -gD_{k_{N_k}} & \dots & \dots & \dots & \omega_{X,k_{N_k}} \end{pmatrix}_{\ell\ell'} \quad (\text{B.12})$$

Starting from this, we can reconstruct the coefficients  $a_{0,1,2,\dots}$  and  $b_{1,2,\dots}$  that build the Hamiltonian in its tridiagonal form. The starting point is the vector describing a single photon state:

$$\mathbf{u}_0 = (1 \quad 0 \quad \dots \quad 0)^T, \quad (\text{B.13})$$

from which we can get:

$$a_0 = \mathbf{u}_0^\dagger \mathbb{H} \mathbf{u}_0 = \nu_{C0} - E_g \quad (\text{B.14a})$$

$$b_1 = |\mathbb{H} \mathbf{u}_0 - a_0 \mathbf{u}_0| = g \sqrt{\sum_{i=1}^{N_k} D_{k_i}^2} \quad (\text{B.14b})$$

$$\mathbf{u}_1 = \frac{\mathbb{H} \mathbf{u}_0 - a_0 \mathbf{u}_0}{b_1} = \frac{1}{\sqrt{\sum_i D_{k_i}^2}} \left( 0 \quad -D_{k_1} \quad -D_{k_2} \quad \dots \quad -D_{k_{N_k}} \right)^T. \quad (\text{B.14c})$$

It is easy to show that there all dependence on the photon energy is contained in  $a_0$  and from the coupling to light in  $b_1$ , while all the following terms in the recursive method are  $g$ -independent and related to the matter degrees of freedom only.

This, together with the renormalization process of the contact interaction seen in Eq. (4.7) gives

$$\begin{aligned} G_C(\omega) &= \frac{1}{\omega + i\eta - a_0 - b_1^2 g_1(\omega)} = \frac{1}{\omega + i\eta - (\epsilon_{C0}) - g^2 \sum_i D_{k_i}^2 g_1(\omega)} \\ &\equiv \frac{1}{\omega + i\eta - (\epsilon_{C0}) - (\Omega/2)^2 G_X(\omega)|_{g=0}}, \end{aligned} \quad (\text{B.15})$$

where we define the exciton Green's function in the weak coupling limit as

$$G_X(\omega)|_{g=0} = \left( \frac{v}{\sqrt{Z_X}} \right)^2 \sum_{i=1}^{N_k} D_{k_i}^2 g_1(\omega), \quad (\text{B.16})$$

where

$$\Omega = \frac{2g}{\mathcal{A}} \sum_{\mathbf{k}} \Phi_{1s\mathbf{k}} = \frac{2g\sqrt{Z_X}}{v} \quad Z_X = \frac{2\pi\epsilon_X}{\mu}. \quad (\text{B.17})$$

Note that it is correct up to a finite shift of the bare photon energy  $\epsilon_{C0} = \delta + \epsilon_{X0} + \left(\frac{\Omega}{2}\right)^2$  (4.8).

The same exact procedure can be applied to the case of  $|\tilde{M}_4\rangle$  (4.18).

## C Finite momentum polaron state

For completeness, we generalize the finite-temperature polaron formalism illustrated in Sec. 3.2 to absorption and photoluminescence at finite momentum. This can in principle be measured in doped semiconductors using angle-resolved photoemission spectroscopy [512, 513]. Similarly to Eq. (3.4), we approximate the exciton operator in the Heisenberg picture at finite momentum

$\hat{x}_{\mathbf{Q}}(t) = e^{i\hat{H}t}\hat{x}_{\mathbf{Q}}e^{-i\hat{H}t}$  as

$$\hat{x}_{\mathbf{Q}}(t) \simeq \varphi_0^{(\mathbf{Q})}(t)\hat{x}_{\mathbf{Q}} + \frac{1}{\mathcal{A}} \sum_{\mathbf{k}, \mathbf{q}} \varphi_{\mathbf{kq}}^{(\mathbf{Q})}(t) \hat{c}_{\mathbf{q}}^\dagger \hat{c}_{\mathbf{k}} \hat{x}_{\mathbf{Q}+\mathbf{q}-\mathbf{k}}. \quad (\text{C.1})$$

The derivation then follows similarly to the zero momentum case. We minimize the error function  $\Delta_{\mathbf{Q}}(t) = \langle \hat{e}_{\mathbf{Q}}(t) \hat{e}_{\mathbf{Q}}^\dagger(t) \rangle_\beta$ , where  $\hat{e}_{\mathbf{Q}}(t) = i\partial_t \hat{x}_{\mathbf{Q}}(t) - [\hat{x}_{\mathbf{Q}}(t), \hat{H}]$ , obtaining the following eigenvalue problem:

$$E^{(\mathbf{Q})} \varphi_0^{(\mathbf{Q})} = \epsilon_{X\mathbf{Q}} \varphi_0^{(\mathbf{Q})} - \frac{v}{\mathcal{A}^2} \sum_{\mathbf{k}, \mathbf{q}} f_{\mathbf{q}} (1 - f_{\mathbf{k}}) \varphi_{\mathbf{kq}}^{(\mathbf{Q})} \quad (\text{C.2a})$$

$$E^{(\mathbf{Q})} \varphi_{\mathbf{kq}}^{(\mathbf{Q})} = E_{X\mathbf{Qkq}} \varphi_{\mathbf{kq}}^{(\mathbf{Q})} - v \varphi_0^{(\mathbf{Q})} - \frac{v}{\mathcal{A}} \sum_{\mathbf{k}'} (1 - f_{\mathbf{k}'}) \varphi_{\mathbf{k}'\mathbf{q}}^{(\mathbf{Q})}, \quad (\text{C.2b})$$

where  $E_{X\mathbf{Qkq}} = \epsilon_{X\mathbf{Q}+\mathbf{q}-\mathbf{k}} + \epsilon_{\mathbf{k}} - \epsilon_{\mathbf{q}}$ . The exciton Green's function can thus be written in terms of the eigenvalues  $E_n^{(\mathbf{Q})}$  and eigenvectors  $\varphi_{n0}^{(\mathbf{Q})}$  as

$$G_X(\omega, \mathbf{Q}) = \sum_n \frac{|\varphi_{n0}^{(\mathbf{Q})}|^2}{\omega - E_n^{(\mathbf{Q})} + i0^+}. \quad (\text{C.3})$$

Equivalently, the exciton Green's function can be written in terms of the exciton self-energy at finite momentum

$$G_X(\omega, \mathbf{Q}) = \frac{1}{\omega - \epsilon_{X\mathbf{Q}} - \Sigma_X(\omega, \mathbf{Q})} \quad (\text{C.4a})$$

$$\Sigma_X(\omega, \mathbf{Q}) = \frac{1}{\mathcal{A}} \sum_{\mathbf{q}} f_{\mathbf{q}} \mathcal{J}(\omega + \epsilon_{\mathbf{q}}, \mathbf{q} + \mathbf{Q}), \quad (\text{C.4b})$$

where the inverse of the  $T$  matrix is defined in Eq. (3.12).

The absorption of a photon with momentum  $\mathbf{Q}$  is given by

$$A_X(\omega, \mathbf{Q}) = -\frac{1}{\pi} \text{Im} G_X(\omega, \mathbf{Q}). \quad (\text{C.5})$$

Absorption and photoluminescence can be connected using detailed balance conditions as derived in Sec. 1.5.3, starting from Fermi's golden rule definitions:

$$A_X(\omega, \mathbf{Q}) = \sum_{n, \nu} \langle n | \hat{\rho}_0 | n \rangle |\langle \nu | \hat{x}_{\mathbf{Q}}^\dagger | n \rangle|^2 \delta(E_{\nu n} - \omega) \quad (\text{C.6a})$$

$$P_X(\omega, \mathbf{Q}) = \sum_{n, \nu} \langle \nu | \hat{\rho} | \nu \rangle |\langle n | \hat{x}_{\mathbf{Q}} | \nu \rangle|^2 \delta(E_{\nu n} - \omega). \quad (\text{C.6b})$$

where  $E_{\nu n} = E_\nu - E_n$ . Thus, the detailed balance condition is identical to that

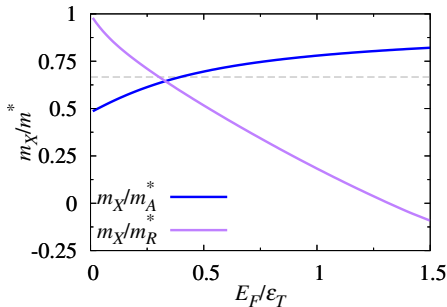


**Fig. D.1:** Inverse of the attractive (solid blue) and repulsive (solid purple) polaron effective masses as a function of doping. As a reference, the inverse of the trion effective masses is shown (dashed gray).

at zero momentum:

$$P_X(\omega, \mathbf{Q}) = \frac{Z_0}{Z_{int}} e^{-\beta\omega} A_X(\omega, \mathbf{Q}) . \quad (\text{C.7})$$

## D Polaron masses at zero temperature

In this appendix, we study the effective masses of both attractive and repulsive polaron branches in the weak coupling regime. We evaluate the polaron masses for both branches, at zero temperature, by evaluating the momentum dependence of their dispersion and by fitting it, at low momentum, with the expression

$$E_{A,R}(\mathbf{Q}) \simeq E_{A,R} + \frac{\mathbf{Q}^2}{2m_{A,R}^*} . \quad (\text{D.1})$$

The results of the fitting are shown in Fig. D.1.

For increasing doping, the repulsive polaron effective mass  $m_R^*$  first increases, and eventually diverges for a critical value of  $E_F \simeq 1.4\epsilon_T$ , at which the repulsive polaron dispersion becomes flat. For larger values of  $E_F$ , the effective mass changes sign and becomes negative, signaling that the repulsive branch develops a minimum at finite center of mass momentum  $\mathbf{Q} \neq \mathbf{0}$ . Note that  $m_R^*$  recovers the exciton mass at zero doping, i.e.,  $m_R^* \rightarrow m_X$  when  $E_F \rightarrow 0$ .

In contrast, the attractive branch effective mass monotonously decreases for increasing doping. When  $E_F \rightarrow 0$ ,  $m_A^*$  does not recover the trion mass which, for the exciton to electron mass ratio  $m_X/m_e = 2$  relevant for TMD monolayers, is  $m_T = 3/2m_X$ . The same result was also found in calculations with a different mass ratio [374]. This is due to the fact that the polaron ansatz  $|P_3^{(\mathbf{Q})}\rangle$  (2.28) which includes a single particle-hole excitation, does not allow to describe the “polaron-molecule” transition, as also explained in Ref. [374].

In order to describe the “polaron-molecule” transition one should instead add a particle-hole dressing to the trion ansatz  $|T_2^{(\mathbf{Q})}\rangle$  (2.20) to define the

dressed trion state

$$|T_4^{(\mathbf{Q})}\rangle = \frac{1}{\sqrt{\mathcal{A}}} \sum_{|\mathbf{k}|, |\mathbf{k}'| > k_F, |\mathbf{q}| < k_F} \eta_{\mathbf{k}\mathbf{k}'\mathbf{q}}^{(\mathbf{Q})} \hat{x}_{\mathbf{Q}+\mathbf{q}-\mathbf{k}-\mathbf{k}'}^\dagger \hat{c}_{\mathbf{k}}^\dagger \hat{c}_{\mathbf{k}'}^\dagger \hat{c}_{\mathbf{q}} |FS\rangle. \quad (\text{D.2})$$

At low enough doping, one would discover that there is a first-order transition from the polaron state  $|P_3^{(0)}\rangle$  to the “molecular” dressed trion state  $|T_4^{(0)}\rangle$ . One can however describe this transition within a polaron description only, by considering a polaron ansatz up to two particle-hole excitations and allowing a finite center of mass momentum  $\mathbf{Q}$  [385], thus considering

$$|P_5^{(\mathbf{Q})}\rangle = \left[ \varphi_0^{(\mathbf{Q})} \hat{x}_{\mathbf{Q}}^\dagger + \frac{1}{\mathcal{A}} \sum_{\mathbf{k}, \mathbf{q}} \varphi_{\mathbf{k}\mathbf{q}}^{(\mathbf{Q})} \hat{x}_{\mathbf{Q}+\mathbf{q}-\mathbf{k}}^\dagger \hat{c}_{\mathbf{k}}^\dagger \hat{c}_{\mathbf{q}} \right. \\ \left. + \frac{1}{2\mathcal{A}^2} \sum_{\mathbf{k}_{1,2}, \mathbf{q}_{1,2}} \varphi_{\mathbf{k}_1\mathbf{k}_2\mathbf{q}_1\mathbf{q}_2}^{(\mathbf{Q})} \hat{x}_{\mathbf{Q}+\mathbf{q}_1+\mathbf{q}_2-\mathbf{k}_1-\mathbf{k}_2}^\dagger \hat{c}_{\mathbf{k}_1}^\dagger \hat{c}_{\mathbf{k}_2}^\dagger \hat{c}_{\mathbf{q}_1} \hat{c}_{\mathbf{q}_2} \right] |FS\rangle. \quad (\text{D.3})$$

Here, the polaron-molecule transition can be described as a transition from  $|P_5^{(0)}\rangle$  to  $|P_5^{(\mathbf{k}_F)}\rangle$  at low enough doping [385].

## E Renormalization procedure beyond the weak coupling limit

We discuss here an improvement of the renormalization procedure employed in Sec. 1.5.2, to increase its accuracy beyond the weak coupling limit. In Sec. 1.5.2 we saw that in the weak coupling limit  $g \ll a_X \varepsilon_X$ , defining the renormalized photon-exciton detuning  $\delta$  as in Eq. (1.68) and the Rabi splitting  $\Omega$  as in Eq. (1.69), enables one to recover the one-particle LP energy of the coupled oscillator model (1.37c). Beyond weak coupling, the exciton wave function is strongly modified by light-matter coupling, thus impacting the detuning and the Rabi splitting. Here, we provide alternative definitions for the effective detuning  $\delta_{\text{eff}}$  and Rabi splitting  $\Omega_{\text{eff}}$  that coincide with the previous ones for  $g \ll a_X \varepsilon_X$ , but whose validity extends beyond this limit. Comparing the two results allows one to estimate the quantitative error made in our study of the evolution of the system phase diagram with increasing Rabi splitting  $\Omega$ .

To renormalize the theory, it is necessary to identify a measurable quantity that can be used to define the renormalized quantities in the theory. Ideally, the quantity we would use would be the photon energy. However, this is not directly measurable, since the renormalization only occurs for a cavity that contains an active medium, and in that case, the photon mode is replaced by the strongly coupled polariton modes. To circumvent this problem, as in

Ref. [140], we define the effective detuning  $\delta_{\text{eff}}$  and Rabi splitting  $\Omega_{\text{eff}}$  in a way analogous to an experimental procedure — by fitting the polariton dispersion to a coupled oscillator model.

In particular, we employ a two-parameter least square fitting procedure to match the LP dispersion  $E$  evaluated numerically from Eqs. (5.13) with the LP dispersion obtained by the coupled oscillator model (1.37c),

$$\omega_{\text{LP}\mathbf{Q}} = E_{X\mathbf{0}} + E_g + \frac{\delta_{\text{eff}} + \frac{\mathbf{Q}^2}{2m_C} + \frac{\mathbf{Q}^2}{2(m_e+m_h)}}{2} - \frac{1}{2} \sqrt{\left( \delta_{\text{eff}} + \frac{\mathbf{Q}^2}{2m_C} - \frac{\mathbf{Q}^2}{2(m_e+m_h)} \right)^2 + \Omega_{\text{eff}}^2}, \quad (\text{E.1})$$

where  $\delta_{\text{eff}}$  and  $\Omega_{\text{eff}}$  are fitting parameters. In Fig. E.1 we compare the results obtained for the fitting parameters  $\delta_{\text{eff}}$  and  $\Omega_{\text{eff}}$  with  $\delta$  and  $\Omega$  as defined in Eqs. (1.68) and (1.69), respectively. In Fig. E.1 (a)-(d) we fix the light-matter coupling  $g$  and vary  $\delta$ , while in Fig. E.1 (e)-(h), we fix  $\delta$  and vary  $g$ . As expected,  $\delta_{\text{eff}} \rightarrow \delta$  and  $\Omega_{\text{eff}} \rightarrow \Omega$  when  $g \ll \varepsilon_X a_X$ . Moreover, we observe that the differences  $|\delta_{\text{eff}} - \delta|$  and  $|\Omega_{\text{eff}} - \Omega|$  remain relatively small also when  $g \gtrsim \varepsilon_X a_X$ . These results allow us to estimate the size of the corrections that would arise from an improved renormalization scheme. We see that these appear small. Nonetheless, there may be some changes in the results of Ch. 5, when studying the phase diagram beyond the  $g \ll \varepsilon_X a_X$  regime.

## F Origin of $E_F^*$ and $\delta^*$

We explain here the origin of the “universal point” ( $E_F^*, \delta^*$ ) found in the phase diagram of Fig. 5.9. Remarkably, exactly at this point there is no  $\Omega$  dependence of either the SF-FF transition (for unscreened interactions) or the SF-N transition (for screened interactions). One way to understand the origin of this universal point is by comparing the many-body LP energy of the SF state at  $\mathbf{Q} = \mathbf{0}$ ,  $E_0$ , with that of the FF phase at  $Q_{\text{min}}$ ,  $E_{Q_{\text{min}}}$ . The two energies clearly coincide at this 1<sup>st</sup> order boundary (for screened interactions the FF phase may be replaced by the N phase if the density is large enough). A limiting case of this boundary occurs when  $\Omega \rightarrow 0$ ; in this limit, the boundary occurs when

$$\delta = E_{XQ_{\text{min}}}^{(E_F)} - E_{X\mathbf{0}}, \quad (\text{F.1})$$

(assuming  $E_F > E_{F0}$ ), where  $E_{XQ_{\text{min}}}^{(E_F)}$  is the many-body exciton (i.e.,  $\Omega = 0$  case) energy of the FF phase for a majority species Fermi energy  $E_F$ . This condition corresponds to a crossing between a photonic SF state and the excitonic FF state. At non-zero  $\Omega$ , the SF state becomes polaritonic.

The existence of the special point  $(E_F^*, \delta^*)$  corresponds to a point where this critical condition is not affected by light-matter coupling. To see this, we consider the following. At each  $E_F$ , we can choose the detuning  $\delta$  so as to satisfy Eq. (F.1), thus on the SF-FF boundary at  $\Omega = 0$ . We then plot in the top panels of Fig. F.1  $E_0 - E_{Q_{\min}}$ , the energy difference between the LP energy at  $\mathbf{Q} = \mathbf{0}$  and  $\mathbf{Q} = Q_{\min}$ , as a function of  $\Omega$ . We plot this energy difference for different values of  $E_F$ . For  $E_F < E_F^*$ , this energy difference decreases with  $\Omega$ . This means that on increasing  $\Omega$ , the SF-FF boundary moves to larger values of the detuning (see Fig. 5.9). Conversely, if  $E_F > E_F^*$ , the energy difference increases with  $\Omega$ , so the SF-FF boundary moves down to lower detuning. Exactly at  $E_F = E_F^*$ , we observe that  $E_0 - E_{Q_{\min}} = 0$ , becomes exactly independent of  $\Omega$ . As such, at this value of  $E_F^*$ , the critical detuning is  $\delta^*$ , independent of  $\Omega$ .

Given the effective  $\Omega$  independence seen at  $E_F^*$ , an alternative way of identifying the value of  $E_F^*$  and  $\delta^*$  is by finding a condition for which the eigenenergy of the variational state becomes independent of the coupling to light. To do this, following Ref. [140], we rewrite the many-body eigenvalue problem of Eqs. (5.13) in terms of the renormalized photon energy  $\omega_{C\mathbf{Q}} = \omega_{C0} + \mathbf{Q}^2/2m_C$  (1.67), to give an expression which is independent of the UV cutoff. We thus separate out the divergent part of the relative wave-function  $\varphi_{\mathbf{k}}^{(\mathbf{Q})}$ ,

$$\varphi_{\mathbf{k}}^{(\mathbf{Q})} = \beta_{\mathbf{k}}^{(\mathbf{Q})} + \frac{g\alpha_0^{(\mathbf{Q})}}{E - \xi_{\mathbf{k}\mathbf{Q}}}, \quad (\text{F.2})$$

and rewrite (5.13) in the following equivalent forms:

$$(E - \xi_{\mathbf{k}\mathbf{Q}}) \beta_{\mathbf{k}}^{(\mathbf{Q})} = -\frac{1}{\mathcal{A}} \sum_{\mathbf{k}' > k_F} V_{\mathbf{k}-\mathbf{k}'} \beta_{\mathbf{k}'\mathbf{Q}} + \frac{g\alpha_0^{(\mathbf{Q})}}{\mathcal{A}} \sum_{\mathbf{k}' > k_F} \frac{V_{\mathbf{k}-\mathbf{k}'}}{-E + \xi_{\mathbf{k}'\mathbf{Q}}} \quad (\text{F.3a})$$

$$\left[ E - \omega_{C\mathbf{Q}} + \frac{g^2}{\mathcal{A}} \left( \sum_{\mathbf{k} > k_F} \frac{1}{-E + \xi_{\mathbf{k}\mathbf{Q}}} - \sum_{\mathbf{k}} \frac{1}{-E_X + \epsilon_{\mathbf{k},1} + \epsilon_{\mathbf{k},2}} \right) \right] \alpha_0^{(\mathbf{Q})} = \frac{g}{\mathcal{A}} \sum_{\mathbf{k} > k_F} \beta_{\mathbf{k}}^{(\mathbf{Q})}. \quad (\text{F.3b})$$

All sums are now convergent. For the solution of these equations to be independent of light-matter coupling means the  $E$  must match the solution at  $g = 0$ , i.e.,

$$E = \omega_{C\mathbf{Q}}. \quad (\text{F.4})$$

This condition corresponds to the system energy  $E$  coinciding with  $\omega_{C\mathbf{Q}}$ , the energy of the photon mode at  $E_F = 0$ . Using Eq. (F.4) in Eq. (F.3b), we obtain

the following equation to define  $E_F^*$ :

$$\sum_{\mathbf{k} > k_F} \frac{1}{-E + \xi_{\mathbf{k}\mathbf{Q}}} - \sum_{\mathbf{k}} \frac{1}{-E_{X0} + \epsilon_{\mathbf{k},1} + \epsilon_{\mathbf{k},2}} = \frac{1}{g\alpha_0^{(\mathbf{Q})}} \sum_{\mathbf{k} > k_F} \beta_{\mathbf{k}}^{(\mathbf{Q})}. \quad (\text{F.5})$$

Note that this condition is indeed independent of  $g$ . To see this, we formally invert Eq. (F.3a), to give  $\beta_{\mathbf{k}}^{(\mathbf{Q})}$ :

$$\beta_{\mathbf{k}}^{(\mathbf{Q})} = g\alpha_0^{(\mathbf{Q})} \sum_{\mathbf{k}' > k_F} (\mathbb{M}_{\mathbf{Q}}^{-1})_{\mathbf{k},\mathbf{k}'} L_{\mathbf{k}'\mathbf{Q}}, \quad (\text{F.6})$$

where the matrix  $\mathbb{M}_{\mathbf{Q}}$  and vector  $L_{\mathbf{Q}}$  in relative momentum space are defined respectively as

$$(\mathbb{M}_{\mathbf{Q}})_{\mathbf{k},\mathbf{k}'} = (E - \xi_{\mathbf{k}\mathbf{Q}}) \delta_{\mathbf{k},\mathbf{k}'} + V_{\mathbf{k}-\mathbf{k}'} \quad (\text{F.7a})$$

$$L_{\mathbf{k}\mathbf{Q}} = \sum_{\mathbf{k}' > k_F} \frac{V_{\mathbf{k}-\mathbf{k}'}}{-E + \xi_{\mathbf{k}'\mathbf{Q}}}. \quad (\text{F.7b})$$

We thus find that Eq. (F.5) is independent of both  $g$  and  $\alpha_0^{(\mathbf{Q})}$ :

$$\begin{aligned} \sum_{\mathbf{k} > k_F} \frac{1}{-E + \xi_{\mathbf{k}\mathbf{Q}}} - \sum_{\mathbf{k}} \frac{1}{-E_{X0} + \epsilon_{\mathbf{k},1} + \epsilon_{\mathbf{k},2}} \\ = \sum_{\mathbf{k} > k_F} \sum_{\mathbf{k}' > k_F} (\mathbb{M}_{\mathbf{Q}}^{-1})_{\mathbf{k},\mathbf{k}'} L_{\mathbf{k}'\mathbf{Q}}. \end{aligned} \quad (\text{F.8})$$

In addition to satisfying Eq. (F.8),  $E_F^*$  lies on the SF-FF (SF-N) boundaries for unscreened (screened) interactions and, thus, it also has to lie on the boundary at  $\Omega = 0$ . With this in mind, we plot in the bottom panels of Fig. F.1 the energy  $\omega_{\mathbf{C0}} = E_{\mathbf{0}}$  obtained by solving Eq. (F.8) at  $\mathbf{Q} = \mathbf{0}$  as a function of  $E_F$ . From the crossing of this curve with that of the FF state in the absence of light, i.e., the FF exciton energy  $E_{X\mathbf{Q}_{min}}^{(E_F)}$  (or, for the screened case, the normal state energy  $E_N$ ), we recover the value of  $E_F^*$ . The corresponding value of the detuning  $\delta^*$  is given by Eq. (F.1) for  $E_F = E_F^*$ , i.e.,  $\delta^* = E_{X\mathbf{Q}_{min}}^{(E_F^*)} - E_{X0}$ . We thus find  $(E_F^*, \delta^*) \simeq (1.55\varepsilon_X, 1.82\varepsilon_X)$  (for screened interactions) and  $(E_F^*, \delta^*) \simeq (1.95\varepsilon_X, 0.91\varepsilon_X)$  (unscreened interactions).

Finally, we remark that the  $g$  independence at  $E_F^*$  does not imply that light and matter are fully decoupled at this point. Indeed, the photon frequency depends on the active medium through the process of renormalization. However, precisely at  $E_F^*$ , the photon self-energy arising due to the light-matter interaction only contains the term that appears in Eq. (1.67), while all other terms cancel. Given the general arguments that led us to determine the point  $(E_F^*, \delta^*)$ , it is likely that it persists as a special point in the photon self-energy

also beyond the variational approach used in this work.

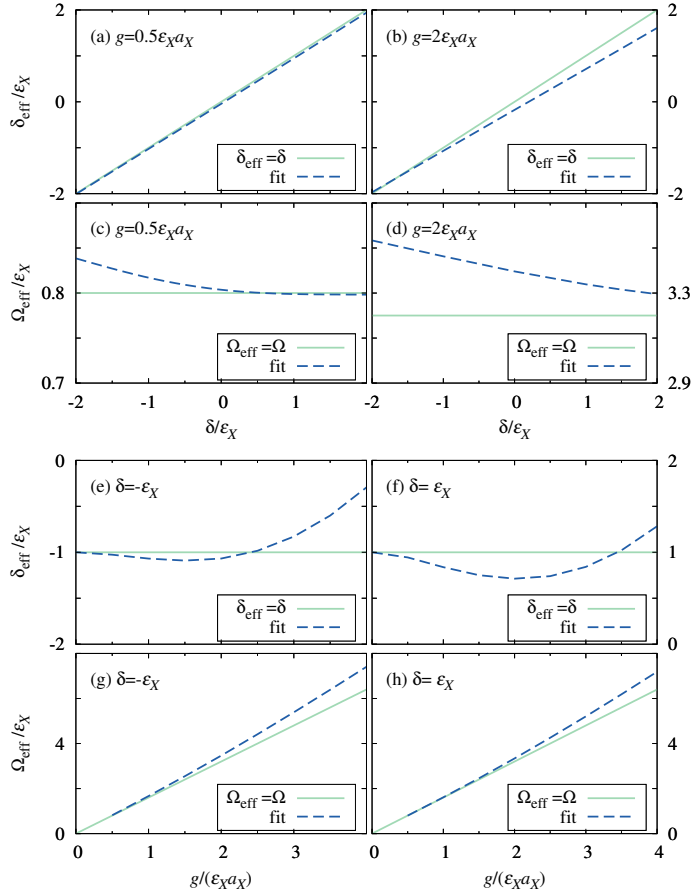


**Fig. E.1:** Comparison between detuning  $\delta$  (1.68) and Rabi splitting  $\Omega$  (1.69), as defined in the renormalization procedure of Sec. 1.5.2, and the respective quantities  $\delta_{\text{eff}}$  and  $\Omega_{\text{eff}}$  obtained by a least square fitting procedure — see text. Parameters are for a GaAs microcavity with a single quantum well ( $d = 0$ ),  $m_e/m_h = 0.25$ , and  $E_F = 0$ .

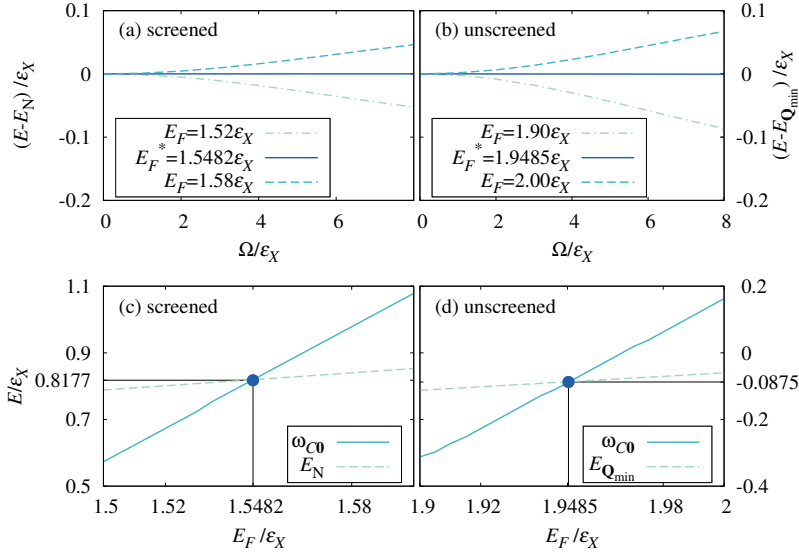


**Fig. F.1:** Illustration of the dependence of energies on Rabi splitting close to  $E_F^*$ . The parameters are for a GaAs heterostructure with a single quantum well  $d = 0$ , mass ratio  $m_2/m_1 = 0.25$ , and for screened (left panels) and unscreened (right panels) interactions. Top panels: energy difference between the many-body polariton SF energy  $E_0$  and the FF energy  $E_{Q_{\min}}$  (top right) or between  $E_0$  and the normal state energy  $E_N$  (top left). For each Fermi energy,  $E_F$ , the detuning is fixed according to Eq. (F.1), describing the SF-FF boundary at  $\Omega = 0$ . Bottom panels: Photon energy  $\omega_{C0}$  satisfying Eq. (F.8) at  $\mathbf{Q} = \mathbf{0}$  and  $E_{Q_{\min}}$  — for the values of  $E_F$  considered in the plot and for screened interactions,  $E_{Q_{\min}}$  coincides with the normal state energy  $E_N$ , i.e.,  $Q_{\min} = k_F \hat{\mathbf{k}}_F$ .

# References

- [1] A. KAVOKIN, J. BAUMBERG, G. MALPUECH and F. LAUSSY:  
*Microcavities*,  
Series on Semiconductor Science and Technology (OUP Oxford, 2011).
- [2] C. KITTEL and P. MCEUEN:  
*Introduction to solid state physics*,  
(John Wiley and Sons, 1953).
- [3] J. FRENKEL:  
On the transformation of light into heat in solids.,  
[Phys. Rev. \*\*37\*\*, 17–44 \(1931\)](#).
- [4] L. APKER and E. TAFT:  
Photoelectric emission from F-centers in KI,  
[Phys. Rev. \*\*79\*\*, 964–966 \(1950\)](#).
- [5] V. AGRANOVICH, D. BASKO, K. SCHMIDT, G. LAROCCA, F. BASSANI, S. FORREST,  
K. LEO and D. LIDZEY:  
Charged Frenkel excitons in organic crystals,  
[Chemical Physics \*\*272\*\*, 159–169 \(2001\)](#).
- [6] F. C. SPANO:  
The spectral signatures of Frenkel polarons in H- and J-aggregates,  
[Accounts of Chemical Research \*\*43\*\*, PMID: 20014774, 429–439 \(2010\)](#).
- [7] G. H. WANNIER:  
The structure of electronic excitation levels in insulating crystals,  
[Phys. Rev. \*\*52\*\*, 191–197 \(1937\)](#).
- [8] N. F. MOTT and M. J. LITTLETON:  
Conduction in polar crystals. electrolytic conduction in solid salts,  
[Trans. Faraday Soc. \*\*34\*\*, 485–499 \(1938\)](#).
- [9] T. TAGUCHI, J. SHIRAFUJI and Y. INUSHI:  
Excitonic emission in cadmium telluride,  
[physica status solidi \(b\) \*\*68\*\*, 727–738 \(1975\)](#).
- [10] R. PÄSSLER, E. GRIEBL, H. RIEPL, G. LAUTNER, S. BAUER, H. PREIS, W. GEBHARDT,  
B. BUDA, D. J. AS, D. SCHIKORA, K. LISCHKA, K. PAPAGELIS and S. VES:  
Temperature dependence of exciton peak energies in ZnS, ZnSe, and ZnTe epitaxial  
films,  
[Journal of Applied Physics \*\*86\*\*, 4403–4411 \(1999\)](#).

- [11] S. B. NAM, D. C. REYNOLDS, C. W. LITTON, R. J. ALMASSY, T. C. COLLINS and C. M. WOLFE:  
Free-exciton energy spectrum in GaAs,  
*Phys. Rev. B* **13**, 761–767 (1976).
- [12] B. MONEMAR, J. P. BERGMAN, I. A. BUYANOVA, W. LI, H. AMANO and I. AKASAKI:  
Free excitons in GaN,  
*MRS Internet Journal of Nitride Semiconductor Research* **1**, 2 (1996).
- [13] S. B. NAM, D. C. REYNOLDS, C. W. LITTON, T. C. COLLINS, P. J. DEAN and R. C. CLARKE:  
Free-exciton energy spectrum in InP in a magnetic field,  
*Phys. Rev. B* **13**, 1643–1648 (1976).
- [14] U. ASAF and I. STEINBERGER:  
Wannier excitons in liquid xenon,  
*Physics Letters A* **34**, 207–208 (1971).
- [15] V. AGRANOVICH, H. BENISTY and C. WEISBUCH:  
Organic and inorganic quantum wells in a microcavity: Frenkel-Wannier-Mott excitons hybridization and energy transformation,  
*Solid State Communications* **102**, 631–636 (1997).
- [16] E. SILINSH and J. EIDUSS:  
*Organic molecular crystals: their electronic states*,  
Springer Series in Solid-State Sciences (Springer Berlin Heidelberg, 1980).
- [17] E. I. RASHBA and M. E. PORTNOI:  
Anyon excitons,  
*Phys. Rev. Lett.* **70**, 3315–3318 (1993).
- [18] J. S. BLAKEMORE:  
Semiconducting and other major properties of gallium arsenide,  
*Journal of Applied Physics* **53**, R123–R181 (1982).
- [19] G. BASTARD:  
*Wave mechanics applied to semiconductor heterostructures*,  
Monographies de physique (Les Editions de Physique, 1988).
- [20] C. WEISBUCH and C. HERMANN:  
Optical detection of conduction-electron spin resonance in GaAs,  $\text{Ga}_{1-x}\text{In}_x\text{As}$ , and  $\text{Ga}_{1-x}\text{Al}_x\text{As}$ ,  
*Phys. Rev. B* **15**, 816–822 (1977).
- [21] L. C. BARCUS, A. PERLMUTTER and J. CALLAWAY:  
Effective mass of electrons in gallium arsenide,  
*Phys. Rev.* **111**, 167–168 (1958).
- [22] H. HAUG and S. W. KOCH:  
*Quantum theory of the optical and electronic properties of semiconductors*,  
4th (WORLD SCIENTIFIC, 2004).
- [23] J. SINGH:  
*Physics of semiconductors and their heterostructures*,  
Electrical engineering series (McGraw-Hill, 1993).
- [24] I. STRZALKOWSKI, S. JOSHI and C. R. CROWELL:  
Dielectric constant and its temperature dependence for GaAs, CdTe, and ZnSe,  
*Applied Physics Letters* **28**, 350–352 (1976).

- [25] W. J. MOORE and R. T. HOLM:  
Infrared dielectric constant of gallium arsenide,  
*Journal of Applied Physics* **80**, 6939–6942 (1996).
- [26] A. FOX:  
*Optical properties of solids*,  
Oxford master series in condensed matter physics (Oxford University Press, 2001).
- [27] D. D. SELL:  
Resolved free-exciton transitions in the optical-absorption spectrum of GaAs,  
*Phys. Rev. B* **6**, 3750–3753 (1972).
- [28] T. KAZIMIERCZUK, D. FRÖHLICH, S. SCHEEL, H. STOLZ and M. BAYER:  
Giant Rydberg excitons in the copper oxide Cu<sub>2</sub>O,  
*Nature* **514**, 343–347 (2014).
- [29] C. KLINGSHIRN:  
*Semiconductor optics*,  
Advanced texts in physics (Springer Berlin Heidelberg, 2007).
- [30] T. C. MCGILL, R. H. MILES, Y. RAJAKARUNANAYAKE and J. O. MCCALDIN:  
II-VI heterostructures and multi-quantum wells,  
edited by T. C. McGill, C. M. Sotomayor Torres and W. Gebhardt, 53–65 (1989).
- [31] G. C. OSBOURN:  
Design of III-V quantum well structures for long-wavelength detector applications,  
**5**, S5 (1990).
- [32] S. ADACHI:  
GaAs, AlAs, and Al<sub>x</sub>Ga<sub>1-x</sub>As: material parameters for use in research and device applications,  
*Journal of Applied Physics* **58**, R1–R29 (1985).
- [33] X. L. YANG, S. H. GUO, F. T. CHAN, K. W. WONG and W. Y. CHING:  
Analytic solution of a two-dimensional hydrogen atom. nonrelativistic theory,  
*Phys. Rev. A* **43**, 1186–1196 (1991).
- [34] R. WINKLER:  
*Spin-orbit coupling effects in two-dimensional electron and hole systems*,  
Springer Tracts in Modern Physics (Springer Berlin Heidelberg, 2003).
- [35] R. C. MILLER, D. A. KLEINMAN, W. T. TSANG and A. C. GOSSARD:  
Observation of the excited level of excitons in GaAs quantum wells,  
*Phys. Rev. B* **24**, 1134–1136 (1981).
- [36] P. HARRISON:  
*Quantum wells, wires and dots*,  
(John Wiley and Sons, Ltd, 2005).
- [37] X.-F. HE:  
Excitons in anisotropic solids: the model of fractional-dimensional space,  
*Phys. Rev. B* **43**, 2063–2069 (1991).
- [38] H. MATHIEU, P. LEFEBVRE and P. CHRISTOL:  
Simple analytical method for calculating exciton binding energies in semiconductor quantum wells,  
*Phys. Rev. B* **46**, 4092–4101 (1992).
- [39] A. H. CASTRO NETO, F. GUINEA, N. M. R. PERES, K. S. NOVOSELOV and A. K. GEIM:  
The electronic properties of graphene,  
*Rev. Mod. Phys.* **81**, 109–162 (2009).

- [40] A. K. GEIM:  
Graphene: status and prospects,  
*Science* **324**, 1530–1534 (2009).
- [41] D. XIAO, G.-B. LIU, W. FENG, X. XU and W. YAO:  
Coupled spin and valley physics in monolayers of MoS<sub>2</sub> and other group-VI dichalcogenides,  
*Phys. Rev. Lett.* **108**, 196802 (2012).
- [42] K. F. MAK, C. LEE, J. HONE, J. SHAN and T. F. HEINZ:  
Atomically thin MoS<sub>2</sub>: a new direct-gap semiconductor,  
*Phys. Rev. Lett.* **105**, 136805 (2010).
- [43] A. K. GEIM and I. V. GRIGORIEVA:  
Van der Waals heterostructures,  
*Nature* **499**, 419–425 (2013).
- [44] F. XIA, H. WANG, D. XIAO, M. DUBEY and A. RAMASUBRAMANIAM:  
Two-dimensional material nanophotonics,  
*Nature Photonics* **8**, 899–907 (2014).
- [45] K. S. NOVOSELOV, A. K. GEIM, S. V. MOROZOV, D. JIANG, Y. ZHANG, S. V. DUBONOS, I. V. GRIGORIEVA and A. A. FIRSOV:  
Electric field effect in atomically thin carbon films,  
*Science* **306**, 666–669 (2004).
- [46] K. MAK, L. JU, F. WANG and T. HEINZ:  
Optical spectroscopy of graphene: from the far infrared to the ultraviolet, English (US),  
*Solid State Communications* **152**, 1341–1349 (2012).
- [47] F. BONACCORSO, Z. SUN, T. HASAN and A. C. FERRARI:  
Graphene photonics and optoelectronics,  
*Nature Photonics* **4**, 611–622 (2010).
- [48] A. SPLENDIANI, L. SUN, Y. ZHANG, T. LI, J. KIM, C.-Y. CHIM, G. GALLI and F. WANG:  
Emerging photoluminescence in monolayer MoS<sub>2</sub>,  
*Nano Letters* **10**, 1271–1275 (2010).
- [49] Y. LIU, Y. GAO, S. ZHANG, J. HE, J. YU and Z. LIU:  
Valleytronics in transition metal dichalcogenides materials,  
*Nano Research* **12**, 2695–2711 (2019).
- [50] E. C. AHN:  
2D materials for spintronic devices,  
*npj 2D Materials and Applications* **4**, 17 (2020).
- [51] P. CUDAZZO, I. V. TOKATLY and A. RUBIO:  
Dielectric screening in two-dimensional insulators: implications for excitonic and impurity states in graphene,  
*Phys. Rev. B* **84**, 085406 (2011).
- [52] A. RAMASUBRAMANIAM:  
Large excitonic effects in monolayers of molybdenum and tungsten dichalcogenides,  
*Phys. Rev. B* **86**, 115409 (2012).
- [53] T. C. BERKELBACH, M. S. HYBERTSEN and D. R. REICHMAN:  
Theory of neutral and charged excitons in monolayer transition metal dichalcogenides,  
*Phys. Rev. B* **88**, 045318 (2013).

- [54] K. F. MAK, K. HE, C. LEE, G. H. LEE, J. HONE, T. F. HEINZ and J. SHAN:  
Tightly bound trions in monolayer MoS<sub>2</sub>,  
*Nature Materials* **12**, 207–211 (2013).
- [55] A. CHERNIKOV, T. C. BERKELBACH, H. M. HILL, A. RIGOSI, Y. LI, B. ASLAN, D. R. REICHMAN, M. S. HYBERTSEN and T. F. HEINZ:  
Exciton binding energy and nonhydrogenic Rydberg series in monolayer WS<sub>2</sub>,  
*Phys. Rev. Lett.* **113**, 076802 (2014).
- [56] S. LEBÈGUE and O. ERIKSSON:  
Electronic structure of two-dimensional crystals from ab initio theory,  
*Phys. Rev. B* **79**, 115409 (2009).
- [57] T. CHEIWCHANCHAMNANGIJ and W. R. L. LAMBRECHT:  
Quasiparticle band structure calculation of monolayer, bilayer, and bulk MoS<sub>2</sub>,  
*Phys. Rev. B* **85**, 205302 (2012).
- [58] A. KORMÁNYOS, V. ZÓLYOMI, N. D. DRUMMOND, P. RAKYTA, G. BURKARD and V. I. FAL'KO:  
Monolayer MoS<sub>2</sub>: trigonal warping, the gamma valley, and spin-orbit coupling effects,  
*Phys. Rev. B* **88**, 045416 (2013).
- [59] A. KORMÁNYOS, G. BURKARD, M. GMITRA, J. FABIAN, V. ZÓLYOMI, N. D. DRUMMOND and V. FAL'KO:  
K · p theory for two-dimensional transition metal dichalcogenide semiconductors,  
*2D Materials* **2**, 022001 (2015).
- [60] G.-B. LIU, W.-Y. SHAN, Y. YAO, W. YAO and D. XIAO:  
Three-band tight-binding model for monolayers of group-VIB transition metal dichalcogenides,  
*Phys. Rev. B* **88**, 085433 (2013).
- [61] T. CAO, G. WANG, W. HAN, H. YE, C. ZHU, J. SHI, Q. NIU, P. TAN, E. WANG, B. LIU and J. FENG:  
Valley-selective circular dichroism of monolayer molybdenum disulphide,  
*Nature Communications* **3**, 887 (2012).
- [62] S. A. VITALE, D. NEZICH, J. O. VARGHESE, P. KIM, N. GEDIK, P. JARILLO-HERRERO, D. XIAO and M. ROTHSCILD:  
Valleytronics: opportunities, challenges, and paths forward,  
*Small* **14**, 1801483 (2018).
- [63] D. ZAMBRANO, P. ORELLANA, L. ROSALES and A. LATGÉ:  
Spin and valley filter based on two-dimensional WSe<sub>2</sub> heterostructures,  
*Phys. Rev. Appl.* **15**, 034069 (2021).
- [64] S. LIU, A. GRANADOS DEL ÁGUILA, X. LIU, Y. ZHU, Y. HAN, A. CHATURVEDI, P. GONG, H. YU, H. ZHANG, W. YAO and Q. XIONG:  
Room-temperature valley polarization in atomically thin semiconductors via chalcogenide alloying,  
*ACS Nano* **14**, PMID: 32806059, 9873–9883 (2020).
- [65] L. L. TAO, A. NAEEMI and E. Y. TSYMBAL:  
Valley-spin logic gates,  
*Phys. Rev. Appl.* **13**, 054043 (2020).
- [66] R. LIU, G. HU, M. DAN, Y. ZHANG, L. LI and Y. ZHANG:  
Piezotronic spin and valley transistors based on monolayer MoS<sub>2</sub>,  
*Nano Energy* **72**, 104678 (2020).

- [67] B. PENG, P. K. ANG and K. P. LOH:  
Two-dimensional dichalcogenides for light-harvesting applications,  
*Nano Today* **10**, 128–137 (2015).
- [68] J. XIAO, M. ZHAO, Y. WANG and X. ZHANG:  
Excitons in atomically thin 2D semiconductors and their applications,  
*Nanophotonics* **6**, 1309–1328 (2017).
- [69] G. WANG, A. CHERNIKOV, M. M. GLAZOV, T. F. HEINZ, X. MARIE, T. AMAND and B. URBASZEK:  
Colloquium: excitons in atomically thin transition metal dichalcogenides,  
*Rev. Mod. Phys.* **90**, 021001 (2018).
- [70] M. R. MOLAS, C. FAUGERAS, A. O. SLOBODENIUK, K. NOGAJEWSKI, M. BARTOS, D. M. BASKO and M. POTEMSKI:  
Brightening of dark excitons in monolayers of semiconducting transition metal dichalcogenides,  
*2D Materials* **4**, 021003 (2017).
- [71] C. ROBERT, B. HAN, P. KAPUSCINSKI, A. DELHOMME, C. FAUGERAS, T. AMAND, M. R. MOLAS, M. BARTOS, K. WATANABE, T. TANIGUCHI, B. URBASZEK, M. POTEMSKI and X. MARIE:  
Measurement of the spin-forbidden dark excitons in MoS<sub>2</sub> and MoSe<sub>2</sub> monolayers,  
*Nature Communications* **11**, 4037 (2020).
- [72] C. ZHANG, A. JOHNSON, C.-L. HSU, L.-J. LI and C.-K. SHIH:  
Direct imaging of band profile in single layer MoS<sub>2</sub> on graphite: quasiparticle energy gap, metallic edge states, and edge band bending,  
*Nano Letters* **14**, PMID: 24783945, 2443–2447 (2014).
- [73] M. M. UGEDA, A. J. BRADLEY, S.-F. SHI, F. H. DA JORNADA, Y. ZHANG, D. Y. QIU, W. RUAN, S.-K. MO, Z. HUSSAIN, Z.-X. SHEN, F. WANG, S. G. LOUIE and M. F. CROMMIE:  
Giant bandgap renormalization and excitonic effects in a monolayer transition metal dichalcogenide semiconductor,  
*Nature materials* **13**, 1091–1095 (2014).
- [74] K. HE, N. KUMAR, L. ZHAO, Z. WANG, K. F. MAK, H. ZHAO and J. SHAN:  
Tightly bound excitons in monolayer WSe<sub>2</sub>,  
*Phys. Rev. Lett.* **113**, 026803 (2014).
- [75] L. H. LI, J. CERVENKA, K. WATANABE, T. TANIGUCHI and Y. CHEN:  
Strong oxidation resistance of atomically thin boron nitride nanosheets,  
*ACS Nano* **8**, PMID: 24400990, 1457–1462 (2014).
- [76] X. CUI, G.-H. LEE, Y. D. KIM, G. AREFE, P. Y. HUANG, C.-H. LEE, D. A. CHENET, X. ZHANG, L. WANG, F. YE, F. PIZZOCCHERO, B. S. JESSEN, K. WATANABE, T. TANIGUCHI, D. A. MULLER, T. LOW, P. KIM and J. HONE:  
Multi-terminal transport measurements of MoS<sub>2</sub> using a van der Waals heterostructure device platform,  
*Nature Nanotechnology* **10**, 534–540 (2015).
- [77] Y. UCHIYAMA, A. KUTANA, K. WATANABE, T. TANIGUCHI, K. KOJIMA, T. ENDO, Y. MIYATA, H. SHINOHARA and R. KITaura:  
Momentum-forbidden dark excitons in hBN-encapsulated monolayer MoS<sub>2</sub>,  
*npj 2D Materials and Applications* **3**, 26 (2019).

- [78] J. WIERZBOWSKI, J. KLEIN, F. SIGGER, C. STRAUBINGER, M. KREMSER, T. TANIGUCHI, K. WATANABE, U. WURSTBAUER, A. W. HOLLEITNER, M. KANIBER, K. MÜLLER and J. J. FINLEY:  
Direct exciton emission from atomically thin transition metal dichalcogenide heterostructures near the lifetime limit,  
[Scientific Reports](#) **7**, 12383 (2017).
- [79] F. CADIZ, E. COURTADE, C. ROBERT, G. WANG, Y. SHEN, H. CAI, T. TANIGUCHI, K. WATANABE, H. CARRERE, D. LAGARDE, M. MANCA, T. AMAND, P. RENUCCI, S. TONGAY, X. MARIE and B. URBASZEK:  
Excitonic linewidth approaching the homogeneous limit in MoS<sub>2</sub>-Based van der Waals Heterostructures,  
[Phys. Rev. X](#) **7**, 021026 (2017).
- [80] N. S. RYTOVA:  
The screened potential of a point charge in a thin film,  
[Moscow University Physics Bulletin](#) **3**, 18 (1967).
- [81] L. V. KELDYSH:  
Coulomb interaction in thin semiconductor and semimetal films,  
[Soviet Journal of Experimental and Theoretical Physics Letters](#) **29**, 658 (1979).
- [82] S. LARENTIS, H. C. P. MOVVA, B. FALLAHAZAD, K. KIM, A. BEHROOZI, T. TANIGUCHI, K. WATANABE, S. K. BANERJEE and E. TUTUC:  
Large effective mass and interaction-enhanced Zeeman splitting of K-valley electrons in MoSe<sub>2</sub>,  
[Phys. Rev. B](#) **97**, 201407 (2018).
- [83] J. DESLIPPE, M. DIPOPPA, D. PRENDERGAST, M. V. O. MOUTINHO, R. B. CAPAZ and S. G. LOUIE:  
Electron–hole interaction in carbon nanotubes: novel screening and exciton excitation spectra,  
[Nano Letters](#) **9**, 1330–1334 (2009).
- [84] D. Y. QIU, F. H. DA JORNADA and S. G. LOUIE:  
Optical spectrum of MoS<sub>2</sub>: many-body effects and diversity of exciton states,  
[Phys. Rev. Lett.](#) **111**, 216805 (2013).
- [85] C. ROBERT, M. A. SEMINA, F. CADIZ, M. MANCA, E. COURTADE, T. TANIGUCHI, K. WATANABE, H. CAI, S. TONGAY, B. LASSAGNE, P. RENUCCI, T. AMAND, X. MARIE, M. M. GLAZOV and B. URBASZEK:  
Optical spectroscopy of excited exciton states in MoS<sub>2</sub> monolayers in van der Waals heterostructures,  
[Phys. Rev. Mater.](#) **2**, 011001 (2018).
- [86] L. V. BUTOV:  
Condensation and pattern formation in cold exciton gases in coupled quantum wells,  
[Journal of Physics: Condensed Matter](#) **16**, R1577 (2004).
- [87] R. RAPAPORT and G. CHEN:  
Experimental methods and analysis of cold and dense dipolar exciton fluids,  
[Journal of Physics: Condensed Matter](#) **19**, 295207 (2007).
- [88] K. SIVALERTPORN, L. MOUCHLIADIS, A. L. IVANOV, R. PHILP and E. A. MULJAROV:  
Direct and indirect excitons in semiconductor coupled quantum wells in an applied electric field,  
[Phys. Rev. B](#) **85**, 045207 (2012).

- [89] A. A. HIGH, A. T. HAMMACK, L. V. BUTOV, M. HANSON and A. C. GOSSARD: Exciton optoelectronic transistor, *Opt. Lett.* **32**, 2466–2468 (2007).
- [90] Y. Y. KUZNETSOVA, M. REMEIK, A. A. HIGH, A. T. HAMMACK, L. V. BUTOV, M. HANSON and A. C. GOSSARD: All-optical excitonic transistor, *Opt. Lett.* **35**, 1587–1589 (2010).
- [91] A. A. HIGH, E. E. NOVITSKAYA, L. V. BUTOV, M. HANSON and A. C. GOSSARD: Control of exciton fluxes in an excitonic integrated circuit, en, *Science* **321**, 229–231 (2008).
- [92] G. GROSSO, J. C. GRAVES, A. HAMMACK, A. HIGH, L. BUTOV, M. HANSON and A. GOSSARD: Excitonic switches operating at around 100 K, in *Conference on lasers and electro-optics 2010* (2010), QFI5.
- [93] G. GUPTA, F. MEMA and R. J. HUETING: Electron-hole bilayer light-emitting device: concept and operation, *Solid-State Electronics* **168**, Special Issue of *Solid-State Electronics*, dedicated to EUROSOI-ULIS 2019, 107726 (2020).
- [94] M. COMBESCOT, R. COMBESCOT and F. DUBIN: Bose–Einstein condensation and indirect excitons: a review, *Reports on Progress in Physics* **80**, 066501 (2017).
- [95] D. V. FIL and S. I. SHEVCHENKO: Electron-hole superconductivity (review), *Low Temperature Physics* **44**, 867–909 (2018).
- [96] X. ZHU, P. B. LITTLEWOOD, M. S. HYBERTSEN and T. M. RICE: Exciton condensate in semiconductor quantum well structures, *Phys. Rev. Lett.* **74**, 1633–1636 (1995).
- [97] P. B. LITTLEWOOD and X. ZHU: Possibilities for exciton condensation in semiconductor quantum-well structures, *Physica Scripta* **1996**, 56 (1996).
- [98] A. V. BALATSKY, Y. N. JOGLEKAR and P. B. LITTLEWOOD: Dipolar superfluidity in electron-hole bilayer systems, *Phys. Rev. Lett.* **93**, 266801 (2004).
- [99] L. LIU, L. ŚWIERKOWSKI, D. NEILSON and J. SZYMA ŃSKI: Static and dynamic properties of coupled electron-electron and electron-hole layers, *Phys. Rev. B* **53**, 7923–7931 (1996).
- [100] S. DE PALO, F. RAPISARDA and G. SENATORE: Excitonic condensation in a symmetric electron-hole bilayer, *Phys. Rev. Lett.* **88**, 206401 (2002).
- [101] L. V. BUTOV, A. C. GOSSARD and D. S. CHEMLA: Macroscopically ordered state in an exciton system, *Nature* **418**, 751–754 (2002).
- [102] D. SNOKE, S. DENEV, Y. LIU, L. PFEIFFER and K. WEST: Long-range transport in excitonic dark states in coupled quantum wells, *Nature* **418**, 754–757 (2002).
- [103] J. A. SEAMONS, D. R. TIBBETTS, J. L. RENO and M. P. LILLY: Undoped electron-hole bilayers in a GaAs/AlGaAs double quantum well, *Applied Physics Letters* **90**, 052103 (2007).

- [104] A. A. HIGH, J. R. LEONARD, A. T. HAMMACK, M. M. FOGLER, L. V. BUTOV, A. V. KAVOKIN, K. L. CAMPMAN and A. C. GOSSARD:  
Spontaneous coherence in a cold exciton gas,  
*Nature* **483**, 584–588 (2012).
- [105] U. SICILIANI DE CUMIS, J. WALDIE, A. F. CROXALL, D. TANEJA, J. LLANDRO, I. FARRER, H. E. BEERE and D. A. RITCHIE:  
A complete laboratory for transport studies of electron-hole interactions in GaAs/AlGaAs ambipolar bilayers,  
*Applied Physics Letters* **110**, 072105 (2017).
- [106] U. SIVAN, P. M. SOLOMON and H. SHTRIKMAN:  
Coupled electron-hole transport,  
*Phys. Rev. Lett.* **68**, 1196–1199 (1992).
- [107] C. SCHINDLER and R. ZIMMERMANN:  
Analysis of the exciton-exciton interaction in semiconductor quantum wells,  
*Phys. Rev. B* **78**, 045313 (2008).
- [108] M. STERN, V. GARMIDER, V. UMANSKY and I. BAR-JOSEPH:  
Mott transition of excitons in coupled quantum wells,  
*Phys. Rev. Lett.* **100**, 256402 (2008).
- [109] B. LAIKHTMAN and R. RAPAPORT:  
Exciton correlations in coupled quantum wells and their luminescence blue shift,  
*Phys. Rev. B* **80**, 195313 (2009).
- [110] V. M. AGRANOVICH, D. M. BASKO, G. C. L. ROCCA and F. BASSANI:  
Excitons and optical nonlinearities in hybrid organic-inorganic nanostructures,  
*Journal of Physics: Condensed Matter* **10**, 9369 (1998).
- [111] C. CIUTI, V. SAVONA, C. PIERMAROCCHI, A. QUATTROPANI and P. SCHWENDIMANN:  
Role of the exchange of carriers in elastic exciton-exciton scattering in quantum wells,  
*Phys. Rev. B* **58**, 7926–7933 (1998).
- [112] M. COMBESCOT, O. BETBEDER-MATIBET and R. COMBESCOT:  
Exciton-exciton scattering: composite boson versus elementary boson,  
*Phys. Rev. B* **75**, 174305 (2007).
- [113] M. COMBESCOT, O. BETBEDER-MATIBET and F. DUBIN:  
The many-body physics of composite bosons,  
*Physics Reports* **463**, 215–320 (2008).
- [114] J. M. BLATT, K. W. BÖER and W. BRANDT:  
Bose-Einstein condensation of excitons,  
*Phys. Rev.* **126**, 1691–1692 (1962).
- [115] L. V. KELDYSH and A. N. KOZLOV:  
Collective Properties of Excitons in Semiconductors,  
*Soviet Journal of Experimental and Theoretical Physics* **27**, 521 (1968).
- [116] J. BARDEEN, L. N. COOPER and J. R. SCHRIEFFER:  
Microscopic theory of superconductivity,  
*Phys. Rev.* **106**, 162–164 (1957).
- [117] K. KÖHLER, H.-J. POLLAND, L. SCHULTHEIS and C. W. TU:  
Photoluminescence of two-dimensional excitons in an electric field: lifetime enhancement and field ionization in GaAs quantum wells,  
*Phys. Rev. B* **38**, 5496–5503 (1988).

- [118] A. L. IVANOV, P. B. LITTLEWOOD and H. HAUG:  
Bose-Einstein statistics in thermalization and photoluminescence of quantum-well excitons,  
*Phys. Rev. B* **59**, 5032–5048 (1999).
- [119] D. BIRKEDAL, J. SINGH, V. G. LYSSENKO, J. ERLAND and J. M. HVAM:  
Binding of quasi-two-dimensional biexcitons,  
*Phys. Rev. Lett.* **76**, 672–675 (1996).
- [120] Y. E. LOZOVIK and V. I. YUDSON:  
Feasibility of superfluidity of paired spatially separated electrons and holes; a new superconductivity mechanism,  
*Soviet Journal of Experimental and Theoretical Physics Letters* **22**, 274 (1975).
- [121] J. E. GOLUB, K. KASH, J. P. HARBISON and L. T. FLOREZ:  
Long-lived spatially indirect excitons in coupled GaAs/Al<sub>x</sub>Ga<sub>1-x</sub>As quantum wells,  
*Phys. Rev. B* **41**, 8564–8567 (1990).
- [122] Z. VÖRÖS, R. BALILI, D. W. SNOKE, L. PFEIFFER and K. WEST:  
Long-distance diffusion of excitons in double quantum well structures,  
*Phys. Rev. Lett.* **94**, 226401 (2005).
- [123] R. RAPAPORT, G. CHEN and S. H. SIMON:  
Nonlinear dynamics of a dense two-dimensional dipolar exciton gas,  
*Phys. Rev. B* **73**, 033319 (2006).
- [124] A. A. HIGH, J. R. LEONARD, M. REMEIKA, L. V. BUTOV, M. HANSON and A. C. GOSSARD:  
Condensation of excitons in a trap,  
*Nano Letters* **12**, PMID: 22509898, 2605–2609 (2012).
- [125] J. KANG, S. TONGAY, J. ZHOU, J. LI and J. WU:  
Band offsets and heterostructures of two-dimensional semiconductors,  
*Applied Physics Letters* **102**, 012111 (2013).
- [126] C. GONG, H. ZHANG, W. WANG, L. COLOMBO, R. M. WALLACE and K. CHO:  
Band alignment of two-dimensional transition metal dichalcogenides: application in tunnel field effect transistors,  
*Applied Physics Letters* **103**, 053513 (2013).
- [127] Y. YU, S. HU, L. SU, L. HUANG, Y. LIU, Z. JIN, A. A. PUREZKY, D. B. GEOHEGAN, K. W. KIM, Y. ZHANG and L. CAO:  
Equally efficient interlayer exciton relaxation and improved absorption in epitaxial and nonepitaxial MoS<sub>2</sub>/WS<sub>2</sub> heterostructures,  
*Nano Letters* **15**, PMID: 25469768, 486–491 (2015).
- [128] P. RIVERA, J. R. SCHAIBLEY, A. M. JONES, J. S. ROSS, S. WU, G. AIVAZIAN, P. KLEMENT, K. SEYLER, G. CLARK, N. J. GHIMIRE, J. YAN, D. G. MANDRUS, W. YAO and X. XU:  
Observation of long-lived interlayer excitons in monolayer MoSe<sub>2</sub>-WSe<sub>2</sub> heterostructures,  
*Nature Communications* **6**, 6242 (2015).
- [129] E. V. CALMAN, M. M. FOGLER, L. V. BUTOV, S. HU, A. MISHCHENKO and A. K. GEIM:  
Indirect excitons in van der Waals heterostructures at room temperature,  
*Nature Communications* **9**, 1895 (2018).

- 
- [130] M. M. FOGLER, L. V. BUTOV and K. S. NOVOSELOV:  
High-temperature superfluidity with indirect excitons in van der Waals heterostructures,  
*Nature Communications* **5**, 4555 (2014).
- [131] F.-C. WU, F. XUE and A. H. MACDONALD:  
Theory of two-dimensional spatially indirect equilibrium exciton condensates,  
*Phys. Rev. B* **92**, 165121 (2015).
- [132] M. ZIMMERMAN, R. RAPAPORT and S. GAZIT:  
Collective interlayer pairing and pair superfluidity in vertically stacked layers of dipolar excitons,  
*Proceedings of the National Academy of Sciences* **119**, e2205845119 (2022).
- [133] Z. WANG, D. A. RHODES, K. WATANABE, T. TANIGUCHI, J. C. HONE, J. SHAN and K. F. MAK:  
Evidence of high-temperature exciton condensation in two-dimensional atomic double layers,  
*Nature* **574**, 76–80 (2019).
- [134] A. PEROT and C. FABRY:  
On the Application of Interference Phenomena to the Solution of Various Problems of Spectroscopy and Metrology,  
*Astrophysical Journal* **9**, 87 (1899).
- [135] H. DENG, H. HAUG and Y. YAMAMOTO:  
Exciton-polariton Bose-Einstein condensation,  
*Rev. Mod. Phys.* **82**, 1489–1537 (2010).
- [136] E. JAYNES and F. CUMMINGS:  
Comparison of quantum and semiclassical radiation theories with application to the beam maser,  
*Proceedings of the IEEE* **51**, 89–109 (1963).
- [137] C. COHEN-TANNOUJDI, B. DIU and F. LALOË:  
*Quantum mechanics, volume 1: basic concepts, tools, and applications*,  
(Wiley, 1992).
- [138] I. CARUSOTTO and C. CIUTI:  
Quantum fluids of light,  
*Rev. Mod. Phys.* **85**, 299–366 (2013).
- [139] J. J. HOPFIELD:  
Theory of the contribution of excitons to the complex dielectric constant of crystals,  
*Phys. Rev.* **112**, 1555–1567 (1958).
- [140] J. LEVINSÉN, G. LI and M. M. PARISH:  
Microscopic description of exciton-polaritons in microcavities,  
*Phys. Rev. Research* **1**, 033120 (2019).
- [141] A. FETTER and J. WALECKA:  
*Quantum theory of many-particle systems*,  
Dover Books on Physics (Dover Publications, 2003).
- [142] W. LANGBEIN, P. BORRI, J. HVAM and D. BIRKEDA:  
Coherent excitonic nonlinearity versus inhomogeneous broadening in single quantum wells,  
*55–56* (1998).

- [143] M. LITINSKAIA, G. LA ROCCA and V. AGRANOVICH:  
Inhomogeneous broadening of polaritons in high-quality microcavities and weak localization,  
[Phys. Rev. B \*\*64\*\*, 165316 \(2001\)](#).
- [144] G. KOCHERSCHIEDT, W. LANGBEIN, U. WOGGON, V. SAVONA, R. ZIMMERMANN, D. REUTER and A. D. WIECK:  
Resonant Rayleigh scattering dynamics of excitons in single quantum wells,  
[Phys. Rev. B \*\*68\*\*, 085207 \(2003\)](#).
- [145] C. W. GARDINER and M. J. COLLETT:  
Input and output in damped quantum systems: quantum stochastic differential equations and the master equation,  
[Phys. Rev. A \*\*31\*\*, 3761–3774 \(1985\)](#).
- [146] C. CIUTI and I. CARUSOTTO:  
Input-output theory of cavities in the ultrastrong coupling regime: the case of time-independent cavity parameters,  
[Phys. Rev. A \*\*74\*\*, 033811 \(2006\)](#).
- [147] J. A. ĆWIK, P. KIRTON, S. DE LIBERATO and J. KEELING:  
Excitonic spectral features in strongly coupled organic polaritons,  
[Phys. Rev. A \*\*93\*\*, 033840 \(2016\)](#).
- [148] S. DATTA:  
*Electronic transport in mesoscopic systems*,  
Cambridge Studies in Semiconductor Physics and Microelectronic Engineering (Cambridge University Press, 1995).
- [149] V. SAVONA, L. ANDREANI, P. SCHWENDIMANN and A. QUATTROPANI:  
Quantum well excitons in semiconductor microcavities: unified treatment of weak and strong coupling regimes,  
[Solid State Communications \*\*93\*\*, 733–739 \(1995\)](#).
- [150] M. SABA, C. CIUTI, J. BLOCH, V. THIERRY-MIEG, R. ANDRÉ, L. S. DANG, S. KUNDERMANN, A. MURA, G. BONGIOVANNI, J. L. STAEHLI and B. DEVEAUD:  
High-temperature ultrafast polariton parametric amplification in semiconductor microcavities,  
[Nature \*\*414\*\*, 731–735 \(2001\)](#).
- [151] X. LIU, T. GALFSKY, Z. SUN, F. XIA, E.-C. LIN, Y.-H. LEE, S. KÉNA-COHEN and V. M. MENON:  
Strong light–matter coupling in two-dimensional atomic crystals,  
[Nature Photonics \*\*9\*\*, 30–34 \(2015\)](#).
- [152] A. KAVOKIN:  
Exciton-polaritons in microcavities: recent discoveries and perspectives,  
[physica status solidi \(b\) \*\*247\*\*, 1898–1906 \(2010\)](#).
- [153] T. LOW, A. CHAVES, J. D. CALDWELL, A. KUMAR, N. X. FANG, P. AVOURIS, T. F. HEINZ, F. GUINEA, L. MARTIN-MORENO and F. KOPPENS:  
Polaritons in layered two-dimensional materials,  
[Nature Materials \*\*16\*\*, 182–194 \(2017\)](#).
- [154] C. SCHNEIDER, M. M. GLAZOV, T. KORN, S. HÖFLING and B. URBASZEK:  
Two-dimensional semiconductors in the regime of strong light-matter coupling,  
[Nature Communications \*\*9\*\*, 2695 \(2018\)](#).

- [155] V. ARDIZZONE, L. D. MARCO, M. D. GIORGI, L. DOMINICI, D. BALLARINI and D. SANVITTO:  
Emerging 2D materials for room-temperature polaritonics,  
*Nanophotonics* **8**, 1547–1558 (2019).
- [156] C. WEISBUCH, M. NISHIOKA, A. ISHIKAWA and Y. ARAKAWA:  
Observation of the coupled exciton-photon mode splitting in a semiconductor quantum microcavity,  
*Phys. Rev. Lett.* **69**, 3314–3317 (1992).
- [157] S. BRODBECK, S. DE LIBERATO, M. AMTHOR, M. KLAAS, M. KAMP, L. WORSCHICH, C. SCHNEIDER and S. HÖFLING:  
Experimental verification of the very strong coupling regime in a GaAs quantum well microcavity,  
*Phys. Rev. Lett.* **119**, 027401 (2017).
- [158] J. BLOCH, T. FREIXANET, J. Y. MARZIN, V. THIERRY-MIEG and R. PLANEL:  
Giant Rabi splitting in a microcavity containing distributed quantum wells,  
*Applied Physics Letters* **73**, 1694–1696 (1998).
- [159] J. KASPRZAK, M. RICHARD, S. KUNDERMANN, A. BAAS, P. JEAMBRUN, J. M. J. KEELING, F. M. MARCHETTI, M. H. SZYMAŃSKA, R. ANDRÉ, J. L. STAEHLI, V. SAVONA, P. B. LITTLEWOOD, B. DEVEAUD and L. S. DANG:  
Bose–Einstein condensation of exciton polaritons,  
*Nature* **443**, 409–414 (2006).
- [160] S. CHRISTOPOULOS, G. B. H. VON HÖGERSTHAL, A. J. D. GRUNDY, P. G. LAGODAKIS, A. V. KAVOKIN, J. J. BAUMBERG, G. CHRISTMANN, R. BUTTÉ, E. FELTIN, J.-F. CARLIN and N. GRANDJEAN:  
Room-temperature polariton lasing in semiconductor microcavities,  
*Phys. Rev. Lett.* **98**, 126405 (2007).
- [161] J. J. BAUMBERG, A. V. KAVOKIN, S. CHRISTOPOULOS, A. J. D. GRUNDY, R. BUTTÉ, G. CHRISTMANN, D. D. SOLNYSHKOV, G. MALPUECH, G. BALDASSARRI HÖGER VON HÖGERSTHAL, E. FELTIN, J.-F. CARLIN and N. GRANDJEAN:  
Spontaneous polarization buildup in a room-temperature polariton laser,  
*Phys. Rev. Lett.* **101**, 136409 (2008).
- [162] G. CHRISTMANN, R. BUTTÉ, E. FELTIN, J.-F. CARLIN and N. GRANDJEAN:  
Room temperature polariton lasing in a GaN/AlGaIn multiple quantum well microcavity,  
*Applied Physics Letters* **93**, 051102 (2008).
- [163] S. DUFFERWIEL, S. SCHWARZ, F. WITHERS, A. A. P. TRICHET, F. LI, M. SICH, O. DEL POZO-ZAMUDIO, C. CLARK, A. NALITOV, D. D. SOLNYSHKOV, G. MALPUECH, K. S. NOVOSELOV, J. M. SMITH, M. S. SKOLNICK, D. N. KRIZHANOVSKII and A. I. TARTAKOVSKII:  
Exciton–polaritons in van der Waals heterostructures embedded in tunable microcavities,  
*Nature Communications* **6**, 8579 (2015).
- [164] Y.-J. CHEN, J. D. CAIN, T. K. STANEV, V. P. DRAVID and N. P. STERN:  
Valley-polarized exciton–polaritons in a monolayer semiconductor,  
*Nature Photonics* **11**, 431–435 (2017).
- [165] Z. SUN, J. GU, A. GHAZARYAN, Z. SHOTAN, C. R. CONSIDINE, M. DOLLAR, B. CHAKRABORTY, X. LIU, P. GHAEMI, S. KÉNA-COHEN and V. M. MENON:  
Optical control of room-temperature valley polaritons,  
*Nature Photonics* **11**, 491–496 (2017).

- [166] X. LIU, W. BAO, Q. LI, C. ROPP, Y. WANG and X. ZHANG:  
Control of coherently coupled exciton polaritons in monolayer tungsten disulphide,  
*Phys. Rev. Lett.* **119**, 027403 (2017).
- [167] J. KHURGIN:  
Excitonic radius in the cavity polariton in the regime of very strong coupling,  
*Solid State Communications* **117**, 307–310 (2001).
- [168] D. S. CITRIN and J. B. KHURGIN:  
Microcavity effect on the electron-hole relative motion in semiconductor quantum wells,  
*Phys. Rev. B* **68**, 205325 (2003).
- [169] A. A. ANAPPARA, S. DE LIBERATO, A. TREDICUCCI, C. CIUTI, G. BIASIOL, L. SORBA and F. BELTRAM:  
Signatures of the ultrastrong light-matter coupling regime,  
*Phys. Rev. B* **79**, 201303 (2009).
- [170] T. NIEMCZYK, F. DEPPE, H. HUEBL, E. P. MENZEL, F. HOCKE, M. J. SCHWARZ, J. J. GARCIA-RIPOLL, D. ZUECO, T. HÜMMER, E. SOLANO, A. MARX and R. GROSS:  
Circuit quantum electrodynamics in the ultrastrong-coupling regime,  
*Nature Physics* **6**, 772–776 (2010).
- [171] G. SCALARI, C. MAISSEN, D. TURČINKOVÁ, D. HAGENMÜLLER, S. D. LIBERATO, C. CIUTI, C. REICHL, D. SCHUH, W. WEGSCHEIDER, M. BECK and J. FAIST:  
Ultrastrong coupling of the cyclotron transition of a 2D electron gas to a thz metamaterial,  
*Science* **335**, 1323–1326 (2012).
- [172] C. R. GUBBIN, S. A. MAIER and S. KÉNA-COHN:  
Low-voltage polariton electroluminescence from an ultrastrongly coupled organic light-emitting diode,  
*Applied Physics Letters* **104**, 233302 (2014).
- [173] A. VASANELLI, Y. TODOROV and C. SIRTORI:  
Ultra-strong light-matter coupling and superradiance using dense electron gases,  
*Comptes Rendus Physique* **17**, Polariton physics / Physique des polaritons, 861–873 (2016).
- [174] A. TIENE, J. LEVINSSEN, M. M. PARISH, A. H. MACDONALD, J. KEELING and F. M. MARCHETTI:  
Extremely imbalanced two-dimensional electron-hole-photon systems,  
*Phys. Rev. Research* **2**, 023089 (2020).
- [175] G. MAHAN:  
*Many-particle physics*,  
Physics of Solids and Liquids (Springer US, 1990).
- [176] Y. B. BAND and D. F. HELLER:  
Relationships between the absorption and emission of light in multilevel systems,  
*Phys. Rev. A* **38**, 1885 (1988).
- [177] S. CHATTERJEE, C. ELL, S. MOSOR, G. KHITROVA, H. M. GIBBS, W. HOYER, M. KIRA, S. W. KOCH, J. P. PRINEAS and H. STOLZ:  
Excitonic photoluminescence in semiconductor quantum wells: plasma versus excitons,  
*Phys. Rev. Lett.* **92**, 067402 (2004).

- [178] T. IHARA, S. MARUYAMA, M. YOSHITA, H. AKIYAMA, L. N. PFEIFFER and K. W. WEST:  
Thermal-equilibrium relation between the optical emission and absorption spectra of a doped semiconductor quantum well,  
*Phys. Rev. B* **80**, 033307 (2009).
- [179] W. E. LIU, Z.-Y. SHI, M. M. PARISH and J. LEVINSSEN:  
Theory of radio-frequency spectroscopy of impurities in quantum gases,  
*Phys. Rev. A* **102**, 023304 (2020).
- [180] A. IMAMOG˘LU, R. J. RAM, S. PAU and Y. YAMAMOTO:  
Nonequilibrium condensates and lasers without inversion: exciton-polariton lasers,  
*Phys. Rev. A* **53**, 4250–4253 (1996).
- [181] J. J. BAUMBERG, P. G. SAVVIDIS, R. M. STEVENSON, A. I. TARTAKOVSKII, M. S. SKOLNICK, D. M. WHITTAKER and J. S. ROBERTS:  
Parametric oscillation in a vertical microcavity: a polariton condensate or micro-optical parametric oscillation,  
*Phys. Rev. B* **62**, R16247–R16250 (2000).
- [182] R. M. STEVENSON, V. N. ASTRATOV, M. S. SKOLNICK, D. M. WHITTAKER, M. EMAM-ISMAIL, A. I. TARTAKOVSKII, P. G. SAVVIDIS, J. J. BAUMBERG and J. S. ROBERTS:  
Continuous wave observation of massive polariton redistribution by stimulated scattering in semiconductor microcavities,  
*Phys. Rev. Lett.* **85**, 3680–3683 (2000).
- [183] C. CIUTI, P. SCHWENDIMANN, B. DEVEAUD and A. QUATTROPANI:  
Theory of the angle-resonant polariton amplifier,  
*Phys. Rev. B* **62**, R4825–R4828 (2000).
- [184] I. CARUSOTTO and C. CIUTI:  
Spontaneous microcavity-polariton coherence across the parametric threshold: quantum Monte Carlo studies,  
*Phys. Rev. B* **72**, 125335 (2005).
- [185] L. S. DANG, D. HEGER, R. ANDRÉ, F. BŒUF and R. ROMESTAIN:  
Stimulation of polariton photoluminescence in semiconductor microcavity,  
*Phys. Rev. Lett.* **81**, 3920–3923 (1998).
- [186] M. RICHARD, J. KASPRZAK, R. ROMESTAIN, R. ANDRÉ and L. S. DANG:  
Spontaneous coherent phase transition of polaritons in CdTe microcavities,  
*Phys. Rev. Lett.* **94**, 187401 (2005).
- [187] I. CARUSOTTO and C. CIUTI:  
Probing microcavity polariton superfluidity through resonant Rayleigh scattering,  
*Phys. Rev. Lett.* **93**, 166401 (2004).
- [188] A. AMO, D. SANVITTO, F. P. LAUSSY, D. BALLARINI, E. D. VALLE, M. D. MARTIN, A. LEMAÎTRE, J. BLOCH, D. N. KRIZHANOVSKII, M. S. SKOLNICK, C. TEJEDOR and L. VIÑA:  
Collective fluid dynamics of a polariton condensate in a semiconductor microcavity,  
*Nature* **457**, 291–295 (2009).
- [189] G. NARDIN, G. GROSSO, Y. LÉGER, B. PI TKA, F. MORIER-GENOUD and B. DEVEAUD-PLÉDRAN:  
Hydrodynamic nucleation of quantized vortex pairs in a polariton quantum fluid,  
*Nature Physics* **7**, 635–641 (2011).

- [190] D. SANVITTO, S. PIGEON, A. AMO, D. BALLARINI, M. DE GIORGI, I. CARUSOTTO, R. HIVET, F. PISANELLO, V. G. SALA, P. S. S. GUIMARAES, R. HOUDRÉ, E. GIACOBINO, C. CIUTI, A. BRAMATI and G. GIGLI:  
All-optical control of the quantum flow of a polariton condensate,  
*Nature Photonics* **5**, 610–614 (2011).
- [191] A. AMO, S. PIGEON, D. SANVITTO, V. G. SALA, R. HIVET, I. CARUSOTTO, F. PISANELLO, G. LEMÉNAGER, R. HOUDRÉ, E. GIACOBINO, C. CIUTI and A. BRAMATI:  
Polariton superfluids reveal quantum hydrodynamic solitons,  
*Science* **332**, 1167–1170 (2011).
- [192] G. GROSSO, G. NARDIN, F. MORIER-GENOUD, Y. LÉGER and B. DEVEAUD-PLÉDRAN:  
Soliton instabilities and vortex street formation in a polariton quantum fluid,  
*Phys. Rev. Lett.* **107**, 245301 (2011).
- [193] A. IMAMO ĞLU, H. SCHMIDT, G. WOODS and M. DEUTSCH:  
Strongly interacting photons in a nonlinear cavity,  
*Phys. Rev. Lett.* **79**, 1467–1470 (1997).
- [194] A. VERGER, C. CIUTI and I. CARUSOTTO:  
Polariton quantum blockade in a photonic dot,  
*Phys. Rev. B* **73**, 193306 (2006).
- [195] S. FERRETTI and D. GERACE:  
Single-photon nonlinear optics with kerr-type nanostructured materials,  
*Phys. Rev. B* **85**, 033303 (2012).
- [196] A. DELTEIL, T. FINK, A. SCHADE, S. HÖFLING, C. SCHNEIDER and A. İMAMO ĞLU:  
Towards polariton blockade of confined exciton–polaritons,  
*Nature Materials* **18**, 219–222 (2019).
- [197] G. MUÑOZ-MATUTANO, A. WOOD, M. JOHNSON, X. VIDAL, B. Q. BARAGIOLA, A. REINHARD, A. LEMAİTRE, J. BLOCH, A. AMO, G. NOGUES, B. BESGA, M. RICHARD and T. VOLZ:  
Emergence of quantum correlations from interacting fibre-cavity polaritons,  
*Nature Materials* **18**, 213–218 (2019).
- [198] L. B. TAN, O. COTLET, A. BERGSCHNEIDER, R. SCHMIDT, P. BACK, Y. SHIMAZAKI, M. KRONER and A. Ç. İMAMO ĞLU:  
Interacting polaron-polaritons,  
*Phys. Rev. X* **10**, 021011 (2020).
- [199] M. D. FRASER, S. HÖFLING and Y. YAMAMOTO:  
Physics and applications of exciton–polariton lasers,  
*Nature Materials* **15**, 1049–1052 (2016).
- [200] C. SCHNEIDER, A. RAHIMI-İMAN, N. Y. KIM, J. FISCHER, I. G. SAVENKO, M. AMTHOR, M. LERMER, A. WOLF, L. WORSCHER, V. D. KULAKOVSKII, I. A. SHELYKH, M. KAMP, S. REITZENSTEIN, A. FORCHEL, Y. YAMAMOTO and S. HÖFLING:  
An electrically pumped polariton laser,  
*Nature* **497**, 348–352 (2013).
- [201] A. AMO, T. C. H. LIEW, C. ADRADOS, R. HOUDRÉ, E. GIACOBINO, A. V. KAVOKIN and A. BRAMATI:  
Exciton–polariton spin switches,  
*Nature Photonics* **4**, 361–366 (2010).
- [202] T. JACQMIN, I. CARUSOTTO, I. SAGNES, M. ABBARCHI, D. D. SOLNYSHKOV, G. MALPUECH, E. GALOPIN, A. LEMAİTRE, J. BLOCH and A. AMO:  
Direct observation of dirac cones and a flatband in a honeycomb lattice for polaritons,  
*Phys. Rev. Lett.* **112**, 116402 (2014).

- [203] R. SU, S. GHOSH, J. WANG, S. LIU, C. DIEDERICHS, T. C. H. LIEW and Q. XIONG: Observation of exciton polariton condensation in a perovskite lattice at room temperature, *Nature Physics* **16**, 301–306 (2020).
- [204] N. G. BERLOFF, M. SILVA, K. KALININ, A. ASKITOPOULOS, J. D. TÖPFER, P. CILIBRIZZI, W. LANGBEIN and P. G. LAGOUDAKIS: Realizing the classical xy hamiltonian in polariton simulators, *Nature Materials* **16**, 1120–1126 (2017).
- [205] D. BALLARINI, A. GIANFRATE, R. PANICO, A. OPALA, S. GHOSH, L. DOMINICI, V. ARDIZZONE, M. DE GIORGI, G. LERARIO, G. GIGLI, T. C. H. LIEW, M. MATUSZEWSKI and D. SANVITTO: Polaritonic neuromorphic computing outperforms linear classifiers, *Nano Letters* **20**, PMID: 32251601, 3506–3512 (2020).
- [206] Y. YE, Z. J. WONG, X. LU, X. NI, H. ZHU, X. CHEN, Y. WANG and X. ZHANG: Monolayer excitonic laser, *Nature Photonics* **9**, 733–737 (2015).
- [207] Y. LI, J. ZHANG, D. HUANG, H. SUN, F. FAN, J. FENG, Z. WANG and C. Z. NING: Room-temperature continuous-wave lasing from monolayer molybdenum ditelluride integrated with a silicon nanobeam cavity, *Nature Nanotechnology* **12**, 987–992 (2017).
- [208] J. SHANG, C. CONG, Z. WANG, N. PEIMYOO, L. WU, C. ZOU, Y. CHEN, X. Y. CHIN, J. WANG, C. SOCI, W. HUANG and T. YU: Room-temperature 2D semiconductor activated vertical-cavity surface-emitting lasers, *Nature Communications* **8**, 543 (2017).
- [209] L. ZHANG, R. GOGNA, W. BURG, E. TUTUC and H. DENG: Photonic-crystal exciton-polaritons in monolayer semiconductors, *Nature Communications* **9**, 713 (2018).
- [210] J. ZHAO, R. SU, A. FIERAMOSCA, W. ZHAO, W. DU, X. LIU, C. DIEDERICHS, D. SANVITTO, T. C. H. LIEW and Q. XIONG: Ultralow threshold polariton condensate in a monolayer semiconductor microcavity at room temperature, *Nano Letters* **21**, PMID: 33797259, 3331–3339 (2021).
- [211] A. F. CROXALL, K. DAS GUPTA, C. A. NICOLL, M. THANGARAJ, H. E. BEERE, I. FARRER, D. A. RITCHIE and M. PEPPER: Anomalous Coulomb drag in electron-hole bilayers, *Phys. Rev. Lett.* **101**, 246801 (2008).
- [212] J. A. SEAMONS, C. P. MORATH, J. L. RENO and M. P. LILLY: Coulomb drag in the exciton regime in electron-hole bilayers, *Phys. Rev. Lett.* **102**, 026804 (2009).
- [213] G. V. ASTAKHOV, V. P. KOCHERESHKO, D. R. YAKOVLEV, W. OSSAU, J. NÜRNBERGER, W. FASCHINGER, G. LANDWEHR, T. WOJTOWICZ, G. KARCEWSKI and J. KOSSUT: Optical method for the determination of carrier density in modulation-doped quantum wells, *Phys. Rev. B* **65**, 115310 (2002).
- [214] A. GABBAY, Y. PREEZANT, E. COHEN, B. M. ASHKINADZE and L. N. PFEIFFER: Fermi edge polaritons in a microcavity containing a high density two-dimensional electron gas, *Phys. Rev. Lett.* **99**, 157402 (2007).

- [215] A. MANASSEN, E. COHEN, A. RON, E. LINDER and L. N. PFEIFFER:  
Exciton and trion spectral line shape in the presence of an electron gas in GaAs/AlAs quantum wells,  
*Phys. Rev. B* **54**, 10609–10613 (1996).
- [216] P. DAWSON, I. GALBRAITH, A. I. KUCHARSKA and C. T. FOXON:  
Low-power, all-optical nonlinear absorption in asymmetric double quantum wells,  
*Applied Physics Letters* **58**, 2889–2891 (1991).
- [217] R. RAPAPORT, E. COHEN, A. RON, E. LINDER and L. N. PFEIFFER:  
Negatively charged polaritons in a semiconductor microcavity,  
*Phys. Rev. B* **63**, 235310 (2001).
- [218] D. BAJONI, M. PERRIN, P. SENELLART, A. LEMAÎTRE, B. SERMAGE and J. BLOCH:  
Dynamics of microcavity polaritons in the presence of an electron gas,  
*Phys. Rev. B* **73**, 205344 (2006).
- [219] A. CHERNIKOV, C. RUPPERT, H. M. HILL, A. F. RIGOSI and T. F. HEINZ:  
Population inversion and giant bandgap renormalization in atomically thin WS<sub>2</sub> layers,  
*Nature Photonics* **9**, 466–470 (2015).
- [220] T. SMOLEŃSKI, O. COTLET, A. POPERT, P. BACK, Y. SHIMAZAKI, P. KNÜPPEL, N. DIETLER, T. TANIGUCHI, K. WATANABE, M. KRONER and A. IMAMOGLU:  
Interaction-induced Shubnikov–de Haas oscillations in optical conductivity of monolayer MoSe<sub>2</sub>,  
*Phys. Rev. Lett.* **123**, 097403 (2019).
- [221] J. LI, M. GORYCA, J. CHOI, X. XU and S. A. CROOKER:  
Many-body exciton and intervalley correlations in heavily electron-doped WSe<sub>2</sub> monolayers,  
*Nano Letters* **22**, PMID: 34918936, 426–432 (2022).
- [222] R.-J. CHANG, Y. SHENG, G. H. RYU, N. MKHIZE, T. CHEN, Y. LU, J. CHEN, J. K. LEE, H. BHASKARAN and J. H. WARNER:  
Postgrowth substitutional tin doping of 2D WS<sub>2</sub> crystals using chemical vapor deposition,  
*ACS Applied Materials and Interfaces* **11**, PMID: 31250625, 24279–24288 (2019).
- [223] H. GAO, J. SUH, M. C. CAO, A. Y. JOE, F. MUJID, K.-H. LEE, S. XIE, P. PODDAR, J.-U. LEE, K. KANG, P. KIM, D. A. MULLER and J. PARK:  
Tuning electrical conductance of MoS<sub>2</sub> monolayers through substitutional doping,  
*Nano Letters* **20**, PMID: 32396734, 4095–4101 (2020).
- [224] L. YANG, K. MAJUMDAR, H. LIU, Y. DU, H. WU, M. HATZISTERGOS, P. Y. HUNG, R. TIECKELMANN, W. TSAI, C. HOBBS and P. D. YE:  
Chloride molecular doping technique on 2D materials: WS<sub>2</sub> and MoS<sub>2</sub>,  
*Nano Letters* **14**, PMID: 25310177, 6275–6280 (2014).
- [225] B. ZHAO, L. LIU, G. CHENG, T. LI, N. QI, Z. CHEN and Z. TANG:  
Interaction of O<sub>2</sub> with monolayer MoS<sub>2</sub>: effect of doping and hydrogenation,  
*Materials and Design* **113**, 1–8 (2017).
- [226] S. NAJMAEI, X. ZOU, D. ER, J. LI, Z. JIN, W. GAO, Q. ZHANG, S. PARK, L. GE, S. LEI, J. KONO, V. B. SHENOY, B. I. YAKOBSON, A. GEORGE, P. M. AJAYAN and J. LOU:  
Tailoring the physical properties of molybdenum disulfide monolayers by control of interfacial chemistry,  
*Nano Letters* **14**, PMID: 24517325, 1354–1361 (2014).

- [227] D.-H. KANG, S. R. DUGASANI, H.-Y. PARK, J. SHIM, B. GNAPAREDDY, J. JEON, S. LEE, Y. ROH, S. H. PARK and J.-H. PARK:  
Ultra-low doping on two-dimensional transition metal dichalcogenides using dna nanostructure doped by a combination of lanthanide and metal ions,  
*Scientific Reports* **6**, 20333 (2016).
- [228] K. XU, Y. WANG, Y. ZHAO and Y. CHAI:  
Modulation doping of transition metal dichalcogenide/oxide heterostructures,  
*J. Mater. Chem. C* **5**, 376–381 (2017).
- [229] Y. LI, C.-Y. XU, P. HU and L. ZHEN:  
Carrier control of MoS2 nanoflakes by functional self-assembled monolayers,  
*ACS Nano* **7**, PMID: 23952126, 7795–7804 (2013).
- [230] D.-H. KANG, M.-S. KIM, J. SHIM, J. JEON, H.-Y. PARK, W.-S. JUNG, H.-Y. YU, C.-H. PANG, S. LEE and J.-H. PARK:  
High-performance transition metal dichalcogenide photodetectors enhanced by self-assembled monolayer doping,  
*Advanced Functional Materials* **25**, 4219–4227 (2015).
- [231] W. H. LEE and Y. D. PARK:  
Tuning electrical properties of 2D materials by self-assembled monolayers,  
*Advanced Materials Interfaces* **5**, 1700316 (2018).
- [232] S. I. TSINTZOS, N. T. PELEKANOS, G. KONSTANTINIDIS, Z. HATZOPOULOS and P. G. SAVVIDIS:  
A GaAs polariton light-emitting diode operating near room temperature,  
*Nature* **453**, 372–375 (2008).
- [233] P. BHATTACHARYA, T. FROST, S. DESHPANDE, M. Z. BATEN, A. HAZARI and A. DAS:  
Room temperature electrically injected polariton laser,  
*Phys. Rev. Lett.* **112**, 236802 (2014).
- [234] G. G. PASCHOS, N. SOMASCHI, S. I. TSINTZOS, D. COLES, J. L. BRICKS, Z. HATZOPOULOS, D. G. LIDZEY, P. G. LAGOUDAKIS and P. G. SAVVIDIS:  
Hybrid organic-inorganic polariton laser,  
*Scientific Reports* **7**, 11377 (2017).
- [235] H. SUCHOMEL, M. KLAAS, S. BETZOLD, P. GAGEL, J. BEIERLEIN, S. KLEMBT, C. SCHNEIDER and S. HÖFLING:  
Spatio-temporal coherence in vertically emitting GaAs-based electrically driven polariton lasers,  
*Applied Physics Letters* **116**, 171103 (2020).
- [236] D. G. SUÁREZ-FORERO, F. RIMINUCCI, V. ARDIZZONE, M. D. GIORGI, L. DOMINICI, F. TODISCO, G. LERARIO, L. N. PFEIFFER, G. GIGLI, D. BALLARINI and D. SANVITTO:  
Electrically controlled waveguide polariton laser,  
*Optica* **7**, 1579–1586 (2020).
- [237] H. SUCHOMEL, S. KLEMBT, T. H. HARDER, M. KLAAS, O. A. EGOROV, K. WINKLER, M. EMMERLING, R. THOMALE, S. HÖFLING and C. SCHNEIDER:  
Platform for electrically pumped polariton simulators and topological lasers,  
*Phys. Rev. Lett.* **121**, 257402 (2018).
- [238] M. AMTHOR, S. WEISSENSEEL, J. FISCHER, M. KAMP, C. SCHNEIDER and S. HÖFLING:  
Electro-optical switching between polariton and cavity lasing in an InGaAs quantum well microcavity,  
*Opt. Express* **22**, 31146–31153 (2014).

- [239] S. BRODBECK, H. SUCHOMEL, M. AMTHOR, T. STEINL, M. KAMP, C. SCHNEIDER and S. HÖFLING:  
Observation of the transition from lasing driven by a bosonic to a fermionic reservoir in a GaAs quantum well microcavity,  
*Phys. Rev. Lett.* **117**, 127401 (2016).
- [240] Y. LIANG and L. YANG:  
Carrier plasmon induced nonlinear band gap renormalization in two-dimensional semiconductors,  
*Phys. Rev. Lett.* **114**, 063001 (2015).
- [241] S. GAO and L. YANG:  
Renormalization of the quasiparticle band gap in doped two-dimensional materials from many-body calculations,  
*Phys. Rev. B* **96**, 155410 (2017).
- [242] F. LIU, M. E. ZIFFER, K. R. HANSEN, J. WANG and X. ZHU:  
Direct determination of band-gap renormalization in the photoexcited monolayer MoS<sub>2</sub>,  
*Phys. Rev. Lett.* **122**, 246803 (2019).
- [243] A. FARIDI, D. CULCER and R. ASGARI:  
Quasiparticle band-gap renormalization in doped monolayer MoS<sub>2</sub>,  
*Phys. Rev. B* **104**, 085432 (2021).
- [244] B. CHAKRABORTY, J. GU, Z. SUN, M. KHATONIAR, R. BUSHATI, A. L. BOEHMKE, R. KOOTS and V. M. MENON:  
Control of strong light–matter interaction in monolayer WS<sub>2</sub> through electric field gating,  
*Nano Letters* **18**, PMID: 30160968, 6455–6460 (2018).
- [245] E. WIGNER:  
On the interaction of electrons in metals,  
*Phys. Rev.* **46**, 1002–1011 (1934).
- [246] N. D. DRUMMOND and R. J. NEEDS:  
Phase diagram of the low-density two-dimensional homogeneous electron gas,  
*Phys. Rev. Lett.* **102**, 126402 (2009).
- [247] M. ZARENIA, D. NEILSON, B. PARTOENS and F. M. PEETERS:  
Wigner crystallization in transition metal dichalcogenides: a new approach to correlation energy,  
*Phys. Rev. B* **95**, 115438 (2017).
- [248] T. SMOLEŃSKI, P. E. DOLGIREV, C. KUHNENKAMP, A. POPERT, Y. SHIMAZAKI, P. BACK, X. LU, M. KRONER, K. WATANABE, T. TANIGUCHI, I. ESTERLIS, E. DEMLER and A. IMAMOĞLU:  
Signatures of wigner crystal of electrons in a monolayer semiconductor,  
*Nature* **595**, 53–57 (2021).
- [249] Y. ZHOU, J. SUNG, E. BRUTSCHEA, I. ESTERLIS, Y. WANG, G. SCURI, R. J. GELLY, H. HEO, T. TANIGUCHI, K. WATANABE, G. ZARÁND, M. D. LUKIN, P. KIM, E. DEMLER and H. PARK:  
Bilayer wigner crystals in a transition metal dichalcogenide heterostructure,  
*Nature* **595**, 48–52 (2021).
- [250] P. AEBI, T. PILLO, H. BERGER and F. LÉVY:  
On the search for Fermi surface nesting in quasi-2D materials,  
*Journal of Electron Spectroscopy and Related Phenomena* **117–118**, Strongly correlated systems, 433–449 (2001).

- [251] K. ROSSNAGEL:  
On the origin of charge-density waves in select layered transition-metal dichalcogenides,  
*Journal of Physics: Condensed Matter* **23**, 213001 (2011).
- [252] X. ZHU, Y. CAO, J. ZHANG, E. W. PLUMMER and J. GUO:  
Classification of charge density waves based on their nature,  
*Proceedings of the National Academy of Sciences* **112**, 2367–2371 (2015).
- [253] Z. XU, H. YANG, X. SONG, Y. CHEN, H. YANG, M. LIU, Z. HUANG, Q. ZHANG, J. SUN, L. LIU and Y. WANG:  
Topical review: recent progress of charge density waves in 2D transition metal dichalcogenide-based heterojunctions and their applications,  
*Nanotechnology* **32**, 492001 (2021).
- [254] M. M. UGEDA, A. J. BRADLEY, Y. ZHANG, S. ONISHI, Y. CHEN, W. RUAN, C. OJEDA-ARISTIZABAL, H. RYU, M. T. EDMONDS, H.-Z. TSAI, A. RISS, S.-K. MO, D. LEE, A. ZETTL, Z. HUSSAIN, Z.-X. SHEN and M. F. CROMMIE:  
Characterization of collective ground states in single-layer NbSe<sub>2</sub>,  
*Nature Physics* **12**, 92–97 (2016).
- [255] M. M. PARISH, F. M. MARCHETTI and P. B. LITTLEWOOD:  
Supersolidity in electron-hole bilayers with a large density imbalance,  
*Europhysics Letters* **95**, 27007 (2011).
- [256] O. COTLET, D. S. WILD, M. D. LUKIN and A. IMAMOGLU:  
Rotons in optical excitation spectra of monolayer semiconductors,  
*Phys. Rev. B* **101**, 205409 (2020).
- [257] P. FULDE and R. A. FERRELL:  
Superconductivity in a strong spin-exchange field,  
*Phys. Rev.* **135**, A550 (1964).
- [258] A. I. LARKIN and Y. N. OVCHINNIKOV:  
Nonuniform state of superconductors,  
*Zh. Eksp. Teor. Fiz.* **47**, [Sov. Phys. JETP20,762(1965)], 1136 (1964).
- [259] M. A. LAMPERT:  
Mobile and immobile effective-mass-particle complexes in nonmetallic solids,  
*Phys. Rev. Lett.* **1**, 450–453 (1958).
- [260] R. A. SURIS:  
Correlation between trion and hole in Fermi distribution in process of trion photo-excitation in doped QWs,  
in *Optical properties of 2D systems with interacting electrons* (Springer Netherlands, 2003), pp. 111–124.
- [261] D. K. EFIMKIN and A. H. MACDONALD:  
Many-body theory of trion absorption features in two-dimensional semiconductors,  
*Phys. Rev. B* **95**, 035417 (2017).
- [262] F. RANA, O. KOKSAL and C. MANOLATOU:  
Many-body theory of the optical conductivity of excitons and trions in two-dimensional materials,  
*Phys. Rev. B* **102**, 085304 (2020).
- [263] F. RANA, O. KOKSAL, M. JUNG, G. SHVETS and C. MANOLATOU:  
Many-body theory of radiative lifetimes of exciton-trion superposition states in doped two-dimensional materials,  
*Phys. Rev. B* **103**, 035424 (2021).

- [264] F. RANA, O. KOKSAL, M. JUNG, G. SHVETS, A. N. VAMIVAKAS and C. MANOLATOU: Exciton-trion polaritons in doped two-dimensional semiconductors, *Phys. Rev. Lett.* **126**, 127402 (2021).
- [265] D. K. EFIMKIN, E. K. LAIRD, J. LEVINSSEN, M. M. PARISH and A. H. MACDONALD: Electron-exciton interactions in the exciton-polaron problem, *Phys. Rev. B* **103**, 075417 (2021).
- [266] M. M. GLAZOV: Optical properties of charged excitons in two-dimensional semiconductors, *The Journal of Chemical Physics* **153**, 034703 (2020).
- [267] A. THILAGAM: Two-dimensional charged-exciton complexes, *Phys. Rev. B* **55**, 7804–7808 (1997).
- [268] E. COURTADE, M. SEMINA, M. MANCA, M. M. GLAZOV, C. ROBERT, F. CADIZ, G. WANG, T. TANIGUCHI, K. WATANABE, M. PIERRE, W. ESCOFFIER, E. L. IVCHENKO, P. RENUCCI, X. MARIE, T. AMAND and B. URBASZEK: Charged excitons in monolayer WSe<sub>2</sub>: experiment and theory, *Phys. Rev. B* **96**, 085302 (2017).
- [269] L. D. LANDAU and E. M. LIFSHITZ: *Quantum Mechanics*, (Pergamon Press, Oxford, 1991).
- [270] R. TEMPELAAR and T. C. BERKELBACH: Many-body simulation of two-dimensional electronic spectroscopy of excitons and trions in monolayer transition metal dichalcogenides, *Nature Communications* **10**, 3419 (2019).
- [271] R. A. SERGEEV and R. A. SURIS: Ground-state energy of X<sup>-</sup> and X<sup>+</sup> trions in a two-dimensional quantum well at an arbitrary mass ratio, *Physics of the Solid State* **43**, 746 (2001).
- [272] R. A. SERGEEV and R. A. SURIS: Singlet and triplet states of X<sup>+</sup> and X<sup>-</sup> trions in two-dimensional quantum wells, *Nanotechnology* **12**, 597 (2001).
- [273] N. P. SANDLER and C. R. PROETTO: Negative-donor centers in two dimensions, *Phys. Rev. B* **46**, 7707–7712 (1992).
- [274] A. MACDONALD: Two-dimensional D<sup>-</sup> centers in the strong magnetic field limit, *Solid state communications* **84**, 109–112 (1992).
- [275] A. B. DZYUBENKO, A. MANDRAY, S. HUANT, A. Y. SIVACHENKO and B. ETIENNE: Triplet transitions of D<sup>-</sup> centers in quantum wells in high magnetic fields, *Phys. Rev. B* **50**, 4687–4691 (1994).
- [276] J. J. PALACIOS, D. YOSHIOKA and A. H. MACDONALD: Long-lived charged multiple-exciton complexes in strong magnetic fields, *Phys. Rev. B* **54**, R2296–R2299 (1996).
- [277] D. M. WHITTAKER and A. J. SHIELDS: Theory of X<sup>-</sup> at high magnetic fields, *Phys. Rev. B* **56**, 15185–15194 (1997).

- [278] A. J. SHIELDS, M. PEPPER, M. Y. SIMMONS and D. A. RITCHIE:  
Spin-triplet negatively charged excitons in GaAs quantum wells,  
*Phys. Rev. B* **52**, 7841–7844 (1995).
- [279] G. FINKELSTEIN, H. SHTRIKMAN and I. BAR-JOSEPH:  
Negatively and positively charged excitons in GaAs/Al<sub>x</sub>Ga<sub>1-x</sub>As quantum wells,  
*Phys. Rev. B* **53**, R1709 (1996).
- [280] D. SANVITTO, D. M. WHITTAKER, A. J. SHIELDS, M. Y. SIMMONS, D. A. RITCHIE  
and M. PEPPER:  
Origin of the oscillator strength of the triplet state of a trion in a magnetic field,  
*Phys. Rev. Lett.* **89**, 246805 (2002).
- [281] A. J. SHIELDS, F. M. BOLTON, M. Y. SIMMONS, M. PEPPER and D. A. RITCHIE:  
Electric-field-induced ionization of negatively charged excitons in quantum wells,  
*Phys. Rev. B* **55**, R1970 (1997).
- [282] B. STÉBÉ and A. AINANE:  
Ground state energy and optical absorption of excitonic trions in two dimensional  
semiconductors,  
*Superlattices and Microstructures* **5**, 545–548 (1989).
- [283] E. A. HYLLEAAS:  
The schrödinger two-electron atomic problem,  
in , Vol. 1, edited by P.-O. Löwdin, *Advances in Quantum Chemistry* (Academic Press,  
1964), pp. 1–33.
- [284] A. ESSER, E. RUNGE, R. ZIMMERMANN and W. LANGBEIN:  
Photoluminescence and radiative lifetime of trions in GaAs quantum wells,  
*Phys. Rev. B* **62**, 8232–8239 (2000).
- [285] S. CHANDRASEKHAR:  
Some remarks on the negative hydrogen ion and its absorption coefficient.,  
*APJ* **100**, 176 (1944).
- [286] R. SURIS, V. KOCHERESHKO, G. ASTAKHOV, D. YAKOVLEV, W. OSSAU, J. NÜRN-  
BERGER, W. FASCHINGER, G. LANDWEHR, T. WOJTOWICZ, G. KARCZEWSKI and J.  
KOSSUT:  
Excitons and trions modified by interaction with a two-dimensional electron gas,  
*physica status solidi (b)* **227**, 343–352 (2001).
- [287] S. GLASBERG, G. FINKELSTEIN, H. SHTRIKMAN and I. BAR-JOSEPH:  
Comparative study of the negatively and positively charged excitons in GaAs quantum  
wells,  
*Phys. Rev. B* **59**, R10425–R10428 (1999).
- [288] O. MAYROCK, H.-J. WÜNSCHE, F. HENNEBERGER, C. RIVA, V. A. SCHWEIGERT and  
F. M. PEETERS:  
Weak localization of biexcitons in quantum wells,  
*Phys. Rev. B* **60**, 5582–5589 (1999).
- [289] C. ZHANG, H. WANG, W. CHAN, C. MANOLATOU and F. RANA:  
Absorption of light by excitons and trions in monolayers of metal dichalcogenide MoS<sub>2</sub>:  
experiments and theory,  
*Phys. Rev. B* **89**, 205436 (2014).
- [290] I. KYLÄNPÄÄ and H.-P. KOMSA:  
Binding energies of exciton complexes in transition metal dichalcogenide monolayers  
and effect of dielectric environment,  
*Phys. Rev. B* **92**, 205418 (2015).

- [291] K. A. VELIZHANIN and A. SAXENA:  
Excitonic effects in two-dimensional semiconductors: path integral Monte Carlo approach,  
*Phys. Rev. B* **92**, 195305 (2015).
- [292] M. Z. MAYERS, T. C. BERKELBACH, M. S. HYBERTSEN and D. R. REICHMAN:  
Binding energies and spatial structures of small carrier complexes in monolayer transition-metal dichalcogenides via diffusion Monte Carlo,  
*Phys. Rev. B* **92**, 161404 (2015).
- [293] D. K. ZHANG, D. W. KIDD and K. VARGA:  
Excited biexcitons in transition metal dichalcogenides,  
*Nano Letters* **15**, PMID: 26422057, 7002–7005 (2015).
- [294] D. W. KIDD, D. K. ZHANG and K. VARGA:  
Binding energies and structures of two-dimensional excitonic complexes in transition metal dichalcogenides,  
*Phys. Rev. B* **93**, 125423 (2016).
- [295] H. BETHE and E. SALPETER:  
*Quantum mechanics of one- and two-electron atoms*,  
(Springer US, 1977).
- [296] T. DEILMANN, M. DRÜPPEL and M. ROHLFING:  
Three-particle correlation from a many-body perspective: trions in a carbon nanotube,  
*Phys. Rev. Lett.* **116**, 196804 (2016).
- [297] M. DRÜPPEL, T. DEILMANN, P. KRÜGER and M. ROHLFING:  
Diversity of trion states and substrate effects in the optical properties of an MoS<sub>2</sub> monolayer,  
*Nature Communications* **8**, 2117 (2017).
- [298] A. TORCHE and G. BESTER:  
First-principles many-body theory for charged and neutral excitations: trion fine structure splitting in transition metal dichalcogenides,  
*Phys. Rev. B* **100**, 201403 (2019).
- [299] A. ARORA, T. DEILMANN, T. REICHENAUER, J. KERN, S. MICHAELIS DE VASCONCELOS, M. ROHLFING and R. BRATSCHITSCH:  
Excited-state trions in monolayer WS<sub>2</sub>,  
*Phys. Rev. Lett.* **123**, 167401 (2019).
- [300] Y. V. ZHUMAGULOV, A. VAGOV, N. Y. SENKEVICH, D. R. GULEVICH and V. PEREBEINOS:  
Three-particle states and brightening of intervalley excitons in a doped MoS<sub>2</sub> monolayer,  
*Phys. Rev. B* **101**, 245433 (2020).
- [301] K. KHENG, R. T. COX, M. Y. D'AUBIGNÉ, F. BASSANI, K. SAMINADAYAR and S. TATARENKO:  
Observation of negatively charged excitons X<sup>-</sup> in semiconductor quantum wells,  
*Phys. Rev. Lett.* **71**, 1752–1755 (1993).
- [302] G. FINKELSTEIN, H. SHTRIKMAN and I. BAR-JOSEPH:  
Optical spectroscopy of a two-dimensional electron gas near the metal-insulator transition,  
*Phys. Rev. Lett.* **74**, 976–979 (1995).

- [303] H. BUHMANN, L. MANSOURI, J. WANG, P. H. BETON, N. MORI, L. EAVES, M. HENINI and M. POTEMSKI:  
Electron-concentration-dependent quantum-well luminescence: evidence for a negatively charged exciton,  
*Phys. Rev. B* **51**, 7969–7972 (1995).
- [304] J. S. ROSS, S. WU, H. YU, N. J. GHIMIRE, A. M. JONES, G. AIVAZIAN, J. YAN, D. G. MANDRUS, D. XIAO, W. YAO and X. XU:  
Electrical control of neutral and charged excitons in a monolayer semiconductor,  
*Nature Communications* **4**, 1474 (2013).
- [305] P. KAPUŚCIŃSKI, D. VACLAVKOVA, M. GRZESZCZYK, A. O. SLOBODENIUK, K. NOGAJEWSKI, M. BARTOS, K. WATANABE, T. TANIGUCHI, C. FAUGERAS, A. BABIŃSKI, M. POTEMSKI and M. R. MOLAS:  
Valley polarization of singlet and triplet trions in a WS<sub>2</sub> monolayer in magnetic fields,  
*Phys. Chem. Chem. Phys.* **22**, 19155–19161 (2020).
- [306] J. JADCZAK, J. KUTROWSKA-GIRZYCKA, P. KAPUŚCIŃSKI, Y. S. HUANG, A. WÓJS and L. BRYJA:  
Probing of free and localized excitons and trions in atomically thin WSe<sub>2</sub>, WS<sub>2</sub>, MoSe<sub>2</sub> and MoS<sub>2</sub> in photoluminescence and reflectivity experiments,  
*Nanotechnology* **28**, 395702 (2017).
- [307] A. CHERNIKOV, A. M. VAN DER ZANDE, H. M. HILL, A. F. RIGOSI, A. VELAUTHAPILLAI, J. HONE and T. F. HEINZ:  
Electrical tuning of exciton binding energies in monolayer WS<sub>2</sub>,  
*Phys. Rev. Lett.* **115**, 126802 (2015).
- [308] J. HUANG, T. B. HOANG and M. H. MIKKELSEN:  
Probing the origin of excitonic states in monolayer WSe<sub>2</sub>,  
*Scientific Reports* **6**, 22414 (2016).
- [309] H. YU, G.-B. LIU, P. GONG, X. XU and W. YAO:  
Dirac cones and dirac saddle points of bright excitons in monolayer transition metal dichalcogenides,  
*Nature Communications* **5**, 3876 (2014).
- [310] A. M. JONES, H. YU, J. R. SCHAIBLEY, J. YAN, D. G. MANDRUS, T. TANIGUCHI, K. WATANABE, H. DERY, W. YAO and X. XU:  
Excitonic luminescence upconversion in a two-dimensional semiconductor,  
*Nature Physics* **12**, 323 (2016).
- [311] A. SINGH, K. TRAN, M. KOLARCZYK, J. SEIFERT, Y. WANG, K. HAO, D. PLESKOT, N. M. GABOR, S. HELMRICH, N. OWSCHIMIKOW, U. WOGGON and X. LI:  
Long-lived valley polarization of intravalley trions in monolayer WSe<sub>2</sub>,  
*Phys. Rev. Lett.* **117**, 257402 (2016).
- [312] Z. WANG, L. ZHAO, K. F. MAK and J. SHAN:  
Probing the spin-polarized electronic band structure in monolayer transition metal dichalcogenides by optical spectroscopy,  
*Nano Letters* **17**, PMID: 28103668, 740–746 (2017).
- [313] A. BOULESBAA, B. HUANG, K. WANG, M.-W. LIN, M. MAHJOURI-SAMANI, C. ROULEAU, K. XIAO, M. YOON, B. SUMPTER, A. PURETZKY and D. GEOHEGAN:  
Observation of two distinct negative trions in tungsten disulfide monolayers,  
*Phys. Rev. B* **92**, 115443 (2015).

- [314] G. PLECHINGER, P. NAGLER, A. ARORA, R. SCHMIDT, A. CHERNIKOV, A. G. DEL ÁGUILA, P. C. CHRISTIANEN, R. BRATSCHITSCH, C. SCHÜLLER and T. KORN:  
Trion fine structure and coupled spin–valley dynamics in monolayer tungsten disulfide,  
*Nature Communications* **7**, 12715 (2016).
- [315] D. VACLAVKOVA, J. WYZULA, K. NOGAJEWSKI, M. BARTOS, A. O. SLOBODENIUK, C. FAUGERAS, M. POTEMSKI and M. R. MOLAS:  
Singlet and triplet trions in WS<sub>2</sub> monolayer encapsulated in hexagonal boron nitride,  
*Nanotechnology* **29**, 325705 (2018).
- [316] S.-Y. SHIAU, M. COMBESCOT and Y.-C. CHANG:  
Way to observe the implausible trion-polariton,  
*EPL (Europhysics Letters)* **117**, 57001 (2017).
- [317] Y. V. ZHUMAGULOV, S. CHIAVAZZO, D. R. GULEVICH, V. PEREBEINOS, I. A. SHELYKH and O. KYRIENKO:  
Microscopic theory of exciton and trion polaritons in doped monolayers of transition metal dichalcogenides,  
*npj Computational Materials* **8**, 92 (2022).
- [318] A. ESSER, R. ZIMMERMANN and E. RUNGE:  
Theory of trion spectra in semiconductor nanostructures,  
*physica status solidi (b)* **227**, 317–330 (2001).
- [319] M. COMBESCOT, O. BETBEDER-MATIBET and F. DUBIN:  
The trion: two electrons plus one hole versus one electron plus one exciton,  
*The European Physical Journal B - Condensed Matter and Complex Systems* **42**, 63–83 (2004).
- [320] M. COMBESCOT, J. TRIBOLLET, G. KARCEWSKI, F. BERNARDOT, C. TESTELIN and M. CHAMARRO:  
Many-body origin of the “trion line” in doped quantum wells,  
*Europhysics Letters* **71**, 431 (2005).
- [321] M. SIDLER, P. BACK, O. COTLET, A. SRIVASTAVA, T. FINK, M. KRONER, E. DEMLER and A. IMAMOGLU:  
Fermi polaron-polaritons in charge-tunable atomically thin semiconductors,  
*Nat. Phys.* **13**, 255 (2016).
- [322] D. K. EFIMKIN and A. H. MACDONALD:  
Exciton-polarons in doped semiconductors in a strong magnetic field,  
*Phys. Rev. B* **97**, 235432 (2018).
- [323] L. D. LANDAU:  
Electron motion in crystal lattices,  
*Phys. Z. Sowjet.* **3**, 664 (1933).
- [324] S. I. PEKAR:  
Local quantum states of electrons in an ideal ion crystal,  
*Zh. Eksp. Teor. Fiz.* **16**, 341–348 (1946).
- [325] H. FRÖHLICH:  
Electrons in lattice fields,  
*Advances in Physics* **3**, 325–361 (1954).
- [326] V. COROPCEANU, J. CORNIL, D. A. DA SILVA FILHO, Y. OLIVIER, R. SILBEY and J.-L. BRÉDAS:  
Charge transport in organic semiconductors,  
*Chemical Reviews* **107**, PMID: 17378615, 926–952 (2007).

- [327] M. WANG, C. BI, L. LI, S. LONG, Q. LIU, H. LV, N. LU, P. SUN and M. LIU: Thermoelectric seebeck effect in oxide-based resistive switching memory, *Nature Communications* **5**, 4598 (2014).
- [328] Y. NATANZON, A. AZULAY and Y. AMOYAL: Evaluation of polaron transport in solids from first-principles, *Israel Journal of Chemistry* **60**, 768–786 (2020).
- [329] J. BARDEEN, G. BAYM and D. PINES: Effective interaction of  $\text{He}^3$  atoms in dilute solutions of  $\text{He}^3$  in  $\text{He}^4$  at low temperatures, *Phys. Rev.* **156**, 207–221 (1967).
- [330] J. KONDO: Resistance minimum in dilute magnetic alloys, *Progress of Theoretical Physics* **32**, 37–49 (1964).
- [331] M. KUTSCHERA and W. WÓJCIK: Proton impurity in the neutron matter: a nuclear polaron problem, *Phys. Rev. C* **47**, 1077–1085 (1993).
- [332] M. M. FORBES, A. GEZERLIS, K. HEBELER, T. LESINSKI and A. SCHWENK: Neutron polaron as a constraint on nuclear density functionals, *Phys. Rev. C* **89**, 041301 (2014).
- [333] H. A. WELDON: Dynamical holes in the quark-gluon plasma, *Phys. Rev. D* **40**, 2410–2420 (1989).
- [334] J. T. DEVREESE and A. S. ALEXANDROV: Fröhlich polaron and bipolaron: recent developments, *Reports on Progress in Physics* **72**, 066501 (2009).
- [335] A. S. ALEXANDROV and J. T. DEVREESE: *Advances in polaron physics*, Vol. 159 (Springer, 2010).
- [336] C. FRANCHINI, M. RETICCIOLI, M. SETVIN and U. DIEBOLD: Polarons in materials, *Nature Reviews Materials* **6**, 560–586 (2021).
- [337] F. CHEVY and C. MORA: Ultra-cold polarized Fermi gases, *Reports on Progress in Physics* **73**, 112401 (2010).
- [338] P. MASSIGNAN, M. ZACCANTI and G. M. BRUUN: Polarons, dressed molecules and itinerant ferromagnetism in ultracold Fermi gases, *Reports on Progress in Physics* **77**, 034401 (2014).
- [339] J. LEVINSSEN and M. M. PARISH: Strongly interacting two-dimensional Fermi gases, *Annual Review of Cold Atoms and Molecules* **3**, 1–75 (2015).
- [340] C. CHIN, R. GRIMM, P. JULIENNE and E. TIESINGA: Feshbach resonances in ultracold gases, *Rev. Mod. Phys.* **82**, 1225–1286 (2010).
- [341] C. KOHSTALL, M. ZACCANTI, M. JAG, A. TRENKWALDER, P. MASSIGNAN, G. M. BRUUN, F. SCHRECK and R. GRIMM: Metastability and coherence of repulsive polarons in a strongly interacting Fermi mixture, *Nature* **485**, 615–618 (2012).

- [342] M. KOSCHORRECK, D. PERTOT, E. VOGT, B. FRÖHLICH, M. FELD and M. KÖHL: Attractive and repulsive Fermi polarons in two dimensions, *Nature* **485**, 619–622 (2012).
- [343] N. DARKWAH OPPONG, L. RIEGGER, O. BETTERMANN, M. HÖFER, J. LEVINSSEN, M. M. PARISH, I. BLOCH and S. FÖLLING: Observation of coherent multiorbital polarons in a two-dimensional Fermi gas, *Phys. Rev. Lett.* **122**, 193604 (2019).
- [344] G. NESS, C. SHKEDROV, Y. FLORSHAIM, O. K. DIESSEL, J. VON MILCZEWSKI, R. SCHMIDT and Y. SAGI: Observation of a smooth polaron-molecule transition in a degenerate Fermi gas, *Phys. Rev. X* **10**, 041019 (2020).
- [345] R. P. A. EMMANUELE, M. SICH, O. KYRIENKO, V. SHAHNAZARYAN, F. WITHERS, A. CATANZARO, P. M. WALKER, M. S. BENIMETSKIY F. A. ANND SKOLNICK, A. I. TARTAKOVSKII, I. A. SHELYKH and D. N. KRIZHANOVSKII: Highly nonlinear trion-polaritons in a monolayer semiconductor, *Nature Communications* **11**, 3589 (2020).
- [346] O. KOKSAL, M. JUNG, C. MANOLATOU, A. N. VAMIVAKAS, G. SHVETS and F. RANA: Structure and dispersion of exciton-trion-polaritons in two-dimensional materials: experiments and theory, *Phys. Rev. Research* **3**, 033064 (2021).
- [347] E. LIU, J. VAN BAREN, Z. LU, T. TANIGUCHI, K. WATANABE, D. SMIRNOV, Y.-C. CHANG and C. H. LUI: Exciton-polaron rydberg states in monolayer MoSe<sub>2</sub> and WSe<sub>2</sub>, *Nature Communications* **12**, 6131 (2021).
- [348] K. XIAO, T. YAN, Q. LIU, S. YANG, C. KAN, R. DUAN, Z. LIU and X. CUI: Many-body effect on optical properties of monolayer molybdenum diselenide, *The Journal of Physical Chemistry Letters* **12**, 2555–2561 (2021).
- [349] J. ZIPFEL, K. WAGNER, M. A. SEMINA, J. D. ZIEGLER, T. TANIGUCHI, K. WATANABE, M. M. GLAZOV and A. CHERNIKOV: Electron recoil effect in electrically tunable MoSe<sub>2</sub> monolayers, *Phys. Rev. B* **105**, 075311 (2022).
- [350] S. SMOLKA, W. WUESTER, F. HAUPT, S. FAELT, W. WEGSCHEIDER and A. IMAMOGLU: Cavity quantum electrodynamics with many-body states of a two-dimensional electron gas, *Science* **346**, 332–335 (2014).
- [351] D. HUANG, K. SAMPSON, Y. NI, Z. LIU, D. LIANG, K. WATANABE, T. TANIGUCHI, H. LI, E. MARTIN, J. LEVINSSEN, M. M. PARISH, E. TUTUC, D. K. EFIMKIN and X. LI: Quantum dynamics of attractive and repulsive polarons in a doped MoSe<sub>2</sub> monolayer, *Phys. Rev. X* **13**, 011029 (2023).
- [352] Z. WANG, J. SHAN and K. F. MAK: Valley- and spin-polarized landau levels in monolayer WSe<sub>2</sub>, *Nature Nanotechnology* **12**, 144–149 (2017).
- [353] T. WANG, Z. LI, Z. LU, Y. LI, S. MIAO, Z. LIAN, Y. MENG, M. BLEI, T. TANIGUCHI, K. WATANABE, S. TONGAY, W. YAO, D. SMIRNOV, C. ZHANG and S.-F. SHI: Observation of quantized exciton energies in monolayer wse<sub>2</sub> under a strong magnetic field, *Phys. Rev. X* **10**, 021024 (2020).

- [354] D. VAN TUAN, S.-F. SHI, X. XU, S. A. CROOKER and H. DERY:  
Six-body and eight-body exciton states in monolayer  $\text{WSe}_2$ ,  
[Phys. Rev. Lett. \*\*129\*\*, 076801 \(2022\)](#).
- [355] D. VAN TUAN and H. DERY:  
Composite excitonic states in doped semiconductors,  
[Phys. Rev. B \*\*106\*\*, L081301 \(2022\)](#).
- [356] A. TIENE, J. LEVINSSEN, J. KEELING, M. M. PARISH and F. M. MARCHETTI:  
Effect of fermion indistinguishability on optical absorption of doped two-dimensional semiconductors,  
[Phys. Rev. B \*\*105\*\*, 125404 \(2022\)](#).
- [357] A. TIENE, B. C. MULKERIN, J. LEVINSSEN, M. M. PARISH and F. M. MARCHETTI:  
Crossover from exciton polarons to trions in doped two-dimensional semiconductors at finite temperature,  
[10.48550/ARXIV.2212.05635 \(2022\)](#).
- [358] K. HAO, L. XU, P. NAGLER, A. SINGH, K. TRAN, C. K. DASS, C. SCHÜLLER, T. KORN, X. LI and G. MOODY:  
Coherent and Incoherent Coupling Dynamics between Neutral and Charged Excitons in Monolayer  $\text{MoSe}_2$ ,  
[Nano Letters \*\*16\*\*, PMID: 27428509, 5109–5113 \(2016\)](#).
- [359] B. C. MULKERIN, A. TIENE, F. M. MARCHETTI, M. M. PARISH and J. LEVINSSEN:  
Virial expansion for the optical response of doped two-dimensional semiconductors,  
[10.48550/ARXIV.2212.05627 \(2022\)](#).
- [360] M. E. SIEMENS, G. MOODY, H. LI, A. D. BRISTOW and S. T. CUNDIFF:  
Resonance lineshapes in two-dimensional Fourier transform spectroscopy,  
[Opt. Express \*\*18\*\*, 17699–17708 \(2010\)](#).
- [361] T. P. LYONS, D. J. GILLARD, C. LEBLANC, J. PUEBLA, D. D. SOLNYSHKOV, L. KLONPM-  
MAKER, I. A. AKIMOV, C. LOUCA, P. MUDULI, A. GENCO, M. BAYER, Y. OTANI, G.  
MALPUECH and A. I. TARTAKOVSKII:  
Giant effective Zeeman splitting in a monolayer semiconductor realized by spin-  
selective strong light–matter coupling,  
[Nature Photonics \*\*16\*\*, 632–636 \(2022\)](#).
- [362] M. A. BASTARRACHEA-MAGNANI, A. CAMACHO-GUARDIAN and G. M. BRUUN:  
Attractive and repulsive exciton-polariton interactions mediated by an electron gas,  
[Phys. Rev. Lett. \*\*126\*\*, 127405 \(2021\)](#).
- [363] I. CARUSOTTO:  
Material makes photons bulky,  
[Physics \*\*13\*\*, 56 \(2020\)](#).
- [364] E. TOGAN, H.-T. LIM, S. FAELT, W. WEGSCHEIDER and A. IMAMOGLU:  
Enhanced interactions between dipolar polaritons,  
[Phys. Rev. Lett. \*\*121\*\*, 227402 \(2018\)](#).
- [365] O. KYRIENKO, D. N. KRIZHANOVSKII and I. A. SHELYKH:  
Nonlinear quantum optics with trion polaritons in 2D monolayers: conventional and  
unconventional photon blockade,  
[Phys. Rev. Lett. \*\*125\*\*, 197402 \(2020\)](#).
- [366] O. COTLE †, F. PIENKA, R. SCHMIDT, G. ZARAND, E. DEMLER and A. IMAMOGLU:  
Transport of neutral optical excitations using electric fields,  
[Phys. Rev. X \*\*9\*\*, 041019 \(2019\)](#).

- [367] T. CHERVY, P. KNÜPPEL, H. ABBASPOUR, M. LUPATINI, S. FÁLT, W. WEGSCHEIDER, M. KRONER and A. IMAMO ĞLU:  
Accelerating polaritons with external electric and magnetic fields,  
*Phys. Rev. X* **10**, 011040 (2020).
- [368] Y. SHIMAZAKI, C. KUHNENKAMP, I. SCHWARTZ, T. SMOLE ŃSKI, K. WATANABE, T. TANIGUCHI, M. KRONER, R. SCHMIDT, M. KNAP and A. IMAMO ĞLU:  
Optical signatures of periodic charge distribution in a Mott-like correlated insulator state,  
*Phys. Rev. X* **11**, 021027 (2021).
- [369] A. POPERT, Y. SHIMAZAKI, M. KRONER, K. WATANABE, T. TANIGUCHI, A. IMAMOĞLU and T. SMOLEŃSKI:  
Optical sensing of fractional quantum Hall effect in graphene,  
*Nano Letters* **22**, PMID: 36124418, 7363–7369 (2022).
- [370] I. SCHWARTZ, Y. SHIMAZAKI, C. KUHNENKAMP, K. WATANABE, T. TANIGUCHI, M. KRONER and A. IMAMOĞLU:  
Electrically tunable Feshbach resonances in twisted bilayer semiconductors,  
*Science* **374**, 336–340 (2021).
- [371] L. R. MEAD and J. GODINES:  
An analytical example of renormalization in two-dimensional quantum mechanics,  
*American Journal of Physics* **59**, 935–937 (1991).
- [372] M. RANDERIA, J.-M. DUAN and L.-Y. SHIEH:  
Bound states, cooper pairing, and Bose condensation in two dimensions,  
*Phys. Rev. Lett.* **62**, 981–984 (1989).
- [373] M. M. PARISH:  
Polaron-molecule transitions in a two-dimensional Fermi gas,  
*Phys. Rev. A* **83**, 051603 (2011).
- [374] M. M. PARISH and J. LEVINSSEN:  
Highly polarized Fermi gases in two dimensions,  
*Phys. Rev. A* **87**, 033616 (2013).
- [375] F. CHEVY:  
Universal phase diagram of a strongly interacting Fermi gas with unbalanced spin populations,  
*Phys. Rev. A* **74**, 063628 (2006).
- [376] R. COMBESCOT and S. GIRAUD:  
Normal state of highly polarized Fermi gases: full many-body treatment,  
*Phys. Rev. Lett.* **101**, 050404 (2008).
- [377] L. POLLET:  
Recent developments in quantum Monte Carlo simulations with applications for cold gases,  
*Reports on Progress in Physics* **75**, 094501 (2012).
- [378] K. VAN HOUCKE, F. WERNER and R. ROSSI:  
High-precision numerical solution of the Fermi polaron problem and large-order behavior of its diagrammatic series,  
*Phys. Rev. B* **101**, 045134 (2020).
- [379] R. COMBESCOT, A. RECATI, C. LOBO and F. CHEVY:  
Normal state of highly polarized Fermi gases: simple many-body approaches,  
*Phys. Rev. Lett.* **98**, 180402 (2007).

- [380] V. NGAMPRUETIKORN, J. LEVINSEN and M. M. PARISH:  
Repulsive polarons in two-dimensional Fermi gases,  
*Europhysics Letters* **98**, 30005 (2012).
- [381] C. FEY, P. SCHMELCHER, A. IMAMOGLU and R. SCHMIDT:  
Theory of exciton-electron scattering in atomically thin semiconductors,  
*Phys. Rev. B* **101**, 051417 (2020).
- [382] O. GOULKO, A. S. MISHCHENKO, N. PROKOF'EV and B. SVISTUNOV:  
Dark continuum in the spectral function of the resonant Fermi polaron,  
*Phys. Rev. A* **94**, 051605 (2016).
- [383] V. HUARD, R. T. COX, K. SAMINADAYAR, A. ARNOULT and S. TATARENKO:  
Bound states in optical absorption of semiconductor quantum wells containing a two-dimensional electron gas,  
*Phys. Rev. Lett.* **84**, 187 (2000).
- [384] R. SCHMIDT, T. ENSS, V. PIETILÄ and E. DEMLER:  
Fermi polarons in two dimensions,  
*Phys. Rev. A* **85**, 021602 (2012).
- [385] R. LIU, C. PENG and X. CUI:  
Emergence of crystalline few-body correlations in mass-imbalanced Fermi polarons,  
*Cell Reports Physical Science* **3**, 100993 (2022).
- [386] D. NANDI, A. D. K. FINCK, J. P. EISENSTEIN, L. N. PFEIFFER and K. W. WEST:  
Exciton condensation and perfect Coulomb drag,  
*Nature* **488**, 481–484 (2012).
- [387] M. BAETEN and M. WOUTERS:  
Many-body effects of a two-dimensional electron gas on trion-polaritons,  
*Phys. Rev. B* **91**, 115313 (2015).
- [388] I. BLOCH, J. DALIBARD and W. ZWERGER:  
Many-body physics with ultracold gases,  
*Rev. Mod. Phys.* **80**, 885–964 (2008).
- [389] A. SCHIROTZEK, C.-H. WU, A. SOMMER and M. W. ZWIERLEIN:  
Observation of Fermi polarons in a tunable Fermi liquid of ultracold atoms,  
*Phys. Rev. Lett.* **102**, 230402 (2009).
- [390] M. CETINA, M. JAG, R. S. LOUS, I. FRITSCHKE, J. T. M. WALRAVEN, R. GRIMM, J. LEVINSEN, M. M. PARISH, R. SCHMIDT, M. KNAP and E. DEMLER:  
Ultrafast many-body interferometry of impurities coupled to a Fermi sea,  
*Science* **354**, 96–99 (2016).
- [391] K. MARTIYANOV, V. MAKHALOV and A. TURLAPOV:  
Observation of a two-dimensional Fermi gas of atoms,  
*Phys. Rev. Lett.* **105**, 030404 (2010).
- [392] B. FRÖHLICH, M. FELD, E. VOGT, M. KOSCHORRECK, W. ZWERGER and M. KÖHL:  
Radio-frequency spectroscopy of a strongly interacting two-dimensional Fermi gas,  
*Phys. Rev. Lett.* **106**, 105301 (2011).
- [393] P. DYKE, E. D. KUHNLE, S. WHITLOCK, H. HU, M. MARK, S. HOINKA, M. LINGHAM, P. HANNAFORD and C. J. VALE:  
Crossover from 2D to 3D in a weakly interacting Fermi gas,  
*Phys. Rev. Lett.* **106**, 105304 (2011).
- [394] S. PALZER, C. ZIPKES, C. SIAS and M. KÖHL:  
Quantum transport through a Tonks-Girardeau gas,  
*Phys. Rev. Lett.* **103**, 150601 (2009).

- [395] F. MEINERT, M. KNAP, E. KIRILOV, K. JAG-LAUBER, M. B. ZVONAREV, E. DEMLER and H.-C. NÄGERL:  
Bloch oscillations in the absence of a lattice,  
*Science* **356**, 945–948 (2017).
- [396] N. B. JØRGENSEN, L. WACKER, K. T. SKALMSTANG, M. M. PARISH, J. LEVINSSEN, R. S. CHRISTENSEN, G. M. BRUUN and J. J. ARLT:  
Observation of attractive and repulsive polarons in a Bose-Einstein condensate,  
*Phys. Rev. Lett.* **117**, 055302 (2016).
- [397] M.-G. HU, M. J. VAN DE GRAAFF, D. KEDAR, J. P. CORSON, E. A. CORNELL and D. S. JIN:  
Bose polarons in the strongly interacting regime,  
*Phys. Rev. Lett.* **117**, 055301 (2016).
- [398] Z. Z. YAN, Y. NI, C. ROBENS and M. W. ZWIERLEIN:  
Bose polarons near quantum criticality,  
*Science* **368**, 190–194 (2020).
- [399] P. TÖRMÄ:  
Physics of ultracold Fermi gases revealed by spectroscopies,  
*Physica Scripta* **91**, 043006 (2016).
- [400] M. PUNK and W. ZWERGER:  
Theory of rf-spectroscopy of strongly interacting fermions,  
*Phys. Rev. Lett.* **99**, 170404 (2007).
- [401] P. MASSIGNAN, G. M. BRUUN and H. T. C. STOOFF:  
Twin peaks in rf spectra of Fermi gases at unitarity,  
*Phys. Rev. A* **77**, 031601 (2008).
- [402] C. J. VALE and M. ZWIERLEIN:  
Spectroscopic probes of quantum gases,  
*Nature Physics* **17**, 1305–1315 (2021).
- [403] Z. YAN, P. B. PATEL, B. MUKHERJEE, R. J. FLETCHER, J. STRUCK and M. W. ZWIERLEIN:  
Boiling a unitary Fermi liquid,  
*Phys. Rev. Lett.* **122**, 093401 (2019).
- [404] C. MORA and F. CHEVY:  
Ground state of a tightly bound composite dimer immersed in a Fermi sea,  
*Phys. Rev. A* **80**, 033607 (2009).
- [405] M. PUNK, P. T. DUMITRESCU and W. ZWERGER:  
Polaron-to-molecule transition in a strongly imbalanced Fermi gas,  
*Phys. Rev. A* **80**, 053605 (2009).
- [406] R. COMBESCOT, S. GIRAUD and X. LEYRONAS:  
Analytical theory of the dressed bound state in highly polarized Fermi gases,  
*Europhysics Letters* **88**, 60007 (2010).
- [407] N. V. PROKOF'EV and B. V. SVISTUNOV:  
Bold diagrammatic Monte Carlo: a generic sign-problem tolerant technique for polaron models and possibly interacting many-body problems,  
*Phys. Rev. B* **77**, 125101 (2008).
- [408] C. J. M. MATHY, M. M. PARISH and D. A. HUSE:  
Trimers, molecules, and polarons in mass-imbalanced atomic Fermi gases,  
*Phys. Rev. Lett.* **106**, 166404 (2011).

- [409] A. M. CLOGSTON:  
Upper limit for the critical field in hard superconductors,  
*Phys. Rev. Lett.* **9**, 266–267 (1962).
- [410] R. CASALBUONI and G. NARDULLI:  
Inhomogeneous superconductivity in condensed matter and QCD,  
*Rev. Mod. Phys.* **76**, 263–320 (2004).
- [411] C. H. SCHUNCK, Y. SHIN, A. SCHIROTZEK, M. W. ZWIERLEIN and W. KETTERLE:  
Pairing without superfluidity: the ground state of an imbalanced Fermi mixture,  
*Science* **316**, 867–870 (2007).
- [412] K. GUBBELS and H. STOOF:  
Imbalanced Fermi gases at unitarity,  
*Physics Reports* **525**, Imbalanced Fermi Gases at Unitarity, 255–313 (2013).
- [413] L. RADZIHOVSKY and D. E. SHEEHY:  
Imbalanced Feshbach-resonant Fermi gases,  
*Rep. Prog. Phys.* **73**, 076501 (2010).
- [414] M. M. PARISH, F. M. MARCHETTI, A. LAMACRAFT and B. D. SIMONS:  
Finite-temperature phase diagram of a polarized Fermi condensate,  
*Nature Physics* **3**, 124–128 (2007).
- [415] D. F. AGTERBERG, J. S. DAVIS, S. D. EDKINS, E. FRADKIN, D. J. VAN HARLINGEN,  
S. A. KIVELSON, P. A. LEE, L. RADZIHOVSKY, J. M. TRANQUADA and Y. WANG:  
The physics of pair-density waves: cuprate superconductors and beyond,  
*Annual Review of Condensed Matter Physics* **11**, 231–270 (2020).
- [416] D. E. SHEEHY and L. RADZIHOVSKY:  
BEC–BCS crossover, phase transitions and phase separation in polarized resonantly-  
paired superfluids,  
*Annals of Physics* **322**, 1790–1924 (2007).
- [417] W. V. LIU and F. WILCZEK:  
Interior gap superfluidity,  
*Phys. Rev. Lett.* **90**, 047002 (2003).
- [418] G. SARMA:  
On the influence of a uniform exchange field acting on the spins of the conduction  
electrons in a superconductor,  
*Journal of Physics and Chemistry of Solids* **24**, 1029–1032 (1963).
- [419] J. R. VARLEY and D. K. K. LEE:  
Structure of exciton condensates in imbalanced electron-hole bilayers,  
*Phys. Rev. B* **94**, 174519 (2016).
- [420] A. STRASHKO, F. M. MARCHETTI, A. H. MACDONALD and J. KEELING:  
Crescent states in charge-imbalanced polariton condensates,  
*Phys. Rev. Lett.* **125**, 067405 (2020).
- [421] F. BRONOLD:  
Absorption spectrum of a weakly n-doped semiconductor quantum well,  
*Phys. Rev. B* **61**, 12620–12623 (2000).
- [422] M. R. CARBONE, M. Z. MAYERS and D. R. REICHMAN:  
Microscopic model of the doping dependence of linewidths in monolayer transition  
metal dichalcogenides,  
*The Journal of Chemical Physics* **152**, 194705 (2020).

- [423] W. E. LIU, J. LEVINSSEN and M. M. PARISH:  
Variational approach for impurity dynamics at finite temperature,  
*Phys. Rev. Lett.* **122**, 205301 (2019).
- [424] X.-J. LIU:  
Virial expansion for a strongly correlated Fermi system and its application to ultracold atomic Fermi gases,  
*Physics Reports* **524**, 37–83 (2013).
- [425] Y. ZHANG, W. ONG, I. ARAKELYAN and J. E. THOMAS:  
Polaron-to-polaron transitions in the radio-frequency spectrum of a quasi-two-dimensional Fermi gas,  
*Phys. Rev. Lett.* **108**, 235302 (2012).
- [426] F. SCAZZA, G. VALTOLINA, P. MASSIGNAN, A. RECATI, A. AMICO, A. BURCHIANTI, C. FORT, M. INGUSCIO, M. ZACCANTI and G. ROATI:  
Repulsive Fermi polarons in a resonant mixture of ultracold  ${}^6\text{Li}$  atoms,  
*Phys. Rev. Lett.* **118**, 083602 (2017).
- [427] H. S. ADLONG, W. E. LIU, F. SCAZZA, M. ZACCANTI, N. D. OPPONG, S. FÖLLING, M. M. PARISH and J. LEVINSSEN:  
Quasiparticle lifetime of the repulsive Fermi polaron,  
*Phys. Rev. Lett.* **125**, 133401 (2020).
- [428] W. E. LIU, Z.-Y. SHI, J. LEVINSSEN and M. M. PARISH:  
Radio-frequency response and contact of impurities in a quantum gas,  
*Phys. Rev. Lett.* **125**, 065301 (2020).
- [429] J. LEVINSSEN and M. M. PARISH:  
Strongly interacting two-dimensional Fermi gases,  
*Annual Review of Cold Atoms and Molecules* **3**, 1–75 (2015).
- [430] R. KUBO:  
Statistical-mechanical theory of irreversible processes. i. general theory and simple applications to magnetic and conduction problems,  
*Journal of the Physical Society of Japan* **12**, 570 (1957).
- [431] P. C. MARTIN and J. SCHWINGER:  
Theory of many-particle systems. i,  
*Phys. Rev.* **115**, 1342 (1959).
- [432] E. H. KENNARD:  
On the thermodynamics of fluorescence,  
*Phys. Rev.* **11**, 29 (1918).
- [433] B. I. STEPANOV:  
Universal relation between the absorption spectra and luminescence spectra of complex molecules,  
*Sov. Phys. Dokl.* **2**, 81 (1957).
- [434] D. E. MCCUMBER:  
Einstein relations connecting broadband emission and absorption spectra,  
*Phys. Rev.* **136**, A954 (1964).
- [435] W. VAN ROOSBROECK and W. SHOCKLEY:  
Photon-radiative recombination of electrons and holes in germanium,  
*Phys. Rev.* **94**, 1558 (1954).
- [436] J. R. ENGELBRECHT and M. RANDERIA:  
Low-density repulsive Fermi gas in two dimensions: bound-pair excitations and Fermi-liquid behavior,  
*Phys. Rev. B* **45**, 12419–12434 (1992).

- [437] J. W. CHRISTOPHER, B. B. GOLDBERG and A. K. SWAN:  
Long tailed trions in monolayer MoS<sub>2</sub>: temperature dependent asymmetry and resulting red-shift of trion photoluminescence spectra,  
*Scientific Reports* **7**, 14062 (2017).
- [438] A. VEDENOV and A. LARKIN:  
Equation of state of a plasma,  
*JETP* **9**, 806 (1959).
- [439] R. L. SIDDON and M. SCHICK:  
Low-density helium monolayers as two-dimensional imperfect gases: an analysis employing the second virial coefficient,  
*Phys. Rev. A* **9**, 907–924 (1974).
- [440] C. HOROWITZ and A. SCHWENK:  
Cluster formation and the virial equation of state of low-density nuclear matter,  
*Nuclear Physics A* **776**, 55–79 (2006).
- [441] T.-L. HO and E. J. MUELLER:  
High temperature expansion applied to fermions near Feshbach resonance,  
*Phys. Rev. Lett.* **92**, 160404 (2004).
- [442] H. HU, X.-J. LIU, P. D. DRUMMOND and H. DONG:  
Pseudogap pairing in ultracold Fermi atoms,  
*Phys. Rev. Lett.* **104**, 240407 (2010).
- [443] C. CHAFIN and T. SCHÄFER:  
Scale breaking and fluid dynamics in a dilute two-dimensional Fermi gas,  
*Phys. Rev. A* **88**, 043636 (2013).
- [444] V. NGAMPRUETIKORN, J. LEVINSEN and M. M. PARISH:  
Pair correlations in the two-dimensional Fermi gas,  
*Phys. Rev. Lett.* **111**, 265301 (2013).
- [445] M. BARTH and J. HOFMANN:  
Pairing effects in the nondegenerate limit of the two-dimensional Fermi gas,  
*Phys. Rev. A* **89**, 013614 (2014).
- [446] V. NGAMPRUETIKORN, M. M. PARISH and J. LEVINSEN:  
High-temperature limit of the resonant Fermi gas,  
*Phys. Rev. A* **91**, 013606 (2015).
- [447] M. SUN and X. LEYRONAS:  
High-temperature expansion for interacting fermions,  
*Phys. Rev. A* **92**, 053611 (2015).
- [448] M. SUN, H. ZHAI and X. CUI:  
Visualizing the Efimov correlation in Bose polarons,  
*Phys. Rev. Lett.* **119**, 013401 (2017).
- [449] A. LARKIN, V. MEL'NIKOV and D. KHMEL'NITSKII:  
Virial expansion for magnetic impurities in metals,  
*JETP* **33**, 458 (1971).
- [450] Y. NISHIDA:  
Electron spin resonance in a dilute magnon gas as a probe of magnon scattering resonances,  
*Phys. Rev. B* **88**, 224402 (2013).
- [451] J. HOFMANN, M. BARTH and W. ZWERGER:  
Short-distance properties of Coulomb systems,  
*Phys. Rev. B* **87**, 235125 (2013).

- [452] S. K. ADHIKARI:  
Quantum scattering in two dimensions,  
*American Journal of Physics* **54**, 362–367 (1986).
- [453] X. LEYRONAS:  
Virial expansion with Feynman diagrams,  
*Physical Review A* **84**, 053633 (2011).
- [454] Y. TANG, L. LI, T. LI, Y. XU, S. LIU, K. BARMAK, K. WATANABE, T. TANIGUCHI,  
A. H. MACDONALD, J. SHAN and K. F. MAK:  
Simulation of hubbard model physics in WSe<sub>2</sub>/WS<sub>2</sub> moiré superlattices,  
*Nature* **579**, 353–358 (2020).
- [455] Y. SHIMAZAKI, I. SCHWARTZ, K. WATANABE, T. TANIGUCHI, M. KRONER and T.  
IMAMOĞLU:  
Strongly correlated electrons and hybrid excitons in a moiré heterostructure,  
*Nature* **580**, 472–477 (2020).
- [456] A. J. CAMPBELL, M. BROTONS-GISBERT, H. BAEK, V. VITALE, T. TANIGUCHI, K.  
WATANABE, J. LISCHNER and B. D. GERARDOT:  
Exciton-polarons in the presence of strongly correlated electronic states in a  
MoSe<sub>2</sub>/WSe<sub>2</sub> moiré superlattice,  
[arXiv:2202.08879](https://arxiv.org/abs/2202.08879) (2022).
- [457] Z. YU and C. J. PETHICK:  
Induced interactions in dilute atomic gases and liquid helium mixtures,  
*Phys. Rev. A* **85**, 063616 (2012).
- [458] J. B. MUIR, J. LEVINSSEN, S. K. EARL, M. A. CONWAY, J. H. COLE, M. WURDACK,  
R. MISHRA, D. J. ING, E. ESTRECHO, Y. LU, D. K. EFIMKIN, J. O. TOLLERUD, E. A.  
OSTROVSKAYA, M. M. PARISH and J. A. DAVIS:  
Interactions between Fermi polarons in monolayer WS<sub>2</sub>,  
*Nature Communications* **13**, 6164 (2022).
- [459] Y. LI, J. LUDWIG, T. LOW, A. CHERNIKOV, X. CUI, G. AREFE, Y. D. KIM, A. M.  
VAN DER ZANDE, A. RIGOSI, H. M. HILL, S. H. KIM, J. HONE, Z. LI, D. SMIRNOV  
and T. F. HEINZ:  
Valley splitting and polarization by the Zeeman effect in monolayer MoSe<sub>2</sub>,  
*Phys. Rev. Lett.* **113**, 266804 (2014).
- [460] D. MACNEILL, C. HEIKES, K. F. MAK, Z. ANDERSON, A. KORMÁNYOS, V. ZÓLYOMI,  
J. PARK and D. C. RALPH:  
Breaking of valley degeneracy by magnetic field in monolayer MoSe<sub>2</sub>,  
*Phys. Rev. Lett.* **114**, 037401 (2015).
- [461] G. AIVAZIAN, Z. GONG, A. M. JONES, R.-L. CHU, J. YAN, D. G. MANDRUS, C. ZHANG,  
D. COBDEN, W. YAO and X. XU:  
Magnetic control of valley pseudospin in monolayer WSe<sub>2</sub>,  
*Nature Physics* **11**, 148–152 (2015).
- [462] A. SRIVASTAVA, M. SIDLER, A. V. ALLAIN, D. S. LEMBKE, A. KIS and A. IMAMOĞLU:  
Valley Zeeman effect in elementary optical excitations of monolayer WSe<sub>2</sub>,  
*Nature Physics* **11**, 141–147 (2015).
- [463] A. V. STIER, K. M. MCCREARY, B. T. JONKER, J. KONO and S. A. CROOKER:  
Exciton diamagnetic shifts and valley Zeeman effects in monolayer WS<sub>2</sub> and MoS<sub>2</sub>  
to 65 Tesla,  
*Nature Communications* **7**, 10643 (2016).

- [464] T. DEILMANN, P. KRÜGER and M. ROHLFING:  
Ab initio studies of exciton  $g$  factors: Monolayer transition metal dichalcogenides in magnetic fields,  
[Phys. Rev. Lett. \*\*124\*\*, 226402 \(2020\)](#).
- [465] Z. EZAWA:  
*Quantum Hall effects: field theoretical approach and related topics*,  
(World Scientific, 2008).
- [466] A. KORMÁNYOS, P. RAKYTA and G. BURKARD:  
Landau levels and Shubnikov–de Haas oscillations in monolayer transition metal dichalcogenide semiconductors,  
[New Journal of Physics \*\*17\*\*, 103006 \(2015\)](#).
- [467] S. N. WALCK and T. L. REINECKE:  
Exciton diamagnetic shift in semiconductor nanostructures,  
[Phys. Rev. B \*\*57\*\*, 9088–9096 \(1998\)](#).
- [468] P. BACK, M. SIDLER, O. COTLET, A. SRIVASTAVA, N. TAKEMURA, M. KRONER and A. IMAMO ĞLU:  
Giant paramagnetism-induced valley polarization of electrons in charge-tunable monolayer MoSe<sub>2</sub>,  
[Phys. Rev. Lett. \*\*118\*\*, 237404 \(2017\)](#).
- [469] M. J. SNELLING, G. P. FLINN, A. S. PLAUT, R. T. HARLEY, A. C. TROPPER, R. ECCLESTON and C. C. PHILLIPS:  
Magnetic  $g$  factor of electrons in GaAs/Al <sub>$x$</sub> Ga<sub>1- $x$</sub> As quantum wells,  
[Phys. Rev. B \*\*44\*\*, 11345–11352 \(1991\)](#).
- [470] S. TARUCHA, H. OKAMOTO, Y. IWASA and N. MIURA:  
Exciton binding energy in GaAs quantum wells deduced from magneto-optical absorption measurement,  
[Solid State Communications \*\*52\*\*, 815–819 \(1984\)](#).
- [471] L. PRICOUPENKO and P. PEDRI:  
Universal (1 + 2)-body bound states in planar atomic waveguides,  
[Phys. Rev. A \*\*82\*\*, 033625 \(2010\)](#).
- [472] G. LI, O. BLEU, M. M. PARISH and J. LEVINSSEN:  
Enhanced scattering between electrons and exciton-polaritons in a microcavity,  
[Phys. Rev. Lett. \*\*126\*\*, 197401 \(2021\)](#).
- [473] G. LI, O. BLEU, J. LEVINSSEN and M. M. PARISH:  
Theory of polariton-electron interactions in semiconductor microcavities,  
[Phys. Rev. B \*\*103\*\*, 195307 \(2021\)](#).
- [474] M. BORN and R. OPPENHEIMER:  
Zur quantentheorie der molekeln,  
[Annalen der Physik \*\*389\*\*, 457 \(1927\)](#).
- [475] V. NGAMPRUETIKORN, M. M. PARISH and J. LEVINSSEN:  
Three-body problem in a two-dimensional Fermi gas,  
[EPL \*\*102\*\*, 13001 \(2013\)](#).
- [476] H. AKBAS and O. T. TURGUT:  
Born-oppenheimer type approximation for a simple renormalizable system,  
in *Mathematical challenges of zero-range physics*, edited by A. Michelangeli (2021), pp. 177–214.
- [477] W. H. PRESS, S. A. TEUKOLSKY, W. T. VETTERLING and B. P. FLANNERY:  
*Numerical recipes*,  
3rd ed. (Cambridge University Press, 2007).

- [478] D. S. PETROV:  
The few-atom problem,  
in Proceedings of the les houches summer schools, session 94, edited by C. Salomon,  
G. V. Shlyapnikov and L. F. Cugliandolo, preprint available at arXiv:1206.5752  
(2013), p. 109.
- [479] M. COMBESCOT and J. TRIBOLLET:  
Trion oscillator strength,  
*Solid State Communications* **128**, 273 (2003).
- [480] J. LEVINSEN, F. M. MARCHETTI, J. KEELING and M. M. PARISH:  
Spectroscopic signatures of quantum many-body correlations in polariton microcavities,  
*Phys. Rev. Lett.* **123**, 266401 (2019).
- [481] R. HAYDOCK, V. HEINE and M. J. KELLY:  
Electronic structure based on the local atomic environment for tight-binding bands,  
*Journal of Physics C: Solid State Physics* **5**, 2845 (1972).
- [482] W. Ł. NAKWASKI:  
Effective masses of electrons and heavy holes in GaAs, InAs, AlAs and their ternary compounds,  
*Physica B Condensed Matter* **210**, 1–25 (1995).
- [483] H. PEELAERS and C. G. VAN DE WALLE:  
Effects of strain on band structure and effective masses in MoS<sub>2</sub>,  
*Physical Review B* **86**, 241401 (2012).
- [484] H. V. PHUC, N. N. HIEU, B. D. HOI, N. V. HIEU, T. V. THU, N. M. HUNG, V. V. ILYASOV, N. A. POKLONSKI and C. V. NGUYEN:  
Tuning the electronic properties, effective mass and carrier mobility of MoS<sub>2</sub> monolayer by strain engineering: first-principle calculations,  
*Journal of Electronic Materials* **47**, 730–736 (2018).
- [485] R. PISONI, A. KORMÁNYOS, M. BROOKS, Z. LEI, P. BACK, M. EICH, H. OVERWEG, Y. LEE, P. RICKHAUS, K. WATANABE, T. TANIGUCHI, A. IMAMOGLU, G. BURKARD, T. IHN and K. ENSSLIN:  
Interactions and magnetotransport through spin-valley coupled Landau levels in monolayer MoS<sub>2</sub>,  
*Phys. Rev. Lett.* **121**, 247701 (2018).
- [486] C. RIVA, F. M. PEETERS and K. VARGA:  
Positively charged magnetoexcitons in a semiconductor quantum well,  
*Phys. Rev. B* **64**, 235301 (2001).
- [487] A. SHIELDS, J. OSBORNE, M. SIMMONS, M. PEPPER and D. RITCHIE:  
Magneto-optical spectroscopy of positively charged excitons in GaAs quantum wells,  
*Phys. Rev. B* **52**, R5523–R5526 (1995).
- [488] K.-S. LEE and E.-H. LEE:  
Optical determination of the heavy-hole effective mass of (In, Ga)As/GaAs quantum wells,  
*ETRI Journal* **17**, 13–24 (1996).
- [489] G. V. ASTAKHOV, D. R. YAKOVLEV, S. A. CROOKER, W. OSSAU, P. C. M. CHRISTIANEN, V. V. RUDENKOV, G. KARCEWSKI, T. WOJTOWICZ and J. KOSSUT:  
Identification of singlet and triplet states of negatively charged excitons in CdTe-based quantum wells,  
*physica status solidi (c)* **1**, 551–554 (2004).

- [490] G. BARTSCH, M. GERBRACHT, D. R. YAKOVLEV, J. H. BLOKLAND, P. C. M. CHRISTIANEN, E. A. ZHUKOV, A. B. DZYUBENKO, G. KARCEWSKI, T. WOJTOWICZ, J. KOSSUT, J. C. MAAN and M. BAYER:  
Positively versus negatively charged excitons: A high magnetic field study of CdTe/Cd<sub>1-x</sub>Mg<sub>x</sub>Te quantum wells,  
*Phys. Rev. B* **83**, 235317 (2011).
- [491] T. BRUNHES, R. ANDRÉ, A. ARNOULT, J. CIBERT and A. WASIELA:  
Oscillator strength transfer from  $X$  to  $X^+$  in a CdTe quantum-well microcavity,  
*Phys. Rev. B* **60**, 11568–11571 (1999).
- [492] A. QARRY, R. RAPAPORT, G. RAMON, E. COHEN, A. RON and L. N. PFEIFFER:  
Polaritons in microcavities containing a two-dimensional electron gas,  
*Semicond. Sci. Technol.* **18**, S331 (2003).
- [493] A. L. SUBAS I, P. PIERI, G. SENATORE and B. TANATAR:  
Stability of Sarma phases in density imbalanced electron-hole bilayer systems,  
*Phys. Rev. B* **81**, 075436 (2010).
- [494] J. J. KINNUNEN, J. E. BAARSMAN, J.-P. MARTIKAINEN and P. TÖRMÄ:  
The Fulde–Ferrell–Larkin–Ovchinnikov state for ultracold fermions in lattice and harmonic potentials: a review,  
*Rep. Prog. Phys.* **81**, 046401 (2018).
- [495] A. BIANCHI, R. MOVSHOVICH, C. CAPAN, P. G. PAGLIUSO and J. L. SARRAO:  
Possible Fulde–Ferrell–Larkin–Ovchinnikov superconducting state in CeCoIn<sub>5</sub>,  
*Phys. Rev. Lett.* **91**, 187004 (2003).
- [496] S. UJI, T. TERASHIMA, M. NISHIMURA, Y. TAKAHIDE, T. KONOIKE, K. ENOMOTO, H. CUI, H. KOBAYASHI, A. KOBAYASHI, H. TANAKA, M. TOKUMOTO, E. S. CHOI, T. TOKUMOTO, D. GRAF and J. S. BROOKS:  
Vortex dynamics and the Fulde–Ferrell–Larkin–Ovchinnikov state in a magnetic-field-induced organic superconductor,  
*Phys. Rev. Lett.* **97**, 157001 (2006).
- [497] R. LORTZ, Y. WANG, A. DEMUER, P. H. M. BÖTTGER, B. BERGK, G. ZWICKNAGL, Y. NAKAZAWA and J. WOSNITZA:  
Calorimetric evidence for a Fulde–Ferrell–Larkin–Ovchinnikov superconducting state in the layered organic superconductor  $\kappa$ -(BEDT–TTF)<sub>2</sub>Cu(NCS)<sub>2</sub>,  
*Phys. Rev. Lett.* **99**, 187002 (2007).
- [498] R. BEYER, B. BERGK, S. YASIN, J. A. SCHLUETER and J. WOSNITZA:  
Angle-dependent evolution of the Fulde–Ferrell–Larkin–Ovchinnikov state in an organic superconductor,  
*Phys. Rev. Lett.* **109**, 027003 (2012).
- [499] G. KOUTROULAKIS, H. KÜHNE, J. A. SCHLUETER, J. WOSNITZA and S. E. BROWN:  
Microscopic study of the Fulde–Ferrell–Larkin–Ovchinnikov state in an all-organic superconductor,  
*Phys. Rev. Lett.* **116**, 067003 (2016).
- [500] S. SUGIURA, T. ISONO, T. TERASHIMA, S. YASUZUKA, J. A. SCHLUETER and S. UJI:  
Fulde–Ferrell–Larkin–Ovchinnikov and vortex phases in a layered organic superconductor,  
*npj Quantum Mater.* **4**, 7 (2019).
- [501] C.-w. CHO, J. H. YANG, N. F. Q. YUAN, J. SHEN, T. WOLF and R. LORTZ:  
Thermodynamic evidence for the Fulde–Ferrell–Larkin–Ovchinnikov state in the KFe<sub>2</sub>As<sub>2</sub> superconductor,  
*Phys. Rev. Lett.* **119**, 217002 (2017).

- [502] Y.-A. LIAO, A. S. C. RITTNER, T. PAPROTTA, W. LI, G. B. PARTRIDGE, R. G. HULET, S. K. BAUR and E. J. MUELLER:  
Spin-imbalance in a one-dimensional Fermi gas,  
*Nature* **467**, 567 (2010).
- [503] X. ZHU, M. S. HYBERTSEN and P. B. LITTLEWOOD:  
Electron-hole system revisited: A variational quantum Monte Carlo study,  
*Phys. Rev. B* **54**, 13575–13580 (1996).
- [504] P. PIERI, D. NEILSON and G. C. STRINATI:  
Effects of density imbalance on the BCS-BEC crossover in semiconductor electron-hole bilayers,  
*Phys. Rev. B* **75**, 113301 (2007).
- [505] K. YAMASHITA, K. ASANO and T. OHASHI:  
Quantum condensation in electron-hole bilayers with density imbalance,  
*Journal of the Physical Society of Japan* **79**, 033001 (2010).
- [506] P. B. LITTLEWOOD, P. R. EASTHAM, J. M. J. KEELING, F. M. MARCHETTI, B. D. SIMONS and M. H. SZYMANSKA:  
Models of coherent exciton condensation,  
*Journal of Physics: Condensed Matter* **16**, S3597 (2004).
- [507] D. JÉROME, T. M. RICE and W. KOHN:  
Excitonic insulator,  
*Phys. Rev.* **158**, 462–475 (1967).
- [508] C. COMTE and P. NOZIÈRES:  
Exciton Bose condensation : the ground state of an electron-hole gas - I. Mean field description of a simplified model,  
*Journal de Physique* **43**, 1069–1081 (1982).
- [509] A. İMAMOĞLU,  
private communication.
- [510] F. A. RASMUSSEN and K. S. THYGESEN:  
Computational 2D materials database: electronic structure of transition-metal dichalcogenides and oxides,  
*The Journal of Physical Chemistry C* **119**, 13169–13183 (2015).
- [511] M. M. UGEDA, A. J. BRADLEY, S.-F. SHI, F. H. DA JORNADA, Y. ZHANG, D. Y. QIU, W. RUAN, S.-K. MO, Z. HUSSAIN, Z.-X. SHEN, F. WANG, S. G. LOUIE and M. F. CROMMIE:  
Giant bandgap renormalization and excitonic effects in a monolayer transition metal dichalcogenide semiconductor,  
*Nat. Mater.* **13**, 1091 (2014).
- [512] J. MADÉO, M. K. L. MAN, C. SAHOO, M. CAMPBELL, V. PAREEK, E. L. WONG, A. AL-MAHBOOB, N. S. CHAN, A. KARMAKAR, B. M. K. MARISERLA, X. LI, T. F. HEINZ, T. CAO and K. M. DANI:  
Directly visualizing the momentum-forbidden dark excitons and their dynamics in atomically thin semiconductors,  
*Science* **370**, 1199 (2020).
- [513] M. K. L. MAN, J. MADÉO, C. SAHOO, K. XIE, M. CAMPBELL, V. PAREEK, A. KARMAKAR, E. L. WONG, A. AL-MAHBOOB, N. S. CHAN, D. R. BACON, X. ZHU, M. M. M. ABDELRASOUL, X. LI, T. F. HEINZ, F. H. DA JORNADA, T. CAO and K. M. DANI:  
Experimental measurement of the intrinsic excitonic wave function,  
*Science Advances* **7**, eabg0192 (2021).



Universidad Autónoma  
de Madrid

---